Title

Controlling the Architecture of Nanoporous Materials to Regulate Thermal Conductivity and Optical Transparency of Energy-Efficient Windows

Author

King, Sophia

Publication Date

2021

Peer reviewed|Thesis/dissertation

UNIVERSITY OF CALIFORNIA

Los Angeles

Controlling the Architecture of Nanoporous Materials to Regulate Thermal Conductivity and Optical Transparency of Energy-Efficient Windows

A dissertation submitted in partial satisfaction of the requirements for the degree of Doctor of Philosophy in Chemistry

by

Sophia King

2021

ABSTRACT OF THE DISSERTATION

Controlling the Architecture of Nanoporous Materials

to Regulate Thermal Conductivity and Optical Transparency

of Energy-Efficient Windows

by

Sophia King

Doctor of Philosophy in Chemistry

University of California, Los Angeles, 2021

Professor Sarah H. Tolbert, Chair

Transparent, insulating coatings can be applied to windows to increase the energy efficiency of buildings. Amorphous material like silica make good thermal insulators due to their local atomic disorder that impedes heat conduction. Pores can additionally be added to the material to further reduce heat conduction by decreasing the material density while adding interfaces that scatter heat carriers. This concept has been extensively used in highly porous silica aerogels, which

are valued for their ultra-low thermal conductivities. However, these aerogels significantly scatter light, and cannot be used for applications that require high optical transparency. This thesis examines four different nanoporous silica networks, synthesized using a combination of template-assisted and template-free methods, to understand the relationship between the structure of each network and its thermal conductivity, and to explore effective, scalable synthetic methods for producing nanoporous materials with optimized porosity.

In the first part of this dissertation (Chapters 2 to 5), we explore the effect of nanoscale architecture on polymer-templated silica-based networks. Silica-based thin films with various types of precursors, pore sizes, particle sizes and dopants in the network are studied. We found that although silica is amorphous, the change in the nanoscale architecture at fixed porosity and changes in the chemical composition of the walls can both be used to tune the thermal conductivity.

In the second part (Chapter 6), we combined the knowledge gained from our thin film studies to synthesize hollow silica shells that can be assembled to produce transparent, thermally insulating monoliths. We optimize the synthesis of hollow silica shells to reduce their sizes from c.a. 30 nm to below 15 nm, and then demonstrate a method to assemble those shells into mechanically robust, monoliths.

In the final part of this work (Chapter 7 and 8), we use small angle X-ray scattering to understand the structural changes that occur when silica precursors react to form wet gels and when those gels are dried to produce monoliths. Insights into the changes in the nanoscale architecture allow us to further optimize the optical transparency and minimize the thermal conductivity of the final monoliths.

This dissertation of Sophia King in approved.

Alexander Spokoyny

Chong Liu

Laurent Pilon

Sarah H. Tolbert, Committee Chair

University of California, Los Angeles

2021

To Lamar, Peanut, Ayodele, Zanaya, Nyanza, Mikayla, Towanna, and the next generation of explorers

TABLE OF CONTENTS

LIST OF FIGURES

Chapter 2: Exploring the Effect of Porous Structure on Thermal Conductivity in Templated Mesoporous Silica Films

Chapter 6: Hierarchical monoliths from sub 50 nm hollow silica shells

Chapter 7: Using Small Angle X-ray Scattering to Examine the Gelling Mechanism in Silica Nanoparticle-based Monoliths

LIST OF TABLES

LIST OF SCHEMES

Chapter 2: Exploring the Effect of Porous Structure on Thermal Conductivity in Templated Mesoporous Silica Films

Chapter 6: Hierarchical monoliths from sub 50 nm hollow silica shells

ACKNOWLEDGEMENTS

I am fortunate that my PhD experience was spent in the dynamic, intellectually challenging, often absurd space that is the Tolbert lab. I am entirely grateful to Sarah for agreeing to be my advisor and providing a nurturing environment that helped me be a better scientist and communicator. There were a few points in my PhD when I would feel overwhelmed, or as though I was not living up to the standard of what an ideal scientist was, and she encouraged me to take as many breaks as I needed, quelled my fears of failure and always encouraged questions (even the ones I thought were stupid). She has interceded for me on multiple occasions that I know of, whether to shield me from sexism or racism, and get me whatever recognition she believed I deserved. For this I am entirely grateful.

My committee members Professor Laurent Pilon, Professor Alexander Spokoyny and Professor Chong Liu were always open for guidance throughout this process and words of wisdom. I want to thank my collaborators, without them I would have just been the person who made transparent, porous materials that looks pretty under the microscope. I appreciate my mentor Yan, for showing me the ropes when I was a baby grad student. I will forever remember her telling me to focus, and, that even in my quest for perfection, I should appreciate the good enough. She was, of course, referring to imaging using one of my favorite instruments, the SEM, but I take life lessons where I can get them. I am also grateful for my mentees, Vivian, Natalie and Darrell. Their diligence and willingness as scientists helped propel my (and their) research to new levels, not only by working adjacently on the respective projects, but also by asking questions that allowed me to think deeply about what needed to be done so that I can communicate with them most effectively. Professor Pilon and his lab – Michal, Tiphaine, Ali and Sara helped tremendously with characterizing many of the materials I work with as well as were always willing to trade supplies

with us. Michal in particular will always stand out as an amazing mentor for all things mesoporous. He taught me so much about the science behind some characterization techniques. I appreciate our Saturday morning TEM sessions, where we sat for hours as he coached me on how to use my other favorite instrument. I also appreciate the willingness of Professor Hu and his lab – Man, Joon, Zihao and Suixuan to attempt to do vital the thermal conductivity measurements on my samples, even when they were not the most ideal samples at time. Professor Dunn and his lab Patricia, Maggie and Danielle were a tremendous resource for synthesis tips and tricks as my focus shifted from thin films to monoliths and were always willing to make samples for us to play around with (but actually characterize) at synchrotron.

My grad school experience would not have been as rich as it was, were it not for the instrument scientists and beamline scientists that shared a world of knowledge and were always quick to maintain broken instruments. As such, I would like to thank Dr. Ignacio Martini for keeping many of the instruments in MIC up and running and personally emailing me when he found out that an instrument I used often was down or lost the sensitivity that I may require. I would also like to thank Ivo and Wong at CNSI EICN and Billy from the Reagan lab and Mit for their help with the TEM. Additionally, I would like to thank the beamline scientists Dr. Chris Tassone, Dr. Ivan Rajkovic and Dr. Anthony Fong for their tremendous help at the Stanford Synchrotron Radiation Lightsource as well as the safety officer Grace Tang for walking us through the process of getting everything approved at the beamline and her willingness to accommodate our last minute adjustments (with the correct paperwork of course!).

My time at UCLA was also enriched by the members of my lab. I consider myself a very needy grad student and I was always able to find help when I needed to learn a new analysis technique, or use a new equipment. Since the culture of the lab is more about assisting each other,

rather than one of competition, I have made some great friends there. Notably, in addition to my mentor and mentees, I am thankful for my quasi-mentors in the Tolbert lab, Patrick for always being willing to read my writing, Terri for life lessons and encouragement, KJ and Ty for showing me the ropes at synchrotron and help presenting and writing. I would also like to acknowledge Tori (best office mate) and Andrew who made up my lunch crew. Pre-pandemic we always insisted on taking an hour off every day, away from office or lab to just unwind, and catch up on shows and our lives. When I first started grad school, the thought of taking any time from lab felt like it would set my progress back by a million years, but as it turns out, our scheduled lunches gave us something to work towards. An hour complaining about our respective projects allowed us to trade ideas ways to troubleshoot solutions as well. I also appreciated Charlene and Shreya who were the best neighbors and lab mates and were always willing to give me rides to and from campus. This turned out to be a great asset during the pandemic, when the thought of spending 45 minutes on public transportation sent my anxiety skyrocketing. I also appreciate the other members of the lab like my cohort mates Jeff, Yiyi (and again Andrew), with whom I struggled together to get homework done, the other older students like Erick, Ben, Stephen and Hyeyeon who made transitioning in grad school a bit less of a scary process, the younger students Sasha, Jack, Matthew, Edgar, Yutong, Shanlin, Joe, Danny, Helen, Casey, Kat, Susan, David, Spencer, Doran and Alex who were always willing to lend a helping hand.

I am also grateful for the INFEWS traineeship. I learnt a lot about the environment and the way me and my work fits in a more global context. More importantly, I made a lot of friends there that will hopefully last beyond graduate school. I am also grateful to the Chemistry Department as a whole, and the friends I made there. Nick, Justyna, Annie and Stephanie for all their help with paperwork, Hattie for being the best custodian, and my shuttle drivers.

In addition to the tremendous support at UCLA, I had a lot of help getting there in the first place. Therefore, I would like to thank my parents. My mother who recognized my desire to learn at a very young age and has essentially moved heaven and earth to ensure that I went as far as I desired to go. Her drive to get things done has inspired me to keep going throughout this entire process. I appreciate my father's stoicism. He taught me independence, and to take a step back whenever things would not go as predicted; to think about the problem and either find another solution, or pivot in a way that resulted in minimal waste of time and resources. I may not have been the doctor he wanted (he insisted I be a physician), but I know that he was proud of the doctor that I was becoming.

I would be remiss to not thank my extended family in Guyana, my brother, sister, cousins, aunts and uncles. They recognized that I was a huge nerd and celebrated me for it. They provided the resources I needed, be it books or their more advanced homework. They took care of me, participated in some of my wacky experiments and overall gave me the support I needed during my formative years and for forever checking up on me – even when I am not the most responsive. My teachers, from Nursery School through Upper 6th Form especially Tr. Michelle, Miss Percival, Miss Liverpool, Mr. Bernard and, of course, Mr. Carryl, my church family and all my friends: thank you for giving me the space to grow, for challenging me to learn and pushing past my comfort zone.

Transitioning to the US was no easy task. Applying to colleges from a different country with limited resources was daunting and I was unsure of where to start. Luckily, I had my cousin Hyo, who took me on campus tours the first time I visited the US and was patient in guiding me through the application process. During times of difficulty, I am grateful to many, like my God-mother, Pauline Jordon, cousins Michele Hazel and her family, sister Ashaka and her mom Yvonne,

cousin Dawn and her family and aunts and uncles who stepped up and ensured that I had everything I needed to continue my studies. At Adelphi, I met some wonderful friends like Rozi, Anustha, Jenn and Bryant, Rayyan, Diana, Vivian, Keanna, Tracy, Anthony and Gharvhel who made my experience there spectacular and my transition from FOB to FAB an easy one. Professors Widera-Kalinowska, Hyatt and Wright served as advisors, mentors and professors and helped direct me on the path that eventually led to me studying at UCLA.

Last, but certainly not least, I would like to thank my loving and supportive husband, Rafal. I appreciate his patience, words of wisdom and encouragement throughout this process. He is truly my best friend.

Thinking about the people and systems in place that have contributed to my success is an overwhelming exercise. I am immensely grateful for the strong support that I have received throughout my lifetime to this point – my formative years, my transition to school in the US and the many battles to financially afford to stay there, my transition to and completion of graduate school.

Previous Publication and Contributions of Co-Authors

Chapter 2 is the published version of Yan Yan, Sophia King, Man Li, Tiphaine Galy, Michal Marszewski, Joon Sang Kang, Laurent Pilon, Yongjie Hu and Sarah H. Tolbert's manuscript titled "Exploring the Effect of Porous Structure on the Thermal Conductivity in Templated Mesoporous Silica Films". Yan lead the synthesis of the films and characterization of the structure of the films, namely the scanning electron microscopy, porosity and pore size, Man and Joon measured the thermal conductivity, Tiphaine helped characterize the porosity of the films. I synthesized half of the films and characterized the structures using grazing-incidence small angle X-ray scattering, transmission electron microscopy and some of the porosity and pore size

measurements. Yan wrote the manuscript while Man, Tiphaine, Michal, Professor Hu, Professor Pilon, Professor Tolbert and I helped edit. Professor Tolbert and I primarily spearheaded the final revisions of this manuscript.

Chapter 3 is the published version of Yan Yan, Man Li, Sophia King, Tiphaine Galy, Michal Marszewski, Joon Sang Kang, Laurent Pilon, Yongjie Hu and Sarah H. Tolbert's manuscript titled "Controlling Thermal Conductivity in Mesoporous Silica Films Using Pore Size and Nanoscale Architecture". Yan lead the synthesis of the films and characterization of the structure of the films, namely the scanning electron microscopy, porosity and pore size, Man and Joon measured the thermal conductivity, Tiphaine helped characterize the porosity of the films. I helped synthesize some of the films and characterized the structures using grazing-incidence small angle X-ray scattering, transmission electron microscopy and some of the porosity and pore size measurements. Yan wrote the manuscript while Man, Tiphaine, Michal, Professor Hu, Professor Pilon, Professor Tolbert and I helped edit. Professor Tolbert and I primarily spearheaded the final revisions of this manuscript.

Chapter 4 is the unpublished version of Vivian Wall, Sophia King, Glareh N. Kashanchi, Suixuan Li, Darrell Henry, Man Li, Tiphaine Galy, Susan Ju, Michal Marszewski, Laurent Pilon, Yongjie Hu and Sarah H. Tolbert's manuscript titled "Understanding the Effect of Nanoparticle Size on the Thermal Conductivity in Amorphous Materials". I lead the synthesis of the films, Vivian helped develop the protocol and synthesize many of the films used, as well as measure the size of the particles. Suixuan and Man helped characterize the thermal conductivity, Glareh and Tiphaine characterized the porosity using an interferometry-based technique, Darrell developed the protocol for exchanging the counter ion of the silica nanoparticles, Michal procured all nanoparticles used, Susan helped with some powder porosimetry measurements. Vivian and I

wrote the manuscript while Suixuan, Glareh, Darrell, Man, Tiphaine, Susan Michal, Professor Hu, Professor Pilon and Professor Tolbert helped edit. This manuscript will be submitted for publication shortly after this dissertation is filed.

Chapter 5 is the published version of Sophia King, Man Li, Tiphaine Galy, Yan Yan, Joon Sang Kang, Victoria M. Basile, Yolanda L. Li, Michal Marszewski, Laurent Pilon, Yongjie Hu and Sarah H. Tolbert's manuscript titled "Examining the Role of Atomic Scale Heterogeneity on the Thermal Conductivity of Transparent, Thermally Insulating, Mesoporous Silica-Titania Thin Films". I lead the synthesis of the films and characterization of the structure of the films, namely the scanning electron microscopy, porosity and pore size, Man and Joon measured the thermal conductivity, Tiphaine helped characterize the porosity of the films. Yan helped with establishing the synthesis protocol and some of the porosity and pore size measurements. Victoria helped with XPS measurements and Yolanda with the solid state NMR. I wrote the manuscript while Man, Michal, Yan, Tiphaine, Joon, Victoria, Yolanda, Professor Hu, Professor Pilon, and Professor Tolbert helped edit. Professor Tolbert and I primarily spearheaded the final revisions of this manuscript.

Chapter 6 is the unpublished version of Sophia King, Glareh N. Kashanchi, Ali Dashti, Vivian Wall, Michal Marszewski, Tiphaine Galy, Susan Ju, Laurent Pilon and Sarah H. Tolbert's manuscript titled "Hierarchical monoliths from sub-50 nm hollow silica shells". I lead the synthesis and structural characterization of the hollow shells and monoliths, namely the transmission electron microscopy and porosity and pore size measurements. Glareh, Vivian and Susan helped with synthesis and monolith assembly. Glareh also measured some of the optical properties of the monoliths. Tiphaine helped to conduct some optical measurements of the monoliths as well. Ali measured the thermal conductivity. Michal helped establish some of the

assembly protocol. I wrote the manuscript while Glareh, Ali, Vivian, Michal, Tiphaine, Susan, Professor Pilon, and Professor Tolbert helped edit. This manuscript will be submitted for publication shortly after this dissertation is filed.

Chapter 7 is an excerpt from the unpublished version of Glareh N. Kashanchi, Sophia King, Susan Ju and Sarah H. Tolbert's manuscript titled "Using Small Angle X-ray Scattering to Examine the Gelling Mechanism in Silica Nanoparticle-based Aerogels". I designed the initial collection and analysis of the X-ray scattering data I also helped with some other structural characterization like TEM and porosimetry. Glareh synthesized all samples, spearheaded their structural characterization and assisted with the X-ray scattering data collection and analysis. She ultimately will continue additional data collection and experimental design. Susan Ju helped with data collection and analysis. Professor Tolbert helped brainstorm parameters to explore and edited this work.

Chapter 8 is an excerpt combined from the two unpublished works. The first is "Drying of Mesoporous Monoliths: from Transparent to White to Transparent Again" by Tiphaine Galy, Sophia C. King, Michal Marszewski, Patricia E. McNeil, Maggie Fox, Ali Dashti, Glareh N. Kashanchi, Glait Bar, Vivian Wall, Bruce S. Dunn, Sarah H. Tolbert and Laurent Pilon. In this work Tiphaine spearheaded the experimental design and optical characterization, I conducted small angle X-ray scattering experiments to understand change in the nanostructure of the samples, Michal, Patricia and Maggie helped with experimental design and sample synthesis, Ali Dashti assisted with some optical measurements and sample preparation, Glareh assisted with small angle X-ray scattering data collection and analysis, Galit helped provided resources to analyze the data, Vivian assisted with data collection. Professor Dunn, Professor Pilon, and Professor Tolbert helped brainstorm parameters to explore and edited this work. This manuscript will be submitted for

publication shortly after this dissertation is filed. The second is titled “Examining the Structural Change in Ambiently-dried Mesoporous Silica Monoliths Dried Under Directional Air Flow” by Glareh N. Kashanchi, Patricia E. McNeil, Sophia King, Susan Ju, Maggie Fox, Bruce Dunn and Sarah H. Tolbert’s manuscript. I designed the initial experiments, data collection and analysis of the X-ray scattering data. Glareh assisted with the initial design and ultimately will continue additional data collection and experimental design. Patricia and Maggie synthesized all samples used and helped brainstorm parameters to explore, Susan Ju helped with data collection and analysis. Professor Dunn, Professor Pilon, and Professor Tolbert helped brainstorm parameters to explore and edited this work.

The research presented in this dissertation was directed by Professor Sarah H. Tolbert and was supported by: U.S. Department of Energy Advanced Research Projects Agency-Energy (ARPA-E) under award DE-AR0000738; NSF-Research Traineeship Innovation at the Nexus of Food, Energy and Water Systems (INFEWS) (Grant DGE-1735325); University of California, Los Angeles (UCLA) Chemistry & Biochemistry Department’s John Stauffer Fellowship and the UCLA Graduate Division Dissertation Year Fellowship. Much of the diffraction data presented here was collected at the Stanford Synchrotron Radiation Lightsource, a national user facility operated by Stanford University on behalf of the U.S. Department of Energy, Office of Basic Science under contract DE-AC02-76SF00515. All of the TEM images presented here were collected using instruments at the Electron Imaging Center for NanoMachines supported by NIH (1S10RR23057 to ZHZ) and CNSI at UCLA. All NMR collected made use of equipment funded by the MRI program of the NSF under Grant 1532232.

VITA

2013-2016	Presidential Scholarship, Adelphi University
2013-2016	Recognition Award, Adelphi University
2013-2016	Math/Science Initiative Award, Adelphi University
2013-2016	Deans' List, Adelphi University
2015	Summer Undergraduate Research, Adelphi University with University of Warsaw
2016	Chemistry Departmental Award, Adelphi University
2016	American Institute of Chemists Student Award, Adelphi University
2016	Bachelors of Science, Chemistry, Adelphi University
2016-2021	Teaching Assistant, UCLA
2017-2021	Volunteer for the California Nanoscience Institute Educational Program
2018	Masters of Science, Chemistry, UCLA
2018	NSF Research Traineeship – INFEWS, UCLA
2018-2020	Treasurer of the UCLA Chapter of the Electrochemical Society
2019	UCLA Research Showcase Fellowship, UCLA
2019	John Stauffer Fellowship, UCLA
2020	Ralph and Charlene Bauer Award, UCLA
2020	Dissertation Year Fellowship, UCLA
2021	John Alan Walker Dissertation Award, UCLA
2021	Leaders in Sustainability Certificate, UCLA

PUBLICATIONS AND PRESENTATIONS

1. Marszewski, M.; King, S. C., Galy, T.; Kashanchi, G. N.; Dashti, A.; Yan, Y.; Li, M.; Butts, D. M.; McNeil, P. E.; Lan, E.; Dunn, B.; Hu, Y.; Tolbert, S. H., Pilon, L. *J. Colloid Interface Sci.*, in press

2. King, S. C.; Li, M.; Galy, T.; Yan, Y.; Kang, J. S.; Basile, V. M.; Li, Y. L.; Marszewski, M.; Pilon, L.; Hu, Y.; Tolbert, S. H. *J. Phys. Chem. C.*, **2020**, *124*, 27442-27452.

3. Butts, D. M.; McNeil, P. E.; Marszewski, M.; Lan, E.; Galy, T.; Li, M.; Kang, J. S.; Ashby, D.; King, S. C.; Tolbert, S. H.; Pilon, L.; Dunn, B. *MRS Energy and Sustainability*, **2020**, *7*, E39.

4. Lin, T.; Dawson, A.; King, S. C.; Yan, Y.; Ashby, D.; Mazzetti, J. A.; Dunn, B. S.; Weker, J. N.; Tolbert, S. H. *ACS Nano*, **2020**, *14*, 14820-14830.

5. Lin, T.; Yan, Y.; King, S. C.; Li, C.-H.; Tolbert, S. H. *ACS Appl. Mater. Interfaces*, **2020**, *12* (30), 33775-33784.

6. Yan, Y.; Li, M.; King, S. C.; Galy, T.; Marszewski, M.; Kang, J. S.; Pilon, L.; Hu, Y.; Tolbert, S. H. *J. Phys. Chem. Lett.*, **2020**, *11*, 3731-3737.

7. Galy, T.; Marszewski, M.; King, S. C.; Yan, Y.; Tolbert, S. H.; Pilon, L. *Microporous and Mesoporous Mater.*, **2020**, *291*, 109677.

8. Yan, Y.; King, S. C.; Li, M.; Galy, T.; Marszewski, M.; Kang, J. S.; Pilon, L.; Hu, Y.; Tolbert, S. H. *J. Phys. Chem. C.* **2019**, *123*, 21721-21730.

9. Marszewski, M.; King, S. C.; Yan, Y.; Galy, T.; Li, M.; Dashti, A.; Kang, J. S.; McNeil, P. E.; Lan, E.; Dunn, B.; Hu, Y.; Tolbert, S. H.; Pilon, L. *ACS Appl. Nano Mater.* **2019**, *2*, 4547-4555.

10. Scholes, D. T.; Yee, P. Y.; McKeown, G. R.; Li, S.; Kang, H.; Lindemuth, J. R.; Xia, X.; King, S. C.; Seferos, D. S.; Tolbert, S. H.; Schwartz, B. J. *Chem. Mater.* **2019**, *31* (1),73–82.

11. Marszewski, M.; Butts, D.; Lan, E.; Yan, Y.; King, S. C.; McNeil, P. E; Galy, T.; Dunn, B.; Tolbert, S. H.; Hu Y.; Pilon, L. *Appl. Phys. Lett.* **2018**, *112*, 201903.

12. Sophia C. King, Glareh Natalie Kashanchi, Sarah H. Tolbert, 2020 SSRL/LCLS User's Meeting, **2020**. (Virtual Poster)

13. Sophia C. King, Glareh Natalie Kashanchi, Vivian Wall, Michal Marszewski, Tiphaine Galy, Man Li, Zihao Qin, Yongjie Hu, Laurent Pilon, Sarah H. Tolbert, ACS Fall 2020 National Meeting, **2020**. (Virtual Talk)

14. Sophia King on behalf of: Yan, Y.; Li, M.; King, S. C.; Galy, T.; Marszewski, M.; Kang, J. S.; Pilon, L.; Hu, Y.; Tolbert, S. H. *J. Phys. Chem. Lett.*, **2020**, *11*, 3731-3737. (Liveslide presentation)

15. Sophia C. King, Vivian Wall, Yan Yan, Man Li, Tiphaine Galy, Joon Sang Kang, Michal Marszewski, Yolanda Li, Laurent Pilon, Yongjie Hu, Sarah H. Tolbert, Seaborg Symposium, **2019**. Los Angeles, CA (Poster)

16. Sophia C. King, Yan Yan, Man Li, Tiphaine Galy, Joon Sang Kang, Michal Marszewski, Yolanda Li, Laurent Pilon, Yongjie Hu, Sarah H. Tolbert, UCLA Chemistry & Biochemistry ACS Research Showcase and Reception at ACS Fall 2019 National Meeting, **2019**, San Diego, CA (Poster)

17. Sophia C. King, Yan Yan, Man Li, Tiphaine Galy, Joon Sang Kang, Michal Marszewski, Yolanda Li, Laurent Pilon, Yongjie Hu, Sarah H. Tolbert, ACS Fall 2019 National Meeting, **2019**, San Diego, CA (Talk)

18. Sophia King, Yan Yan, Man Li, Tiphaine Galy, Vivian Wall, Joon Sang Kang, Michal Marszewski, Sarah H. Tolbert, IMMS10, **2018,** Los Angeles, CA (Poster)

19. Sophia King, Yan Yan, Man Li, Tiphaine Galy, Joon Sang Kang, Michal Marszewski, Sarah H. Tolbert, Seaborg Symposium, **2017**, Los Angeles, CA (Poster)

20. Sophia King, NY-ACS Undergraduate Research Symposium, **2016**, Bronx, NY (Talk)

CHAPTER 1

Introduction

Space heating and cooling of residential buildings accounted for about 40% of the energy consumed in 2018 in the United States.[1] A significant fraction of this energy was used to maintain the temperature of a unit when heat was lost or gained across roofs, walls, floors, and windows. While a plethora of technologies have been developed to increase the insulating ability of walls, roofs and floors, consumers have very limited options when it comes to more energy efficient windows.[2,3] This is due to the need for windows to be optically transparent, a property that many insulators do not possess. To combat this issue, many buildings have switched from single- to multi-pane windows that better prevent heat conduction. However, retrofitting to these technologies can be costly since the window frame must be changed in addition to the glass itself. By designing thermally insulating coatings that can be directly deposited onto the glass of the existing windows, consumers can decrease the energy lost across windows while retaining their current window specifications.

A potential candidate for these thermally insulating coating is porous glass.[4,5] Glass is intrinsically transparent, and as a result it is currently used in most current window architectures. In addition, the atomic scale disorder (amorphous nature) of glass, combined with the presence of many solid/air interfaces in a porous network, makes the conduction of heat across the material difficult. The combination of these properties has enabled significant reduction in the thermal conductivity of bulk glass from 1.4 $W\ m^{-1}\ K^{-1}$ to 0.015 $W\ m^{-1}\ K^{-1}$ in highly porous silica aerogels (glass with at least 95% porosity).[6,7] However, silica aerogels generally do not possess the superior optical transparency of glass since they contain large pores that contribute to scattering of visible light.[8] This dissertation focuses on rectifying these often conflicting issues of high optical transparency and low thermal conductivity by designing new transparent insulators using mesoporous silica materials that can be applied to windows.

Mesoporous silica, with pore sizes between 5-50 nm can be synthesized using either template-assisted or template-free techniques with precursors that are either molecular-based that reacts to

form a nanoscale network, or from pre-formed colloids that assemble into networks. In the first part of this dissertation (Chapters 2 - 5) we use template-assisted synthesis to study the effect of nanoscale architecture on the thermal conductivity of mesoporous silica-based thin films. In template-assisted synthesis, the silica precursors self-assembles around a sacrificial template that is removed by physical or chemical treatment, leaving behind a porous thin film.[9] This simple and tunable technique we can readily change the type of precursor (NP or molecular based), the template size which influences pore size and the composition of the network at a range of porosities. This allows us to easily study the effect of nanoscale architecture, such as precursor type,[10] pore size[11] and nanoparticle size (which may influence the path length for heat conduction), and the incorporation of dopants, on thermal conductivity with a wide range of porosities.[12]

For the second part of this dissertation (Chapter 6) we use the insights gained from the thin film studies to synthesize precursors that can be scaled up in an industrial setting. There, we synthesize hollow silica shells using a template-assisted technique referred to as single micelle templating.[13] To date we have successfully synthesized hollow silica shells and reduced the diameters from 30 to 12 nm with core diameters from 15 to 7 nm, respectively to reduce optical scattering. We then assemble these shells to produce a mesoporous monolith using a scalable, template-free process. In the more scalable template-free process, the network forms by random aggregation of nanoparticles in solution.[14] Random pores are then created when the solvent is removed from the interconnected gel network. The optical, properties of these hollow shell-based monoliths were determined.

Finally, in the third part of this dissertation (Chapters 7 & 8) we use small angle X-ray scattering (SAXS) to study and optimize the structure of mesoporous monoliths made from the template-free approach as they gel at different temperatures or dry in a controlled stream of air. In these scalable monoliths, the size of the primary particles that form the network and the resulting pore size control the scattering of visible light, while the total porosity and the tortuosity of the network is related to its ability to prevent heat carrier transport.[15] Using SAXS, we can observe the change in size of primary particles in our network as they grow, as well as the arrangement of these primary particles

into a network with time. This allows us to identify specific events in the structural evolution that control thermal conductivity or optical haze.

Overall, these approaches work synergistically as insights gained from studying films made using the template-assisted technique as well as studying the silica network during processing can be used to tune the properties of template-free monoliths in order to achieve desired optical properties and thermal conductivity in scalable materials.

References

(1) U. S Energy Information Administration. Consumption and Efficiency https://www.eia.gov/consumption/ .

(2) Energy, U. S. D. of. Insulation https://www.energy.gov/energysaver/weatherize/insulation .

(3) Energy Department of the United States of America. Quadrennial Technology Review: An Assessment of Energy Technologies and Research Opportunities; 2015.

(4) Rubin, M.; Lampert, C. M. Transparent Silica Aerogels for Window Insulation. *Sol. Energy Mater.* **1983**, *7*, 393–400.

(5) Wittwer, V. Development of Aerogel Windows. *J. Non. Cryst. Solids* **1992**, *145*, 233–236.

(6) Wray, K. L.; Connolly, T. J. Thermal Conductivity of Clear Fused Silica at High Temperatures. *J. Appl. Phys.* **1959**, *30*, 1702–1705.

(7) Hrubesh, L. W.; Pekala, R. W. Thermal Properties of Organic and Inorganic Aerogels. *J. Mater. Res.* **1994**, *9*, 731–738.

(8) Jensen, K. I.; Schultz, J. M.; Kristiansen, F. H. Development of Windows Based on Highly Insulating Aerogel Glazings. *J. Non. Cryst. Solids* **2004**, *350*, 351–357.

(9) Brinker, C. J. Evaporation-Induced Self-Assembly: Functional Nanostructures Made Easy. *MRS Bull.* **2004**, *29*, 631–640.

(10) Yan, Y.; King, S. C.; Li, M.; Galy, T.; Marszewski, M.; Kang, J. S.; Pilon, L.; Hu, Y.; Tolbert, S. H. Exploring the Effect of Porous Structure on Thermal Conductivity in Templated Mesoporous Silica Films. *J. Phys. Chem. C* **2019**, *123*, 21721–21730.

(11) Yan, Y.; Li, M.; King, S.; Galy, T.; Marszewski, M.; Kang, J. S.; Pilon, L.; Hu, Y.; Tolbert, S. H. Controlling Thermal Conductivity in Mesoporous Silica Films Using Pore Size and Nanoscale Architecture. *J. Phys. Chem. Lett.* **2020**, *11*, 3731–3737.

(12) King, S. C.; Li, M.; Galy, T.; Yan, Y.; Kang, J. S.; Basile, V. M.; Li, Y. L.; Marszewski, M.; Pilon, L.; Hu, Y.; Tolbert, S. H. Examining the Role of Atomic Scale Heterogeneity on the Thermal Conductivity of Transparent, Thermally Insulating, Mesoporous Silica−titania Thin Films. *J. Phys. Chem. C* **2020**, *124*, 27442–27452.

(13) Tang, J.; Zhou, X.; Zhao, D.; Lu, G. Q.; Zou, J.; Yu, C. Hard-Sphere Packing and Icosahedral Assembly in the Formation of Mesoporous Materials. *J. Am. Chem. Soc.* **2007**, *129*, 9044–9048.

(14) Marszewski, M.; King, S. C.; Yan, Y.; Galy, T.; Li, M.; Dashti, A.; Butts, M.; Kang, J. S.; Mcneil, P. E.; Lan, E.; Tolbert, S. H.; Dunn, B.; Pilon, L. Thick Transparent Nanoparticle-Based Mesoporous SiO2 Monolithic Slabs by Template-Free Sol-Gel Synthesis on Omniphobic Liquid Substrates at Ambient Conditions. 1–23.

(15) Wang, B. Y. P.; Emmerling, A.; Tappert, W.; Spormann, O.; Fricke, J. Investigations with SAXS. *J. Appl. Crystallogr.* **1991**, *24*, 777–780.

CHAPTER 2

Exploring the Effect of Porous Structure on Thermal Conductivity in Templated Mesoporous Silica Films

Chapter 2 describes our work to understand how the constituents of the silica network (discrete nanoparticle-based vs. continuous sol-gel-based) could influence the thermal conductivity of the network.

A reprint of the supporting information is given in Appendix A.

Exploring the Effect of Porous Structure on Thermal Conductivity in Templated Mesoporous Silica Films

Yan Yan,[†] Sophia C. King,[†] Man Li,[‡] Tiphaine Galy,[‡] Michal Marszewski,[‡] Joon Sang Kang,[‡] Laurent Pilon,[‡] Yongjie Hu,[‡] and Sarah H. Tolbert*[,†,§]

[†]Department of Chemistry and Biochemistry, University of California—Los Angeles, Los Angeles, California 90095-1569, United States

[‡]Department of Mechanical and Aerospace Engineering, University of California—Los Angeles, Los Angeles, California 90095-1597, United States

[§]Department of Materials Science and Engineering, University of California—Los Angeles, Los Angeles, California 90095-1595, United States

ABSTRACT: This work elucidates the effect of porous structure on thermal conductivity of mesoporous amorphous silica. Sol–gel and nanoparticle-based mesoporous amorphous silica thin films were synthesized by evaporation-induced self-assembly using either tetraethyl orthosilicate or premade silica nanoparticles as the framework precursors with block copolymers Pluronic P123 or Pluronic F127 as template. The films were characterized with scanning- and transmission-electron microscopy, two-dimensional grazing-incidence small-angle X-ray scattering, ellipsometric porosimetry, and UV–vis reflectance spectroscopy. The thermal conductivity of the mesoporous films, at room temperature and in vacuum, was measured by time-domain thermoreflectance. The films were 150 to 800 nm thick with porosities ranging from 9% to 69%. Their pore diameters were between 3 and 19 nm, and their thermal conductivities varied between 0.07 and 0.66 W/m.K. The thermal conductivity decreased strongly with increasing porosity and was also affected by the structure of the silica framework (continuous or nanoparticulate) and the pore size. A simple porosity weighted effective medium approximation was used to explain the observed trend in thermal conductivity. These results give new insight into thermal transport in nanostructured materials, and suggest design rules of the nanoscale architecture to control the thermal conductivity of mesoporous materials for a wide range of applications.

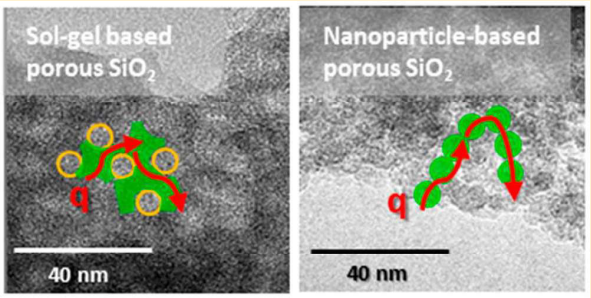

1. INTRODUCTION

Over the last few decades, mesoporous silica has been widely studied due to its simple synthesis and easily controlled structural properties. It is often used in a wide range of applications including thermally insulating materials, low-k dielectrics,[1,2] MEMS,[3,4] and window insulation.[5] Mesoporous silica is typically prepared by either template-free[6−10] or template-assisted synthesis.[11−14] In the template-free synthesis, random porosity is created by controlled gelation of dissolved molecular precursors and subsequent removal of the solvent. For instance, silica aerogels, prepared by supercritical drying of silica sol–gel without template, can reach porosities of 99%[15] and thermal conductivity of 0.013 W/m·K at room temperature and atmospheric pressure.[16] Similarly, silica ambigels can be synthesized by drying template-free silica precursors at ambient temperature and pressure. For example, Chang et al.[17] synthesized hydrophobic mesoporous silica by ambient drying and achieved a porosity of 97% and thermal conductivity of 0.034 W/m·K. However, due to high porosity and wide pore size distribution, silica aerogels and ambigels often do not have sufficient mechanical strength and/or optical transparency for a number of potential thermal barrier applications.[18]

By contrast, in template-assisted syntheses, the pores are formed by controlled gelation of molecular precursors around a template that is subsequently removed by physical or chemical treatment. Common templates include inorganic hard templates,[19,20] organic surfactants,[21,22] block copolymers,[23−26] and preformed polymer colloids.[27,28] In this approach, the pore volume and the pore size are easily controlled by choosing the amount and type of template so that pores can be kept small and homogeneous and scattering can be minimized, if needed. Several studies[29,30] report a thermal conductivity of 0.3–0.35 W/m·K at a porosity of ~30% in templated porous silica.

Received: April 22, 2019
Revised: July 24, 2019
Published: August 27, 2019

Mesoporous silica has significantly lower thermal conductivity than bulk silica for several reasons.[30,31] First, the reduced volume of the solid phase reduces the heat conduction pathways. Second, the structural factors such as pore size and its distribution can also contribute to reduction in thermal conductivity of mesoporous silica, since the mean free path of heat carriers can be suppressed due to the boundary scattering near nanosized pores.[32−35] Finally, the interfacial resistance between nanodomains can also further decrease the effective thermal conductivity. Notably, the effects of these various nanostructural factors on the thermal conductivity of mesoporous silica has not been well documented to date.

Some examples of the existing data comes from Coquil et al.,[29] who reported the cross-plane thermal conductivity of highly ordered cubic and hexagonal mesoporous amorphous silica thin films synthesized by block copolymer templating methods. They found that the average thermal conductivity was 0.3 W/mK for silica films with cubic (3D interconnected) pore structure and 25% porosity and 0.2 W/mK for silica films with a hexagonal pore structure (linear pores) and 44% porosity. They concluded that the thermal conductivity decreases with increasing porosity and is independent of film thickness. This previous work found little variation with pore diameter and wall thickness, but the mesoporous silica films explored in that study all had porosity that fell in the relatively narrow range of 20−50%. More importantly, films with different pore symmetries could not be made with the same fractional porosity. Hopkins et al.[30] confirmed that mesoporous silica films prepared by templating methods had low thermal conductivity of around 0.3 W/mK at porosity around 25% percent, using time-domain thermoreflectance technique. Fang et al.[36,37] further compared thermal conductivity of mesoporous crystalline TiO_2 films prepared by a sol−gel synthesis and mesoporous TiO_2 films made from TiO_2 nanocrystals. They showed that the thermal conductivity of nanocrystal-based TiO_2 films was 40% lower than that of mesoporous TiO_2 films prepared by a sol−gel synthesis. They attributed these results to the facts that (1) the nanocrystal-based films had additional microporosity between TiO_2 nanocrystals, (2) the nanocrystals were smaller than the polycrystalline domains in the sol−gel films, and (3) the poorly connected nanocrystals caused significant phonon scattering at the interfaces between nanocrystals. These examples show that structural factors indeed play a significant role in heat transfer though mesoporous materials. Since it has recently been revealed from both experimental work and atomistic simulation that some heat carriers in amorphous silica have propagating features,[38,39] similar confinement phenomenon of heat carriers may also exist in mesoporous silica, despite its amorphous nature.

In this study, we further elucidate the effects of structural factors on thermal conductivity of mesoporous amorphous silica with specific emphasis on the effects of (1) porosity, (2) silica nanotexture (i.e., continuous vs particulate frameworks), and (3) pore size. A wide variety of sol−gel and nanoparticle-based mesoporous amorphous silica thin films are synthesized and characterized in terms of porosity, pore size, film thickness, and thermal conductivity. The results are analyzed and compared to the effective medium approximation model. Physical arguments are provided to relate the thermal conductivity of mesoporous silica to its nanoscale architecture.

2. EXPERIMENTAL SECTION

2.1. Materials. The following materials were obtained from commercial suppliers and used without further purification: colloidal suspension of SiO_2 nanoparticles (15 wt %, Nalco 2326, ammonia-stabilized colloidal silica, d = 5 nm, Nalco Chemical Company), triblock copolymer Pluronic P123 ($EO_{20}PO_{70}EO_{20}$, M_w = 5800 Da, BASF), triblock copolymer Pluronic F127 ($EO_{100}PO_{65}EO_{100}$, M_w = 12600 Da, BASF), tetraethyl orthosilicate (98%, Acros Organics), hydrochloric acid (Certified ACS Plus, Fisher Scientific), and ethanol (200 proof, Rossville Gold Shield).

2.2. Synthesis. Both sol−gel and nanoparticle-based mesoporous silica thin films were prepared by polymer templated evaporation-induced self-assembly (Scheme 1).

Scheme 1. Synthesis of Sol-Gel and Nanoparticle-Based Mesoporous Silica Films Produced via Evaporation Induced Self-Assembly, Using Pluronic Surfactants as Template and TEOS or Preformed Silica Nanoparticles as Inorganic Precursors

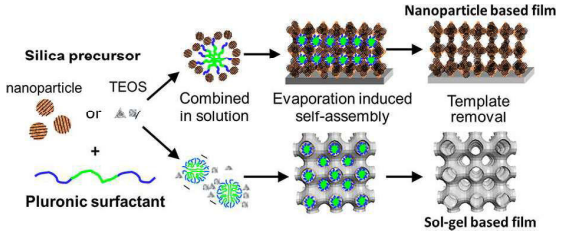

Tetraethyl orthosilicate (TEOS) was used as a silica precursor for the sol−gel films while premade silica nanoparticles were used as building blocks for the nanoparticle-based films. In both instances, triblock copolymers Pluronic P123 or Pluronic F127 were used as the structure-directing agents. The solution containing the precursors and the block copolymers was spin-coated on a silicon substrate. Upon evaporation, the system self-assembled into an organic−inorganic nanocomposite. Subsequently, the nanocomposite films were calcined to remove the block copolymer and develop the mesoporous structure.

Nanoparticle-Based Mesoporous Silica Films. First, a stock solution of polymer was made by dissolving 0.678 g of Pluronic P123 or Pluronic F127 in 3 mL deionized water. The stock polymer solution was then mixed with the colloidal suspension of SiO_2 nanoparticles to produce a solution with polymer/SiO_2 mass ratio m_{poly}/m_{SiO2} between 0.1 and 3 g/g. Then, 80 μL of the polymer−silica solution was spin-coated onto a 1 × 1 in^2 Si substrates. The film's thickness was adjusted by controlling the spin speed. The dried films were calcined in air at 350 °C for 30 min using 2 °C/min temperature ramp to remove the polymer. Nanoparticle-based silica powders were also synthesized from the same solutions for heat capacity measurements. Instead of spin-coating, these solutions were evaporated in a Petri dish at ambient condition for 1 day and collected in powdered form after calcination at 350 °C for 3 h in oxygen using a ramp rate of 5 °C/min for both heating and cooling. The powders were calcined for a longer time than the films to fully remove all of the polymer template from the micron scale grains of the powder sample. Since the calcination was done at such a low temperature, it is assumed that there was no significant difference in silica structure of the films and the powders.

Sol–gel Based Mesoporous Silica Films. This method was adapted from the literature.[40] First, 25 mg of Pluronic F127 or Pluronic P123 was dissolved in 0.6 mL of ethanol and 0.16 mL of 0.05 M HCl. A certain amount of tetraethyl orthosilicate (TEOS) was added to the mixture to achieve a polymer to silica mass ratio m_{poly}/m_{SiO2} between 0.1 and 3. Then, 80 μL of the polymer–silica solution was spin-coated onto a 1 × 1 in^2 Si substrates. The film thickness was adjusted by controlling the spin speed. The dried films were calcined in air at 350 °C for 30 min using 2 °C/min temperature ramp to remove the polymer. Sol–gel silica powders were made from the same solutions for heat capacity measurements. Instead of spin-coating, the solutions were evaporated in a Petri dish at ambient condition for 1 day and collected in powdered form after calcination at 350 °C for 3 h in oxygen, again using a ramp rate of 5 °C/min for both heating and cooling. Here again, the powders were calcined for a longer time than the films to fully remove all of the polymer template from the micron scale grains of the powder samples. Since the calcination was done at such a low temperature, it is assumed that there was no significant difference in silica structure of the films and the powders.

2.3. Structural Characterization. Scanning Electron Microscopy (SEM) images were obtained using a model JEOL JSM-6700F field emission electron microscope with 5 kV accelerating voltage and secondary electron detector configuration. Transmission Electron Microscopy (TEM) images were obtained using a Technai G^2 TF20 High-Resolution EM, CryoEM and CryoET (FEI) at an accelerating voltage 200 kV and a TIETZ F415MP 16 megapixel 4k × 4k CCD detector. Two-dimensional grazing incidence small-angle X-ray scattering (2D-GISAXS) data were collected at the Stanford Synchrotron Lightsource (SSRL) using beamlines 1–5 with a wavelength of 0.1033 nm operated at an X-ray energy of 12.002 keV with a sample-to-detector distance of 2.870 m using a Rayonix-165 CCD detector. The data were then calibrated using silver behenate and reduced using the Nika package from Igor Pro.[41]

Ellipsometric porosimetry was performed on a PS-1100 instrument from Semilab using toluene as the adsorbate at ambient conditions to quantify porosity and pore size. The instrument used a UV–vis CCD detector adapted to a grating spectrograph to analyze the signal reflected by the sample. The light source was a 75 W Hamamatsu xenon lamp and the measurements were performed in the spectral range from 275–990 nm. Data analysis was performed using the associated Spectroscopic Ellipsometry Analyzer software assuming that the pores were cylindrical.

An optical reflectance based method was also used to verify the porosity and measure the film thickness. The experimental spectral normal-hemispherical reflectance $R_{exp,\lambda}$ was measured with a Shimadzu UV3101 PC UV–vis spectrophotometer equipped with a Shimadzu ISR3000 integrating sphere. The reference intensity was measured using a high specular reflection standard mirror by Ocean Optics (NIST certified STAN-SSH). The reflectance was measured in the visible range between 400 and 800 nm with a 1 nm spectral resolution. The porosity (ϕ) was then evaluated using a Maxwell-Garnett model using the refractive index ($n_{c,\lambda}$) retrieved from the reflectance measurement. The uncertainty of the retrieved porosity ($\Delta\phi$) was evaluated using the equation:

$$\Delta\phi = \sqrt{\left(\frac{\partial\phi}{\partial n_{eff,\lambda}}\Delta n_{aff,\lambda}\right)^2 + \left(\frac{\partial\phi}{\partial n_{c,\lambda}}\Delta n_{c,\lambda}\right)^2} \quad (1)$$

where the uncertainty of the refractive index of silica ($\Delta n_{c,\lambda}$) was calculated to be twice the standard deviation of $n_{c,\lambda}$ given by the Sellmeier formula over the 400–800 nm wavelength range.[42] This was found to be ($\Delta n_{c,\lambda}$) = 0.009 for all mesoporous silica films. The uncertainty, $\Delta n_{eff,\lambda}$, associated with the retrieved $n_{eff,\lambda}$ was found to be 0.003 for mesoporous silica films. Here, $\Delta n_{eff,\lambda}$ is defined as the average absolute difference between the refractive index used to predict the ideal spectral normal-hemispherical reflectance and the refractive index retrieved from the noisy normal-hemispherical reflectance.

2.4. Thermal Properties Characterization. Since the thickness of these mesoporous silica films was less than 1 μm, only a few thermal characterization techniques are suitable, including the 3ω method[29,43] and time-domain thermoreflectance (TDTR).[30,44] Considering the simpler fabrication processes and previously reported success of TDTR for extremely porous silica aerogel,[30] TDTR was used here for systematically investigating thermal conductivity of the various mesoporous silica films. Details of the TDTR setup are presented in Scheme 2. The detailed working principles and

Scheme 2. Experimental Setup for the Time-Domain Thermoreflectance (TDTR) Method Used for Thermal Conductivity Measurement on Mesoporous Silica Films on Si Substrate

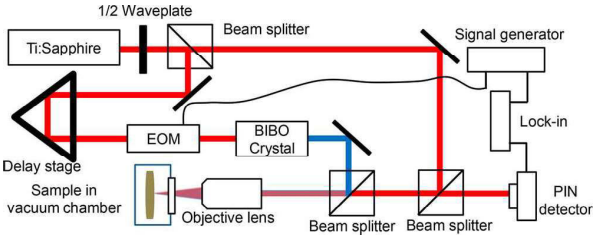

experimental setup can be found elsewhere.[45–48] In brief, a thin aluminum film (80 nm) was deposited by e-beam evaporation on the top surface of the samples. This film served as both a transducer to convert laser energy to thermal energy and a temperature sensor. The absorbed energy from the pump beam at 400 nm leads to an instantaneous temperature rise. The probe beam at 800 nm wavelength was used to continuously detect temperature decay by measuring reflectance using a photodiode. The delay time between pump pulse and probe pulse can be controlled with temporal resolution higher than subpicosecond. Next, the full transient decay curve from −100 to 5000 ps was fitted with a thermal diffusion model to obtain the thermal effusivity of the sample, which can be related to the thermal conductivity using the volumetric heat capacity.[44] To account for potential differences in the local thermal conductivity induced by variations in the nanoscale random network of silica, a large laser spot size of 20 μm in diameter was used. Similarly, to correct for the macroscale inhomogeneity of the mesoporous films and to ensure the reliability of the thermal conductivity data, TDTR measurements were repeated at 10 different locations on a 1 × 1 cm^2 surface area of the sample. Before all TDTR measurements, the samples were dehydrated by heating on a hot plate at 150 °C for more than 12 h. The thermal conductivity of the dehydrated samples was measured in a

vacuum chamber with pressure less than 1 Pa at room temperature.

The specific heat capacity of the different mesoporous power silica samples of different porosities was measured using a Perkin-Elmer DSC 8000, a dual furnace differential scanning calorimeter equipped with an IntraCooler. This method was reported previously.[49] In brief, the samples were prepared in Al pans with vented covers to facilitate water loss at high temperatures. The specific heat capacity of each sample was measured using a step scan isothermal method from 20 to 30 °C with a 5 °C min^{-1} scan and 1.5 min hold at every 1 °C interval. The thermal conductivity of the films, κ, was retrieved from the thermal effusivity (e) obtained from TDTR and the c_p obtained from DSC using the equation:

$$\kappa_{\text{eff}} = \frac{e_{\text{eff}}^2}{C_{v,\text{eff}}} \tag{2}$$

Here, the volumetric heat capacity ($C_{v,\text{eff}}$) is estimated using the silica volume fraction ($\phi_{SiO_2} = 1 - \phi$), the silica density (ρ_{SiO_2}), and the measured specific heat capacity (c_{p,SiO_2}) of the silica samples as shown in the following:[49]

$$C_{v,\text{eff}} = \phi_{SiO_2}\rho_{SiO_2}c_{p,SiO_2} \tag{3}$$

The relative uncertainty of the thermal conductivity was then calculated as eq 4.

$$\frac{\Delta\kappa_{\text{eff}}}{\kappa_{\text{eff}}} = \sqrt{\left(\frac{\Delta e_{\text{eff}}^2}{e_{\text{eff}}^2}\right)^2 + \left(\frac{\Delta\phi_{SiO_2}}{\phi_{SiO_2}}\right)^2 + \left(\frac{\Delta c_{p,\text{eff}}}{c_{p,\text{eff}}}\right)^2} \tag{4}$$

Here, Δe_{eff}^2 was estimated as the standard deviation of a mean value of ten measurements, $\Delta\phi_{SiO_2} = \Delta\phi$, which was calculated using the method described in Section 2.3, and $\Delta c_{p,\text{eff}}$ was calculated based on the standard deviation of eight measured samples, four of which were nanoparticle-based and four of which were sol–gel based, as shown in the Supporting Information (SI) in Table S1.

3. RESULTS AND DISCUSSION

3.1. Structural Characterization. In this study, a wide variety of mesoporous silica thin films with different frameworks, porosities, and pore sizes were prepared to examine the effects of the nanoscale architecture on their thermal conductivity. The mesoporous silica thin films were prepared by evaporation induced self-assembly as previously described (Scheme 1). Different porosities, pore sizes, and wall thicknesses were achieved by varying the mass ratio of triblock copolymer template to silica.

Figure 1 shows typical SEM images of the sol–gel and nanoparticle-based mesoporous silica films. All films had well-developed mesoporosity with pore diameter ca. 10 nm throughout the structure and a smooth crack-free surface. The sol–gel based films displayed a more ordered porous structure with a continuous silica framework (Figure 1a) while the nanoparticle-based films had somewhat disordered pores and visible boundaries between the silica nanoparticles (Figure 1b).

To examine the local structure of the pore walls, we turn to transmission electron microscopy. Figure 2 shows TEM images of sol–gel and nanoparticle-based mesoporous silica films to illustrate the difference in frameworks between the two types of mesoporous materials. In the sol–gel mesoporous film (Figure 2a), the silica exists in a continuous molecular network where the wall thickness is fairly uniform and determined by both the pore size and porosity. In the nanoparticle-based film (Figure 2b), by contrast, individual silica nanoparticles are connected

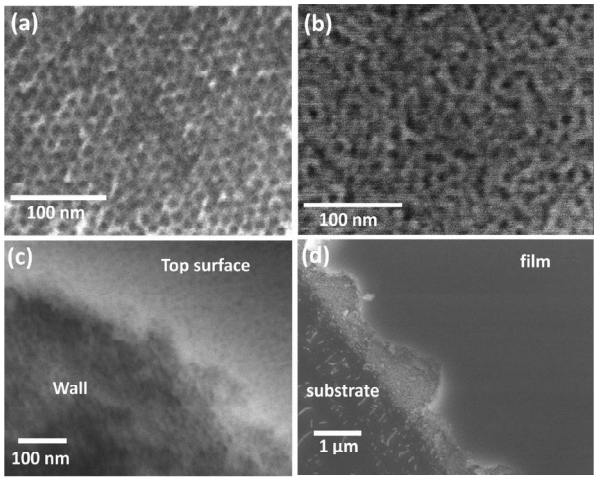

Figure 1. Typical scanning electron microscope images of mesoporous silica films. (a) Sol–gel based and (b) nanoparticle-based mesoporous silica films. (c) Zoomed in SEM of a cross-sectional of a razor blade cut in a nanoparticle-based mesoporous silica film showing homogeneous porosity through the film. (d) Zoomed out SEM of a mesoporous silica film on top of a Si substrate. Similar smooth, crack-free surfaces are observed for both sol–gel and nanoparticle-based silica films.

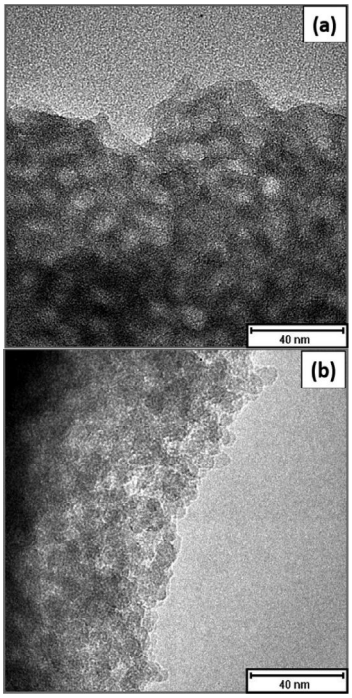

Figure 2. Transmission electron microscopy images of F127 templated (a) sol–gel and (b) nanoparticle-based mesoporous silica films. The images clearly show that the sol–gel network is continuously connected, while the nanoparticle-based films are composed of individual nanoparticles overlapping each other.

and partially fused, with walls formed by one or multiple stacked nanoparticles.

Two-dimensional grazing-incidence small-angle X-ray scattering (2D-GISAXS) measurements were used to examine the mesoporous structure of the prepared films. Figure 3a and b

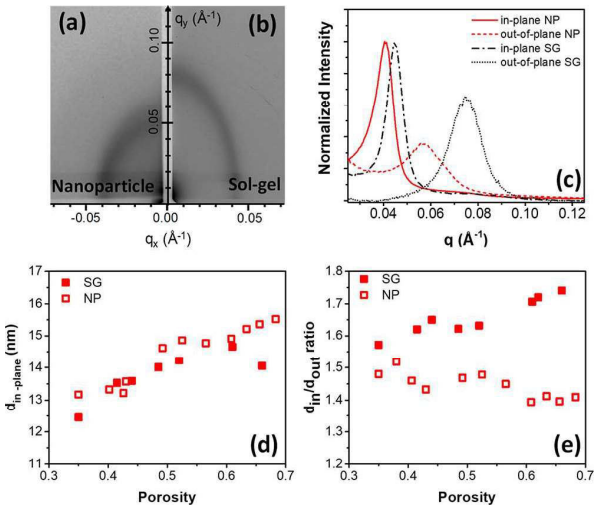

Figure 3. Small angle X-ray scattering of sol–gel (SG) and nanoparticle-based (NP) mesoporous silica films. A representative 2D-GISAXS pattern of a nanoparticle-based (a) and sol–gel based (b) mesoporous silica film. (c) Integrated intensity patterns converted from the 2D-GISAXS pattern along the q_x- and q_y-directions corresponding to in-plane and out-of-plane scattering for a typical sol–gel and nanoparticle-based films. (d) In-plane distance as a function of porosity and (e) ratio of in-plane distance/out-of-plane distance as a function of porosity for F127-templated sol–gel (SG) and nanoparticle-based (NP) films.

shows a representative 2D-GISAXS pattern of mesoporous nanoparticle based and sol–gel silica thin films, respectively. The diffraction arc along the q_x- and q_y- directions indicate that the films had ordered porosity both in the plane of the substrate and perpendicular to it. Figure 3b shows the integrated spectra from the 2D-GISAXS pattern of Figure 3a and b in both the in-plane (parallel to the substrate, q_x) and out-of-plane (perpendicular to the substrate, q_y) directions. Both in-plane and out-of-plane 2D-GISAXS featured a single diffraction peak indicating partly disordered porosity. These observations are consistent with the SEM images of the films (Figure 1). The in-plane diffraction peaks of both sol–gel and nanoparticle-based films had an intensity greater than twice that of the out-of-plane diffraction peak. This was due to the limited film thickness (<800 nm), which resulted in fewer scattering unit cells in the direction perpendicular to the substrate.

Film shrinkage during heat treatment could be seen by the fact that the in-plane scattering peak was at lower q than the out-of-plane peak. Since $q = 2\pi/d$, the interplane spacing d between repeating unit cells of mesopores along the direction perpendicular to the substrate was shorter than that in the direction parallel to the substrate. This indicates that during heat treatment the film shrank more in the direction perpendicular to the substrate than in the in-plane direction, which was pinned to the substrate, assuming that the as-synthesized film originally had isotropic pore spacing in all directions. The in-plane diffraction peak was observed in nearly all samples, while the out-of-plane diffraction peak was missing for samples with $m_{poly}/m_{SiO2} > 2$ and $m_{poly}/m_{SiO2} < 0.4$. For $m_{poly}/m_{SiO2} > 2$, the pores along the direction perpendicular to the substrate experienced extreme shrinkage during heat treatment due to the high porosity obtained for large m_{poly}/m_{SiO2} ratios. This extreme shrinkage destroyed the order along the q_y-direction resulting in the featureless 2D-GISAXS. On the other hand, for $m_{poly}/m_{SiO2} < 0.4$, the films were progressively thinner, with less repeat units, resulting in broader and weaker out-of-plane diffraction peak, until its complete disappearance.

Figure 3d compares the in-plane spacing, $d_{in\text{-}plane}$, calculated from the position of the in-plane diffraction peak for F127-templated sol–gel and nanoparticle-based mesoporous SiO_2 films with different porosities. The in-plane spacing, $d_{in\text{-}plane}$, increased almost linearly with the porosity for both sol–gel and nanoparticle-based films, which indicates that the pores, and likely the pore walls, grew larger with the increasing porosity. However, sol–gel and nanoparticle-based mesoporous silica films displayed different values and trends in the $d_{in\text{-}plane}/d_{out\text{-}of\text{-}plane}$ ratio as a function of porosity as shown in Figure 3e. In sol–gel based films, d_{in}/d_{out} ratio increased as porosity increased, as the films with higher porosity shrank more in the perpendicular direction to the substrate, leading to a smaller d_{out}. However, in nanoparticle-based films, the d_{in}/d_{out} ratio was relatively independent of porosity, likely because the preformed nanoparticle-based network underwent less shrinkage. Overall the d_{in}/d_{out} ratios at all porosities were higher in sol–gel based films than those in nanoparticle-based films due to the difference in shrinkage perpendicular to the substrate.

The porosity and pore size were further analyzed by ellipsometric porosimetry using toluene as an adsorbate.[50] Figure 4 shows adsorption/desorption isotherms and pore size distribution for sol–gel (Figure 4a) and nanoparticle-based (Figure 4b) silica films templated with Pluronic P123 for m_{poly}/m_{SiO2} = 1.5. Both isotherms were of type IV with H2(b)

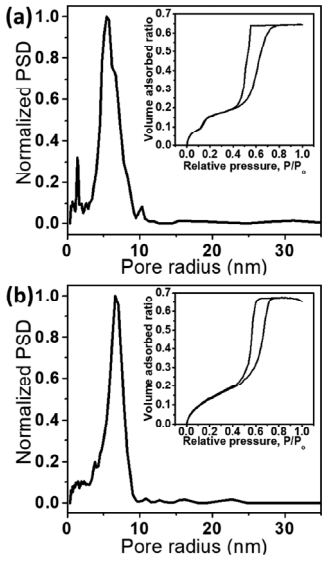

Figure 4. Typical pore size distributions (PSDs) and the corresponding adsorption–desorption isotherm obtained from ellipsometric porosimetry using toluene as the adsorbate at ambient conditions for (a) sol–gel and (b) nanoparticle-based silica thin films synthesized with a 1.5 g/g P123 to silica ratio.

hysteresis loops according to the IUPAC classification.[51,52] Type IV isotherms demonstrate the presence of mesopores, with H2(b) hysteresis loops indicating a complex pore structure with some pore blocking.[53] The steep adsorption increase at high relative pressures, corresponding to capillary condensation in mesopores, suggests a fairly narrow pore size distribution.[54] This is consistent with the 2D-GISAXS patterns in Figure 3a and b, which indicate some periodicity in the samples, similar to more ordered counterparts such as the F127 templated cubic FDU-12 and P123 templated hexagonal SBA-15.[23,26,55] For these ordered materials, the derivative of the adsorption curve is often associated with the size of pore cages, while the desorption curve reports on constrictions or neck in the pores, but necessarily with less quantitative size information.[26] Both films had similar porosity (~65%) and similar adsorption pore sizes (10–14 nm). The sol–gel film also displayed a step in the isotherm at lower pressure ($P/P_o \approx 0.15$) that was not present in the nanoparticle-based films. The step corresponds to micropores with diameter ~3 nm created inside the mesopore walls by the block copolymer chains.[56,57]

Figure 5a and b summarizes the dependence of porosity on the polymer to silica mass ratio (m_{poly}/m_{SiO2}) in sol–gel and nanoparticle-based mesoporous silica films, respectively. The porosity in both sol–gel and nanoparticle-based films gradually increased up to 70% with increasing amount of polymer up to mass ratios $m_{poly}/m_{SiO2} > 2$. Further increase in m_{poly}/m_{SiO2} resulted in more shrinkage during heating instead of higher porosity. The sol–gel based silica system displays a wide range of porosity from 0% to 70% as any amount of polymer beyond the critical micelle concentration produced porosity in the final film. By contrast, the porosity of the nanoparticle-based films featured a lower limit around 35% due to the intrinsic porosity between randomly packed nanoparticles.

The average pore diameter of mesoporous silica films also increased with the increasing m_{poly}/m_{SiO2}, as shown in Figure 5c. This was in agreement with the increasing $d_{in\text{-}plane}$ spacing observed in the SAXS data. In addition, the average pore diameter was slightly larger in films templated with Pluronic F127 than in those templated with Pluronic P123, for a given m_{poly}/m_{SiO2} ratio. This was due to the larger molecular weight of Pluronic F127 (M_w = 12 700 Da) compared to Pluronic P123 (M_w = 5800 Da). We note that although the pore sizes for both sol–gel and nanoparticle-based films made from the same polymer template are similar at a given porosity, the distribution of wall thicknesses between the pores is not necessarily the same, since the precursors are different. Interestingly, despite the fact that the porosity no longer changed for $m_{poly}/m_{SiO2} > 2$ g/g, the average pore size continues to increase. Table S2 summarizes the porosity and film thickness of the various mesoporous silica thin films investigated in this work.

3.2. Thermal Conductivity Measurements. The key goal of this work is to correlate pore structure with thermal conductivity, and so in this section, we relate these various structural properties to the thermal conductivity, as measured by TDTR. Thermal conductivity data measured under vacuum is presented in Figure 6 below and listed in Table S2. Further discussion of this data and the trends can be found below.

Previous studies on thermal transport in mesoporous silica mostly focused on a narrow range of porosity.[29,30] Here, the thermal conductivity of mesoporous silica with a wide range of porosity was systematically studied. We also report, for the first time, the thermal conductivity of nanoparticle-based mesoporous silica films. Figure 6 shows the thermal conductivity as a function of porosity for both sol–gel based (Figure 6a) and nanoparticle-based (Figure 6b) mesoporous silica films. As

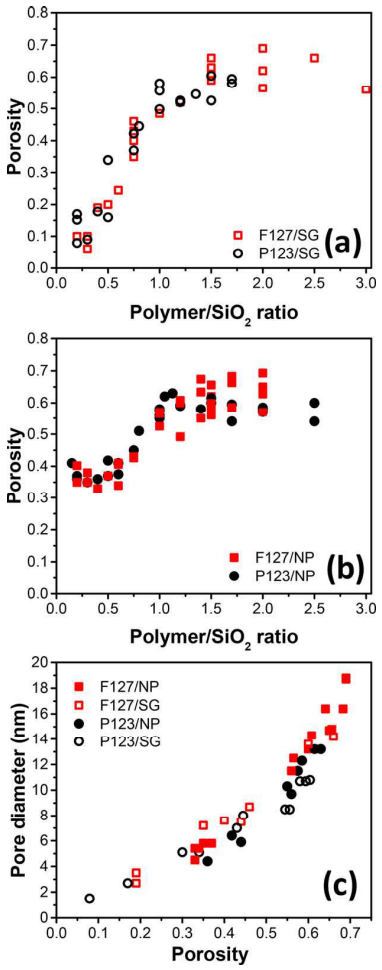

Figure 5. Porous structure characterized by ellipsometric porosimetry using toluene as the adsorbate at ambient conditions. Porosity as a function of polymer/silica ratio for (a) sol–gel (SG) and (b) nanoparticle-based (NP) mesoporous silica films. Samples were templated with either P123 or F127 block copolymers, as indicated on the figure. (c) Average pore diameter as a function of porosity in Pluronic surfactant-templated porous sol–gel and nanoparticle-based mesoporous silica films.

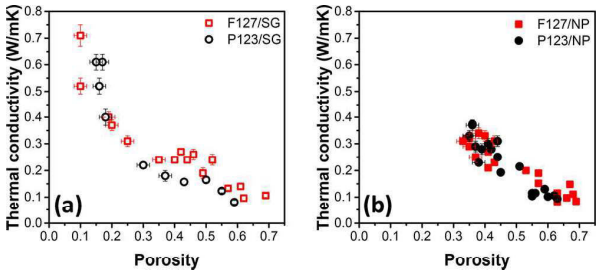

Figure 6. Thermal conductivity as a function of porosity for F127 and P123 templated (a) sol–gel (SG) silica and (b) nanoparticle-based (NP) silica mesoporous films measured under vacuum. No clear trends with the type of template used are observed, but there is a strong variation in thermal conductivity with porosity.

expected, the thermal conductivity decreased with increasing porosity,[30,57] and thermal conductivities below 0.1 W/mK were achieved in both sol–gel and nanoparticle-based silica mesoporous films with porosities larger than 60%. Figure 6 also shows a stronger dependence of the thermal conductivity on the porosity in sol–gel mesoporous silica films compared with nanoparticle-based films, an observation that will be discussed further below.

In these amorphous porous materials, the heat is carried by nonpropagating vibrational modes whose coherent lengths should be much smaller than the silica wall thickness. In this case, an effective medium approximation (EMA) can be used to model the effect of porosity.[58] Figure 7 plots the thermal

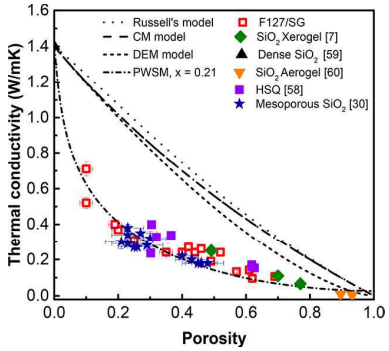

Figure 7. Thermal conductivity as a function of porosity for Pluronic F127 templated sol–gel silica films measured under vacuum, compared with a range of data for mesoporous silica reported in the literature[7,30,58–60] and several commonly used EMAs. Only the PWSM model accurately described the trends in the data.

conductivity of F127-templated sol–gel based mesoporous silica together with that of dense silica,[59] hydrogen-silsesquioxane (HSQ),[58] cubic and hexagonal mesoporous silica,[30] silica xerogel,[7] silica aerogel,[60] as well as predictions from several EMAs for the effective thermal conductivity of two phase media.[61] It is interesting to note that the thermal conductivity of the present mesoporous silica follows a similar porosity dependency to those previously reported despite major differences in synthesis and nanoscale architecture.

To understand the strong porosity dependence of the thermal conductivity, we first compared our data with EMAs based on classic heat conduction theory. For example, Russell's model was used for predicting the effective thermal conductivity κ_{eff} of bulk materials with spherical pores and is expressed as follows:[62]

$$\text{Russell's model } \kappa_{eff} = \kappa_{SiO_2}\frac{(1-\phi_p^{2/3})}{(1-\phi_p^{2/3}+\phi_p)} \quad (5)$$

where ϕ_p is the porosity and κ_{SiO_2} is the thermal conductivity of bulk silica. However, this prediction strongly overestimated the thermal conductivity of the different mesoporous silica, likely due to the major difference in morphology. The Clausius-Mossotti (CM) model and differential-effective-medium (DEM) theory have also been applied to predict the effective thermal conductivity of porous solid with ordered arrangement of identical pores[58] and are expressed as follows:

$$\text{CM model } \kappa_{eff} = \kappa_{SiO_2}\frac{(1-\phi_p)}{(1+0.5\phi_p)} \quad (6)$$

$$\text{DEM model } \kappa_{eff} = \kappa_{SiO_2}(1-\phi_p)^{1.5} \quad (7)$$

Unfortunately, both of these EMAs failed to capture the porosity dependence. Possible reasons include the fact that they ignore the pore shape, pore size, and the physical mechanisms responsible for energy transport in amorphous silica. Another model, which combines the classical series model with a parallel model $\kappa_{eff} = \kappa_{SiO_2}(1-\phi_p)$, called porosity weighted simple medium (PWSM) model has also been used to account for the porous structural parameters by using a fitting parameter x.[60] Considering the disperse phase in the pores to be vacuum, the PWSM simplifies to the following:[30]

$$\text{PWSM model } \kappa_{eff} = \kappa_{SiO_2}(1-\phi_p)(1-\phi_p^x) \quad (8)$$

Fitting the PWSM to our experimental measurements on F127-templated sol–gel films yielded $x = 0.21$, which is slightly larger than the value of $x = 0.17$ reported by Coquil et al.[27] The difference is likely due to the narrower range of porosity in the previous work (25–45%) compared to the present study (10–60%). Although it is difficult to physically interpret the meaning of x, this model is useful in predicting the thermal conductivity of mesoporous silica in the porosity range 10–60%.

The effects of solid framework morphology on the thermal transport in mesoporous silica was also explored by comparing the thermal conductivity of sol–gel and nanoparticle-based mesoporous silica films. For crystalline titania, these two morphologies showed very different results,[37] so it is interesting to see how they compare in an amorphous material like silica. As shown in Figure 8, although both kinds of mesoporous films

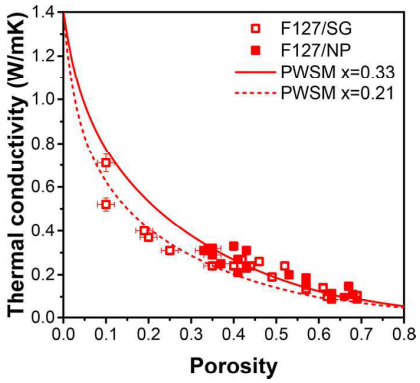

Figure 8. Thermal conductivity as a function of porosity for Pluronic surfactant templated sol–gel (SG) and nanoparticle-based (NP) mesoporous silica films measured under vacuum and fitted with the PWSM model. While both films show decreasing thermal conductivity with increasing porosity, the porosity dependence is influenced by the nanoscale architecture of the film.

feature decreasing thermal conductivity with increasing porosity, there are some observable differences. Near the lower porosity limit (~35%), the thermal conductivity of nanoparticle-based silica films was about 30% higher than that of sol–gel based films. However, for porosity above 45%, the difference in thermal conductivity between these two types of mesoporous frameworks became negligible. The PWSM model was fitted for each type of mesoporous silica thin films yielding $x = 0.21$ for sol–gel and $x = 0.33$ for nanoparticle-based silica mesoporous films. This suggests that the nanoparticle-based films offer more through-plane heat conduction pathways than

the sol–gel films. In nanoparticle-based films, the size of the connections between nanoparticles should be mainly determined by the diameter of each silica nanoparticle and thus should be porosity independent. Since the size of the nanoparticles is uniform throughout the network, the heat conduction has equal probability to go along all joined nanoparticle chains, as modeled by the parallel model. In contrast, the sol–gel mesoporous films feature thin necks whose size decreases with decreasing pore size. The thin necks in the sol–gel networks should contribute significantly to the thermal resistance, resulting in low thermal conductivity in sol–gel mesoporous silica films at lower porosity.

Moreover, Figure 6a indicates that sol–gel based Pluronic F127-templated mesoporous silica films had a slightly higher thermal conductivity than those templated with P123. Since Pluronic F127 forms bigger micelles due its larger molecular weight, it typically forms larger pores. This suggests that sol–gel based silica films with smaller pore size have lower thermal conductivity. For a given porosity, smaller pore size is associated with thinner wall and thus should result in more scattering events for heat carriers at the boundaries of those walls. In contrast, nanoparticle-based silica films showed almost no effect of pore size on the thermal conductivity. This is most likely due to the fact that in the nanoparticle-based framework, scattering of heat carriers is dominated by the colloidal building blocks, rather than by the thickness of the walls.

4. CONCLUSIONS

This work presented synthesis, characterization, and cross-plane thermal conductivity measurements at room temperature of sol–gel and nanoparticle-based mesoporous amorphous silica thin films with various thicknesses, pore sizes, and porosities. The following conclusions can be drawn from the data presented here:

(1) Porosity plays a dominant role in lowering the thermal conductivity in both sol–gel and nanoparticle-based mesoporous silica films. The thermal conductivity depends nonlinearly on porosity. The average thermal conductivity of mesoporous silica films with porosity of 60% was measured as 0.1 ± 0.03 W/m·K at room temperature.

(2) The building block of the porous framework affects how thermal conductivity changes with porosity, with sol–gel films showing a steeper dependence on porosity than nanoparticle based films.

(3) For a given porosity, the thermal conductivity of sol–gel mesoporous silica decreases with decreasing pore size. This is likely due to thinner walls associated with smaller pores resulting in stronger scattering of heat carriers. The pore size has little effect on the thermal conductivity of nanoparticle-based mesoporous silica films, however, likely because the mean free path for thermal carriers is dominated by the nanoparticle itself, rather than the pore size.

Taken together, these results begin to paint a fuller picture of the roles of pore size, wall thickness, total porosity, and pore structure in determining the thermal conductivity of homogeneous, templated mesoporous silica materials.

■ ASSOCIATED CONTENT

Supporting Information

The Supporting Information is available free of charge on the ACS Publications website at DOI: 10.1021/acs.jpcc.9b03767.

The specific heat capacities used and details of the porosity, film thicknesses, and thermal conductivity of the thin film samples (PDF)

■ AUTHOR INFORMATION

Corresponding Author

*Phone: (310) 206-4767. E-mail: tolbert@chem.ucla.edu.

ORCID

Michal Marszewski: 0000-0002-4157-3046
Laurent Pilon: 0000-0001-9459-8207
Yongjie Hu: 0000-0001-7225-1130
Sarah H. Tolbert: 0000-0001-9969-1582

Notes

The authors declare no competing financial interest.

■ ACKNOWLEDGMENTS

We acknowledge the funding support from U.S. Department of Energy (DOE), Advanced Research Projects Agency-energy (ARPA-e) under Award Number DE-AR0000738. Author Y.Y. acknowledges fellowship support from the China Scholarship Council (CSC). The authors acknowledge the use of instruments at the Electron Imaging Center for NanoMachines supported by NIH (1S10RR23057) and the California NanoSystems Institute (CNSI) at UCLA. This manuscript contains X-ray diffraction data collected at the Stanford Synchrotron Radiation Lightsource. Use of the Stanford Synchrotron Radiation Lightsource, SLAC National Accelerator Laboratory, is supported by the U.S. Department of Energy, Office of Science, Office of Basic Energy Sciences, under Contract DE-AC02-76SF00515.

■ REFERENCES

(1) Maex, K.; Baklanov, M. R.; Shamiryan, D.; Lacopi, F.; Brongersma, S. H.; Yanovitskaya, Z. S. Low dielectric constant materials for microelectronics. *J. Appl. Phys.* **2003**, *93*, 8793–8841.

(2) Peercy, P. S. The drive to miniaturization. *Nature* **2000**, *406*, 1023.

(3) Veres, J.; Ogier, S. D.; Leeming, S. W.; Cupertino, D. C.; Mohialdin Khaffaf, S. Low-k insulators as the choice of dielectrics in organic field-effect transistors. *Adv. Funct. Mater.* **2003**, *13*, 199–204.

(4) Vigliante, A.; Kasper, N.; Brechbuehl, J.; Nolot, E. Applications of x-ray characterization for advanced materials in the electronics industry. *Metall. Mater. Trans. A* **2010**, *41*, 1167–1173.

(5) Powell, M. J.; Quesada-Cabrera, R.; Taylor, A.; Teixeira, D.; Papakonstantinou, I.; Palgrave, R. G.; Sankar, G.; Parkin, I. P. Intelligent multifunctional $VO_2/SiO_2/TiO_2$ coatings for self-cleaning, energy-saving window panels. *Chem. Mater.* **2016**, *28*, 1369–1376.

(6) Jain, A.; Rogojevic, S.; Ponoth, S.; Gill, W. N.; Plawsky, J. L.; Simonyi, E.; Chen, S.-T.; Ho, P. S. Processing dependent thermal conductivity of nanoporous silica xerogel films. *J. Appl. Phys.* **2002**, *91*, 3275–3281.

(7) Hu, C.; Morgen, M.; Ho, P. S.; Jain, A.; Gill, W. N.; Plawsky, J. L.; Wayner, P. C. Thermal conductivity study of porous low- *k* dielectric materials. *Appl. Phys. Lett.* **2000**, *77*, 145–147.

(8) Jin, C.; Luttmer, J. D.; Smith, D. M.; Ramos, T. A. Nanoporous silica as an ultralow-k dielectric. *MRS Bull.* **1997**, *22*, 39–42.

(9) Koebel, M.; Rigacci, A.; Achard, P. Aerogel-based thermal superinsulation: An overview. *J. Sol-Gel Sci. Technol.* **2012**, *63*, 315–339.

(10) Deng, Z.; Wang, J.; Wu, A.; Shen, J.; Zhou, B. High strength SiO_2 aerogel insulation. *J. Non-Cryst. Solids* **1998**, *225*, 101−104.
(11) Eggiman, B. W.; Tate, M. P.; Hillhouse, H. W. Rhombohedral structure of highly ordered and oriented self-assembled nanoporous silica thin films. *Chem. Mater.* **2006**, *18*, 723−730.
(12) Alberius, P. C. A.; Frindell, K. L.; Hayward, R. C.; Kramer, E. J.; Stucky, G. D.; Chmelka, B. F. General predictive syntheses of cubic, hexagonal, and lamellar silica and titania mesostructured thin films. *Chem. Mater.* **2002**, *14*, 3284−3294.
(13) Lu, Y.; Ganguli, R.; Drewien, C. A.; Anderson, M. T.; Brinker, C. J.; Gong, W.; Guo, Y.; Soyez, H.; Dunn, B.; Huang, M. H.; Zink, J. I. Continuous formation of supported cubic and hexagonal mesoporous films by sol−gel dip-coating. *Nature* **1997**, *389*, 364.
(14) Zhao, D.; Feng, J.; Huo, Q.; Melosh, N.; Fredrickson, G.; Chmelka, B.; Stucky, G. Triblock co-polymer syntheses of mesoporous silica with periodic 50 to 300 angstrom pores. *Science* **1998**, *279*, 548−552.
(15) Hedrick, J. L.; Miller, R. D.; Hawker, C. J.; Carter, K. R.; Volksen, W.; Yoon, D. Y.; Trollsås, M. Templating nanoporosity in thin-film dielectric insulators. *Adv. Mater.* **1998**, *10*, 1049−1053.
(16) Venkateswara Rao, A.; Pajonk, G. M.; Haranath, D. Synthesis of hydrophobic aerogels for transparent window insulation applications. *Mater. Sci. Technol.* **2001**, *17*, 343−348.
(17) Wei, T.; Chang, T.; Lu, S.; Chang, Y. Preparation of monolithic silica aerogel of low thermal conductivity by ambient pressure drying. *J. Am. Ceram. Soc.* **2007**, *90*, 2003−2007.
(18) Jelle, B. P.; Baetens, R.; Gustavsen, A. Aerogel insulation for building applications. *Energy Build* **2011**, *43*, 761−769.
(19) Strubel, P.; Thieme, S.; Biemelt, T.; Helmer, A.; Oschatz, M.; Bruckner, J.; Althues, H.; Kaskel, S. ZnO hard templating for synthesis of hierarchical porous carbons with tailored porosity and high performance in lithium-sulfur battery. *Adv. Funct. Mater.* **2015**, *25*, 287−297.
(20) Schlottig, F.; Textor, M.; Georgi, U.; Roewer, G. Template synthesis of SiO_2 nanostructures. *J. Mater. Sci. Lett.* **1999**, *18*, 599−601.
(21) Cai, Q.; Lin, W.-Y.; Xiao, F.-S.; Pang, W.-Q.; Chen, X.-H.; Zou, B.-S. The preparation of highly ordered MCM-41 with extremely low surfactant concentration. *Microporous Mesoporous Mater.* **1999**, *32*, 1−15.
(22) Kresge, C. T.; Leonowicz, M. E.; Roth, W. J.; Vartuli, J. C.; Beck, J. S. Ordered mesoporous molecular sieves synthesized by a liquid-crystal template mechanism. *Nature* **1992**, *359*, 710−712.
(23) Zhao, D.; Sun, J.; Li, Q.; Stucky, G. D. Morphological control of highly ordered mesoporous silica SBA-15. *Chem. Mater.* **2000**, *12*, 275−279.
(24) Suzuki, K.; Ikari, K.; Imai, H. Synthesis of silica nanoparticles having a well-ordered mesostructure using a double surfactant system. *J. Am. Chem. Soc.* **2004**, *126*, 462−463.
(25) Smarsly, B.; Grosso, D.; Brezesinski, T.; Pinna, N.; Boissière, C.; Antonietti, M.; Sanchez, C. Highly crystalline cubic mesoporous TiO_2 with 10-nm pore diameter made with a new block copolymer template. *Chem. Mater.* **2004**, *16*, 2948−2952.
(26) Rauda, I. E.; Buonsanti, R.; Saldarriaga-Lopez, L. C.; Benjauthrit, K.; Schelhas, L. T.; Stefik, M.; Augustyn, V.; Ko, J.; Dunn, B.; Wiesner, U.; et al. General method for the synthesis of hierarchical nanocrystal-based mesoporous materials. *ACS Nano* **2012**, *6*, 6386−6399.
(27) Coquil, T.; Richman, E. K.; Hutchinson, N. J.; Tolbert, S. H.; Pilon, L. Thermal conductivity of cubic and hexagonal mesoporous silica thin films. *J. Appl. Phys.* **2009**, *106*, 1−11.
(28) Guillemot, F.; Brunet-Bruneau, A.; Bourgeat-Lami, E.; Gacoin, T.; Barthel, E.; Boilot, J. − P. Latex-templated silica films: Tailoring porosity to get a stable low-refractive index. *Chem. Mater.* **2010**, *22*, 2822−2828.
(29) Hatton, B.; Mishchenko, L.; Davis, S.; Sandhage, K. H.; Aizenberg, J. Assembly of large area, hightly ordered, crack-free inverse opal films. *Proc. Natl. Acad. Sci. U. S. A.* **2010**, *107*, 10354−10359.
(30) Hopkins, P. E.; Kaehr, B.; Phinney, L. M.; Koehler, T. P.; Grillet, A. M.; Dunphy, D.; Garcia, F.; Brinker, C. J. Measuring the thermal conductivity of porous, transparent SiO_2 films with time domain thermoreflectance. *J. Heat Transfer* **2011**, *133*, 61601.
(31) Smith, D. S.; Alzina, A.; Bourret, J.; Nait-Ali, B.; Pennec, F.; Tessier-Doyen, N.; Otsu, K.; Matsubara, H.; Elser, P.; Gonzenbach, U. T. Thermal conductivity of porous materials. *J. Mater. Res.* **2013**, *28*, 2260−2272.
(32) Lee, J.; Lim, J.; Yang, P. Ballistic phonon transport in holey silicon. *Nano Lett.* **2015**, *15*, 3273−3279.
(33) Yang, L.; Yang, N.; Li, B. Extreme low thermal conductivity in nanoscale 3d si phononic crystal with spherical pores. *Nano Lett.* **2014**, *14*, 1734−1738.
(34) Song, D.; Chen, G. Thermal conductivity of periodic micro-porous silicon films. *Appl. Phys. Lett.* **2004**, *84*, 687−689.
(35) Tang, G. H.; Bi, C.; Zhao, Y.; Tao, W. Q. Thermal transport in nano-porous insulation of aerogel: Factors, models and outlook. *Energy* **2015**, *90*, 701−721.
(36) Fang, J.; Reitz, C.; Brezesinski, T.; Nemanick, E. J.; Kang, C. B.; Tolbert, S. H.; Pilon, L. Thermal conductivity of highly-ordered mesoporous titania thin films from 30 to 320 K. *J. Phys. Chem. C* **2011**, *115*, 14606−14614.
(37) Coquil, T.; Reitz, C.; Brezesinski, T.; Nemanick, E. J.; Tolbert, S. H.; Pilon, L. Thermal conductivity of ordered mesoporous titania films made from nanocrystalline building blocks and sol-gel reagents. *J. Phys. Chem. C* **2010**, *114*, 12451−12458.
(38) Yang, L.; Zhang, Q.; Cui, Z.; Gerboth, M.; Zhao, Y.; Xu, T. T.; Walker, D. G.; Li, D. Ballistic phonon penetration depth in amorphous silicon dioxide. *Nano Lett.* **2017**, *17*, 7218−7225.
(39) Larkin, J. M.; McGaughey, A. J. H. Thermal conductivity accumulation in amorphous silica and amorphous silicon. *Phys. Rev. B: Condens. Matter Mater. Phys.* **2014**, *89*, 1−12.
(40) Dunphy, D. R.; Sheth, P. H.; Garcia, F. L.; Brinker, C. J. Enlarged pore size in mesoporous silica films templated by Pluronic F127: Use of poloxamer mixtures and increased template/SiO_2 ratios in materials synthesized by evaporation-induced self-assembly. *Chem. Mater.* **2015**, *27*, 75−84.
(41) Ilavsky, J. Nika: Software for two-dimensional data reduction. *J. Appl. Crystallogr.* **2012**, *45*, 324−328.
(42) Malitson, I. H. Interspecimen comparison of the refractive index of fused silica. *J. Opt. Soc. Am.* **1965**, *55*, 1205−1209.
(43) Cahill, D. G.; Goodson, K.; Majumdar, A. Thermometry and thermal transport in micro/nanoscale solid-state devices and structures. *J. Heat Transfer* **2002**, *124*, 223.
(44) Cahill, D. G. Analysis of heat flow in layered structures for time-domain thermoreflectance. *Rev. Sci. Instrum.* **2004**, *75*, 5119−5122.
(45) Li, M.; Kang, J. S.; Hu, Y. Anisotropic thermal conductivity measurement using a new asymmetric-beam time-domain thermoreflectance (AB-TDTR) method. *Rev. Sci. Instrum.* **2018**, *89*, 84901.
(46) Kang, J. S.; Wu, H.; Hu, Y. Thermal properties and phonon spectral characterization of synthetic boron phosphide for high thermal conductivity applications. *Nano Lett.* **2017**, *17*, 7507−7514.
(47) Kang, J. S.; Ke, M.; Hu, Y. Ionic intercalation in two-dimensional van der Waals materials: In-situ characterization and electrochemical control of the anisotropic thermal conductivity of black phosphorus. *Nano Lett.* **2017**, *17*, 1431−1438.
(48) Kang, J. S.; Li, M.; Wu, H.; Nguyen, H.; Hu, Y. Experimental observation of high thermal conductivity in boron arsenide. *Science* **2018**, *361*, 575−578.
(49) Marszewski, M.; Butts, D.; Lan, E.; Yan, Y.; King, S. C.; McNeil, P. E.; Galy, T.; Dunn, B.; Tolbert, S. H.; Hu, Y.; et al. Effect of surface hydroxyl groups on heat capacity of mesoporous silica. *Appl. Phys. Lett.* **2018**, *112*, 201903.
(50) Baklanov, M. R.; Mogilnikov, K. P.; Polovinkin, V. G.; Dultsev, F. N. Determination of pore size distribution in thin films by ellipsometric porosimetry. *J. Vac. Sci. Technol., B: Microelectron. Process. Phenom.* **2000**, *18*, 1385−1391.
(51) Haul, R.; Gregg, S. J.; Sing, K. S. W. Adsorption, surface area and porosity. *Berichte der Bunsengesellschaft für Phys. Chemie* **1982**, *86*, 957.
(52) Thommes, M.; Kaneko, K.; Neimark, A. V.; Olivier, J. P.; Rodriguez-Reinoso, F.; Rouquerol, J.; Sing, K. S. W. Physisorption of

gases, with special reference to the evaluation of surface area and pore size distribution (IUPAC Technical Report). *Pure Appl. Chem.* **2015**, *87*, 1051−1069.
(53) Thommes, M.; Smarsly, B.; Groenewolt, M.; Ravikovitch, P. I.; Neimark, A. V. Adsorption hysteresis of nitrogen and argon in pore networks and charaterization of novel micro-and mesoporous silicas. *Langmuir* **2006**, *22*, 756−764.
(54) Kruk, M.; Jaroniec, M.; Ko, C. H.; Ryoo, R. Characterization of the porous structure of SBA-15. *Chem. Mater.* **2000**, *12*, 1961−1968.
(55) Fan, J.; Yu, C.; Gao, F.; Lei, J.; Tian, B.; Wang, L.; Luo, Q.; Tu, B.; Zhou, W.; Zhao, D. Cubic mesoporous silica with large controllable entrance sizes and advanced adsorption properties. *Angew. Chem., Int. Ed.* **2003**, *42*, 3146−3150.
(56) Ryoo, R.; Ko, C. H.; Kruk, M.; Antochshuk, V.; Jaroniec, M. Block-Copolymer-Templated Ordered Mesoporous Silica: Array of Uniform Mesopores or Mesopore−Micropore Network? *J. Phys. Chem. B* **2000**, *104*, 11465−11471.
(57) Tsui, B.-Y.; Yang, C.-C.; Fang, K.-L. Anisotropic thermal conductivity of nanoporous silica film. *IEEE Trans. Electron Devices* **2004**, *51*, 20−27.
(58) Costescu, R. M.; Bullen, A. J.; Matamis, G.; O'Hara, K. E.; Cahill, D. G. Thermal conductivity and sound velocities of hydrogen-silsesquioxane low-k dielectrics. *Phys. Rev. B: Condens. Matter Mater. Phys.* **2002**, *65*, 942051−942056.
(59) Cahill, D. G. thermal conductivity measurement from 30 to 750 K: The 3ω method. *Rev. Sci. Instrum.* **1990**, *61*, 802−808.
(60) Fricke, J.; Lu, X.; Wang, P.; Büttner, D.; Heinemann, U. Optimization of monolithic silica aerogel insulants. *Int. J. Heat Mass Transfer* **1992**, *35*, 2305−2309.
(61) Pietrak, K.; Winiewski, T. S. A review of models for effective thermal conductivity of composite materials. *Open Access J. J. Power Technol.* **2015**, *95*, 14−24.
(62) Russell, H. W. Principles of heat flow in porous insulators. *J. Am. Ceram. Soc.* **1935**, *18*, 1−5.

CHAPTER 3

Controlling Thermal Conductivity in Mesoporous Silica Films Using Pore Size and Nanoscale Architecture

Chapter 3 describes our work to understand the thickness of the silica may influence the thermal conductivity of a silica network. The silica walls were made from either discrete nanoparticles or continuous sol-gel walls.

A reprint of the supporting information is given in Appendix B.

Controlling Thermal Conductivity in Mesoporous Silica Films Using Pore Size and Nanoscale Architecture

Yan Yan, Man Li, Sophia King, Tiphaine Galy, Michal Marszewski, Joon Sang Kang, Laurent Pilon, Yongjie Hu, and Sarah H. Tolbert*

ABSTRACT: This work investigates the effect of wall thickness on the thermal conductivity of mesoporous silica materials made from different precursors. Sol–gel- and nanoparticle-based mesoporous silica films were synthesized by evaporation-induced self-assembly using either tetraethyl orthosilicate or premade silica nanoparticles. Since wall thickness and pore size are correlated, a variety of polymer templates were used to achieve pore sizes ranging from 3–23 nm for sol–gel-based materials and 10–70 nm for nanoparticle-based materials. We found that the type of nanoscale precursor determines how changing the wall thickness affects the resulting thermal conductivity. The data indicate that the thermal conductivity of sol–gel-derived porous silica decreased with decreasing wall thickness, while for nanoparticle-based mesoporous silica, the wall thickness had little effect on the thermal conductivity. This work expands our understanding of heat transfer at the nanoscale and opens opportunities for tailoring the thermal conductivity of nanostructured materials by means other than porosity and composition.

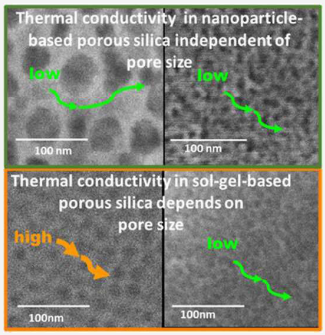

Thermal transport at the nanoscale has been an area of intense research due to various applications of nanostructured materials including thermoelectrics,[1,2] thermally insulating materials,[3,4] and thermal interface materials.[5] Nanostructuring offers unprecedented opportunities for controlling thermal transport by tuning various structural parameters.[6] Many structural factors such as pore size, total porosity, surface or interface structure, defect density, and impurities[7−10] can significantly influence the thermal conductivity of nanoscale materials. In particular, porous materials can be used as a platform for studying size effects due to their tunable syntheses and high surface area.[11] Although the size effect in crystalline materials is quite well understood,[12−14] the size effect on the thermal conductivity of amorphous materials remains underdeveloped.

Porous silica, which is based on an amorphous silica network, has received significant attention, since its high porosity can result in large reductions in thermal conductivity[11,15−17] For instance, aerogels, composed of chains of silica nanoparticles, feature extremely low thermal conductivities (0.013 W/m K) and have been used for thermal insulation in a variety of applications.[18−24] Several studies[17,25] have shown that the thermal conductivity of dense silica thin films is independent of film thickness when the thickness is greater than 100 nm, suggesting that any propagating modes contributing to the thermal conductivity have mean free paths (MFPs) below 100 nm.[12] In addition, the effective thermal conductivity of mesoporous silica at room temperature has been shown to decrease rapidly with increasing porosity.[16,26,27] Hu et al.[28] proposed phenomenological, ad hoc two-phase mixture models that described the dependence of thermal conductivity on porosity.

Notably, the effect of pore size on the thermal conductivity of nanoporous silica remains unclear. In theory, the intensity of scattering would depend on the size of the solid backbone. While pore size and wall thickness are not rigorously linked, they are generally correlated in most solution-derived porous materials. As such, with a porous structure, the MFP should be reduced when it is comparable to the pore size.[29] Some experimental studies, however, have suggested that the thermal conductivity of mesoporous silica was independent of pore size.[26,30] However, these studies only focused on silica aerogel or sol–gel networks and sampled a limited range of pore sizes. Jain et al. showed that the thermal conductivity of xerogel films depended on the pore size distribution, with micropores contributing the most to phonon scattering.[29] However, due to the different preparation processes, these samples may have different amounts of cracks, defects, and impurities that also contribute to phonon scattering, making the comparison challenging. In our previous work,[31] we suspected a dependence of thermal conductivity on pore size in mesoporous silica; however, the evidence was not strong enough to warrant a conclusion. Thus, the investigation should be extended to a

Received: February 11, 2020
Accepted: April 17, 2020
Published: April 17, 2020

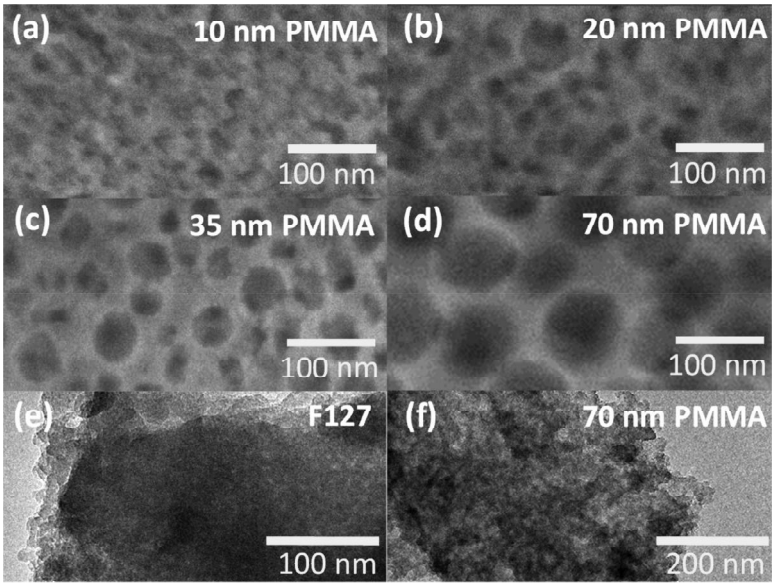

Figure 1. SEM (a–d) and transmission electron microscopy (TEM) (e,f) images of NP-based mesoporous silica films templated with PMMA colloids or Pluronic F127 with average sizes of (a) 10, (b) 20, (c) 35, (d,f) 70, and (e) 10–16 nm.

broader pore size range to gain better insight into the effect of pore size on the thermal conductivity of mesoporous silica.

The present study discusses the effect of pore size on the effective thermal conductivity of mesoporous silica films with a wide range of pore sizes and two different silica frameworks, i.e., a continuous matrix synthesized using sol–gel methods or a discontinuous network made from discrete nanoparticles. A number of sol–gel (SG)- and nanoparticle (NP)-based mesoporous silica thin films with different pore sizes were synthesized under the same conditions to reduce the effect of impurities and defects. The effective thermal conductivity in the out-of-plane direction was measured with time domain thermoreflectance (TDTR)[32,33] in vacuum at room temperature to eliminate the contribution of the gas phase on thermal transport. During thermal treatment, these films shrink in an anisotropic manner, with a greater degree of shrinkage in the out-of-plane direction compared to the in-plane direction. As such, we are measuring the upper limit of the thermal conductivity, since the porosity in the out-of-plane direction may be lower than in the in-plane direction.

Multiple NP-based mesoporous silica films with pore diameters in the range of 10–70 nm were synthesized using PMMA colloids or Pluronic triblock copolymers as the template to thoroughly examine the effect of pore size on the thermal conductivity. Figure 1a–d shows scanning electron microscopy (SEM) images of porous silica films templated with different sizes of PMMA. The average pore size estimated from the SEM images matched the average size of PMMA colloids used for the synthesis, with wide pore size distributions due to the polydisperisity of the PMMA colloids. In addition, the increase in the wall thickness of the NP-based films with increasing average pore size can be directly observed.

Figure 1e,f shows TEM images of typical F127-templated and 70 nm PMMA-templated NP-based mesoporous silica films. Since the samples were obtained from thick films, the pores are not easily visualized in transmission unless the sample is viewed directly down a pore axis, which is improbable for these disordered porous networks. Instead, one sees only differences in contrast in the films due to the absence of nanoparticles in some regions, which indicates the presence of pores somewhere within the thickness of the sample. While the pores are not easy to see, the nanoparticle building blocks are easier to observe. Figure S1 shows an image with both the pores and nanoparticle building blocks outlined for clarity. Because the nanoparticles used for all films were the same size, an increase in the thickness of the walls simply requires more nanoparticles stacked together.

The porosity and pore size distributions of NP-based mesoporous silica films templated with Pluronic F127 were analyzed by ellipsometric porosimetry at ambient temperature using toluene as the adsorbate.[34] The NP-based silica films templated with PMMA colloids could not be measured using ellipsometric porosimetry due to their large pores that scatter the light used in the ellipsometric measurement. As a result, the porosity and the pore size were measured using N_2 adsorption porosimetry on the NP-based mesoporous silica powders templated with PMMA colloids that were prepared in the same conditions as their corresponding films. Figure 2 shows the adsorption–desorption isotherms and pore size distributions for representative NP-based mesoporous silica films templated with Pluronic F127 and PMMA colloids. Both isotherms were of type IV(a) with an H2(b) hysteresis loop according to the IUPAC classification,[35,36] which indicates mesopores connected by narrow necks. The slope of the adsorption isotherm as a function of relative pressure was much steeper in the F127-templated sample (Figure 2a) than in the PMMA-templated sample (Figure 2b), suggesting a narrower pore size distribution.[37] The difference in the degree of polydispersity was also observed in the pore size distribution (Figure 2c,d). In fact, the PMMA-templated films had a bimodal pore size distribution, indicated by the two different hysteresis regions at P/P_0 = 0.45–0.75 for small pores and at P/P_0 = 0.9–1 for larger pores (Figure 2b). The small pores corresponded to the intrinsic gaps between the silica nanoparticles and ranged from 4 to 6 nm in diameter. The

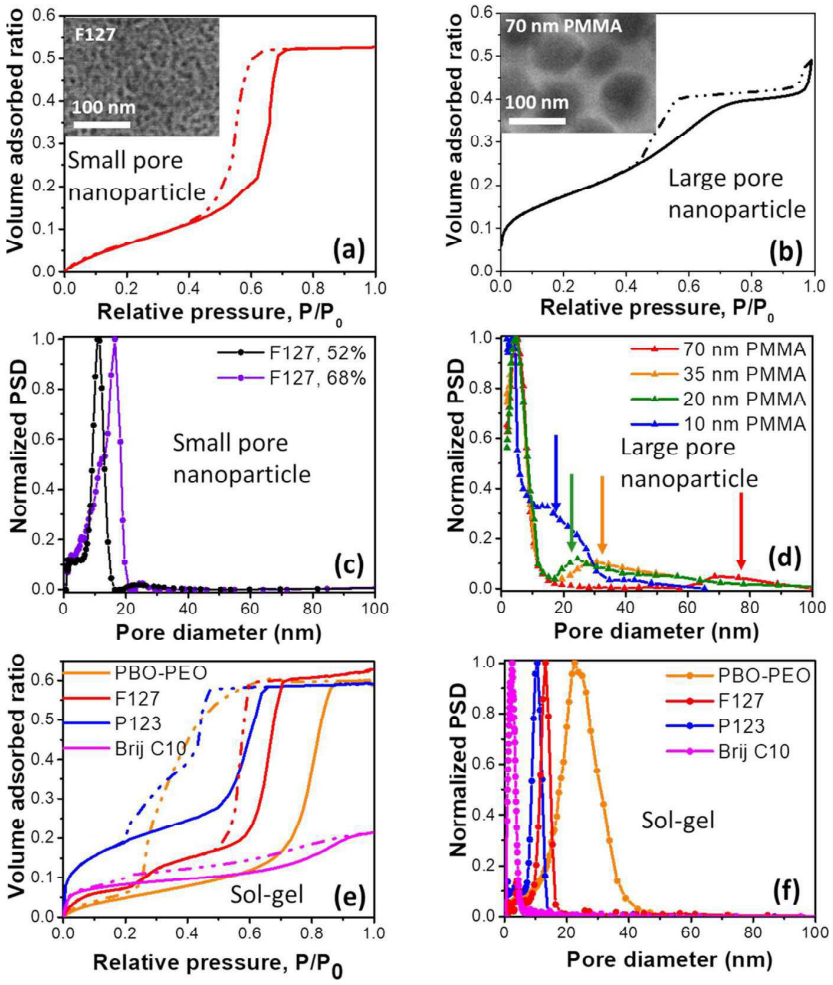

Figure 2. Isotherms and pore size distributions for NP- and SG-based mesoporous silica films templated with various polymers and surfactants. (a) Toluene adsorption/desorption isotherms for an F127-templated NP-based mesoporous silica film with a porosity of 52.5%. (b) Nitrogen adsorption/desorption isotherms for 70 nm PMMA-templated NP-based mesoporous silica with a porosity of 49%. (c) Number-weighted pore size distributions (PSDs) for F127-templated NP-based mesoporous silica films with the porosities indicated. (d) Number-weighted PSD for NP-based mesoporous silica materials with different PMMA templates. The pores between 2 and 4 nm are derived from the intrinsic gaps between the nanoparticle, while those indicated by the colored arrows are derived from the removal of the PMMA template. (e) Representative toluene adsorption/desorption isotherms for SG-based mesoporous silica films synthesized with different templates. (f) Representative number-weighted PSDs for SG-based mesoporous silica films with different templates. Insets in (a) and (b) are representative SEM images of NP-based mesoporous silica films templated with F127 and 70 nm PMMA, respectively. The pore diameters from porosimetry matched those observed in SEM images.

Table 1. Structural Characterization and Thermal Conductivity of F127- and PMMA-Templated NP-Based Mesoporous Silica Films[a]

template	porosity (%)	average interparticle pore diameter (nm)	average templated pore diameter (nm)	measured wall thickness (nm)	thermal conductivity (W/mK)
10 nm PMMA	65 ± 1	3 ± 2	10 ± 10	14 ± 4	0.096 ± 0.006
F127	68 ± 1	-	16 ± 2	7 ± 1	0.107 ± 0.005
35 nm PMMA	71 ± 1	4 ± 3	30 ± 10	25 ± 6	0.098 ± 0.005
F127	53 ± 1	-	11 ± 2	7 ± 1	0.19 ± 0.01
10 nm PMMA	49 ± 1	3 ± 2	10 ± 10	14 ± 1	0.24 ± 0.01
20 nm PMMA	50 ± 1	5 ± 3	27 ± 7	15 ± 5	0.21 ± 0.02
70 nm PMMA	49 ± 1	5 ± 3	74 ± 9	38 ± 15	0.19 ± 0.01

[a]Average pore diameters from the gaps between particles and voids from template removal are included.

large pores corresponded to the voids left after removing the PMMA template, and their size ranged from 15 to 68 nm, depending on the size of the PMMA colloids used. By contrast, the pore size distribution of NP-based mesoporous silica films templated with Pluronic F127 showed only one peak. This can be attributed to the fact that the size distributions of the

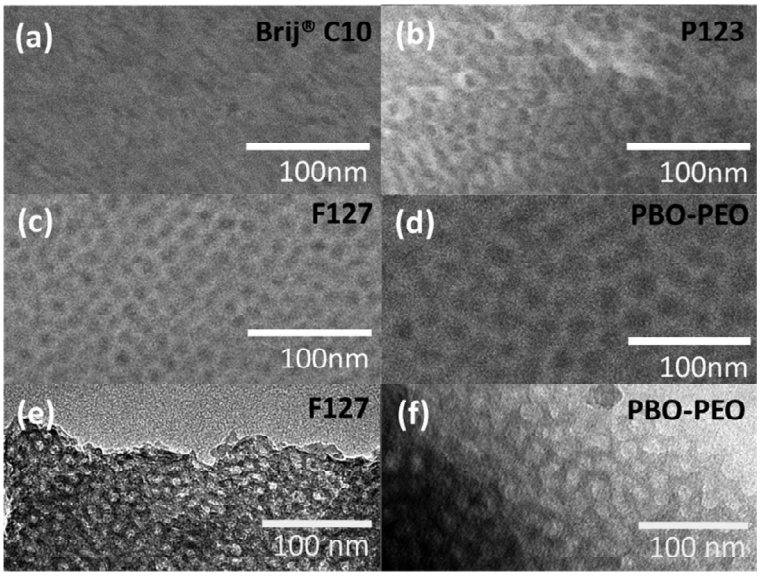

Figure 3. SEM (a–d) and TEM images (e,f) of SG-based mesoporous silica films templated by (a) BrijC10, (b) Pluronic P123, (c,e) Pluronic F127, and (d,f) PBO–PEO block copolymer. Films had increasing pore size from (a) to (d).

interparticle porosity and of the template-derived porosity were similar and overlapped.

Table 1 summarizes the structural characterization and thermal conductivity of two groups of NP-based mesoporous silica films with similar porosities but different pore diameters. The two different pore diameter values for PMMA-templated materials correspond to the intrinsic gaps between the silica nanoparticles and the voids left after removing the PMMA template, respectively. The first group had a porosity of 65–71% and pore diameter of 15–28 nm, while the second group had a porosity of 49–53% and pore diameter of 10–68 nm. The thickness of the pore walls was estimated from the SEM images. Table 1 indicates that NP-based mesoporous silica films with similar porosities had similar effective thermal conductivities despite having very different average pore sizes and, as a result, different wall thicknesses. We hypothesize that this observation is due to the fact that the thermal transport in NP-based films was determined by the heat carrier scattering between particles as well as at the boundary of each nanoparticle, both of which depend on the nanoparticle size rather than on the wall thickness.

To examine the effect of pore size on the thermal conductivity of sol–gel mesoporous silica films (SG-based mesoporous silica), multiple SG-based mesoporous silica films with pore diameters in the range of 3–23 nm were synthesized using different organic templates. Here, PMMA colloids could not be used as templates, as they are incompatible with the solvents used for sol–gel synthesis (the PMMA colloids aggregate and precipitate in ethanol). Figure 3 shows typical SEM images of the SG-based mesoporous silica films synthesized with these different templates. Those templated with CTAB and BrijC10 had very small pores between 1 and 4 nm in diameter. On the other hand, the films templated with different sized PBO–PEO block copolymers had large pores with diameters between 15 and 25 nm (Figure 3d). The block-copolymer-templated films displayed fairly ordered porous structures, as shown in Figure 3b–d. This was further supported by two-dimensional grazing-incidence small-angle X-ray scattering (2D-GISAXS) patterns, which are shown in Figure S2. The diffraction arc indicates that the pores are at least partly ordered. The intensity around the arc is not fully uniform, however, because there are only a finite number of repeat distances in the out-of-plane direction, while there is effectively an infinite number in the in-plane direction. Moreover, the in- and out-of-plane lattice spacings are also not the same, because more shrinkage occurs in the direction normal to the substrate, compared to in-plane. The result is a continuous distribution with broader peaks occurring at a higher q in the out-of-plane direction and narrower peaks occurring at a lower q in the in-plane direction. To rapidly quantify this distribution, here we report only the in-plane peak positions from Figure S2c, but all orientations are present. As expected, the inter-repeat distance, d, calculated as $d = 2\pi/q$, increases as the template size increased. Finally, TEM images (Figure 3e,f) show clear pores, which again arise because the ordered porosity allows transmission images to be collected in which all the pores line up on top of each to make clear regions of dark and light contrast.

The porosity and pore size of SG-based mesoporous silica films were measured by ellipsometric porosimetry using toluene as the adsorbate. Figure 2e,f shows toluene adsorption–desorption isotherms and pore size distributions for representative SG-based mesoporous silica films templated with BrijC10, Pluronic P123, Pluronic F127, and PBO–PEO. Here also, the hysteresis loops in the isotherms indicated the presence of mesopores connected by narrow necks. Most of the samples had a fairly narrow pore size distribution. The pore sizes from the ellipsometric porosimetry measurement were in agreement with estimates from SEM images. The pore walls' thickness w of SG-based mesoporous silica films was calculated by combining the pore radius r from ellipsometric porosimetry with the interplane spacing d from 2D-GISAXS using the equation[38]

$$w = 2\left(\frac{d}{\sqrt{3}} - r\right) \quad (1)$$

Table 2. Structural Characterization and Thermal Conductivity of SG-Based Mesoporous Silica Films Synthesized with Different Templates

template	porosity (%)	pore diameter (nm)	unit cell repeating distance (nm)	wall thickness (nm)[a]	thermal conductivity in vacuum (W/mK)
P123	59 ± 1	10 ± 1	13 ± 1	5 ± 1	0.081 ± 0.006
F127	62 ± 1	13 ± 1	14 ± 1	3 ± 1	0.096 ± 0.009
PBO–PEO	60 ± 1	24 ± 5	35 ± 3	16 ± 6	0.21 ± 0.01
P123	43 ± 1	6 ± 1	11 ± 5	7 ± 5	0.157 ± 0.008
F127	44 ± 1	8 ± 2	14 ± 1	8 ± 2	0.24 ± 0.01
PBO–PEO	44 ± 1	14 ± 7	23 ± 1	13 ± 7	0.29 ± 0.02
CTAB	16 ± 2	2 ± 1	N/A	2 ± 1	0.31 ± 0.02
BrijC10	21 ± 2	2 ± 1	N/A	2 ± 1	0.28 ± 0.02
P123	18 ± 2	3 ± 1	N/A	4 ± 1	0.40 ± 0.02
F127	19 ± 2	4 ± 1	N/A	5 ± 2	0.41 ± 0.02

[a]Wall thickness calculated from GISAXS and porosimetry data. For samples without GISAXS data, a range was estimated from SEM images.

In general, sol–gel silica films made with larger templates also displayed thicker walls. For films that lacked periodicity (at a low m_{poly}/m_{SiO_2} ratio or templated by CTAB and BrijC10), a range of wall thicknesses were measured and estimated from SEM images.

To isolate the effect of wall thickness from porosity on the thermal conductivity, Table 2 and Figure 4 summarize the characterization of three groups of SG-based mesoporous silica films with similar porosities but different pore diameters and wall thicknesses. The first group had a porosity of 59–62% and pore diameter ranging from 10 to 23 nm, the second group had a porosity of 43–45% and pore diameter ranging from 5 to 15 nm, while the third group had a porosity of 18–22% and pore diameter ranging from 2 to 4 nm. Table 2 indicates that SG-based mesoporous silica films with a similar porosity but larger pore size had larger effective thermal conductivity. For a given porosity, the SG-based mesoporous silica films templated with CTAB and BrijC10 had lower thermal conductivity than films templated with Pluronic P123 templates, followed by films templated with Pluronic F127 and then PBO–PEO. This order correlated with the pore sizes created by these templates in SG-based mesoporous silica films.

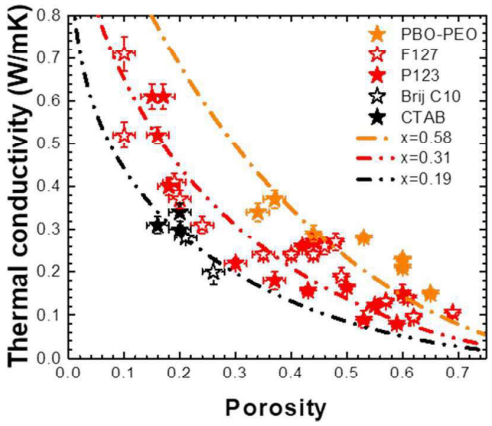

Figure 4. Thermal conductivity as a function of porosity for SG-based mesoporous silica films templated using different polymer templates to provide a range of pore diameters (BrijC10 and CTAB from 2 to 4 nm, F127 and P123 from 5 to 15 nm, PBO–PEO from 15 to 25 nm), measured under vacuum. Dashed lines correspond to fits to the PWSM model with fit values shown in the legend.

Such a positive correlation between pore size and thermal conductivity at a fixed porosity had been previously observed in porous crystals.[39–41] In crystals, the heat is carried by traveling phonons with a certain distribution of phonon MFPs. The scattering of phonons at the boundary between pores and the solid phase can reduce the effective phonon MFPs and thus the thermal conductivity. Thus, the intrinsic mean free path determines the maximum pore size that would affect the thermal conductivity. For example, in silicon, the suppression of phonon MFPs can be significant when the pore size is about 1 μm, because the intrinsic MFPs of a substantial portion of phonons can exceed 1 μm.[14] Analogous to silicon, the correlation between pore size and thermal conductivity in amorphous SG-based mesoporous silica films can also be attributed to the vibrational modes scattering near the pores. Importantly, it indicates that the MFPs for a non-negligible fraction of the vibrational modes are between 1 to 10 nm. This result is also consistent with the recent molecular dynamic simulation results and experimental results from ballistic transport across $Si/SiO_2/Si$ nanostructures.[17,42]

A porosity weighted simple medium (PWSM) model has been proposed to account for the combined effect of pore size and shape and thermal contact between particles by using a fitting parameter x.[26,43] The parameter x can vary between 0 and infinity, corresponding to the serial and parallel effective medium approximations, respectively. This model has been used extensively for various porous materials including silica xerogels[28] and templated mesoporous silica.[26,44] Considering that the disperse phase in the pores of our sol–gel mesoporous silica films is vacuum, the PWSM model simplifies to[26]

$$\kappa_{eff} = \kappa_{SiO_2}(1 - \phi_p)(1 - \phi_p^x) \quad (2)$$

Fitting the PWSM model to our experimental data yielded x = 0.19, 0.31, and 0.58 for small (CTAB and BrijC10), medium (P123 and F127), and large (PBO–PEO) pore sizes, respectively. Figure 4 plots the effective thermal conductivities of sol–gel-based mesoporous silica films as a function of porosity and compares them with the three predictions obtained from eq 2. A value of x approaching 0 corresponds to the asymptotic case captured by the serial model, which can be physically represented as a lamellar structure consisting of a series of silica layers separated by layers of air, all aligned with the layers perpendicular to the direction of heat flow; this results in the lowest thermal conductivity possible for a given porosity. We find that x increases as the pore size and corresponding wall thickness increase, suggesting that thicker walls enhanced the through-plane heat conduction captured in

the limiting case by the parallel model (which physically corresponds to the same alternating air and silica layers, this time with the layers oriented parallel to the direction of heat flow). In an attempt to more explicitly capture the effect of pore size on the thermal conductivity of our material, Figure S3 further shows the same data fit with a model developed by Alvarez et al. that contains explicit pore size dependence.[45] While the fit parameters are reasonable, the fit quality is relatively poor, likely because the model was developed for crystalline porous materials.

Overall, in this work, we examined how wall thickness controls thermal conductivity for mesoporous silica materials with different pore sizes and corresponding wall thicknesses that are made from different building blocks. We find a fundamental difference in how wall thickness effects thermal conductivity in SG-based versus NP-based mesoporous silica films. As revealed by the TEM images in Figure 1e,f, the walls of the NP-based film are made of discrete interconnected silica nanoparticles, which suggests that the characteristic length limiting the vibrational MFP is the size of the silica nanoparticles, not the thickness of the walls. As such, changing the pore size, and ultimately the wall thickness, should not significantly affect effective thermal conductivity. By contrast, SG-based mesoporous silica is composed of a continuous network surrounding mesopores. Here, the characteristic length limiting the vibrational MPF is the thickness of the pore walls. Because SG-based mesoporous silica with a large pore size also tends to have large wall thickness, heat carriers traveling in SG-based mesoporous silica with large pores will experience less scattering, resulting in higher effective thermal conductivity.

This work thus helps expand our understanding of heat transfer at the nanoscale and opens new avenues for tailoring the thermal conductivity of nanostructured materials by means other than porosity or composition. These results also help to explain some of the seemingly contradictory data in the literature. Depending on the exact synthesis conditions, nontemplated sol–gel materials can be composed of more continuous, filamentous materials or more aggregated nanoparticles.[27] With our new understanding, it would be expected that thermal conductivity in some systems would depend strongly on wall thickness, while in others, it would not.

EXPERIMENTAL METHODS

Sol–gel- and nanoparticle-based mesoporous silica thin films were prepared by evaporation-induced self-assembly according to previously reported methods.[31] Detailed procedures of the synthesis and characterization of the films are provided in the Supporting Information.

ASSOCIATED CONTENT

Supporting Information

The Supporting Information is available free of charge at https://pubs.acs.org/doi/10.1021/acs.jpclett.0c00464.

Details of synthesis, structural characterization, and thermal conductivity measurement; TEM images for nanoparticle-based films; 2D-GISAXS data for SG-based mesoporous silica films; thermal conductivity vs porosity curves for sol–gel-based samples fit using an alternative model (PDF)

AUTHOR INFORMATION

Corresponding Author

Sarah H. Tolbert – *Department of Chemistry and Biochemistry and Department of Materials Science and Engineering, UCLA, Los Angeles, California 90095-1569, United States;* orcid.org/0000-0001-9969-1582; Email: tolbert@chem.ucla.edu

Authors

Yan Yan – *Department of Chemistry and Biochemistry, UCLA, Los Angeles, California 90095-1569, United States*

Man Li – *Department of Mechanical Engineering, UCLA, Los Angeles, California 90095, United States*

Sophia King – *Department of Chemistry and Biochemistry, UCLA, Los Angeles, California 90095-1569, United States*

Tiphaine Galy – *Department of Mechanical Engineering, UCLA, Los Angeles, California 90095, United States*

Michal Marszewski – *Department of Mechanical Engineering, UCLA, Los Angeles, California 90095, United States;* orcid.org/0000-0002-4157-3046

Joon Sang Kang – *Department of Mechanical Engineering, UCLA, Los Angeles, California 90095, United States*

Laurent Pilon – *Department of Mechanical Engineering, UCLA, Los Angeles, California 90095, United States;* orcid.org/0000-0001-9459-8207

Yongjie Hu – *Department of Mechanical Engineering, UCLA, Los Angeles, California 90095, United States;* orcid.org/0000-0001-7225-1130

Complete contact information is available at: https://pubs.acs.org/10.1021/acs.jpclett.0c00464

Notes

The authors declare no competing financial interest.

ACKNOWLEDGMENTS

This work was supported by the U.S. Department of Energy (DOE), Advanced Research Projects Agency-Energy (ARPA-E) under Award Number DE-AR0000738. Y.Y. is grateful to the Chinese Scholar Council for financial support in the form of a graduate fellowship. The authors acknowledge the use of instruments at the Electron Imaging Center for NanoMachines supported by NIH (1S10RR23057) and the California NanoSystems Institute (CNSI) at UCLA. This manuscript contains X-ray data that were collected at the Stanford Synchrotron Radiation Lightsource. Use of the Stanford Synchrotron Radiation Lightsource, SLAC National Accelerator Laboratory, is supported by the U.S. Department of Energy, Office of Science, Office of Basic Energy Sciences, under Contract DE-AC02-76SF00515.

REFERENCES

(1) Boukai, A. I.; Bunimovich, Y.; Tahir-Kheli, J.; Yu, J.-K.; Goddard, W. A., III; Heath, J. R. Silicon Nanowires as Efficient Thermoelectric Materials. *Nature* **2008**, *451* (7175), 168–171.

(2) Dresselhaus, M. S.; Chen, G.; Tang, M. Y.; Yang, R. G.; Lee, H.; Wang, D. Z.; Ren, Z. F.; Fleurial, J.; Gogna, P. New Directions for Low-Dimensional Thermoelectric Materials. *Adv. Mater.* **2007**, *19* (8), 1043–1053.

(3) Costescu, R. M. Ultra-Low Thermal Conductivity in W/Al_2O_3 Nanolaminates. *Science* **2004**, *303* (5660), 989–990.

(4) Hrubesh, L. W.; Pekala, R. W. Thermal Properties of Organic and Inorganic Aerogels. *J. Mater. Res.* **1994**, *9* (03), 731–738.

(5) Prasher, R. Thermal Interface Materials: Historical Perspective, Status, and Future Directions. *Proc. IEEE* **2006**, *94* (8), 1571−1586.
(6) Cahill, D. G.; Ford, W. K.; Goodson, K. E.; Mahan, G. D.; Majumdar, A.; Maris, H. J.; Merlin, R.; Phillpot, S. R. Nanoscale Thermal Transport. *J. Appl. Phys.* **2003**, *93* (2), 793−818.
(7) Sansoz, F. Surface Faceting Dependence of Thermal Transport in Silicon Nanowires. *Nano Lett.* **2011**, *11* (12), 5378−5382.
(8) Gu, H.; Wang, H. Effect of Strain on Thermal Conductivity of Amorphous Silicon Dioxide Thin Films: A Molecular Dynamics Study. *Comput. Mater. Sci.* **2018**, *144*, 133−138.
(9) Alam, M. T.; Raghu, A. P.; Haque, M. A.; Muratore, C.; Voevodin, A. A. Structural Size and Temperature Dependence of Solid to Air Heat Transfer. *Int. J. Therm. Sci.* **2013**, *73*, 1−7.
(10) Tian, Z.; Hu, H.; Sun, Y. A Molecular Dynamics Study of Effective Thermal Conductivity in Nanocomposites. *Int. J. Heat Mass Transfer* **2013**, *61* (1), 577−582.
(11) Hopkins, P. E.; Rakich, P. T.; Olsson, R. H.; El-Kady, I. F.; Phinney, L. M. Origin of Reduction in Phonon Thermal Conductivity of Microporous Solids. *Appl. Phys. Lett.* **2009**, *95* (16), 161902.
(12) Marconnet, A. M.; Asheghi, M.; Goodson, K. E. From the Casimir Limit to Phononic Crystals: 20 Years of Phonon Transport Studies Using Silicon-on-Insulator Technology. *J. Heat Transfer* **2013**, *135* (6), 061601.
(13) Zhang, H.; Hua, C.; Ding, D.; Minnich, A. J. Length Dependent Thermal Conductivity Measurements Yield Phonon Mean Free Path Spectra in Nanostructures. *Sci. Rep.* **2015**, *5* (1), 9121.
(14) Hu, Y.; Zeng, L.; Minnich, A. J.; Dresselhaus, M. S.; Chen, G. Spectral Mapping of Thermal Conductivity through Nanoscale Ballistic Transport. *Nat. Nanotechnol.* **2015**, *10* (8), 701−706.
(15) Deng, Z.; Wang, J.; Wu, A.; Shen, J.; Zhou, B. High Strength SiO2 Aerogel Insulation. *J. Non-Cryst. Solids* **1998**, *225*, 101−104.
(16) Hopkins, P. E.; Kaehr, B.; Phinney, L. M.; Koehler, T. P.; Grillet, A. M.; Dunphy, D.; Garcia, F.; Brinker, C. J. Measuring the Thermal Conductivity of Porous, Transparent SiO2 Films With Time Domain Thermoreflectance. *J. Heat Transfer* **2011**, *133* (6), 061601.
(17) Larkin, J. M.; McGaughey, A. J. H. Thermal Conductivity Accumulation in Amorphous Silica and Amorphous Silicon. *Phys. Rev. B: Condens. Matter Mater. Phys.* **2014**, *89* (14), 1−12.
(18) Schmidt, M.; Schwertfeger, F. Applications for Silica Aerogel Products. *J. Non-Cryst. Solids* **1998**, *225*, 364−368.
(19) Reim, M.; Reichenauer, G.; Körner, W.; Manara, J.; Arduini-Schuster, M.; Korder, S.; Beck, A.; Fricke, J. Silica-Aerogel Granulate − Structural, Optical and Thermal Properties. *J. Non-Cryst. Solids* **2004**, *350*, 358−363.
(20) Reim, M.; Körner, W.; Manara, J.; Korder, S.; Arduini-Schuster, M.; Ebert, H.-P.; Fricke, J. Silica Aerogel Granulate Material for Thermal Insulation and Daylighting. *Sol. Energy* **2005**, *79* (2), 131−139.
(21) Baetens, R.; Jelle, B. P.; Gustavsen, A. Aerogel Insulation for Building Applications: A State-of-the-Art Review. *Energy Build* **2011**, *43* (4), 761−769.
(22) Chen, K.; Neugebauer, A.; Goutierre, T.; Tang, A.; Glicksman, L.; Gibson, L. J. Mechanical and Thermal Performance of Aerogel-Filled Sandwich Panels for Building Insulation. *Energy Build* **2014**, *76*, 336−346.
(23) Venkateswara Rao, A.; Pajonk, G. M.; Haranath, D. Synthesis of Hydrophobic Aerogels for Transparent Window Insulation Applications. *Mater. Sci. Technol.* **2001**, *17* (3), 343−348.
(24) Wei, T.; Chang, T.-F.; Lu, S.; Chang, Y. Preparation of Monolithic Silica Aerogel of Low Thermal Conductivity by Ambient Pressure Drying. *J. Am. Ceram. Soc.* **2007**, *90* (7), 2003−2007.
(25) Shenogin, S.; Bodapati, A.; Keblinski, P.; McGaughey, A. J. H. Predicting the Thermal Conductivity of Inorganic and Polymeric Glasses: The Role of Anharmonicity. *J. Appl. Phys.* **2009**, *105* (3), 034906.
(26) Coquil, T.; Richman, E. K.; Hutchinson, N. J.; Tolbert, S. H.; Pilon, L. Thermal Conductivity of Cubic and Hexagonal Mesoporous Silica Thin Films. *J. Appl. Phys.* **2009**, *106* (3), 034910.
(27) Lu, X.; Caps, R.; Fricke, J.; Alviso, C. T.; Pekala, R. W. Correlation between Structure and Thermal Conductivity of Organic Aerogels. *J. Non-Cryst. Solids* **1995**, *188* (3), 226−234.
(28) Hu, C.; Morgen, M.; Ho, P. S.; Jain, A.; Gill, W. N.; Plawsky, J. L.; Wayner, P. C. Thermal Conductivity Study of Porous Low- *k* Dielectric Materials. *Appl. Phys. Lett.* **2000**, *77* (1), 145−147.
(29) Jain, A.; Rogojevic, S.; Ponoth, S.; Gill, W. N.; Plawsky, J. L.; Simonyi, E.; Chen, S.-T.; Ho, P. S. Processing Dependent Thermal Conductivity of Nanoporous Silica Xerogel Films. *J. Appl. Phys.* **2002**, *91* (5), 3275−3281.
(30) Liu, J.; Gan, D.; Hu, C.; Kiene, M.; Ho, P. S.; Volksen, W.; Miller, R. D. Porosity Effect on the Dielectric Constant and Thermomechanical Properties of Organosilicate Films. *Appl. Phys. Lett.* **2002**, *81* (22), 4180−4182.
(31) Yan, Y.; King, S. C.; Li, M.; Galy, T.; Marszewski, M.; Kang, J. S.; Pilon, L.; Hu, Y.; Tolbert, S. H. Exploring the Effect of Porous Structure on Thermal Conductivity in Templated Mesoporous Silica Films. *J. Phys. Chem. C* **2019**, *123* (35), 21721−21730.
(32) Li, M.; Kang, J. S.; Hu, Y. Anisotropic Thermal Conductivity Measurement Using a New Asymmetric-Beam Time-Domain Thermoreflectance (AB-TDTR) Method. *Rev. Sci. Instrum.* **2018**, *89* (8), 084901.
(33) Kang, J. S.; Li, M.; Wu, H.; Nguyen, H.; Hu, Y. Experimental Observation of High Thermal Conductivity in Boron Arsenide. *Science* **2018**, *361* (6402), 575−578.
(34) Baklanov, M. R.; Mogilnikov, K. P.; Polovinkin, V. G.; Dultsev, F. N. Determination of Pore Size Distribution in Thin Films by Ellipsometric Porosimetry. *J. Vac. Sci. Technol., B: Microelectron. Process. Phenom.* **2000**, *18* (3), 1385−1391.
(35) Gregg, S. J.; Sing, K. S. W. *Adsorption, Surface Area and Porosity*, Second ed; Academic Press Inc., Ltd: London, 1982.
(36) Thommes, M.; Kaneko, K.; Neimark, A. V.; Olivier, J. P.; Rodriguez-Reinoso, F.; Rouquerol, J.; Sing, K. S. W. Physisorption of Gases, with Special Reference to the Evaluation of Surface Area and Pore Size Distribution (IUPAC Technical Report). *Pure Appl. Chem.* **2015**, *87* (9−10), 1051−1069.
(37) Kruk, M.; Jaroniec, M.; Ko, C. H.; Ryoo, R. Characterization of the Porous Structure of SBA-15. *Chem. Mater.* **2000**, *12* (7), 1961−1968.
(38) Smarsly, B.; Gibaud, A.; Ruland, W.; Sturmayr, D.; Brinker, C. J. Quantitative SAXS Analysis of Oriented 2D Hexagonal Cylindrical Silica Mesostructures in Thin Films Obtained from Nonionic Surfactants. *Langmuir* **2005**, *21* (9), 3858−3866.
(39) Song, D.; Chen, G. Thermal Conductivity of Periodic Microporous Silicon Films. *Appl. Phys. Lett.* **2004**, *84* (5), 687−689.
(40) Tang, J.; Wang, H. T.; Lee, D. H.; Fardy, M.; Huo, Z.; Russell, T. P.; Yang, P. Holey Silicon as an Efficient Thermoelectric Material. *Nano Lett.* **2010**, *10* (10), 4279−4283.
(41) Seol, J. H.; Barth, D. S.; Zhu, J.; Ćoso, D.; Hippalgaonkar, K.; Lim, J.; Han, J.; Zhang, X.; Majumdar, A. Tunable Thermal Conductivity in Mesoporous Silicon by Slight Porosity Change. *Appl. Phys. Lett.* **2017**, *111* (6), 063104.
(42) Yang, L.; Zhang, Q.; Cui, Z.; Gerboth, M.; Zhao, Y.; Xu, T. T.; Walker, D. G.; Li, D. Ballistic Phonon Penetration Depth in Amorphous Silicon Dioxide. *Nano Lett.* **2017**, *17* (12), 7218−7225.
(43) Fricke, J.; Lu, X.; Wang, P.; Büttner, D.; Heinemann, U. Optimization of Monolithic Silica Aerogel Insulants. *Int. J. Heat Mass Transfer* **1992**, *35* (9), 2305−2309.
(44) Zhu, W.; Zheng, G.; Cao, S.; He, H. Thermal Conductivity of Amorphous SiO2thin Film: A Molecular Dynamics Study. *Sci. Rep.* **2018**, *8* (1), 1−9.
(45) Alvarez, F. X.; Jou, D.; Sellitto, A. Pore-Size Dependence of the Thermal Conductivity of Porous Silicon: A Phonon Hydrodynamic Approach. *Appl. Phys. Lett.* **2010**, *97* (3), 033103.

CHAPTER 4

Understanding the Effect of Nanoparticle Size on the Thermal Conductivity in Amorphous Materials

In this work we examine the effect of nanoparticle size on the thermal conductivity of mesoporous silica material made from colloidal precursors. Porous thin films were synthesized using a polymer templating technique, employing commercial colloidal silica solutions containing nanoparticles 6, 9, and 22 nm in diameter as the silica source, and PMMA colloids as the template. The ratio of polymer to silica was then varied to produce films with a range of porosities. The thermal conductivities of the films were measured using time domain thermal reflectance (TDTR), revealing that for the particle sizes studied, there was a weak dependence of thermal conductivity on particle size. This weak dependence was assigned to increased interfacial scattering of heat carriers at the boundaries of the smaller nanoparticles. This work adds to our understanding of the effect of nanostructuring on heat transport in amorphous material systems and improves our ability to design low thermal conductivity materials.

The study of thermal transport is integral to the development of effective materials for circuitry, thermoelectrics, and energy conservation.[1–8] One class of materials of interest in such fields is thermally insulating materials, leading to the exploration of strategies for lowering thermal conductivity.[2,6,8,9] Nanostructuring has been shown to offer an easy route to reduce thermal conductivity due to the variety of structural parameters that can be tuned on the nanoscale.[7,9] In particular, amorphous silica networks with nanoscale pores are of great interest because of their demonstrated ability to reach very low thermal conductivity at high porosity.[9–13] Pores lower the effective thermal conductivity by both reducing the effective density, which decreases heat carrier transport, and by increasing internal surfaces that scatter heat carriers.[14–18] However, increasing the porosity of such materials limits their possible applications, since the low density often makes these materials fragile and opaque. As a result, identifying other factors that could decrease thermal conductivity would open up new avenues in the design of insulating materials.

In crystalline materials, particle size effects have been harnessed an effective strategy to tune thermal conductivity. Heat carrier propagate in these materials in the form of lattice vibrations called phonons.[7,8,16] On scales smaller than the phonon mean free path, phonon transport, and therefore thermal conductivity, has been shown to decrease with decreasing feature size.[2,7,18–21] In amorphous materials, however, the influence of feature size on the thermal conductivity is less understood.[22] Heat transfer in amorphous materials is carried out via many vibrational modes, including propagons, which behave like phonons but with much shorter mean free paths due to the lack of structural order in amorphous networks.[16,17,23] Thus, prevailing theory suggests that heat transfer in amorphous materials is too disordered for any size effects to exist.[19] However, Gao, T. and Jelle, B. P. calculated the intrinsic solid-state thermal conductivity of silica nanoparticles as a function of particle size and found a weak size effect in the thermal conductivity.[19] In addition,

Yan, Y. *et al.* recently examined the effect of pore wall thickness on thermal conductivity for amorphous mesoporous silica thin films made from a sol—gel precursor as well as from a commercial nanoparticle precursor.[1] There, they found that for a given porosity in a continuous sol—gel-based silica network, the thermal conductivity decreased as the thickness of the silica walls decreased. However, no trend in the thermal conductivity with wall thickness was observed for films made from discrete nanoparticle-precursors. They attributed this lack of correlation to the nanoparticles making up the walls were the same size, and those nanoparticle-building block were the key size-determining unit, not the overall wall thickness. In this work, we are interested in building upon these studies to experimentally explore the existence of any nanoparticle size effects on the thermal conductivity of amorphous silica nanoparticle-based films.

Using a template-assisted technique, combined with three sizes of commercially obtained silica colloids for the silica framework, we synthesized porous, nanoparticle-based silica thin films. The precursors used and their sizes are depicted in Figure 4.1. The diameters of the commercial silica colloids were 6 ± 1 nm, 9 ± 2 nm and 22 ± 2 nm, here called NP6, NP9, and NP22, respectively. All silica nanoparticles were reasonably monodisperse, but as the particle size increased, polydispersity also increased. This is observed in Figure 4.1 as an increase in the bredth of the histograms going from NP6 (Figure 4.1(b)) to NP9 (Figure 4.1(d)) to NP22 (Figure 4.1(f)). The silica colloids were combined with in-house synthesized PMMA colloids that served as the polymer template. The PMMA colloids had a diameter of 62 ± 7 nm, as depicted in the SEM (Figure 4.1(g)) and the histogram of the measured diameters (Figure 4.1(h)). Porosity was tuned by varying the ratio of polymer template to silica precursor. Solutions of the silica and PMMA colloids were spin-coated to produce smooth films, calcined to remove the polymer template, and measured using time domain thermoreflectance (TDTR) to obtain the thermal conductivity.

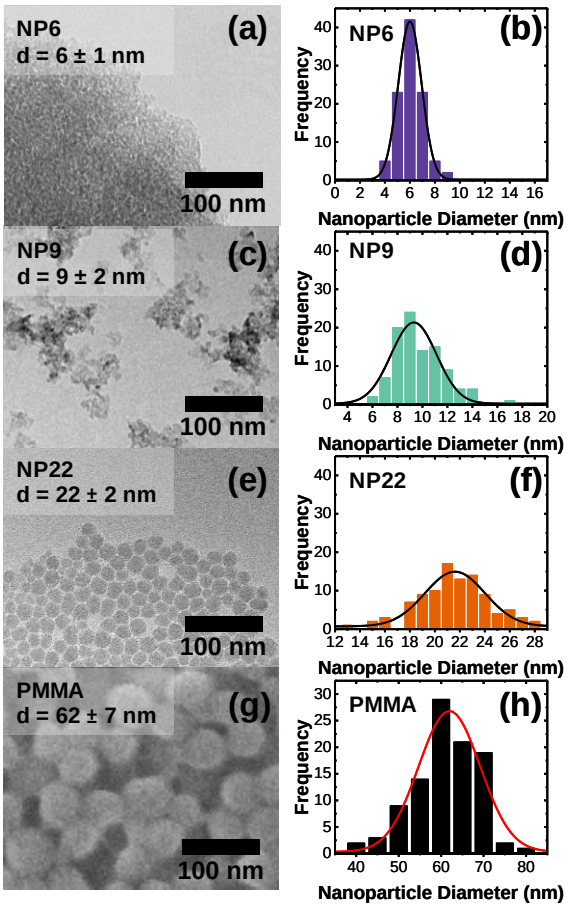

Figure 4.1. Electron microscope images and size analysis of the precursor solutions used to make the mesoporous silica films. Transmission electron micrographs (a), (c), (e) and histograms of nanoparticle diameter distributions (b), (d), (f) for commercial silica solutions of diameters 6 ± 1 nm (a) and (b), 9 ± 2 nm (c) and (d), and 22 ± 2 nm (e) and (f). Scanning electron micrograph (g) and histogram of the measured diameters of the PMMA colloids used as the polymer template.

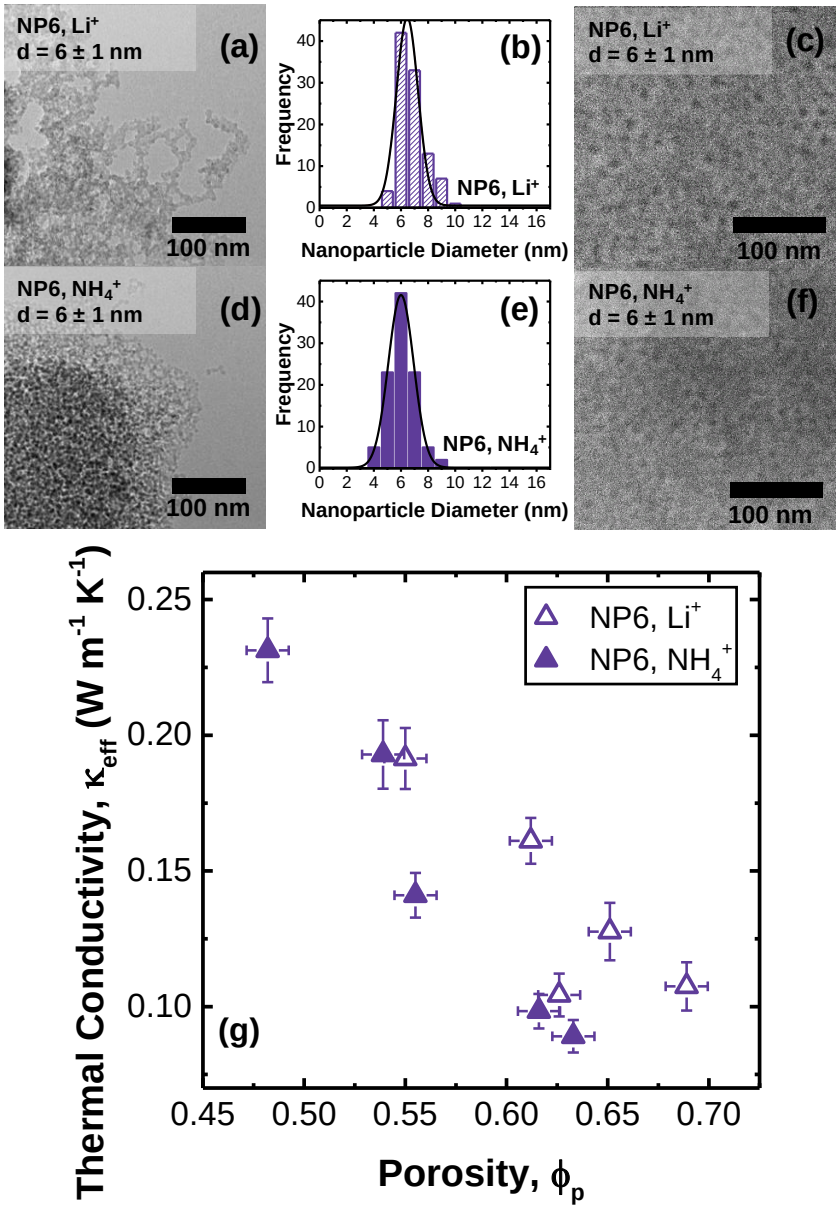

Figure 4.2. Characterization of the commercial 6 ± 1 nm silica (NP6) particles stabilized with Li^+ (as purchased) and NH_4^+ (ion-exchanged). TEM images depict the Li^+- stabilized (a), and the ion-exchanged NH_4^+-stabilized (d) 6 nm silica nanoparticles. Histograms are used to quantify the measured diameters of the Li^+- stabilized (b), and the ion-exchanged NH_4^+-stabilized (e) 6 nm silica nanoparticles, showing that the size distributions are similar. SEM images of films synthesized using Li^+- stabilized (c), and the ion-exchanged NH_4^+-stabilized (f) 6 nm silica nanoparticles with Pluronic F127 as the pore-forming template show that on the nanoscale, the structure of the films is similar. Thermal conductivity as a function of porosity for the Li^+- stabilized and the ion-exchanged NH_4^+-stabilized 6 nm silica nanoparticles shows that the counter-ion does affects the thermal conductivity of the samples, with ammonium counterions producing lower thermal conductivity.

As purchased, the NP9 and NP22 commercial silica colloids are both stabilized with NH_4^+ counter-ions, but the NP6 solution is stabilized with Li^+. To ensure that possible differences in thermal conductivity result from differences in nanoparticle size rather than counter-ion, the Li^+ stabilizing the NP6 solution was exchanged to NH_4^+ using a batch ion exchange process, as described in the Supporting Information. Figure 4.2 shows the basic characterization of the Li^+- and NH_4^+-stabilized NP6 solutions and resulting films. The nanoparticles have approximately the same diameters, as is observed in the TEM images in Figures 4.2(a) and 4.2(d) and the histograms of the measured diameters in Figures 4.2(b) and 4.2(e). High magnification SEM images of the samples, templated with the triblock copolymer F127 (Figures 4.2(c) and 4.2(f)), show that exchanging the cation does not affect the porous structure of the films. When we examine the thermal conductivity of a small sample set of films made from the Li^+- and NH_4^+-stabilized nanoparticles, however, we see that the films made from the NH_4^+-stabilized colloids have overall lower thermal conductivities than those made from the Li^+-stabilized colloids. We hypothesize that this difference is due to the fact that the NH_4^+ salt is volatile at the temperatures used for film calcination while the Li^+ salt does not evaporate and thus should remain in the film and may contribute to the thermal conductivity. Therefore, to ensure that the counter-ion does not affect the measured thermal conductivity of the samples, only NH_4^+-stabilized silica colloids were used.

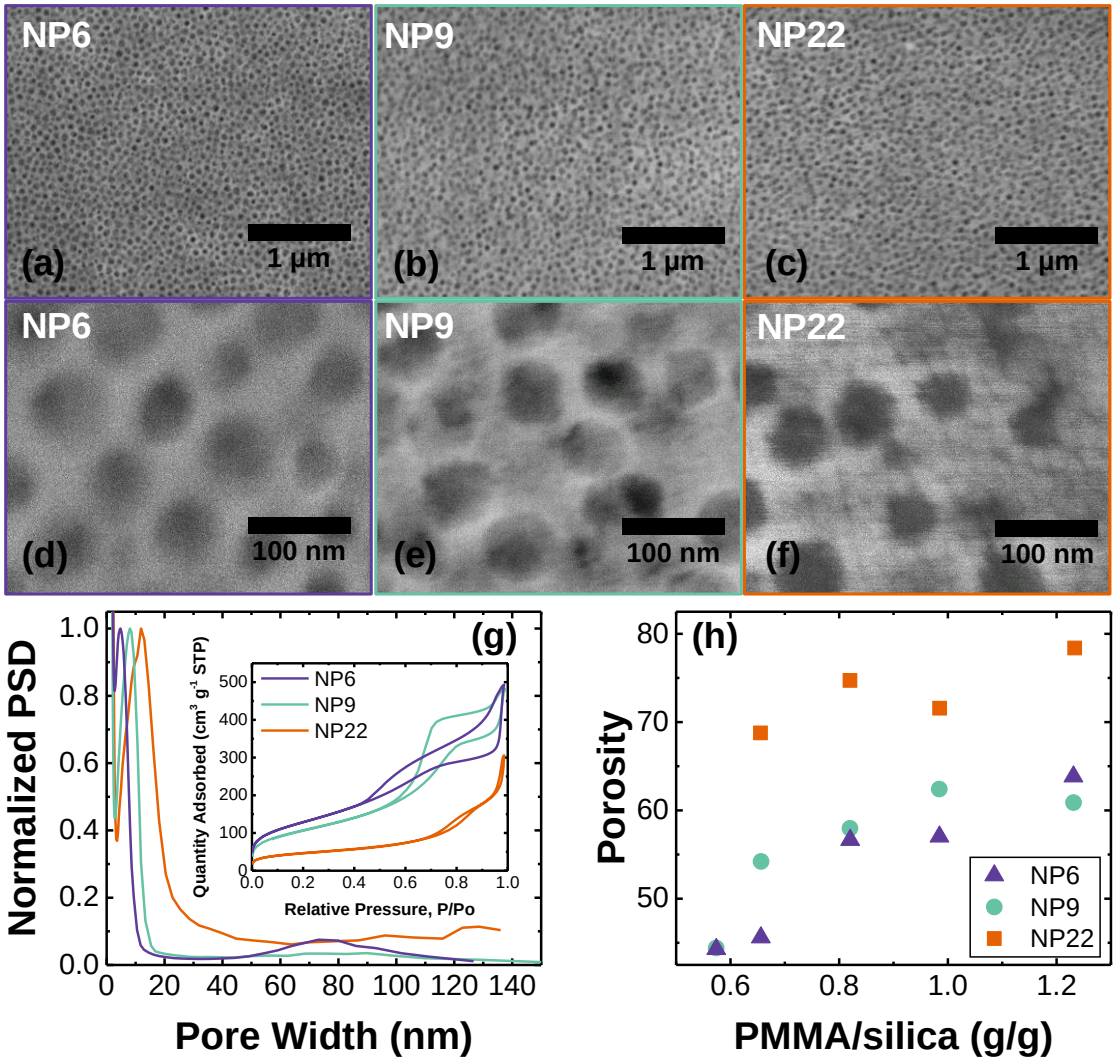

Figure 4.3. Structural characterization of porous samples made with silica colloids of different sizes, showing the range of porosities used. (a)-(c) Low magnification scanning electron micrographs of PMMA template silica films made from commercial colloidal silica solutions with colloid sizes of (a) 6 ± 1 nm, (b) 9 ± 2 nm and (c) 22 ± 2 nm. These low magnification images show that the pores are well distributed in the silica network. (d)-(f) High magnification scanning electron micrographs of PMMA template silica films made from commercial colloidal silica solutions with colloid sizes of (d) 6 ± 1 nm, (e) 9 ± 2 nm and (f) 22 ± 2 nm. The individual nanoparticles can be observed as the diameter of the nanoparticles increases. (g) Normalized number-weighted pore size distributions (PSD) with the inset showing the nitrogen adsorption/desorption isotherms measured at 77 K on powdered samples made from PMMA and commercial silica solutions of different diameters at a 1 g/g PMMA/silica ratio. The pore widths between 0 and 20 nm are from intrinsic gaps between the particles while those above 50 nm are due to the polymer templating. (h) Porosities of PMMA templated films used in this study obtained from optical interferometry.

The silica and PMMA colloids were combined in PMMA/silica (g/g) ratios ranging from 0.6 to 1.2 to produce smooth, crack free films with varying porosities. The porous structure of the samples was characterized as shown in Figure 4.3. From the SEM images in Figures 4.3(a) to 4.3(f), we can clearly see the porous structure of representative films made from the NP6, NP9, and NP22 silica colloids. The lower magnification images, Figures 4.3(a) to 4.3(c), show that the films produced are smooth and homogenous with pores well distributed in the network. We also observe that the pore sizes for all samples are approximately the same, which is expected as the same PMMA template was used to make all films. In the higher magnification SEM images, Figures 4.3(d) to 4.3(f), we see that the silica colloids that constitute each network are of different sizes and that as the size of the colloids increases, the ability to resolve the individual particles increases as well. Pore size was characterized by nitrogen porosimetry conducted at 77 K. Figure 4.3(g) shows the pore size distribution of representative porous powder samples made from each colloid solution at a 1 g/g PMMA/silica ratio. From the pore size distributions in Figure 4.3(g) we see that each sample has two distinct pore sizes. The first pore size is due to the intrinsic gaps between the nanoparticles. This gap size increases from 5 ± 3 nm to 8 ± 3 nm to 11 ± 5 nm as the nanoparticle size increases from 6 nm to 9 nm to 22 nm, respectively. There is a second pore size observed at approximately 80 nm due to the PMMA templated pores. This pore size distribution is fairly broad as a result of the polydispersity of the template used. The nitrogen adsorption/desorption isotherms of the samples, shown in the inset of Figure 4.3(g), are complex. According to the IUPAC classification,[24,25] the general shape of the nitrogen adsorption-desorption isotherms at relative pressure less than 0.9 resembles that of a Type IV(a) isotherm with an H2(b) hysteresis loop. Such isotherms are typical of mesoporous materials with fairly narrow pore size distributions with pores connected by narrow necks. This hysteresis is due to the intrinsic gap

between the nanoparticles. Above a relative pressure of 0.9, the volume of nitrogen absorbed does not plateau as is typical of mesoporous samples. Instead, there is another increase in the volume adsorbed that is typical of macroporous samples, resulting from the large pores created by the PMMA template. As the nanoparticle size increases, there is an increase in relative pressure where the volume of adsorbed nitrogen increases, resulting in the observed trend of increasing pore size. Since the pores created by the PMMA colloids are just outside the range that can be accurately determined by nitrogen porosimetry, the total porosity measured on the colloidal powders using nitrogen adsorption is not necessarily and accurate description of the total porosity of the films. As such, we used an interferometry-based technique to retrieve the total porosity of the films used for the thermal conductivity measurements. The details of this interferometry technique have been previously described.[26] From the retrieved porosities depicted in Figure 4.3(h) we see that, in general, the porosity of the films increases as the ratio of PMMA/silica increases. The samples made from the NP6 and NP9 colloids have similar porosities while those made from the NP22 colloids have significantly greater porosities. This increased porosity for the larger colloids is most likely due to the larger intrinsic gaps between colloids in these samples.

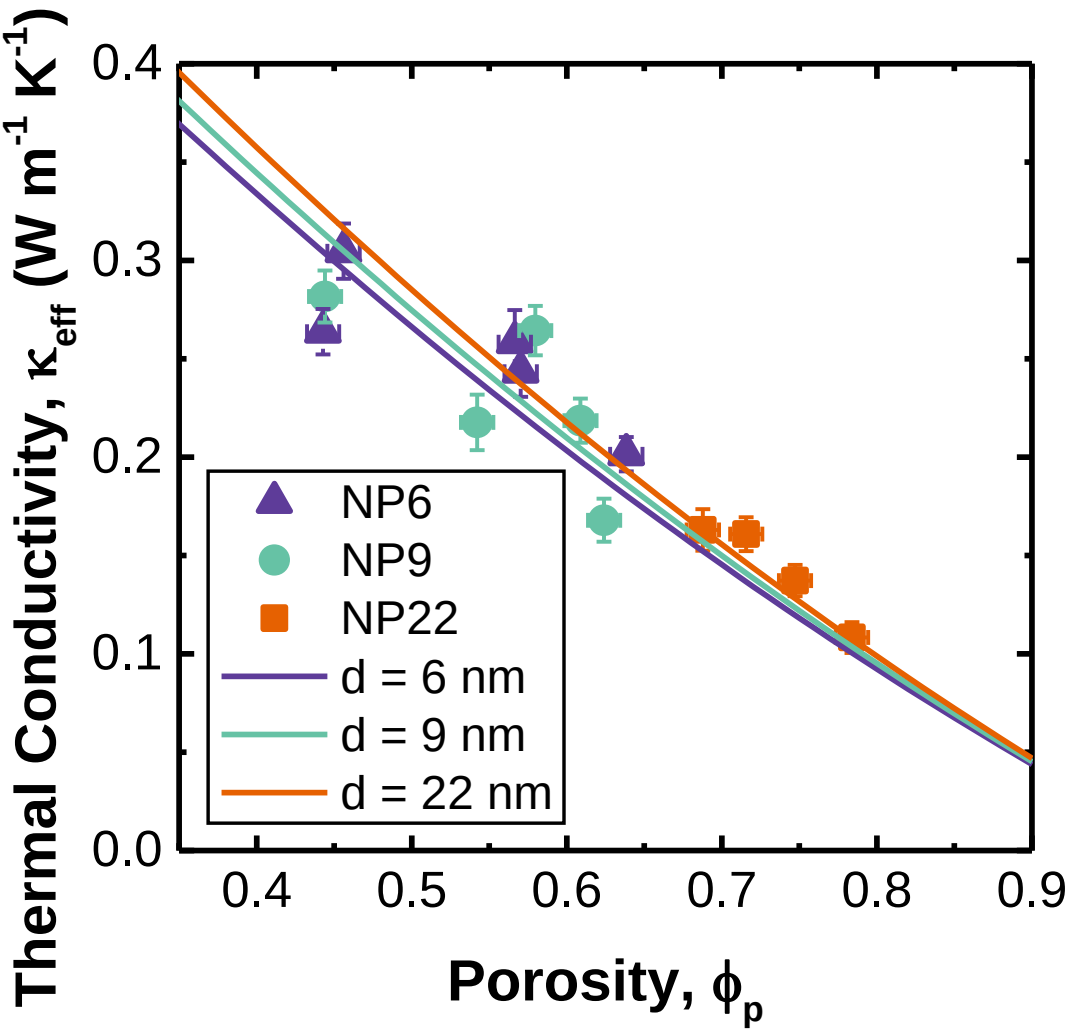

Figure 4.4. Porosity-dependent effective thermal conductivity of silica nanoparticle-based, PMMA templated films silica films made from 6 ± 1, 9 ± 2 and 22 ± 2 nm silica nanoparticles fitted with Equation 3. All films were dried under vacuum at 150 °C before the thermal conductivity measurements conducted to remove and adsorbed water.

The effective thermal conductivity of the PMMA-templated films as a function of porosity is plotted in Figure 4.4. The thermal conductivity seems to mostly trend with porosity, with a subtle increase as the particle size increases. In our previous work,[1] we observed a very distinct increase in the porosity-dependent thermal conductivity when the thickness of the continuous, molecular-based silica walls forming around the pores was increased from ~2 nm up to ~25 nm. This led us to hypothesize that such a distinct difference in porosity-dependent thermal conductivity would

also occur if the walls were made of nanoparticles with different diameters. However, a large change was not observed in the present study, and only small differences were observed. We believe that this was due to our inability to acquire nanoparticles with diameters closer to the mean free path-length of heat carriers in amorphous silica (c.a. 1 nm) and study size effects with such particles.[27]

To try to capture the effect of nanoparticle size on the thermal conductivity of the films, we examined the phenomenological model postulated by Liang and Li[28] to predict the thermal conductivity of individual semiconductor nanowires and nanoparticles, as well as dense thin films. Gao and Jelle[19] showed that this model gives good predictions for amorphous silica nanoparticles. The model is given by

$$\frac{\kappa_p}{\kappa_{SiO_2}} = p.\exp\left(-\frac{l_0}{d}\right).\left[\exp\left(\frac{1-\alpha}{d/L_0-1}\right)\right]^{3/2} \quad (1)$$

where κ_p is the effective thermal conductivity of the nanomaterial (in our case, the silica nanoparticles). p describes the roughness of the surface and can vary from 0 to 1, with 1 representing a smooth surface with a high probability of specular scattering and 0 a very rough surface with a high probability of diffuse scattering. Note that the parameter p for synthesized nanoparticles was reported as approximately 0.4.[19,29] Here, l_0 is the phonon mean free path of silica at room temperature; d is the nanoparticle diameter; $\alpha = 1 + {2S_V}/{3R}$ is a material constant that depends on the universal gas constant, R = 8.31451 J mol^{-1} K^{-1}, and on the bulk vibrational entropy $\left(S_V = {H_m}/{T_m} - R\right)$, where H_m= 9580 J mol^{-1} and T_m = 1986 K are the melting enthalpy and the melting temperature, respectively.[30] Finally, L_0 is a critical size at which all atoms are located at

the surface of the nanomaterial and is given by $L_0 = 2(3-\beta)w$, where β is a dimension parameter (β =0 for nanoparticles) and w is the interatomic distance (w = 0.16 nm for Si-O bonds).[31]

The effective thermal conductivity of our mesoporous thin films with porosity ϕ_p was predicted using Russell's model,[32] which is used for predicting the thermal conductivity of bulk material with spherical pores and is given by

$$\kappa_{eff} = \kappa_{SiO_2} \frac{\left(1-{\phi_p}^{2/3}\right)}{\left(1-{\phi_p}^{2/3}+\phi_p\right)}. \quad (2)$$

The particle thermal conductivity was then predicted by Equation (1) so that

$$\frac{\kappa_{eff}}{\kappa_{SiO_2}} = \frac{\left(1-{\phi_p}^{2/3}\right)}{\left(1-{\phi_p}^{2/3}+\phi_p\right)} p \exp\left(-\frac{l_0}{L}\right) \left[\exp\left(\frac{1-\alpha}{L/L_0-1}\right)\right]^{3/2}. \quad (3)$$

Applying Equation (3) to the films made with the different nanoparticle sizes yields the predictions shown in Figure 4.4 for each particle diameter. Through least square fitting, the data was best described using a mean free path l_0 = 0.42 nm and a particle roughness p = 0.44. These fits are shown in Figure 4.4.

We can compare the phonon mean free path l_0 described by Equation (3) to the value determined by the kinetic theory. The kinetic theory relates the thermal conductivity of bulk silica κ_{SiO_2} to the phonon mean free path l_0 such that $\kappa_{SiO_2} = \frac{1}{3}\rho_{SiO_2} c_{v,SiO_2} v l_0$. [27] Here, ρ_{SiO_2} is the density of silica (= 2200 kg m^{-3}),[33] c_{v,SiO_2} is our previously measured specific heat capacity at constant volume (= 750 J kg^{-1} K^{-1}),[1,34] and v is the average sound velocity in the material, obtained from the longitudinal v_l and transversal v_t wave vectors given by $v = \frac{1}{3}v_l + \frac{2}{3}v_t$, with v_l = 5968 m s^{-1} and v_t = 3764 × m s^{-1}.[33] From this kinetic model, a phonon mean free path of l_0 = 0.57 nm

in bulk silica (κ_{SiO_2}= 1.4 W m^{-1} K^{-1}) was retrieved, which agrees reasonably well with the value of l_0 = 0.42 nm that was obtained from Equation (3). We also note that the values of l_0 = 0.42 nm and p = 0.44 are similar to those calculated by Gao and Jelle[19] for individual amorphous silica nanoparticles, l_0 = 0.59 nm and p = 0.4.

The mean free path l_0 retrieved is significantly smaller than the size of the nanoparticles. As such, we believe that the marginal decrease in the thermal conductivity observed when the nanoparticle size decreases is not due to heat carrier confinement. Rather, as the diameters of the particles become smaller, the number of particles that make up the wall increases, as does the number of interfaces that are responsible for scattering heat carriers. Therefore, the decrease in thermal conductivity may be due an increase in interfacial propagon scattering, which may also be partly responsible for the size-dependent thermal conductivity previously observed in pore walls.[1] As such, these results indicate that unless extremely small structures can be fabricated, the best way to reduce thermal conductivity is by maximizing the interfaces for heat scattering. This can be done through the use of smaller particles, thin walls, or novel materials like hollow shells or core-shell nanoparticles. Importantly, unless extremely small structures can be produced, size effects alone appear not to be a good method to lower thermal conductivity in nanoporous materials built from amorphous building blocks.

Conclusions

This work studies the effect of nanoparticle size on the thermal conductivity of amorphous silica films. We found a weak dependence of thermal conductivity on the diameter of silica nanoparticles, which we attribute to an increase in the number of interfacial scattering centers. The mean free path for heat carriers extracted from the measured thermal conductivity as a function of porosity across a range silica colloid sizes was in reasonable agreement with previous

measurements for bulk amorphous silica. As such, these results indicate that size effects are not an effective way to lower that thermal conductivity in amorphous silica materials unless very small size can be reached. The better way to design low thermal conductivity materials is to maximize the number of heat scattering interfaces. This work thus adds to our growing understanding of the effect of structure on heat transport in amorphous, nanoporous systems.

References

(1) Yan, Y.; Li, M.; King, S. C.; Galy, T.; Marszewski, M.; Kang, J. S.; Pilon, L.; Hu, Y.; Tolbert, S. H. Controlling Thermal Conductivity in Mesoporous Silica Films Using Pore Size and Nanoscale Architecture. *J. Phys. Chem. Lett.* **2020**, acs.jpclett.0c00464. https://doi.org/10.1021/acs.jpclett.0c00464.

(2) Zhang, H.; Minnich, A. J. The Best Nanoparticle Size Distribution for Minimum Thermal Conductivity. *Sci. Rep.* **2015**, *5* (1), 1–5. https://doi.org/10.1038/srep08995.

(3) Pop, E. Energy Dissipation and Transport in Nanoscale Devices. *Nano Research*. Tsinghua University Press 2010, pp 147–169. https://doi.org/10.1007/s12274-010-1019-z.

(4) Dresselhaus, M. S.; Chen, G.; Tang, M. Y.; Yang, R. G.; Lee, H.; Wang, D. Z.; Ren, Z. F.; Fleurial, J.; Gogna, P. New Directions for Low-Dimensional Thermoelectric Materials. *Adv. Mater.* **2007**, *19* (8), 1043–1053. https://doi.org/10.1002/adma.200600527.

(5) Costescu, R. M. Ultra-Low Thermal Conductivity in W/Al2O3 Nanolaminates. *Science (80-.).* **2004**, *303* (5660), 989–990. https://doi.org/10.1126/science.1093711.

(6) Hrubesh, L. W.; Pekala, R. W. Thermal Properties of Organic and Inorganic Aerogels. *J. Mater. Res.* **1994**, *9* (03), 731–738. https://doi.org/10.1557/JMR.1994.0731.

(7) Cahill, D. G.; Ford, W. K.; Goodson, K. E.; Mahan, G. D.; Majumdar, A.; Maris, H. J.;

Merlin, R.; Phillpot, S. R. Nanoscale Thermal Transport. *J. Appl. Phys.* **2003**, *93* (2), 793–818. https://doi.org/10.1063/1.1524305.

(8) Cahill, D. G.; Braun, P. V; Chen, G.; Clarke, D. R.; Fan, S.; Goodson, K. E.; King, W. P.; Mahan, G. D.; Majumdar, A.; Maris, H. J.; et al. Nanoscale Thermal Transport. II. 2003–2012. *Appl. Phys. Rev.* **2014**, *1*, 011305. https://doi.org/10.1063/1.4832615.

(9) Yan, Y.; Li, M.; King, S.; Galy, T.; Marszewski, M.; Kang, J. S.; Pilon, L.; Hu, Y.; Tolbert, S. H. Controlling Thermal Conductivity in Mesoporous Silica Films Using Pore Size and Nanoscale Architecture. *J. Phys. Chem. Lett.* **2020**, *11* (9), 3731–3737. https://doi.org/10.1021/acs.jpclett.0c00464.

(10) Hopkins, P. E.; Rakich, P. T.; Olsson, R. H.; El-Kady, I. F.; Phinney, L. M. Origin of Reduction in Phonon Thermal Conductivity of Microporous Solids. *Appl. Phys. Lett.* **2009**, *95* (16), 2007–2010. https://doi.org/10.1063/1.3250166.

(11) Hopkins, P. E.; Kaehr, B.; Phinney, L. M.; Koehler, T. P.; Grillet, A. M.; Dunphy, D.; Garcia, F.; Brinker, C. J. Measuring the Thermal Conductivity of Porous, Transparent SiO2 Films With Time Domain Thermoreflectance. *J. Heat Transfer* **2011**, *133* (6), 061601. https://doi.org/10.1115/1.4003548.

(12) Deng, Z.; Wang, J.; Wu, A.; Shen, J.; Zhou, B. High Strength SiO2 Aerogel Insulation. *J. Non. Cryst. Solids* **1998**, *225*, 101–104. https://doi.org/10.1016/S0022-3093(98)00106-9.

(13) Larkin, J. M.; McGaughey, A. J. H. Thermal Conductivity Accumulation in Amorphous Silica and Amorphous Silicon. *Phys. Rev. B - Condens. Matter Mater. Phys.* **2014**, *89* (14), 1–12. https://doi.org/10.1103/PhysRevB.89.144303.

(14) Zhou, W.; Cheng, Y.; Chen, K.; Xie, G.; Wang, T.; Zhang, G. Thermal Conductivity of Amorphous Materials. *Adv. Funct. Mater.* **2019**, 1903829. https://doi.org/10.1002/adfm.201903829.

(15) Zhang, H.; Hua, C.; Ding, D.; Minnich, A. J. Length Dependent Thermal Conductivity Measurements Yield Phonon Mean Free Path Spectra in Nanostructures. *Sci. Rep.* **2015**, *5* (1), 9121. https://doi.org/10.1038/srep09121.

(16) King, S. C.; Li, M.; Galy, T.; Yan, Y.; Kang, J. S.; Basile, V. M.; Li, Y. L.; Marszewski, M.; Pilon, L.; Hu, Y.; et al. Examining the Role of Atomic Scale Heterogeneity on the Thermal Conductivity of Transparent, Thermally Insulating, Mesoporous Silica−titania Thin Films. *J. Phys. Chem. C* **2020**, *124* (50), 27442–27452. https://doi.org/10.1021/acs.jpcc.0c06697.

(17) Wingert, M. C.; Zheng, J.; Kwon, S.; Chen, R. Thermal Transport in Amorphous Materials: A Review. *Semicond. Sci. Technol.* **2016**, *31* (11), 113003. https://doi.org/10.1088/0268-1242/31/11/113003.

(18) Hu, Y.; Zeng, L.; Minnich, A. J.; Dresselhaus, M. S.; Chen, G. Spectral Mapping of Thermal Conductivity through Nanoscale Ballistic Transport. *Nat. Nanotechnol.* **2015**, *10* (8), 701–706. https://doi.org/10.1038/nnano.2015.109.

(19) Gao, T.; Jelle, B. P. Thermal Conductivity of Amorphous Silica Nanoparticles. *J. Nanoparticle Res.* **2019**, *21* (6), 108. https://doi.org/10.1007/s11051-019-4556-8.

(20) Marconnet, A. M.; Asheghi, M.; Goodson, K. E. From the Casimir Limit to Phononic Crystals: 20 Years of Phonon Transport Studies Using Silicon-on-Insulator Technology. *J. Heat Transfer* **2013**, *135* (6), 061601. https://doi.org/10.1115/1.4023577.

(21) Prasher, R. Thermal Interface Materials: Historical Perspective, Status, and Future Directions. *Proc. IEEE* **2006**, *94* (8), 1571–1586. https://doi.org/10.1109/JPROC.2006.879796.

(22) Tsui, B.-Y.; Yang, C.-C.; Fang, K.-L. Anisotropic Thermal Conductivity of Nanoporous Silica Film. *IEEE Trans. Electron Devices* **2004**, *51* (1), 20–27. https://doi.org/10.1109/TED.2003.820790.

(23) Allen, P. B.; Feldman, J. L.; Fabian, J.; Wooten, F. Diffusons, Locons and Propagons: Character of Atomie Yibrations in Amorphous Si. *Philos. Mag. B Phys. Condens. Matter; Stat. Mech. Electron. Opt. Magn. Prop.* **1999**, *79* (11–12), 1715–1731. https://doi.org/10.1080/13642819908223054.

(24) Thommes, M.; Kaneko, K.; Neimark, A. V; Olivier, J. P.; Rodriguez-reinoso, F.; Rouquerol, J.; Sing, K. S. W. Physisorption of Gases , with Special Reference to the Evaluation of Surface Area and Pore Size Distribution (IUPAC Technical Report). **2015**, *87*, 1051–1069. https://doi.org/10.1515/pac-2014-1117.

(25) Gregg, S. J.; Sing, K. S. W.; Salzberg, H. W. Adsorption Surface Area and Porosity. *J. Electrochem. Soc.* **1967**, *114* (11), 279Ca. https://doi.org/10.1149/1.2426447.

(26) Galy, T.; Marszewski, M.; King, S.; Yan, Y.; Tolbert, S. H.; Pilon, L. Comparing Methods for Measuring Thickness , Refractive Index , and Porosity of Mesoporous Thin Films. *Microporous Mesoporous Mater.* **2020**, *291*, 109677. https://doi.org/10.1016/j.micromeso.2019.109677.

(27) Kittel, C. Interpretation of the Thermal Conductivity of Glasses. *Phys. Rev.* **1949**, *75* (6), 972–974. https://doi.org/10.1103/PhysRev.75.972.

(28) Liang, L. H.; Li, B. Size-Dependent Thermal Conductivity of Nanoscale Semiconducting Systems. *Phys. Rev. B - Condens. Matter Mater. Phys.* **2006**, *73* (15), 1–4. https://doi.org/10.1103/PhysRevB.73.153303.

(29) Teja, A. S.; Beck, M. P.; Yuan, Y.; Warrier, P. The Limiting Behavior of the Thermal Conductivity of Nanoparticles and Nanofluids. *J. Appl. Phys.* **2010**, *107* (11). https://doi.org/10.1063/1.3354094.

(30) Lorenz, P.; Zhao, X.; Ehrhardt, M.; Zagoranskiy, I.; Zimmer, K.; Han, B. Nano and Micro Structuring of Fused Silica Using Time-Delay Adjustable Double Flash Ns-Laser Radiation. In *Laser-based Micro- and Nanoprocessing XII*; Klotzbach, U., Washio, K., Kling, R., Eds.; SPIE, 2018; p 59. https://doi.org/10.1117/12.2288294.

(31) Brown, I. D.; Shannon, R. D. Empirical Bond-strength–Bond-length Curves for Oxides. *Acta Crystallogr. Sect. A* **1973**, *29* (3), 266–282. https://doi.org/10.1107/S0567739473000689.

(32) Russell, H. W. Principles of Heat Flow in Porous Insulators*. *J. Am. Ceram. Soc.* **1934**, *18* (1), 1–5.

(33) Johnstone, A. H. CRC Handbook of Chemistry and Physics-69th Edition Editor in Chief R. C. Weast, CRC Press Inc., Boca Raton, Florida, 1988, Pp. 2400, Price £57.50. ISBN 0-8493-0369-5. *J. Chem. Technol. Biotechnol.* **2007**, *50* (2), 294–295. https://doi.org/10.1002/jctb.280500215.

(34) Yan, Y.; King, S. C.; Li, M.; Galy, T.; Marszewski, M.; Kang, J. S.; Pilon, L.; Hu, Y.; Tolbert, S. H. Exploring the Effect of Porous Structure on Thermal Conductivity in Templated Mesoporous Silica Films. *J. Phys. Chem. C* **2019**, *123* (35), 21721–21730.

CHAPTER 5

Examining the Role of Atomic Scale Heterogeneity on the Thermal Conductivity of Transparent, Thermally Insulating, Mesoporous Silica-Titania Thin Films

Chapter 5 describes our work exploring the effect of nanoscale homogeneity of a mixed silica-titania mesoporous network.

This chapter was reprinted with permission from King, S. C.; Li, M.; Galy, T.; Yan, Y.; Kang, J. S.; Basile, V. M.; Li, Y. L.; Marszewski, M.; Pilon, L.; Hu, Y.; et al. Examining the Role of Atomic Scale Heterogeneity on the Thermal Conductivity of Transparent, Thermally Insulating, Mesoporous Silica−Titania Thin Films. J. Phys. Chem. C 2020, 124 (50), 27442–27452.

A reprint of the supporting information is given in Appendix D

Examining the Role of Atomic Scale Heterogeneity on the Thermal Conductivity of Transparent, Thermally Insulating, Mesoporous Silica–Titania Thin Films

Published as part of The Journal of Physical Chemistry virtual special issue "Emily A. Carter Festschrift".

Sophia C. King, Man Li, Tiphaine Galy, Yan Yan, Joon Sang Kang, Victoria M. Basile, Yolanda L. Li, Michal Marszewski, Laurent Pilon, Yongjie Hu, and Sarah H. Tolbert*

ABSTRACT: This paper examines the effect of compositional heterogeneity on the thermal conductivity of transparent, mesoporous silica–titania composites that contain either 10 or 20 mol % titania. The relative hydrolysis rates of the silica and titania precursors were modified to control their compositional heterogeneity, while the ratio of polymer to inorganic precursors (silica + titania) was varied to control the porosity of the films. All films were optically transparent at thicknesses up to 1 μm with transmittance above 90% and haze below 5% at visible wavelengths. It was found that the heterogeneity of the titania species in the 10 mol % titania samples could be easily tailored from highly dispersed titania to a composition with heterogeneous silica-rich and titania-rich domains. By contrast, samples with 20 mol % titania always showed a heterogeneous titania distribution. The results show that mesoporous films with more homogeneously distributed titania had a lower thermal conductivity at all porosities, likely due to increases in propagon and diffuson scattering as a result of the increased number density of titania heteroatom scattering centers. These results increase our understanding of heat carrier propagation in amorphous materials and add to the design rules for creating amorphous, optically clear, low thermal conductivity materials.

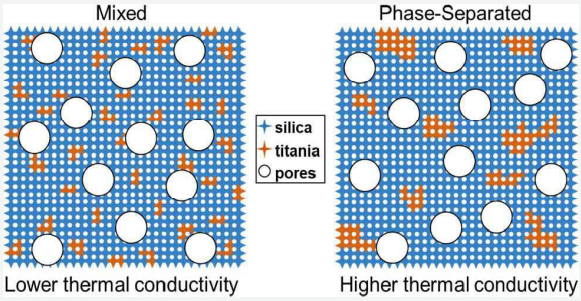

INTRODUCTION

Using materials as thermal insulation to separate hot from cold is a pursuit as old as humankind. As rocks, wood, and fur have given way to designer materials, so have the challenges that can be addressed. This includes creating materials with extraordinarily low thermal conductivity[1−3] and creating materials that can survive at extremely high temperatures.[4−7] In this work, we tackle another challenge in this field, which is the optimization of materials with both low thermal conductivity and high optical clarity for applications such as window insulation. Here we specifically focus on templated nanoporous networks made from combinations of amorphous silica and titania and explore the role of compositional heterogeneity in controlling thermal conductivity.

Crystalline materials are often good conductors of heat because their long-range atomic-scale order facilitates heat carrier propagation via lattice vibrations (or phonons).[8−10] In amorphous materials, however, the disorder and randomized atomic positions are not conducive to phonon transport, resulting in a significantly reduced mean free path for the carriers. In such systems, heat is transferred via propagons (propagating vibrational modes that are similar to phonons but with much shorter mean free paths), diffusons (delocalized, but nonpropagating vibrational modes), and, to a lesser extent, locons (localized vibrational modes).[8−12] To further reduce the thermal conductivity of amorphous materials, one must decrease heat carrier mobility. Often, this is achieved by making a material porous, which reduces the effective density of the material and, as a result, heat carrier transport.[12,13] Porosity also has the added benefits of increasing internal surfaces, which can act as scattering centers, and of spatial confinement of heat carriers, both of which can be reasonably well accounted for in crystalline materials with well-defined phonon distributions.[14,15] By contrast, the fundamental relationship between the structure of amorphous, porous

Received: July 22, 2020
Revised: October 15, 2020
Published: December 7, 2020

materials and their thermal conductivity is still not well understood beyond the aforementioned density effects.[12,16]

As a result, improving thermal resistance in porous insulators is typically achieved by increasing their porosity, which often negatively impacts other performance metrics and limits practical application of the resulting materials. For instance, silica aerogels can reach thermal conductivities as low as 0.015 W m^{-1} K^{-1} under ambient conditions when the porosity exceeds 95%.[17] However, such large porosity results in poor mechanical integrity of aerogels.[1,18,19] In addition, the large pores that form in connection with the increased porosity strongly scatter visible light, rendering aerogels opaque or translucent.[19,20] Thus, establishing new methods for reducing thermal conductivity of porous insulators is of paramount importance and can lead to the development of better thermal insulators with both mechanical robustness and high optical transparency for applications in energy-saving architectural glass[21] and solar–thermal energy conversion systems.[22]

Many structural effects on thermal conductivity in templated mesoporous materials have already been reported, such as the role of precursor type (discrete nanocrystals vs continuous sol–gel), wall thickness, and pore packing (cubic vs hexagonal).[23−26] In nontemplated porous silica, the fractal dimension has also been shown to influence the thermal conductivity.[27−29]

In bulk systems, composition can also be used to reduce thermal conductivity. For example, in crystalline materials, the addition of point defects in the form of atomic or isotopic dopants has been computationally and experimentally shown to scatter phonons at the boundaries of the defects.[5,30−34] Seyf and Henry computationally showed that as the concentration of defects increases in a crystal, the population of propagating modes rapidly changes to nonpropagating diffusons and locons.[34] This decrease in phonon propagation leads to a reduction in the thermal conductivity of the material. For amorphous systems, Choy et al. measured the thermal conductivity of different metallic glasses and separated the electronic and nonelectronic contributions to the thermal conductivity.[35,36] They found that for metal–metalloid glasses, the thermal conductivity decreased as more chemical elements were added to the alloy. More specifically, they found that the nonelectronic or vibrational component of the thermal conductivity decreased significantly as the complexity of the chemical composition increased. This was attributed to increased vibrational scattering with increases in the degree of disorder due to the large number of components of the alloys. While these studies demonstrate that the thermal conductivity of crystals and amorphous insulators can be reduced using compositional heterogeneity, the thermal conductivities reported were all greater than 5 W m^{-1} K^{-1} because the materials studied were either crystalline or metallic. As a result, it is still not clear if compositional heterogeneity in a material can have a significant impact in ultralow thermal conductivity applications.

Unfortunately, it is quite challenging to find systems suitable for the study of solid-solution effects on thermal conductivity in materials with thermal conductivities on the order of 0.1 W m^{-1} K^{-1}. To begin with, there is a small range of amorphous oxides that mix well enough to form solid solutions with variable heterogeneity.[37,38] Ideally, we would like to use a silica-based network because, in addition to being transparent, they are intrinsically amorphous and easy to form into nanoporous networks with controllable pore sizes—all favorable properties for low thermal conductivity. We then need to add another metal oxide that can form a well-mixed network, while maintaining the favorable low thermal conductivity and optical properties. Mesoporous silica–titania composites have been studied as thermal insulators,[3,39] and the synthesis of silica–titania glasses has been rigorously explored for optical, electronic, and catalytic applications.[40−44] It has been shown by using X-ray absorption near edge structures (XANES), extended X-ray absorption fine structures (EXAFS), Fourier transform infrared spectroscopy (FTIR), nuclear magnetic resonance spectroscopy (NMR), and X-ray photoelectron spectroscopy (XPS) that at low concentrations of titania (<15 mol %), silica–titania forms a solid solution when synthesized by sol–gel based methods.[45−51] Moreover, the heterogeneity of the silica–titania network can be controlled at these low concentrations of titania (<15 mol %) by tailoring the relative hydrolysis rates of the molecular precursors for silica and titania.[46,50,51] Finally, when annealed at moderate temperatures (<450 °C), the crystallization of titania can be suppressed at large silica concentrations.[42,43,52] Silica–titania is therefore the ideal system for this study as it allows us to create amorphous, porous materials with variable homogeneity and good optical quality.

With these ideas as a backdrop, this study aims to elucidate the effect of chemical homogeneity on the thermal conductivity of mesoporous silica–titania composites. To do so, mesoporous silica–titania thin films were synthesized with either 10 or 20 mol % titania, at porosities ranging from to 25 to 60%. For the samples made with 10 mol % titania, the level of homogeneity was controlled by varying the relative hydrolysis rates of the silica and titania precursors. Given the limited solubility of titania in silica at concentrations exceeding 15 mol %, the samples made with 20 mol % titania acted as a control to assess the effect of the synthetic methods on thermal conductivity, as these samples should show phase-separated titania across all synthetic conditions. The structure of the films was characterized with scanning electron microscopy (SEM), transmission electron microscopy (TEM), ellipsometric porosimetry, optical interfereometry, optical interfereometry, and two-dimensional grazing incidence small-angle X-ray scattering (2D-GISAXS). Their composition and homogeneity were characterized with energy-dispersive X-ray spectroscopy (EDS), XPS, solid state ^{29}Si NMR, and FTIR. Finally, their effective thermal conductivity was measured using time-domain thermoreflectance (TDTR).

METHODS

Materials. The following materials were obtained from commercial suppliers and used without further purification: triblock copolymer Pluronic F127 ($PEO_{100}PPO_{65}PEO_{100}$, M_w = 12600, BASF), tetraethyl orthosilicate (TEOS, 98%, Acros Organics), titanium isopropoxide (TIPO, 98%, Acros Organics), 2,4-pentanedione (acetylacetone, 99%, Acros Organics), 2,4-pentanedione (acetylacetone, 99%, Acros Organics), hydrochloric acid (Certified ACS Plus, Fisher Scientific), and ethanol (EtOH, 200 proof, Rossville Gold Shield).

Synthesis. The synthesis of mesoporous silica–titania mixed films was adapted from the works of Dong et al. and Dunphy et al.[43,53] F127:EtOH:HCl:H_2O:TIPO:TEOS were combined in a 7.4:50:6.1:0.06:x:(1 − x) molar ratio, where x is 0.1 or 0.2. In a typical synthesis of silica–titania with molar ratio 90–10 and m_{poly}/m_{inorg} = 1.5 g/g, 280 mg of Pluronic surfactant F127 ($PEO_{100}PPO_{65}PEO_{100}$) was first added to 6

mL of ethanol, 0.325 mL of doubly distilled water, and 0.425 mL of 37% HCl under rapid stirring at 60 °C until the polymer was fully dissolved. Then, 0.62 mL of TEOS was added to the reaction mixture, followed by the dropwise addition of 0.1 mL of TIPO. The reaction was left to stir for 5 h at 60 °C.

To increase the compositional homogeneity of the mixture, a modified synthesis was adapted from Chen et al.[51] In the modified synthesis of silica–titania with molar ratio 90–10 and m_{poly}/m_{inorg} = 1.5 g/g, 0.1 mL of TIPO was combinreaction mixture, followed by the dropwise additioned with 0.03 mL of acetylacetone in 1 mL of ethanol and stirred for an hour at 60 °C. Concurrently, in a separate flask, 0.62 mL of TEOS was combined with 0.053 mL of H_2O in 1 mL of ethanol and stirred for an hour at 60 °C. Then, both solutions were added to a solution of 280 mg of F127 in a mixture of 4 mL of ethanol, 0.27 mL of water, and 0.425 mL of 37% HCl and stirred for 4 h. Full details of the regular and modified syntheses are included in Table S1.

To obtain films of thicknesses >200 nm, the solutions were concentrated by rotary evaporation at 80 mTorr in a 60 °C temperature bath for 10 min. Films were made by spin coating the solutions onto silicon wafers or 1 mm thick glass microscope slides. The films were then calcined under flowing O_2 by first holding at 350 °C for 6 h and then at 400 °C for 2 h to remove all polymer template and ensure that the titania was in its fully oxidized form. A ramp rate of 2 °C min^{-1} was used for both heating and cooling.

Substrate free powdered samples for NMR and FTIR analyses were made by evaporating the same solutions used for film formation in Petri dishes for 3–7 days at humidity >50%. The resulting powders were then calcined in flowing O_2 at 400 °C for ~12 h (until all of the polymer was removed).

Characterization. The structure of the samples was examined with scanning electron microscopy (SEM), transmission electron microscopy (TEM), ellipsometric porosimetry, N_2 porosimetry, two-dimensional grazing incidence small-angle X-ray scattering (2D-GISAXS), and two-dimensional grazing incidence wide-angle X-ray scattering (2D-GIWAXS). The composition and chemical bonding were further examined using EDS, XPS, solid-state ^{29}Si NMR, and FTIR. The thermal conductivity was measured using a time domain thermoreflectance (TDTR) technique, with the specific heat capacity c_p of representative powdered measured through differential scanning calorimetry (DSC). The full details of these characterization methods are given in the Supporting Information.

RESULTS AND DISCUSSION

Using polymer templating methods at acidic pH, sol–gel based mesoporous silica–titania (ST) films were synthesized at ratios of 10 mol % (ST10) and 20 mol % titania (ST20). The hydrolysis rate of the silica precursor, tetraethyl orthosilicate (TEOS), is much slower than that of the titania precursor, titanium isopropoxide (TIPO), leading to the formation of titania-rich nanodomains in the solid network when these precursors are simply mixed. The homogeneity of the titania within the matrix can, however, be adjusted by tuning the hydrolysis rates of their molecular precursors.[43] Specifically, at concentrations less than 15 mol % of titania, a more homogeneous network of silica–titania can be obtained by simultaneously increasing the hydrolysis rate of TEOS through prehydrolysis with water, while reducing the hydrolysis rate of TIPO through the use of a chelating ligand such as acetylacetone.[38,46,49,51] This method was applied to mesoporous silica–titania films with ratios of 10 and 20 mol % titania. The full synthetic details are given in Table S1 of the Supporting Information, where the samples were labeled as regularly synthesized (reg), where the silica and titania precursors were just mixed and added to the network, or modified (mod) where the synthesis was modified such that the hydrolysis rates of the precursors were better matched. The 20 mol % titania samples served as a control for the differences in synthetic method, as this sample should have titania-rich nanodomains with both synthetic methods because of the high titania concentration.

Structural Characterization. The SEM images of the ST10reg and ST20reg composites in Figures 1a and 1b show

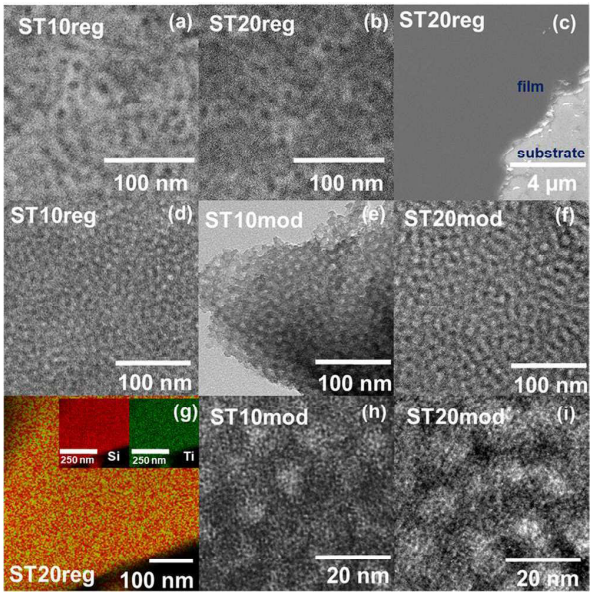

Figure 1. Electron micrographs and electron spectroscopy showing the structure and composition of the mesoporous silica–titania composites. (a, b) Scanning electron micrograph (SEM) of (a) an ST10reg and (b) an ST20reg sample showing the porous structure. (c) Low-magnification SEM image of a typical ST20reg sample showing the homogeneity and lack of large scale defects in these porous films. (d–f) Transmission electron micrographs (TEM) of a typical (d) ST10reg, (e) ST10mod, and (f) ST20mod sample also showing the porous structure. (g) Energy-dispersive X-ray spectroscopy (EDS) map of an ST20reg sample showing good mixing in the silica–titania composite. (h, i) High-resolution TEM (HR-TEM) of a typical (h) ST10reg and (i) ST20mod sample showing a lack of lattice fringes in the amorphous pore walls of these samples.

that homogeneous mesoporous silica–titania composite films were successfully synthesized. As shown in the low-magnification image in Figure 1c, the synthesized films are smooth and lack significant defects such as cracks, phase separation, or large pores, which is favorable, as these features would scatter light.[54] The TEM images in Figures 1d–f indicate that all porous silica–titania network was continuous, with homogeneously dispersed small pores; this is true for both the regular and modified syntheses. The EDS map of a typical ST20reg film in Figure 1g shows that the silica–titania composite was well mixed at the resolution of EDS mapping (~20 nm), even for the ST20 films, which we expect to show

the most phase separation. Data for ST10reg are similar (see Figure S1). This indicates that other methods will need to be employed to quantify compositional heterogeneity in these films. The lack of lattice fringes in the HR-TEM images of Figures 1h and 1i further suggests that the titania remained amorphous in both the ST10reg and ST20reg samples. This is corroborated by the lack of diffraction peaks in the reduced two-dimensional grazing incidence X-ray scattering (2D-GIWAXS) data in Figure S2. This lack of crystallinity of titania was expected since the presence of a high percentage of silica has been shown to suppress the crystallization of titania.[43] Additionally, the films were calcined at 400 °C, a relatively low temperature for titania crystallization.[52,55−58]

We conducted transmittance and haze measurements to further examine the optical quality of films coated on 1 mm thick glass microscope slides. Here the total transmittance of the films quantifies the percent of light transmitted through the film, including light lost to reflection, while haze is a measure of the clarity of the material and quantifies only scattering (see the Supporting Information for more details). In general, films of good optical quality have transmittance above 90% and haze below 5%.[54] Figure 2 compares the normal-hemispherical

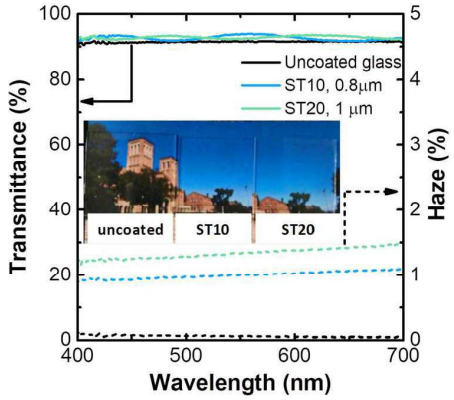

Figure 2. Normal-hemispherical transmittance−haze measurements across the visible spectrum for uncoated glass and typical ST10 and ST20 samples. Photos of the uncoated glass and ST10 and ST20 samples are shown in the inset.

transmittance and haze of typical ST10 and ST20 films to that of an uncoated glass slide along with photographs of the films. Both coated samples featured similar high transmittance values in excess of 90%. The ST10-coated sample had a haze on the order of 1%, which is lower than the ST20-coated sample. Because both coated samples had haze values that were below 2%, they do not significantly scatter light in the visible regime and are therefore suitable as coatings for applications where optical transparency is desired.

To quantify the degree of heterogeneity in the silica−titania films, solid-state ^{29}Si NMR and FTIR were used to examine local bonding between Si and Ti; this was done because EDS mapping was unable to resolve the heterogeneity in the composites. In a typical ^{29}Si NMR spectrum, the Q peaks are indicative of Si−O−M bonds, where M represents any atom. A Q^4 peak indicates a Si atom bonded to only O−Si moieties. A Q^3 peak indicates a Si atom with three such bonds and one O−heteroatom bond, such as the Ti in our system. The ratio of the areas of the Q^3/Q^4 peaks can be used to quantify homogeneity. Given the same silica−titania ratio, a higher ratio of Q^3/Q^4 peaks indicates that titania is more homogeneously distributed in the silica network at the atomic scale. By contrast, when silica and titania separate into two phases, they form more Si−O−Si and Ti−O−Ti and less Si−O−Ti bonds. FTIR can also be used to study the homogeneity of the mixed system by directly probing the absorption of the Si−O−Ti stretch. The greater the intensity of the stretch, the greater the number of Si−O−Ti bonds and the more homogeneously distributed the titania. As such, both methods can be used to quantitatively determine the extent to which titania is distributed in the silicate structure.

The NMR spectra plotted in Figures 3a and 3b indicate that the relative Q^3/Q^4 peak area ratio for the ST10mod sample was 0.71 (Figure 3b), while it was only 0.60 for the ST10reg sample (Figure 3a). This suggests that there is a more homogeneous distribution of titania in the solid network produced when the hydrolysis rates of the molecular precursors were better matched. Likewise, the stronger intensity of the Si−O−Ti stretching absorption band at 950 cm^{-1} for the ST10mod film compared to the ST10reg film (Figure 3c) confirms that titania in the modified sample is indeed more homogeneously distributed. By contrast, modifying the synthesis of the ST20 films had no significant effect on the distribution of titania in the silica matrix. While the Q^3/Q^4 area ratios are higher for all the ST20 samples due to the larger titania content, both ST20reg and ST20mod films had comparable Q^3/Q^4 area ratios of 0.78 and 0.79, respectively, according to the NMR spectra plotted in Figures 3d and 3e. Similarly, the intensities of the Si−O−Ti IR absorption bands were the same for the ST20reg and ST20mod samples plotted in Figure 3f. The similarity of ST20reg and ST20mod was likely due to the limited solubility of titania in silica at 20 mol % which has been reported in the literature.[49] As a result, unlike the ST10 films, the homogeneity of the ST20 films could not be tailored by controlling the hydrolysis rates of the molecular precursors. The ST20 samples are thus ideal experimental controls to determine whether changes in thermal conductivity, discussed below, should be attributed primarily to changes in the titania distribution within the material or are simply due to differences in the synthetic method. Overall, using a templated sol−gel based method yielded amorphous, mesoporous silica−titania films with good optical quality and controllable atomic-scale mixing of the silica and titania in the network at low titania concentrations.

X-ray photoelectron spectroscopy was conducted to further quantify the ratio of silica:titania, as well as to quantify any defects in the mixed, mesoporous structure. High-resolution XPS spectra of the Si 2p peak, the Ti 2p peaks, and O 1s peak from representative ST10reg, ST10mod, ST20reg, and ST20mod samples are depicted in Figure S3. A summary of the deconvoluted peak positions and their respective areas and relevant ratios are given in Table 1. The area ratios of the Si 2p and Ti 2p peaks were used to quantify the ratio of Si:Ti on the surface of the films. The ratios of Si:Ti were found to be 90:10, 89:11, 85:15, and 83:17 on the surface of the ST10reg, ST10mod, ST20reg, and ST20mod films, respectively. For the ST10 samples, these compositions are in good agreement with those determined from EDS (92:8 ± 2), confirming that there is little to no enrichment of Si or Ti on the surface of the films compared to the bulk material. For the ST20 samples, however, the Ti content (15% for ST20reg, 17% for ST20mod) is lower than determined from EDS (80:20 ± 1), likely as a result of surface enrichment with Si. We hypothesize

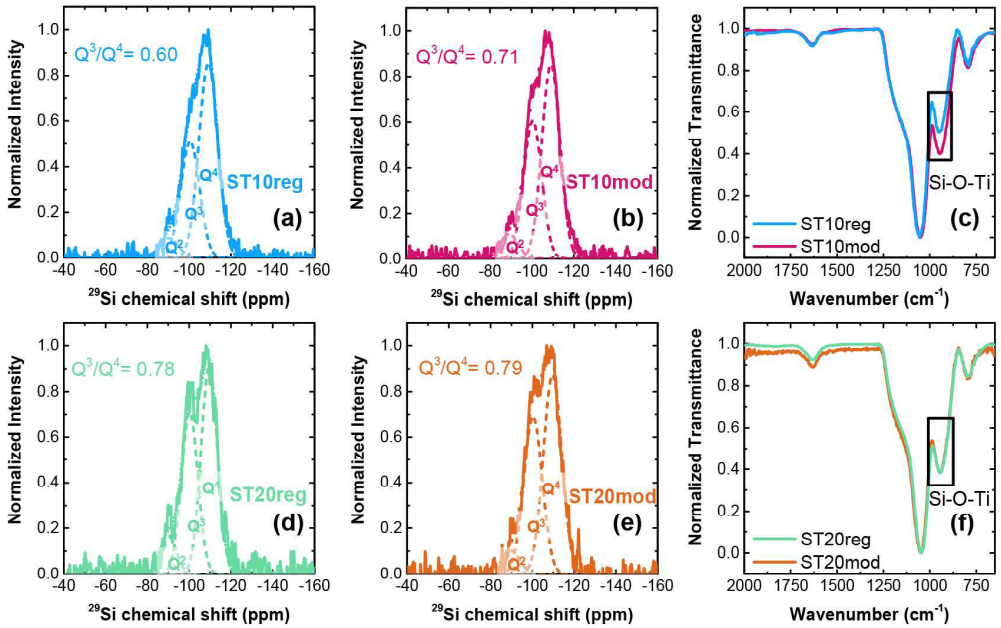

Figure 3. Examining the effect of synthesis parameters on the homogeneity of mesoporous mixed silica–titania powders. (a, b) Solid-state ^{29}Si NMR with the Q^3/Q^4 peak area ratio shown as an inset for ST10 powders made by using the regular and modified synthetic methods, respectively. (c) FTIR absorption for ST10reg and ST10mod showing differences in the Si–O–Ti vibrational mode. (d, e) Solid-state ^{29}Si NMR with the Q^3/Q^4 peak area ratio again shown as an inset for ST20 powders made by using the regular and modified synthetic methods, respectively. (f) FTIR absorption for ST20reg and ST20mod showing no differences in the intensity of the Si–O–Ti vibrational mode.

Table 1. Peak Positions and Areas Obtained from XPS for the Four Mesoporous Silica–Titania Composites Explored in This Work

peak designation	sample	ST10reg	ST10mod	ST20reg	ST20mod
Si 2p	peak position (eV)	103.5	103.7	103.3	103.1
	peak area	23.78	23.88	21.76	21.40
Ti $2p_{1/2}^{3+}$	peak position (eV)	464.0	463.7	463.1	463.4
	peak area	0.10	0.09	0.03	0.09
Ti $2p_{1/2}^{4+}$	peak position (eV)	465.5	465.5	465.1	465.0
	peak area	0.79	0.85	1.22	1.36
Ti $2p_{3/2}^{3+}$	peak position (eV)	458.3	457.9	457.3	457.4
	peak area	0.20	0.18	0.06	0.19
Ti $2p_{3/2}^{4+}$	peak position (eV)	459.8	459.7	459.3	459.2
	peak area	1.58	1.70	2.43	2.73
O 1s Ti–O	peak position (eV)	530.9	531.0	530.8	530.6
	peak area	5.19	5.14	9.99	11.01
O 1s Si–O	peak position (eV)	532.6	532.7	532.6	532.4
	peak area	68.36	68.15	64.52	63.22
relative area ratio Si 2p:Ti 2p (%)		90:10	89:11	85:15	83:17
relative area ratio Ti $2p^{4+}$:Ti $2p^{3+}$ (%)		89:11	90:10	98:02	94:06
relative area ratio Si–O:Ti–O (%)		93:07	93:07	87:13	87:13
O 1s/(Si 2p + Ti 2p)		2.78	2.74	2.92	2.88

that since the titania precursors hydrolyze faster than those of silica, they may form small titania domains, which then get encapsulated by the silica when it eventually hydrolyzes and condenses, leading to surface Si enrichment.

Additional insight could be gained by examining the peak shift and other relative area ratios in each spectrum. The Si 2p peak positions (Figures S3a,d,g,j) are all lower than that of pure silica (104.1 eV).[45] These shifts to lower binding energies are expected, since Ti is less electronegative than Si (1.5 for Ti vs 1.9 for Si). When we compare the ST10 films with peaks centered at 103.5–103.7 eV to those from ST20 samples that have peak positions at 103.1–103.4 eV, we observe a slightly larger shift for the ST20 samples, consistent with the higher Ti content.

Next, we look at the Ti 2p peaks to elucidate the fraction of nonoctahedral titania in the network. The typical Ti 2p peaks are split into Ti $2p_{1/2}$ and Ti $2p_{3/2}$ as a result of spin–orbit coupling, as shown in Figures S3b,e,h,k. Deconvolution of these peaks shows that while the films are made up primarily of Ti^{4+}, there is some Ti^{3+} present from TiO_x species where $x < 2$. These TiO_x species arise from defects in the structure as a result of the incorporation of octahedral titania into tetrahedral silica sites.[59] To quantify the nonoctahedral titania, we calculated the ratio of Ti $2p^{4+}$:Ti $2p^{3+}$. The ST10reg, ST10mod, ST20reg, and ST20mod samples have Ti $2p^{4+}$:Ti $2p^{3+}$ ratios of 89:11, 90:10, 98:2, and 96:4, respectively. The data indicate that there is significantly more Ti^{3+}, suggesting more nonoctahedral titania, in the ST10 samples than the ST20 materials. This observation was expected, as the ST10 samples were better mixed and contained smaller titania domains than the ST20 films. We believe that the smaller domains of the ST10 films consisted of more frustrated titania species in the silica network, while the larger titania domains in

the ST20 films would contain a greater number of stable Ti−O−Ti bonds and overall more octahedral titania in the network. The similarity of the ST10reg and ST10mod samples, however, indicates that nonoctahedral titania is not primarily responsible for the differences in thermal conductivity presented below.

Finally, we examine both the relative ratios and peak shifts of the O 1s peaks. The O 1s peaks in Figure S3c,f,h,l can be deconvoluted into two peaks: Si−O at 532.4−532.7 eV and Ti−O at 530.6−531.0 eV. Typically, the O 1s peak of pure silica is centered around 533 eV.[45,60] When titania is added to the network, the binding energy shifts to lower eV as a result of adding a less electronegative species in the network. A clear second peak appears at about 530.5 eV when the concentration of titania exceeds 10 wt % (~8 mol %) because of the formation of phase-separated Ti−O−Ti bonds. This peak continues to slowly shift to 329 eV as the concentration of titania increases toward a pure titania network. It is therefore not a surprise that the Ti−O peak in the ST20 films (binding energies 530.8 eV (ST20reg) and 530.6 eV (ST20mod)) were lower than those of the ST10 films (binding energies 530.9 eV (ST10reg) and 531.0 eV (ST10mod). In agreement with the NMR data, the sample that should have the most Si−O−Ti bonds (ST10mod) also showed the highest Ti−O binding energy. Moreover, as expected, the ST20 films (with Si−O:Ti−O ratios of 87:13 and 85:15 for ST20reg and ST20mod, respectively) also contained a larger fraction of Ti−O bonds than the ST10 films (with Si−O:Ti−O ratios of 93:07 for both ST10reg and ST10mod). Interestingly, however, the composition of Si derived from the Si−O:Ti−O ratios is larger than those previously derived from the Si 2p:Ti 2p peak areas. This is likely due to the fact that oxygen in mixed Si−O−Ti bonds can appear under the Si−O envelope at low Ti concentrations.[61,62] In addition to the larger ratios of Si, the ratios of O/(Si + Ti) of all samples are greater than 2. These superstoichiometric ratios indicate the presence of extra oxygen in the network, most likely from surface hydroxyl groups in these porous, high-surface-area networks. The −OH peak positions overlap with the Si−O and Ti−O peaks, so we were unable to accurately determine the concentration of hydroxyl groups on the surface. Overall, XPS corroborates many of the conclusions about mixing and elemental composition drawn from NMR and EDS and provides further insight into defect density and surface structure.

The porosity and pore size distribution of the mesoporous silica−titania network were quantified using ellipsometric porosimetry[63] at room temperature with toluene as the adsorbate, and by an interferometry-based technique.[64] Figure 4a shows that the porosity of the films increased from 24 to 60% as more Pluronic F127 was added until the polymer/inorganic mass ratio (m_{poly}/m_{inor}) reached 2.2. Beyond this limit, we observed a decrease in porosity for the ST10reg samples, likely due to increased pore shrinkage during calcination, so 2.2 was set as the limit for all other materials. Figure 4b shows typical adsorption−desorption isotherms for ST20mod samples made with different amounts of polymer. According to the IUPAC classification, all isotherms were of type IV(a) with H2(b) hysteresis loops, signifying that the films were mesoporous with some pore blocking.[65,66] Figure 4c shows that the average pore radii ranged between 2 and 3 nm, and the pore radius distribution broadened as the amount of polymer template increased.

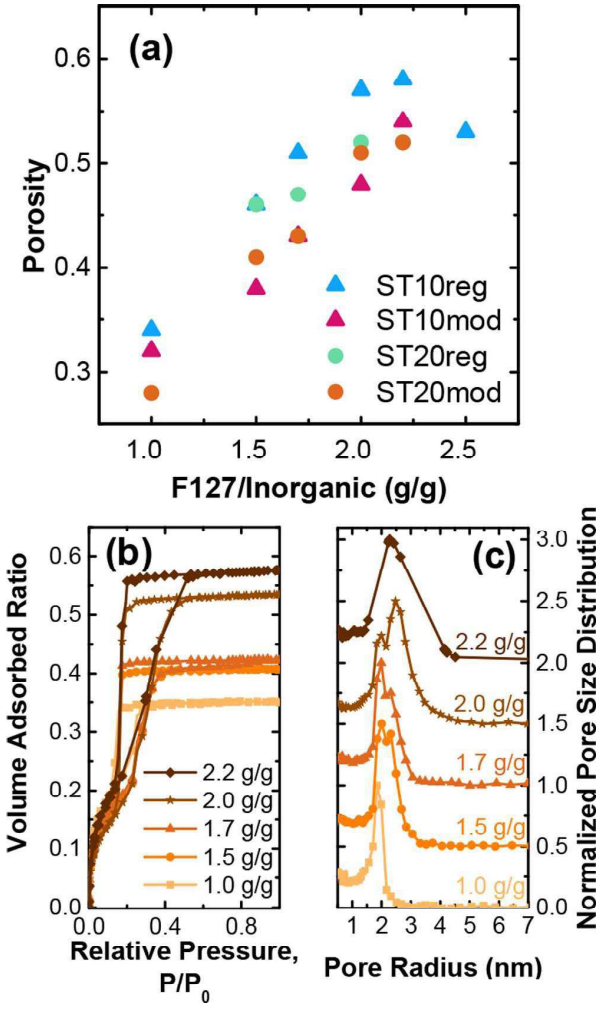

Figure 4. Characterization of the pore structure of the films studied. (a) Porosity as a function of Pluronic F127/(silica + titania) mass ratio for all silica−titania films studied. (b) Toluene adsorption−desorption isotherms and (c) pore size distribution curves for ST20mod samples made from different F127/(silica + titania) mass ratios (given on each graph). Pore size distribution curves are offset by 0.5 units. Overall, total porosity, pores size, and pore heterogeneity all increase as the relative fraction of polymer template increases up to a F127/inorganic mass ratio of 2.2 g/g.

To further examine the effect of polymer addition on the structure of the silica−titania network, two-dimensional grazing incidence X-ray scattering (2D-GISAXS) experiments were performed. Figures 5a−d show 2D-GISAXS patterns of typical ST10 and ST20 films made using both synthetic methods. The full arc in the q_x and q_y directions indicates that all films had ordered porosity, both in the plane of the film and perpendicular to the substrate, in the out-of-plane direction. Figures 5e and 5f plot the reduced 1D graphs that resulted from integrating the intensities of the 2D-GISAXS patterns at 10°−30° and 70°−90° from the origin. These 1D graphs provide information about the pore repeat distance both in- and out-of-plane. For all samples, the out-of-plane peaks are at higher q than the in-plane peaks, indicating that the pores shrink normal to the substrate. The out-of-plane peaks also have lower intensities as a result of the finite film thickness.

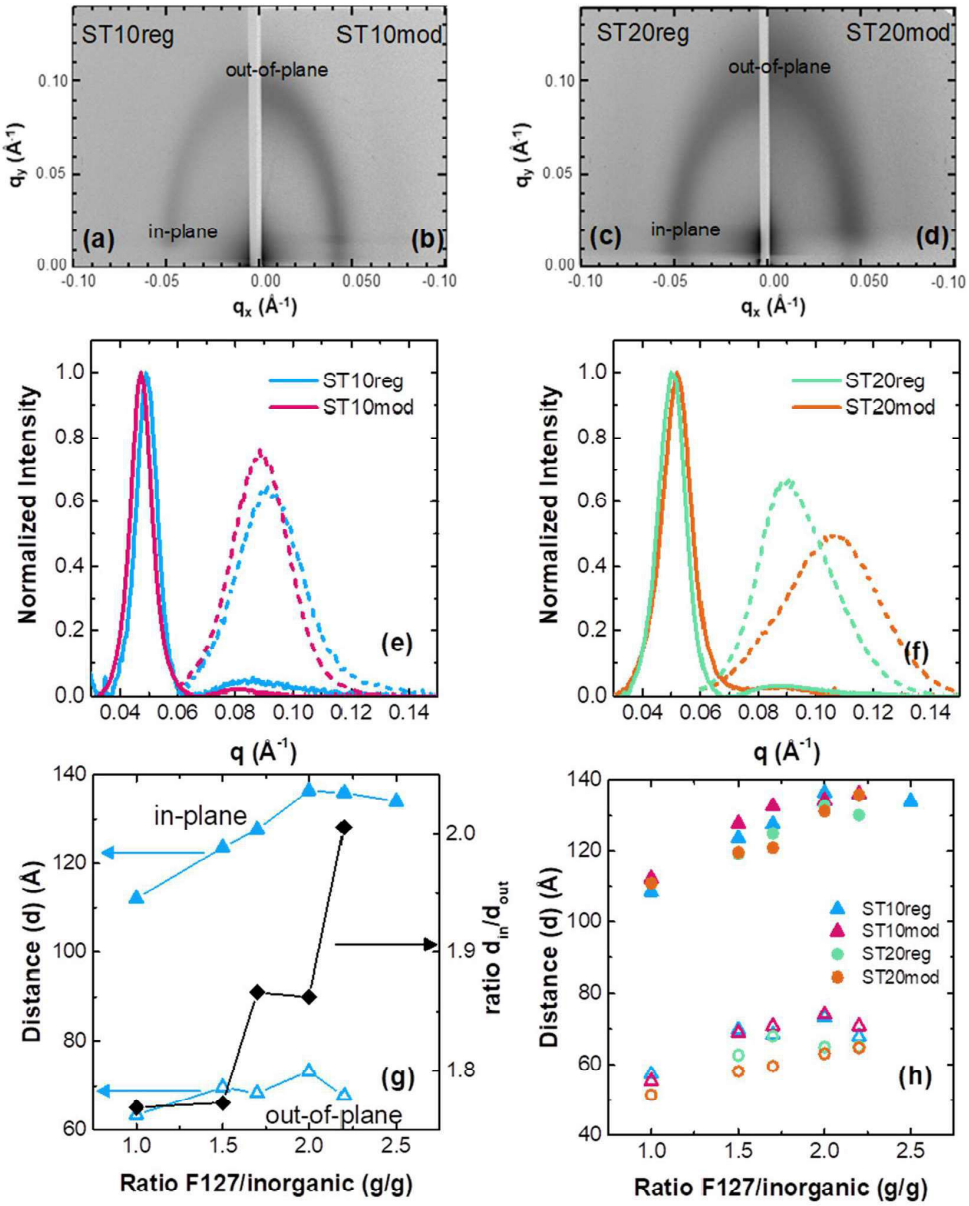

Figure 5. (a–d) Two-dimensional grazing incidence small-angle X-ray scattering (2D-GISAXS) pattern from typical (a) ST10reg, (b) ST10mod, (c) ST20reg, and (d) ST20mod samples. (e, f) The one-dimensional scattering profiles obtained by integrating the intensities of the 2D-GISAXS patterns over the angular range 10°–30° (in-plane) and 70°–90° (out-of-plane) for the ST10 and ST20 samples, respectively. (g) In-plane and out-of-plane pore-repeat distances and the ratio of those two distances as a function of polymer:silica mass ratio for the ST10reg samples. (h) In-plane and out-of-plane distances as a function of polymer:silica mass ratio for all silica–titania samples studied here.

The in-plane data show a weak peak at around 0.09 Å^{-1}, in addition to the main peak at around 0.05 Å^{-1}. These peaks can be indexed to the 100 and 110 planes of a hexagonal lattice (space group *p6mm*) with a ratio of 1:$\sqrt{3}$.[43,67–69] Compared to the other silica–titania samples, the out-of-plane peak of the ST20mod occurs at slightly higher *q*, indicating additional pore shrinkage in the ST20mod samples. Other than this shift, the data for the 10% and 20% titania samples are nearly identical, indicating that these samples are all structurally similar at the nanoscale.

Figure 5g shows the gradual increase in the in- and out-of-plane pore-repeat distances for all m_{poly}/m_{inor} ratios less than 2.0 for the ST10reg series. When m_{poly}/m_{inor} > 2.0, the in- and out-of-plane spaces both begin to decrease, presumably because of pore collapse upon heating due to the very thin walls. Additionally, as the amount of polymer added to the composite increased, so did the pore anisotropy, with much smaller pores sizes observed in the out-of-plane direction. This trend continued up to m_{poly}/m_{inor} = 2.5, which showed no out-of-plane diffraction, suggesting either total pore collapse or disordering in the out-of-plane direction. This destruction of

the pore order along with the decrease in porosity of the ST10reg sample at m_{poly}/m_{inor} = 2.5 shown in Figure 4a lead us to limit all other syntheses in this work to m_{poly}/m_{inor} ratios less than 2.5. Figure 5h shows similar in- and out-of-plane distances as a function of m_{poly}/m_{inor} for all materials used in this work. Similar trends are observed in all materials.

Effect of Compositional Heterogeneity on the Thermal Conductivity. Figure 6 plots the thermal conductivity as a function of porosity for all mesoporous silica–titania films used in this work. Figure 6a shows that at comparable porosities, the modified samples with their homogeneous titania distribution (ST10mod) have lower thermal conductivities than their less homogeneous counterparts (ST10reg). As established by the ^{29}Si NMR and FTIR spectra of Figures 3a–c, at a titania concentration of 10%, the modified films contain more homogeneously distributed Ti scattering centers than those synthesized using the regular method. In amorphous materials, heat is transported mainly by the propagons and diffusons. The former are similar to phonons in crystalline materials while the latter stem from the diffusion of vibrational modes.[11] The homogeneously distributed titania apparently serve as effective scattering centers for propagons and thus reduce their mean free path. Moreover, the more homogeneous the distribution of heteroatoms, the higher the degree of atomic disorder in the material. As a result, we hypothesize that this homogeneous distribution of heteroatoms results in a higher degree of randomness of vibrational modes, which reduces the thermal coupling of different modes and impedes the diffusion of thermal energy.

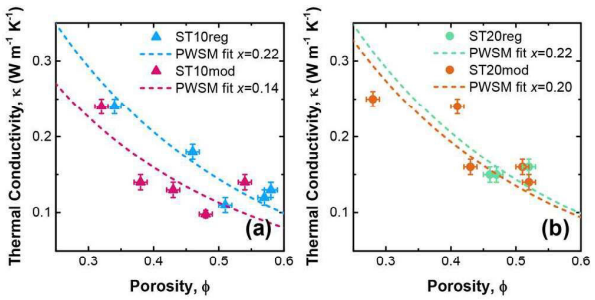

Figure 6. Effect of chemical homogeneity and fractional porosity on the thermal conductivity of mesoporous mixed silica–titania thin films synthesized with (a) 10 mol % and (b) 20 mol % titania. Here κ refers to κ_{eff}, as defined below.

On the other hand, Figure 6b shows that the cross-plane thermal conductivities of the ST20reg and ST20mod films were nearly identical at similar porosities. As illustrated in Figures 3d–f, the homogeneities of these samples were very similar, despite differences in their syntheses. This is likely due to fact that the titania concentration exceeds the solubility limit in all ST20 silica–titania composite, resulting in a similarly inhomogeneous distribution of titania scattering centers. This supports the idea that the lower thermal conductivity of the ST10mod film compared with ST10reg is due to higher homogeneity and not due to other effects originating from the differences in the two synthetic methods.

These trends can be quantified by fitting the data in Figures 6a and 6b with the porosity weighted simple medium (PWSM) model (dashed lines in Figure 6) to show the effects of titania concentration and heterogeneity on the thermal conductivity of the porous network. The PWSM model is often used to qualitatively describe heat conduction in porous material,[70] according to the following equation.

$$\kappa_{eff} = \kappa_{dense}(1 - \phi)(1 - \phi^{x})$$

Here, κ_{eff} and κ_{dense} correspond to the thermal conductivity of the porous and analogous fully dense material, ϕ is the porosity, and x is an empirical fitting parameter that can vary from 0 to 1 to indicate the alignment of the heat conducting components of the sample. When x = 0, it indicates that the heat conduction components are fully aligned in series while x = 1 indicates parallel alignment. By fitting our data to the PWSM model, we determined that the less well mixed ST10reg, ST20reg, and ST20mod samples all have similar PWSM fits with x = 0.22, 0.22, and 0.20, respectively. On the other hand, the ST10mod samples, with the more homogeneously distributed titania, produced a PWSM fit of x = 0.14, suggesting that the ST10mod films conduct heat in a more serial manner, likely due to increased heat carrier scattering that prevents effective parallel heat conduction. Overall, these results suggest that for the same concentration of atomic defects smaller, more dispersed scattering centers are better at reducing thermal conductivity than larger, less dispersed ones.

Figure 7 compares the thermal conductivity of the present silica–titania composite films with that of mesoporous nanoparticle-based and sol–gel silica films reported from ref 23 that were synthesized using similar methods with F127 block copolymer as the template. The data show that adding either 10 or 20 mol % titania resulted in reduced thermal conductivity compared to the pure silica films, presumably because all Ti incorporation provides additional centers that scattered propagons and diffusons, thus reducing the thermal conductivity of those samples, regardless of the compositional homogeneity. In agreement with this idea, PWSM fits to pure silica samples, published previously, produce a value of x = 0.31, which is higher than any of the titania-containing samples.[26] This suggests that all titania incorporation frustrates parallel heat conduction. When we further compare all the samples that show titania clustering, that is, the ST10reg

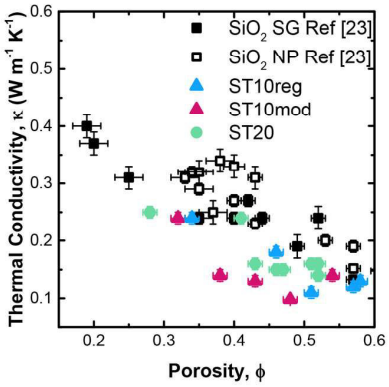

Figure 7. Porosity-dependent thermal conductivity comparing F127 templated mesoporous silica–titania to F127 templated mesoporous silica samples from ref 23 made from continuous sol–gel and discrete nanoparticle-based precursors. The ST20reg and ST20mod samples were combined and all labeled as ST20, since the differences in synthesis did not result in any significant difference in the thermal conductivity.

sample and all ST20 samples, we observe that the ST20 samples had lower thermal conductivities than the ST10reg samples. We hypothesize that this occurred because the ST20 samples have overall more heat carrier scattering sites than the ST10reg samples, thereby lowering the thermal conductivity. However, the more homogeneously distributed ST10mod samples showed the lowest thermal conductivity of all of them, even compared to the ST20 samples that have a higher concentration of Ti. These data suggest that for lowering thermal conductivity, having more dispersed heat carrier scattering centers is overall more effective than adding a larger mole fraction of potential scattering sites.

CONCLUSIONS

This study furthers our understanding of heat carrier propagation in amorphous porous materials and introduces new design rules for insulating materials and coatings. From our data, we found that adding titania to the silicate matrix lowers the thermal conductivity of the matrix as a result of introducing additional heat-carrier scattering centers. By comparing both the concentration and the compositional heterogeneity of the scattering sites, we found that the most chemically homogeneous materials with the most distributed scattering sites were more efficient at reducing heat carrier transport than samples with inhomogeneous distributions of scattering centers at either equivalent or higher concentrations. This indicates that the effect of atomic homogeneity is greater than the effect of the total concentration of the heat carrier scattering centers.

Because theories of thermal transport for amorphous materials, particularly when combined with nanoscale porosity, are less developed than those for crystalline materials, this work adds porosity-dependent data on well-characterized materials that can be used for future modeling studies. It is our hope that the thermal transport data on materials with both more and less homogeneously distributed titanium atoms, in particular, will be helpful in understanding the factors that control heat carrier scattering in amorphous materials, where classic phonon transport mechanisms are not applicable.

ASSOCIATED CONTENT

Supporting Information

The Supporting Information is available free of charge at https://pubs.acs.org/doi/10.1021/acs.jpcc.0c06697.

> Details of synthesis, structural characterization, and thermal conductivity measurement; tables of synthesis, NMR analysis, and specific heat capacities used in thermal conductivity calculation; additional EDS maps with analysis for Si and Ti content; representative XPS spectra; reduced 2D-GIWAXS patterns (PDF)

AUTHOR INFORMATION

Corresponding Author

Sarah H. Tolbert — *Department of Chemistry and Biochemistry, California NanoSystems Institute, and Department of Materials Science and Engineering, University of California, Los Angeles, Los Angeles, California 90095-1569, United States;* orcid.org/0000-0001-9969-1582; Phone: (310) 206-4767; Email: tolbert@chem.ucla.edu

Authors

Sophia C. King — *Department of Chemistry and Biochemistry, University of California, Los Angeles, Los Angeles, California 90095-1569, United States*

Man Li — *Department of Mechanical Engineering, University of California, Los Angeles, Los Angeles, California 90095-1597, United States*

Tiphaine Galy — *Department of Mechanical Engineering, University of California, Los Angeles, Los Angeles, California 90095-1597, United States*

Yan Yan — *Department of Chemistry and Biochemistry, University of California, Los Angeles, Los Angeles, California 90095-1569, United States*

Joon Sang Kang — *Department of Mechanical Engineering, University of California, Los Angeles, Los Angeles, California 90095-1597, United States*

Victoria M. Basile — *Department of Chemistry and Biochemistry, University of California, Los Angeles, Los Angeles, California 90095-1569, United States*

Yolanda L. Li — *Department of Chemistry and Biochemistry, University of California, Los Angeles, Los Angeles, California 90095-1569, United States*

Michal Marszewski — *Department of Mechanical Engineering, University of California, Los Angeles, Los Angeles, California 90095-1597, United States;* orcid.org/0000-0002-4157-3046

Laurent Pilon — *Department of Mechanical Engineering, Institute of the Environment and Sustainability, and California NanoSystems Institute, University of California, Los Angeles, Los Angeles, California 90095-1597, United States;* orcid.org/0000-0001-9459-8207

Yongjie Hu — *Department of Mechanical Engineering, University of California, Los Angeles, Los Angeles, California 90095-1597, United States*

Complete contact information is available at: https://pubs.acs.org/10.1021/acs.jpcc.0c06697

Notes

The authors declare no competing financial interest.

ACKNOWLEDGMENTS

We acknowledge funding support from the U.S. Department of Energy (DOE), Advanced Research Projects Agency-Energy (ARPA-E), under Award DE-AR0000738. S.C.K. and T.G. are fellows of the NRT-INFEWS: Integrated Urban Solutions for Food, Energy, and Water Management program (Grant DGE-1735325). The authors acknowledge the use of instruments at the Electron Imaging Center for NanoMachines supported by NIH (1S10RR23057) and the California NanoSystems Institute (CNSI) at UCLA. This manuscript contains X-ray data that were collected at the Stanford Synchrotron Radiation Lightsource. Use of the Stanford Synchrotron Radiation Lightsource, SLAC National Accelerator Laboratory, is supported by the U.S. Department of Energy, Office of Science, Office of Basic Energy Sciences, under Contract DE-AC02-76SF00515. The NMR in this work made use of equipment supported by the MRI program of the National Science Foundation under Grant 1532232.

REFERENCES

(1) Randall, J. P.; Meador, M. A. B.; Jana, S. C. Tailoring Mechanical Properties of Aerogels for Aerospace Applications. *ACS Appl. Mater. Interfaces* **2011**, *3*, 613−626.

(2) Marszewski, M.; King, S. C.; Yan, Y.; Galy, T.; Li, M.; Dashti, A.; Butts, D. M.; Kang, J. S.; McNeil, P. E.; Lan, E.; et al. Thick Transparent Nanoparticle-Based Mesoporous Silica Monolithic Slabs for Thermally Insulating Window Materials. *ACS Appl. Nano Mater.* **2019**, *2*, 4547−4555.
(3) Kwon, Y. G.; Choi, S. E. Y.; Kang, E. S.; Baek, S. S. U. Ambient-Dried Silica Aerogel Doped with TiO_2 Powder for Thermal Insulation. *J. Mater. Sci.* **2000**, *35*, 6075−6079.
(4) Marino, K. A.; Hinnemann, B.; Carter, E. A. Atomic-Scale Insight and Design Principles for Turbine Engine Thermal Barrier Coatings from Theory. *Proc. Natl. Acad. Sci. U. S. A.* **2011**, *108*, 5480−5487.
(5) Klemens, P. G.; Gell, M. Thermal Conductivity of Thermal Barrier Coatings. *Mater. Sci. Eng., A* **1998**, *245*, 143−149.
(6) Padture, N. P.; Gell, M.; Jordan, E. H. Thermal Barrier Coatings for Gas-Turbine Engine Applications. *Science* **2002**, *296*, 280−284.
(7) Jarvis, E. A.; Carter, E. A. The Role of Reactive Elements in Thermal Barrier Coatings. *Comput. Sci. Eng.* **2002**, *4*, 33−41.
(8) Tritt, T. M. *Thermal Conductivity Theory, Properties and Applications*; Kluwer Academic/Plenum Publishers: New York, 2004.
(9) Cahill, D. G.; Ford, W. K.; Goodson, K. E.; Mahan, G. D.; Majumdar, A.; Maris, H. J.; Merlin, R.; Phillpot, S. R. Nanoscale Thermal Transport. *J. Appl. Phys.* **2003**, *93*, 793−818.
(10) Cahill, D. G.; Braun, P. V.; Chen, G.; Clarke, D. R.; Fan, S.; Goodson, K. E.; King, W. P.; Mahan, G. D.; Majumdar, A.; Maris, H. J.; et al. Nanoscale Thermal Transport. II. 2003−2012. *Appl. Phys. Rev.* **2014**, *1*, 011305.
(11) Allen, P. B.; Feldman, J. L.; Fabian, J.; Wooten, F. Diffusons, Locons and Propagons: Character of Atomic Vibrations in Amorphous Si. *Philos. Mag. B* **1999**, *79*, 1715−1731.
(12) Wingert, M. C.; Zheng, J.; Kwon, S.; Chen, R. Thermal Transport in Amorphous Materials: A Review. *Semicond. Sci. Technol.* **2016**, *31*, 113003.
(13) Zhou, W.; Cheng, Y.; Chen, K.; Xie, G.; Wang, T.; Zhang, G. Thermal Conductivity of Amorphous Materials. *Adv. Funct. Mater.* **2020**, *30*, 1903829.
(14) Zhang, H.; Hua, C.; Ding, D.; Minnich, A. J. Length Dependent Thermal Conductivity Measurements Yield Phonon Mean Free Path Spectra in Nanostructures. *Sci. Rep.* **2015**, *5*, 9121.
(15) Hu, Y.; Zeng, L.; Minnich, A. J.; Dresselhaus, M. S.; Chen, G. Spectral Mapping of Thermal Conductivity through Nanoscale Ballistic Transport. *Nat. Nanotechnol.* **2015**, *10*, 701−706.
(16) Tsui, B.-Y.; Yang, C.-C.; Fang, K.-L. Anisotropic Thermal Conductivity of Nanoporous Silica Film. *IEEE Trans. Electron Devices* **2004**, *51*, 20−27.
(17) Hrubesh, L. W.; Pekala, R. W. Thermal Properties of Organic and Inorganic Aerogels. *J. Mater. Res.* **1994**, *9*, 731−738.
(18) Gross, J.; Reichenauer, G.; Fricke, J. Mechanical Properties of SiO_2 Aerogels. *J. Phys. D: Appl. Phys.* **1988**, *21*, 1447−1451.
(19) Shimizu, T.; Kanamori, K.; Maeno, A.; Kaji, H.; Doherty, C. M.; Falcaro, P.; Nakanishi, K. Transparent, Highly Insulating Polyethyl- and Polyvinylsilsesquioxane Aerogels: Mechanical Improvements by Vulcanization for Ambient Pressure Drying. *Chem. Mater.* **2016**, *28*, 6860−6868.
(20) Kistler, S. S. Coherent Expanded Aerogels and Jellies. *Nature* **1931**, *127*, 741−741.
(21) Rubin, M.; Lampert, C. M. Transparent Silica Aerogels for Window Insulation. *Sol. Energy Mater.* **1983**, *7*, 393−400.
(22) Gunay, A. A.; Kim, H.; Nagarajan, N.; Lopez, M.; Kantharaj, R.; Alsaati, A.; Marconnet, A.; Lenert, A.; Miljkovic, N. Optically Transparent Thermally Insulating Silica Aerogels for Solar Thermal Insulation. *ACS Appl. Mater. Interfaces* **2018**, *10*, 12603−12611.
(23) Yan, Y.; King, S. C.; Li, M.; Galy, T.; Marszewski, M.; Kang, J. S.; Pilon, L.; Hu, Y.; Tolbert, S. H. Exploring the Effect of Porous Structure on Thermal Conductivity in Templated Mesoporous Silica Films. *J. Phys. Chem. C* **2019**, *123*, 21721−21730.
(24) Fang, J.; Reitz, C.; Brezesinski, T.; Nemanick, E. J.; Kang, C. B.; Tolbert, S. H.; Pilon, L. Thermal Conductivity of Highly-Ordered Mesoporous Titania Thin Films from 30 to 320 K. *J. Phys. Chem. C* **2011**, *115*, 14606−14614.
(25) Coquil, T.; Richman, E. K.; Hutchinson, N. J.; Tolbert, S. H.; Pilon, L. Thermal Conductivity of Cubic and Hexagonal Mesoporous Silica Thin Films. *J. Appl. Phys.* **2009**, *106*, 034910.
(26) Yan, Y.; Li, M.; King, S.; Galy, T.; Marszewski, M.; Kang, J. S.; Pilon, L.; Hu, Y.; Tolbert, S. H. Controlling Thermal Conductivity in Mesoporous Silica Films Using Pore Size and Nanoscale Architecture. *J. Phys. Chem. Lett.* **2020**, *11*, 3731−3737.
(27) Lu, X.; Caps, R.; Fricke, J.; Alviso, C. T.; Pekala, R. W. Correlation between Structure and Thermal Conductivity of Organic Aerogels. *J. Non-Cryst. Solids* **1995**, *188*, 226−234.
(28) Emmerling, A.; Fricke, J.; Hubland, A. Scaling Properties and Structure of Aerogels. *J. Sol-Gel Sci. Technol.* **1997**, *8*, 781−788.
(29) Fricke, J.; Lu, X.; Wang, P.; Büttner, D.; Heinemann, U. Optimization of Monolithic Silica Aerogel Insulants. *Int. J. Heat Mass Transfer* **1992**, *35*, 2305−2309.
(30) Callaway, J.; von Baeyer, H. C. Effect of Point Imperfection on Lattice Thermal Conductivity. *Phys. Rev.* **1960**, *120*, 1149−1154.
(31) Callaway, J. Model for Lattice Thermal Conductivity at Low Temperatures. *Phys. Rev.* **1959**, *113*, 1046−1051.
(32) Klemens, P. G. Thermal Resistance Due to Point Defects at High Temperatures. *Phys. Rev.* **1960**, *119*, 507−509.
(33) Klemens, P. G. The Scattering of Low-Frequency Lattice Waves by Static Imperfections. *Proc. Phys. Soc., London, Sect. A* **1955**, *68*, 1113−1128.
(34) Seyf, H. R.; Henry, A. A Method for Distinguishing between Propagons, Diffusions, and Locons. *J. Appl. Phys.* **2016**, *120*, No. 025101.
(35) Choy, C. L.; Tong, K. W.; Wong, H. K.; Leung, W. P. Thermal Conductivity of Amorphous Alloys above Room Temperature. *J. Appl. Phys.* **1991**, *70*, 4919−4925.
(36) Choy, C. L.; Leung, W. P.; Ng, Y. K. Thermal Conductivity of Metallic Glasses. *J. Appl. Phys.* **1989**, *66*, 5335−5339.
(37) Varshneya, A. K.; Mauro, J. C. *Fundamentals of Inorganic Glasses*, 3rd ed.; Elsevier: 2019.
(38) Yoldas, B. E. Introduction and Effect of Structural Variations in Inorganic Polymers and Glass Networks. *J. Non-Cryst. Solids* **1982**, *51*, 105−121.
(39) Woo, H.; Char, K. Transparent Organosilicate Hybrid Films with Thermally Insulating and UV-Blocking Properties Based on Silica/Titania Hybrid Hollow Colloidal Shells. *Macromol. Res.* **2013**, *21*, 1004−1010.
(40) Que, W.; Sun, Z.; Zhou, Y.; Lam, Y. L.; Chan, Y. C.; Kam, C. H. Optical and Mechanical Properties of TiO_2/SiO_2/Organically Modified Silane Composite Films Prepared by Sol-Gel Processing. *Thin Solid Films* **2000**, *359*, 177−183.
(41) Emili, M.; Incoccia, L.; Mobilio, S.; Fagherazzi, G.; Guglielmi, M. Structural Investigations of TiO_2-SiO_2 Glassy and Glass-Ceramic Materials Prepared by the Sol-Gel Method. *J. Non-Cryst. Solids* **1985**, *74*, 129−146.
(42) Yoldas, B. E. Formation of Titania-Silica Glasses by Low Temperature Chemical Polymerization. *J. Non-Cryst. Solids* **1980**, *38*−*39*, 81−86.
(43) Dong, W.; Sun, Y.; Lee, C. W.; Hua, W.; Lu, X.; Shi, Y.; Zhang, S.; Chen, J.; Zhao, D. Controllable and Repeatable Synthesis of Thermally Stable Anatase Nanocrystal-Silica Composites with Highly Ordered Hexagonal Mesostructures. *J. Am. Chem. Soc.* **2007**, *129*, 13894−13904.
(44) Jung, H.; Kim, Y. H.; Kim, J.; Yoon, T. S.; Kang, C. J.; Yoon, S.; Lee, H. H. Analog Memristive Characteristics of Mesoporous Silica-Titania Nanocomposite Device Concurrent with Selection Diode Property. *ACS Appl. Mater. Interfaces* **2019**, *11*, 36807−36816.
(45) Stakheev, A. Y.; Shpiro, E. S.; Apijok, J. XPS and XAES Study of TiO_2-SiO_2 Mixed Oxide System. *J. Phys. Chem.* **1993**, *97*, 5668−5672.
(46) Delattre, L.; Babonneau, F. ^{17}O Solution NMR Characterization of the Preparation of Sol−Gel Derived SiO_2/TiO_2 and SiO_2 /ZrO_2 Glasses. *Chem. Mater.* **1997**, *9*, 2385−2394.

(47) Davis, R. J.; Liu, Z. Titania-Silica: A Model Binary Oxide Catalyst System. *Chem. Mater.* **1997**, *9*, 2311−2324.
(48) Liu, Z.; Davis, R. J. Investigation of the Structure of Microporous Ti-Si Mixed Oxides by X-Ray, UV Reflectance, FT-Raman, and FT-IR Spectroscopies. *J. Phys. Chem.* **1994**, *98*, 1253−1261.
(49) Dirken, P. J.; Smith, M. F.; Whitfield, H. J. ^{17}O and ^{29}Si Solid State NMR Study of Atomic Scale Structure in Sol-Gel-Prepared TiO_2-SiO_2 materials. *J. Phys. Chem.* **1995**, *99*, 395−401.
(50) Pickup, D. M.; Mountjoy, G.; Wallidge, G. W.; Anderson, R.; Cole, J. M.; Newport, R. J.; Smith, M. E. A Structural Study of $(TiO_2)_x(SiO_2)_{1-x}$ (x = 0.18, 0.30 and 0.41) Xerogels Prepared Using Acetylacetone. *J. Mater. Chem.* **1999**, *9*, 1299−1305.
(51) Chen, H.; Huang, S.; Perng, T. Preparation and Characterization of Molecularly Homogeneous Silica − Titania Film by Sol − Gel Process with Different Synthetic Strategies. *ACS Appl. Mater. Interfaces* **2012**, *4*, 5188−5195.
(52) Yang, L.-L.; Lai, Y.-S.; Chen, J. S.; Tsai, P. H.; Chen, C. L.; Chang, C. J. Compositional Tailored Sol-Gel SiO_2 − TiO_2 Thin Films: Crystallization, Chemical Bonding Configuration, and Optical Properties. *J. Mater. Res.* **2005**, *20*, 3141−3149.
(53) Dunphy, D. R.; Sheth, P. H.; Garcia, F. L.; Brinker, C. J. Enlarged Pore Size in Mesoporous Silica Films Templated by Pluronic F127: Use of Poloxamer Mixtures and Increased Template/SiO_2 Ratios in Materials Synthesized by Evaporation-Induced Self-Assembly. *Chem. Mater.* **2015**, *27*, 75−84.
(54) Busato, S.; Perevedentsev, A. A Simple Imaging-Based Technique for Quantifying Haze and Transmittance of Materials. *Polym. Eng. Sci.* **2018**, *58*, 345−352.
(55) Calleja, G.; Serrano, D. P.; Sanz, R.; Pizarro, P. Mesostructured SiO_2 -Doped TiO_2 with Enhanced Thermal Stability Prepared by a Soft-Templating Sol − Gel Route. *Microporous Mesoporous Mater.* **2008**, *111*, 429−440.
(56) Chao, S.; Wang, W.-H.; Hsu, M.-Y.; Wang, L.-C. Characteristics of Ion-Beam-Sputtered High-Refractive-Index TiO_2-SiO_2 Mixed Films. *J. Opt. Soc. Am. A* **1999**, *16*, 1477.
(57) Chen, J.-S.; Chao, S.; Kao, J.-S.; Niu, H.; Chen, C.-H. Mixed Films of TiO_2−SiO_2 Deposited by Double Electron-Beam Coevaporation. *Appl. Opt.* **1996**, *35*, 90.
(58) Chao, S.; Chang, C.-K.; Chen, J.-S. TiO_2−SiO_2 Mixed Films Prepared by the Fast Alternating Sputter Method. *Appl. Opt.* **1991**, *30*, 3233.
(59) Xie, C.; Xu, Z.; Yang, Q.; Xue, B.; Du, Y.; Zhang, J. Enhanced Photocatalytic Activity of Titania-Silica Mixed Oxide Prepared via Basic Hydrolyzation. *Mater. Sci. Eng., B* **2004**, *112*, 34−41.
(60) Netterfield, R. P.; Martin, P. J.; Pacey, C. G.; Sainty, W. G.; McKenzie, D. R.; Auchterlonie, G. Ion-assisted Deposition of Mixed TiO_2 -SiO_2 Films. *J. Appl. Phys.* **1989**, *66*, 1805−1809.
(61) Paparazzo, E.; Fanfoni, M.; Severini, E.; Priori, S. Evidence of Si−OH Species at the Surface of Aged Silica. *J. Vac. Sci. Technol., A* **1992**, *10*, 2892−2896.
(62) Paparazzo, E. On the XPS Analysis of Si-OH Groups at the Surface of Silica. *Surf. Interface Anal.* **1996**, *24*, 729−730.
(63) Baklanov, M. R.; Mogilnikov, K. P.; Polovinkin, V. G.; Dultsev, F. N. Determination of Pore Size Distribution in Thin Films by Ellipsometric Porosimetry. *J. Vac. Sci. Technol., B: Microelectron. Process. Phenom.* **2000**, *18*, 1385−1391.
(64) Galy, T.; Marszewski, M.; King, S.; Yan, Y.; Tolbert, S. H.; Pilon, L. Comparing Methods for Measuring Thickness, Refractive Index, and Porosity of Mesoporous Thin Films. *Microporous Mesoporous Mater.* **2020**, *291*, 109677.
(65) Thommes, M.; Kaneko, K.; Neimark, A. V.; Olivier, J. P.; Rodriguez-Reinoso, F.; Rouquerol, J.; Sing, K. S. W. Physisorption of Gases, with Special Reference to the Evaluation of Surface Area and Pore Size Distribution (IUPAC Technical Report). *Pure Appl. Chem.* **2015**, *87*, 1051−1069.
(66) Sing, K. S. W.; Everett, D. H.; Haul, R. A. W.; Moscou, L.; Pierotti, R. A.; Rouquerol, J.; Siemieniewska, T. Reporting Physisorption Data for Gas/Solid Systems with Special Reference to the Determination of Surface Area and Porosity. *Pure Appl. Chem.* **1985**, *57*, 603−619.
(67) Yang, P.; Zhao, D.; Margolese, D. I.; Chmelka, B. F.; Stucky, G. D. Block Copolymer Templating Syntheses of Mesoporous Metal Oxides with Large Ordering Lengths and Semicrystalline Framework. *Chem. Mater.* **1999**, *11*, 2813−2826.
(68) Tian, B.; Liu, X.; Tu, B.; Yu, C.; Fan, J.; Wang, L.; Xie, S.; Stucky, G. D.; Zhao, D. Self-Adjusted Synthesis of Ordered Stable Mesoporous Minerals by Acid−Base Pairs. *Nat. Mater.* **2003**, *2*, 159−163.
(69) Li, D.; Zhou, H.; Honma, I. Design and Synthesis of Self-Ordered Mesoporous Nanocomposite through Controlled in-Situ Crystallization. *Nat. Mater.* **2004**, *3*, 65−72.
(70) Pietrak, K.; Wisniewski, T. S. A Review of Models for Effective Thermal Conductivity of Composite Materials. *J. Power Technol.* **2015**, *95*, 14−24.

CHAPTER 6

Hierarchical monoliths from sub 50 nm hollow silica shells

The intrinsic pores and multiple heat scattering interfaces of hollow silica shells make them interesting building blocks for hierarchical mesoporous monoliths. In this work, we use hollow silica shells synthesized using a single micelle templating technique with tetraethylorthosilicate (TEOS) as our silica source. We first systematically tuned the synthesis of hollow silica shells to understand the individual effect of each parameter on the total diameter (d_{tot}) and core diameter (d_{core}). By adjusting the ratio of each precursor, we reduced the size of the shells to range from d_{tot} of 32 nm and d_{core} of 17 nm to shells with d_{tot} of 13 nm and d_{core} of 7 nm. We then used nanoparticle aggregation to form monoliths of the polymer-filled silica nanoparticles, and calcined them to produce free-standing monoliths of hollow silica shells. Using different-sized shells, we are able to produce the hierarchical monoliths with optical transmittance ranging from 50% to 80%.

Introduction

Mesoporous materials such as hollow silica shells and their hierarchical monoliths, are of interest for applications in biomedicine, agriculture, catalysis, and thermal insulation owing to their high surface areas, low densities, low toxicities, ultra-low thermal conductivities, and mechanical robustness.[1–3] There is particular interest in the use of mesoporous silica aerogels in monolith or granular form for use as transparent insulating coatings for window glazings or skylights to reduce energy consumption.[4–9] For window glazing, the coating needs to be optically transparent in addition to having a low thermal conductivity. To increase transparency, all features of the coatings – pores, particles, and defects, need to be small enough to prevent optical scattering.[10] For skylights, high optical transparency is not as integral.

Hollow silica shells, in the shape of rods, cubes, or spheres, are synthesized by hydrolyzing and condensing silica precursors around a template that is subsequently removed. The template that constitutes the core can be either hard or soft.[11] Hard templates consist of pre-formed colloids with fixed sizes and shapes made from either inorganic (metal, salt, or oxide) or organic (polymethylmethacrylate or polystyrene) precursors.[11–16] In comparison, soft templates, like emulsions of surfactants or block-copolymer micelles, have more dynamic and flexible structures with their features determined by intermolecular interactions.[11,17–19] After the silica precursor condenses on the surface of the core, the template is removed by physical or chemical treatment to produce the hollow shell.

The synthesis of hollow silica spheres using block-copolymer templating (also referred to as single micelle templating) is of particular interest for this study, since monodisperse silica shells with diameters below 50 nm can easily be synthesized using this technique. Block-copolymers containing hydrophobic and hydrophilic components, such as poly (propylene oxide) (PPO) and poly (ethylene oxide) (PEO), respectively, can form micelles in solution. Typically, the micelle templating process is used to produce ordered mesoporous monoliths. However, under the correct synthetic conditions, block-copolymer templating can be used to produce individual nanoparticles. Specifically, the micelles need to be stabilized with an appropriate hydrophobic additives (often a benzene-derivative)[20]. This stabilizes the PPO core of the micelles so that the micelles are less dynamic and thus more similar to a hard template. To avoid the formation of a consolidated network, the mass ratios of the silica precursor to polymer needs to be less than 2.8 g/g regardless of the silica source.[21,22] Additionally, the synthesis is generally conducted in strongly acidic conditions to slow down the hydrolysis rate of the silica precursor, although shells synthesized at neutral pH levels have been reported.[23] Additionally, while the presence of salt has been shown to

aid in the synthesis of shells by reducing their total diameters and improving monodispersity, it is not essential for the formation of hollow silica shells.[20,22,24] Of particular note in this work is the development of methods to produce shells that are significantly smaller than those previously reported. This size optimization may find applications in a range of fields.

After the nanoparticles are synthesized, the hollow shells can be formed into hierarchical monoliths, typically through a sintering process or via an evaporation induced self-assembly process.[25] However, the resulting materials often have low porosity and high nanoparticle contact, which can increase heat conduction along the silica backbone. One method that is yet to be explored to produce hierarchical monoliths of hollow shells via controlled aggregation or gelling, similar to that used to produce aerogels or ambigels.[4,7,26,27] In this process, the silica precursors react and aggregate to form an interconnected gel filled with an aqueous or alcoholic solvent. The solvent in the gel is then gradually exchanged to one that exerts little capillary pressure on the network, which is then removed to produce a mesoporous network with randomly sized pores. Recently, Marszewski *et al.* demonstrated that the process can be adapted to produce silica nanoparticle-based monoliths that are highly porous and semi-transparent. [28] To induce gelling, they reduce the surface charge of silica nanoparticles by lowering the pH of the solution. Using this technique, they were able to produce monoliths with porosities between 70 – 81% with visible transmittances between 75 – 83%.

In this work, we use single micelle templating to synthesize hollow silica shells, and then assemble the shells into hierarchical monoliths. The synthesis was modified to reduce the size of the shells, and the very small shells described here may find applications outside of controlled thermal conductivity. The small shells were then assembled in solution and the process was

optimized to produce free-standing hierarchical monoliths. The porosities of resulting monoliths varied from 68 to 85%.

Experimental

Synthesis of hollow silica shells

Hollow silica shells were synthesized using a single micelle templating technique (Scheme 3.2.1) adapted from Tang *et. al*.[21] In a typical synthesis, for example one with the molar ratio of F108:HCl:xylenes:TEOS of 0.01:19:1.8:1, 0.5 g of the non-ionic block-copolymer Pluronic F108 ($PEO_{132}PPO_{50}PEO_{132}$) was dissolved in 30 mL of 2 M HCl at room temperature. After one hour of rapid stirring, 0.7 mL xylenes was added to the solution and the emulsion was left to stir for an additional 2 hours. To the emulsion, 0.7 mL of TEOS was added dropwise and the contents were allowed to stir for 12 hours. The synthetic parameters were tuned as described in Table 1 to examine their effect on the size of the hollow silica shell. To remove excess polymer template and xylenes, liquid-liquid extraction of the hollow shell solution with toluene was conducted. In general, 30 mL of hollow shells solution was extracted using 50 mL of toluene, and the process was performed in triplicate. To characterize the as-synthesized shells, an aliquot of the extracted solution was dried at 80 °C then calcined in flowing oxygen by first heating under a ramp of 1 °C min^{-1}, holding at 250 °C for 6 hours, then at 400 °C for an additional 6 hours, and then cooling under a ramp of 1 °C min^{-1}.

Synthesis and post-synthetic treatment of shells to form monoliths:

To assemble the shells into monoliths, the synthesis was scaled six-fold. After the liquid-liquid extraction, the solution was left partially covered for at least 5 hours to allow for the evaporation of any residual benzene derivatives (xylenes, toluene). In an attempt to facilitate gelation and

strengthen the gel network, the shell solution was either (1) heat-treated or (2) the pH was adjusted almost to the point of gelation.

To heat treat the samples, the extracted hollow shell solution was placed into a Teflon autoclave at 80 °C for 2 days. The warm solution was then poured into a Teflon mold coated with Fluorinert FC-70 PFC oil, covered, and left to gel and shrink. The heat-treated samples are denoted by HT. For the pH adjusted samples, the pH of the shell solution was increased to 8. To do so, 40 mL of the extracted solution was first diluted to 70 mL using distilled water to avoid premature aggregation of the shells upon addition of base. Then, approximately 7 mL of 4 M NH_4OH was then added over the course of 30 minutes to the diluted shell solution in 1 mL increments while rapidly stirring to slowly adjust the pH to 8. This diluted, pH-adjusted solution was then concentrated using ultrafiltration. In general, 70 mL of the pH adjusted hollow shell solution was concentrated to 55 mL via pressure ultrafiltration using a Sartorius® Vivacell 100 ultrafiltration unit with gentle shaking. The concentration process took approximately 2 hours, after which the solution was again placed in a Teflon mold coated with the Fluorinert FC-70 PFC oil, covered and left to gel and shrink. The pH-adjusted samples are denoted by PA.

After the gel shrank to about 60 % of its original diameter and fully detached from the walls of the container (approximately 5 days for both heat-treated and pH-adjusted samples), it was carefully removed from the Teflon mold and solvent exchanged.

Solvent exchange, drying, and calcination of hollow shell monoliths:

A basic outline of the solvent exchange, drying, and calcination process is depicted in Scheme 1 and is similar to the ambient drying technique reported for ambigels, but with additional steps to remove the polymer template from inside the shell.[4] The wet gel was first placed in a 1:1 water:ethanol mixture for 3 hours then transferred to a 100% ethanol solution for an additional 3

hours. The ethanol solution was then replaced with a mixture of 2 vol% of bistriethoxysilane in ethanol followed by 5 drops of concentrated HCl. The gel was left in this solution for at least 8 hours to facilitate further cross-linking and therefore increase the structural robustness. After this time, the gel was transferred to an acidified ethanol solution (0.73% concentrated HCl in ethanol) and placed in an oven at 60 °C for at least 4 hours to dissolve some of the polymer from the core of the composite.[29] This acidified ethanol wash was conducted in triplicate. The gel was then transferred to a 1:1 mixture of ethanol:heptane, followed by three final solvent exchanges in pure heptane. The gel was then placed in a partially closed container to slowly dry. After the gel was fully dried (approximately 2-3 days), the dried slab was first heated at 250 °C for 6 hours then calcined at 400 °C for an additional 6 hours at a ramp and cool down rate of 1 °C min^{-1} in flowing oxygen.

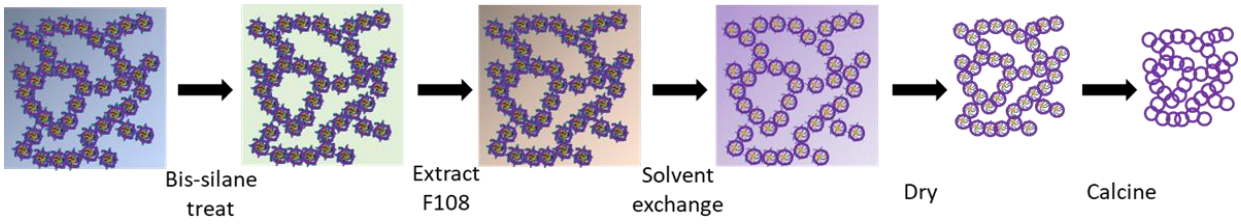

Scheme 6.1. Outline of the solvent exchange process.

Results

Hollow shells synthesized using single micelle templating with TEOS as the silica source were used to create hierarchical porous monoliths. We used TEOS as the silica source since it hydrolyses and condenses to form pure silica shells, which has reactive groups on the surface of the particles that can crosslink during assembly to help the shells aggregate into monoliths. The synthesis of the hollow shells was conducted in the absence of salts because we found that the salts were very hard to subsequently remove, and would crystallize during the assembly of the colloids

into monoliths. The current salt-free syntheses of hollow shells presented in the literature typically gives shells with total diameters c.a. 30 nm.[20] Structural characterization of fully calcined shells synthesized in-house using previously reported salt-free synthesis methods is given in Figure 6.1. This sample serves as the starting point for our further optimization. The rings observed in the transmission electron microscope (TEM) image of Figure 6.1(a) verify the formation of hollow silica shells. Here, the edge of the shell is darker than the interior since it has more material for the electron beam to penetrate. The porosity of the sample was obtained from the total volume adsorbed during N_2 porosimetry, measured at 77 K and depicted in Figure 6.1(b). The isotherms obtained are type IV(a), as is typical of mesoporous materials. There are two distinct regions in the N_2 porosimetry isotherm: the first uptick, at $P/P_0 \leq 0.9$, is due to the hollow interior of the shells, while the second, at $P/P_0 \geq 0.9$, is due to absorption from larger pores that are created by inter-particle stacking. The pore size distribution (PSD) was obtained from the adsorption branch of the isotherm using the Barrett-Joyner-Halenda (BJH) method with KJS correction. Like the isotherm, the PSD also shows two distinct regions from the two types of pores, with hollow interior (d_{core}) pores indicated by the peak centered at 24 ± 3 nm and the inter-particle stacking ($d_{i\text{-}p}$) pores showing up at pore widths greater than 30 nm. In addition, the PSD reveals the presence of microporous windows in the shells at pore widths less than 7 nm.

Unfortunately, with a total diameter of 32 nm, the hollow shells would significantly scatter light and thus reduce the optical transmittance, motivating an interest in smaller hollow shells.[10,30] It has also been shown that the intrinsic gaps between particles correlate with the size of the particles,[31] therefore having smaller particles to assemble into monoliths would reduce optical scattering for the pores between the particles as well. As such, we set out to amend our synthesis to reduce the size of the shells, then assemble these smaller shells into monoliths.

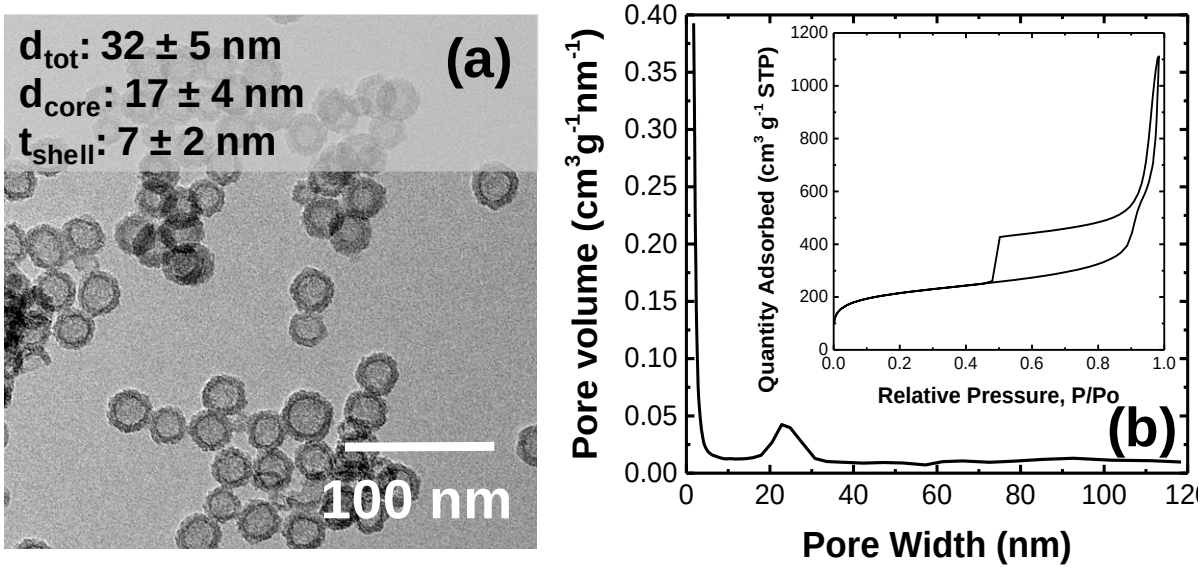

Figure 6.1. Structural characterization of typical hollow silica shells. (a) transmission electron microscope (TEM) image of the hollow shells and (b) pore size distribution with porosimetry isotherms inset of the hollow shells obtained from N_2 adsorption porosimetry at 77 K.

Adjusting synthetic parameters to reduce the size of the hollow shells

In single-micelle templating with block-copolymer micelles, silica-micelle composites are formed via an interfacial templating condensation process. When the Pluronic block copolymer is added to the aqueous HCl solution, it self-assembles to form spherical micelles. The hydrophobic xylenes preferentially interact with the hydrophobic PPO groups of the micelle cores by suppressing the equilibrium exchange of the hydrophobic and hydrophilic blocks of the block copolymer. When the hydrophobic TEOS is added to the emulsion network, it enters the xylene-stabilized PPO core. At the PPO-PEO interface of the micelle, TEOS hydrolyses and condenses to form silica.[32] There has been significant work in the literature examining the effect of various synthetic parameters on the size of hollow shells made from this technique. We used these established trends to synthesize smaller shells that will reduce light scattering in our monoliths.

The synthesis of hollow silica shells can be tailored by adjusting three key parameters: the pH of the solution, [33] the size of the micelle core,[20,24,34] and the ratio of the silica precursor (TEOS) to the number of micelles.[20,21,34] Particle sizes obtained by TEM and their pore size distributions obtained from N_2 porosimetry are given in Table 6.1. Samples are named HS-abcd where HS refers to the hollow shell solution and (a), (b), (c), and (d) refer to molar ratios added to the solution relative to the typical salt-free synthesis (HS-1111) for HCl, Pluronic F108, xylenes, and TEOS, respectively.

Table 6.1. Synthetic parameters and resulting hollow shell characteristics

Sample name	molar ratio added				§Diameter (nm)		§Shell Thickness, t_{shell} (nm)	¶Core width (nm)
	HCl	F108	Xylenes	TEOS	Total, d_{tot}	Core, d_{core}		
HS- 1111	19.0	0.01	1.8	1	32 ± 5	17 ± 4	7 ± 2	24 ± 3
HS-½111	9.5	0.01	1.8	1	22 ± 2	13 ± 3	4 ± 1	13 ± 2
HS-⅓111	6.3	0.01	1.8	1	16 ± 2	8 ± 1	4 ± 1	9 ± 3
HS- 1211	19.0	0.02	1.8	1	23 ± 2	15 ± 2	4 ± 1	14 ± 2
HS- 1311	19.0	0.03	1.8	1	13 ± 2	6 ± 1	3 ± 1	9 ± 1
HS- 1121	19.0	0.01	3.6	1	26 ± 2	15 ± 2	5 ± 1	16 ± 1
HS- 1131	19.0	0.01	5.4	1	18 ± 3	12 ± 2	3 ± 1	10 ± 1
HS- 1221	19.0	0.02	3.6	1	20 ± 1	13 ± 1	3 ± 1	15 ± 2
HS- 1331	19.0	0.03	5.4	1	13 ± 1	7 ± 1	3 ± 1	6 ± 1

§Measured from TEM using ImageJ

¶Retrieved from N_2 porosimetry at 77 K using the KJS model.

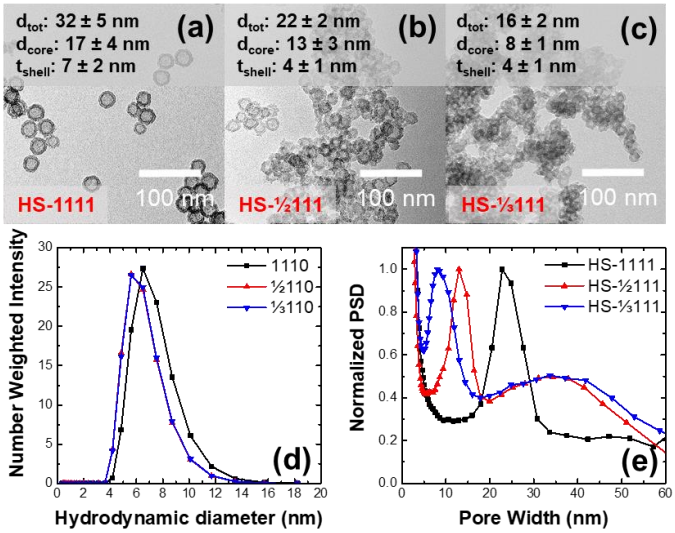

Figure 6.2. Examining the effect of hydrochloric acid concentration [HCl] on the structure of silica shells. TEM images of shells made from (a) 2 M, (b) 1 M and, (c) 0.67 M HCl showing the decrease in the diameter of the silica shells as the concentration of HCl is decreased. (d) Number-weighted intensity distribution of the hydrodynamic diameters of the micelles at different [HCl] obtained from dynamic light scattering. The diameters of the micelles decrease when the [HCl] decreases from 2 M to 1 M, but then does not change further at 0.67 M. (e) The normalized pore size distributions (normalized PSD) of the hollow silica shells with varying concentrations of HCl showing a continuous decrease in core size with decreasing [HCl].

Effect of HCl concentration

First we examined the effect of decreasing the pH of the solution on the size of the shells from 2 M to 1 M to 0.67 M in samples HS-1111, HS-½111, HS-⅓111, respectively. When we decreased the concentration of the hydrochloric acid the size of the shells decreased, as shown in Figures 6.2(a) to 6.2(c). This is thought to be due in part to a decrease in micelle size in the more acidic environment. The decrease in [HCl] decreases the H-bonding in the aqueous solvent, which then decreases the hydration of the micelle. While this change in hydration has been shown to have no effect on the PPO core of the micelles,[35] as the H-bonding decreases, the EO chains are less stretched, and, as a result, the overall size of the micelle decreases. The decrease in micelle size with decreasing [HCl] is observed using DLS, as shown in Figure 6.2(d). Upon reduction of the

[HCl] from 2 M to 1 M, but not upon further reduction from 1 M to 0.67 M. The differences in the d_{core} obtained from the TEM images (Figures 6.2(a-c)) and normalized PSD (Figure 6.2(e)) for 1 M to 0.67 M when no micelle size change is observed can be explained by the fact that the concentration of acid also greatly influences the hydrolysis and condensation rates of the silica precursor, where a slower hydrolysis or condensation rate could lead to smaller shells.[36] In agreement with this idea, the pore sizes of the resulting hollow silica shells obtained from porosimetry (Figure 6.2(e)) and measured from TEM (Figures 6.2(a-c)) decrease with decreasing acid concentration. When [HCl] decreases, there is also an increase in shell aggregation as observed from the TEM images in Figures 6.2(a) to 6.2(c). This increased aggregation is likely due to the decrease in the density positive charges on the silica surface; higher charge density or zeta potential is known to increase the inclination for the micelles to aggregate.

Effect of micelle constituents

We next examined the effect of varying the mass of F108 added (HS-1111, HS-1211, HS-1311), the effect of varying the volume of xylenes added (HS-1111, HS-1121, HS-1131), and the coupled effect of varying both components (HS-1111, HS-1221, HS-1331) on the micelle size and the size of the resulting hollow shells.

Pluronic F108: As the concentration of Pluronic F108 in solution increases, the size of the resulting shells decreases, as depicted in the TEM images, Figures 6.3(a) – 6.3(c). From DLS in Figure 6.3(d), the size of the micelles remained constant when the concentration of F108 was increased from a relative molar content of 0.01 to 0.02, but increased slightly at a relative molar content of 0.03, the highest concentration of Pluronic F108. A similar trend has been reported in the literature for aqueous solutions of Pluronic micelles.[37] There, while the size also initially remained the same, a dramatic increase was observed for higher weight contents of the Pluronic

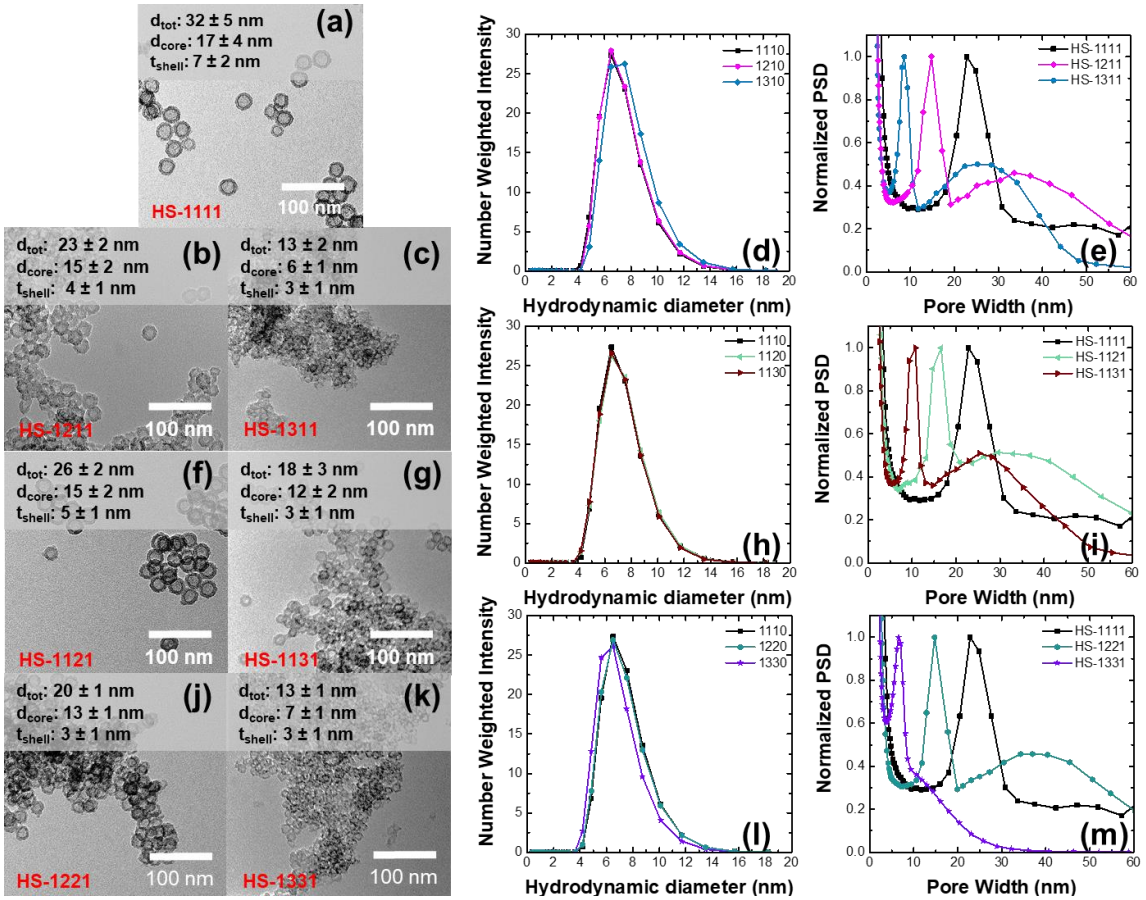

Figure 6.3. Examining the effect of micelle constituents on the structure of silica shells. Part (a) shows a reference TEM image of HS-1111 synthesized using the parameters from literature. TEM images (b) and (c) and DLS spectra (d-e) demonstrate the effect of changing the mass of F108 added to the size of hollow silica shells. Panels (f-i) illustrate the effect of changing the volume of xylenes added to the solution on the size of the hollow shells produced and panels (j-m) show the influence of changing both F108 and xylenes content on the size of the resulting shells

block copolymers as a result of polymer aggregation. We hypothesize that the very small increase in our data indicates that we are primarily in the low concentration regime, and may be affected by the presence of xylenes. Despite the similar micelle sizes observed in our DLS data, both the core size and the overall size of the shells decrease as the F108 concentration, and therefore micelle concentration, increases. This can be seen in the decrease in d_{tot} and d_{core} measured from TEM in Figures 6.3(a) - 6.3(c) and the decrease in d_{core} measured via N_2 porosimetry in Figure 6.3(e). These decreases are likely the result of silica partitioning. If we assume that TEOS distributes equally in

each micelle, as the number of micelles increases, the ratio of silica/micelle decreases. As a result, there is less TEOS in each xylene-stabilized PPO core to hydrolyzes and condenses at the PPO-PEO interface and form silica, resulting in smaller particles. In addition to a decrease in core and shell size, there is some increased polydispersity in the shells produced, most likely due to a lower ratio of xylenes/polymer which could result in less stable micelles.

Xylenes: Organic solvents like xylenes are often used to dissolve the PPO core and act as pore expanders in synthesis of porous materials.[20,38,39] However, we observe that instead of an increase in pore size when the concentration of xylenes increases in samples, there is a decrease in d_{core}, as shown in the TEM images Figures 6.3(a), 6.3(f) and 6.3(g), and in the N_2 porosimetry, Figure 6.3(i). However, DLS of the micelles, Figure 6.3(h), shows that the micelles are all approximately the same size. This suggests that the PPO core of the micelle is fully saturated with xylenes and there is an excess that goes to the exterior of the micelles and causes the micelle to shrink. Previous reports of this phenomenon attribute this shrinkage to a repulsion between the PEO blocks of the polymer and the excess xylenes.[24,40] We hypothesize that the reduction in d_{core} may due to some partitioning of the TEOS into the excess xylenes and out of the PPO cores, which would produce a similar effect to adding more F108, as previously observed.

F108 and xylenes: The overall solution is more concentrated when the ratio of both F108 and xylenes are increased. From the DLS in Figure 6.3(l), the peak intensities of the micelle diameters are all similar. However, although the maximum sits at a similar diameter value as the other samples, for the highest concentration of micelles (1331) the overall number weighted intensities are shifted slightly to smaller sizes. This may be due to the lower water content in the more concentrated solutions. It has been shown that when the water content increases, the micelle tends to become larger and more asymmetric.[37] However, in the range examined, this asymmetry

is not observed. When the different concentrations of micelles are coated with equal amounts of silica, there are significant decreases in both d_{tot} and d_{core} from TEM (Figures 6.3(a), 6.3(j) and 6.3(k)), as well as in d_{core} from N_2 porosimetry (Figure 6.3(m)). This decrease is also most likely the result of the aforementioned TEOS partitioning, where there is a smaller volume of TEOS per micelle as the concentration of xylene-stabilized micelles increases.

Overall, we were able to systematically reduce the size of the shells from a total diameter of 32 ± 5 nm and a shell thickness of 7 ± 2 nm, to a total diameter of 13 ± 1 nm and a shell thickness of 3 ± 1 nm. With these new colloidal building blocks in hand, we set out to assemble the hollow silica shells in to mesoporous monoliths.

Solution Purification and Monolith Assembly

We first employed a liquid-liquid extraction with toluene to purify the solution by removing any excess polymer and xylenes, which is needed to facilitate gelation. Since the block copolymer interacts with both the aqueous and organic layers, a significant emulsion layer forms between them which slowly dissipates with each extraction. An aliquot

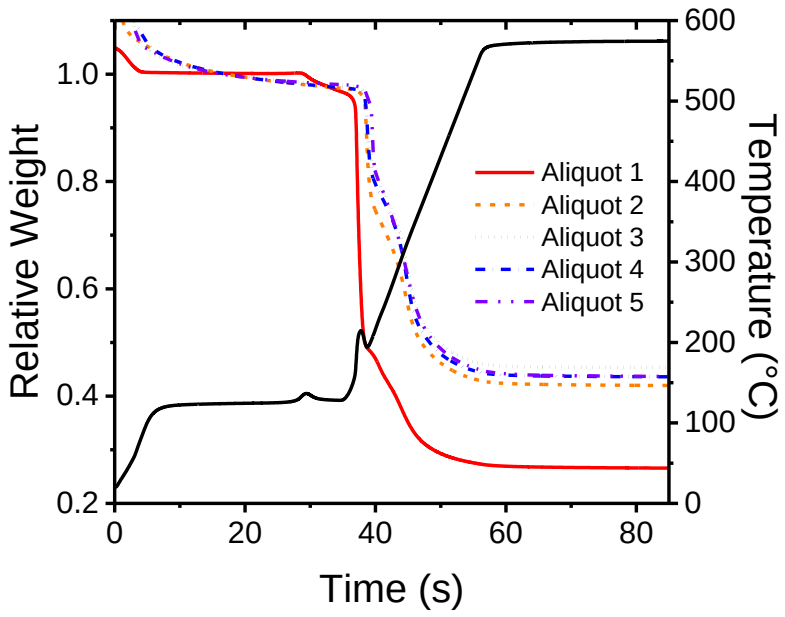

Figure 6.4. Thermogravimetric analysis (TGA) of compounds extracted from hollow silica shell solutions during purificaion using liquid-liquid extractions with toluene. The relative mass lost for each aliquot, as a function of time, is shown on the left while the temperature changed at that time for the first aliquot is shown on the right.

of the toluene and emulsion layer were retained and dried at 80 °C to produce a powdered sample of the residue, then analyzed by thermogravimetric analysis (TGA) in air to quantify the decrease in polymer content of the sample after each extraction (Figure 6.4). The change in the relative mass as a function of time and the temperature at that time are shown on the left and right axes, respectively. The samples were first held at 120 °C for 30 minutes to remove any remaining solvent, then heated to 575 °C and held for 20 minutes to completely remove the Pluronic block copolymer. There is a sudden temperature increase at 40 minutes from 153 °C to 213 °C, and for the first aliquot, there is an accompanying rapid mass drop from ~ 95% to 50%. The temperature increase is due to an exothermic combustion of the PEO blocks. There is then a more gradual mass loss as the temperature continues to increase to 575 °C, then the relative masses of all samples plateau as all polymer is removed and only silica remains. The mass retrieved at the plateau after the combustion of the polymer all belonged to silica. For aliquot 1 about 26% of the total mass remained, while for the subsequent washes, 42 to 43% of the total mass remained. Therefore, by liquid-liquid extraction, we were able to reduce the mass of polymer in the toluene – emulsion mixture from 74 % to 57 %. Liquid-liquid extraction was therefore able to remove about 17% of the polymer from the solution. We believe this 17% was uncoated polymer that was in excess in solution, while the approximately 57% of polymer that remained was coated with silica and thus could not be removed using this technique.

After the solution was purified, it was either heat treated in a Teflon autoclave at 80 °C for 3 days, or the pH was adjusted to approximately 7. The solutions were then poured in to Teflon molds and left to gel. Figure ES1 shows that the hollow shells could successfully gel, and that they dry into a polymer filled composite. To form slabs of hollow silica shells however, we incorporated a solvent exchange procedure that served to reduce shrinkage of the final monolith, strengthen the

silica network, and remove some of the polymer in the network before the monoliths were calcined. Solvent exchange was initiated after the gels detached completely from the walls of the container and shrunk to about 60% of their original volume. There, the solvent in the pores of the gel was gradually exchanged from water to heptane. The heptane has a lower surface tension than water, which reduces the capillary forces exerted on the pores as the solvent evaporates during the drying process. This gradual exchange is thoroughly described in the experimental and involves first exchanging the solvent to ethanol, incorporating intermediate steps of a bissilane treatment followed by a polymer etching process in ethanol, and finally exchanging to heptane. The gels were treated with a bissilane linker to help strengthen the gel network. To produce monoliths of hollow shells, the polymer, which contributes to approximately 57 wt% of dried composite, needed to be removed. One common method of polymer removal is through calcination. However, the energy used to thermally remove the polymer ruins the structural integrity of the monoliths and results in significant cracking, as shown by the optical images in Figure ES2. Alternatively, it has been shown that the polymer can be removed through extraction using an acidified ethanol solution at

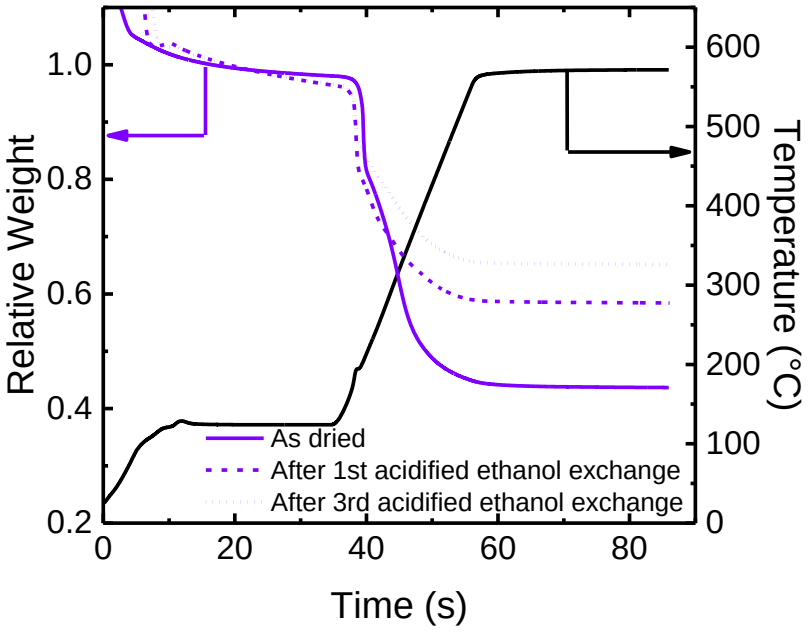

Figure 6.5. TGA of a sample of hollow silica shells showing temperature profile as the hollow shell is heated (black line) and the mass loss due to Pluronic F108 combustion (colored lines) before and after one (1) and three (3) acidic ethanol washes to remove the polymer.

60 °C.[29] An acidified ethanol wash was thus employed and was found to significantly reduced the amount of polymer in the composite. The mass lost from the composite was reduced from approximately 56% of the composite monolith to about 41% after the first extraction. After three washes, the polymer constituted approximately 35% of the composite, as demonstrated by the TGA data presented in Figure 6.5.

After polymer removal, the solvents remaining in the gels were further exchanged to heptane, since heptane's low surface tension has been shown to significant relieve cracking upon drying. The gels were then dried and calcined to produce monoliths of hollow silica shells. The preparation details of each monolith are shown in Table ES1. The selected silica shell-based hollow monoliths (HM) that were characterized with TEM and are referred to as HM-d_{tot}/d_{core}, followed by either HT for heat treated or PA for pH adjusted, to distinguish between the gelling procedures. It should be noted that for these samples, d_{tot} and d_{core} refer to the total and core diameters of the shells measured by TEM from the calcined monolith.

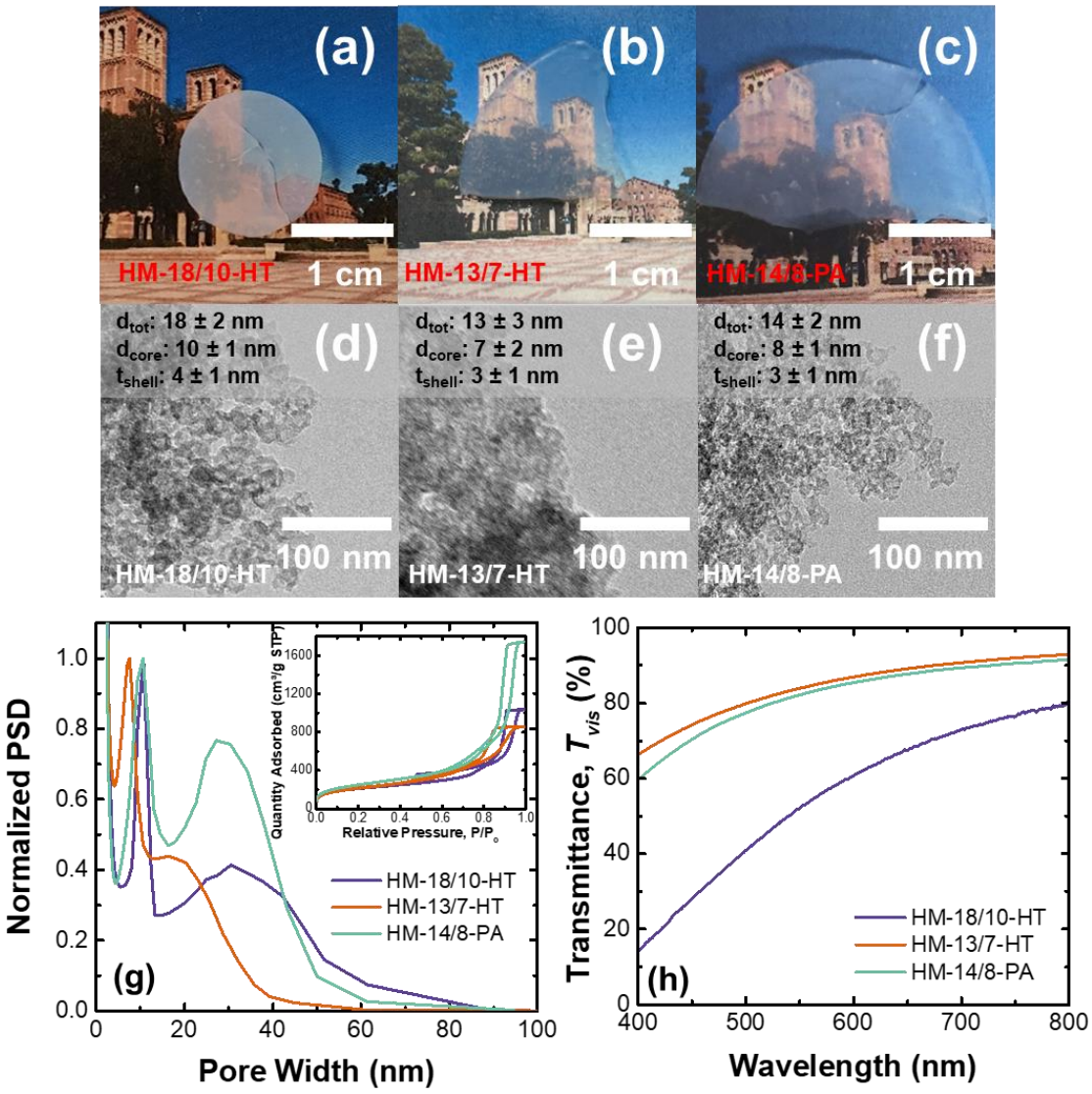

Figure 6.6. Structural and optical characterization of hierarchical hollow shell-based monoliths. (a) – (c) Photographs of monoliths assembled from hollow shells of different sizes and gelling conditions. (a) Photograph of monolith HM-18/10-HT that was assembled from silica shells with d_{tot} = 18 nm and d_{core} = 10 nm; the shells were heat treated at 80 °C for 3 days to facilitate gelling. (b) Photograph of monolith HM-13/7-HT that was assembled from silica shells with d_{tot} = 13 nm and d_{core} = 7 nm; the shells were heat treated at 80 °C for 3 days to facilitate gelling. (c) Photograph of monolith HM-14/8-PA that was assembled from silica shells with d_{tot} = 14 nm and d_{core} = 8 nm. To facilitate gelling, the pH of the solution was adjusted to 8. Corresponding TEM images of powdered suspensions made from pieces of monoliths HM-18/10-HT (d), HM-13/7-HT (e), and HM-14/8-PA (f). All images show that the hollow shells were not damaged during the assembly process. (g) Normalized pore size distribution with N_2 adsorption-desorption isotherm measured at 77 K inset of HM-18/10-HT, HM-13/7-HT, and HM-14/8-PA. (h) Optical transmittance of the monoliths characterized here.

The full structural characterization of three hollow silica shell-based monoliths referred to as HM-18/10-HT HM-13/7-HT and HM-14/8-PA is shown in Figure 6.6. The photographs in Figures 6.6(a) – 6.6(c) show that the shells could indeed be assembled into monoliths, while the TEM images of HM-18/10-HT, HM-13/7-HT and HM-14/8-PA (Figures 6.6(d) – 6.6(f), respectively) clearly show the that constituents of the monoliths were still hollow shells after the assembly process. Likewise, the expected double adsorption steps of the N_2 adsorption isotherm and double peaks in the pore size distributions of Figure 6.6(g) are observed for all monoliths, which also suggests that the hollow shell character is retained upon assembly of the monolith. The porosity of the samples was calculated from the peak volume adsorbed and found to be 78 % for HM-18/10-HT, 74 % for HM-13/7-HT and 85 % for HM-14/8-PA. Generally, for a given gelling procedure (HT or PA), the larger the d_{tot} of the shells, the higher the porosity. In addition, for the monoliths assembled from hollow shells synthesized using the same solution, pH adjustment increases the porosity significantly compared to heat treatment.

The normal-hemispherical transmittance of the free-standing monoliths from Figures 6.6(a)-6.6(c) is shown in Figure 6.6(f). The optical transmittance ranged from 50 – 80 % depending on the sample studied. Increased scattering from pores or particles is generally responsible for reduced optical transmittance. From Figure 6.6(f) it can be observed that the transmittance increased as the d_{tot} decreased. The largest source of optical scattering is from the larger inter-particle distance (d_{i-p}), which also decreased as the size of the shells decreased. This trend is shown in Figure 6.6(g) and is shown even more clearly in the normalized volume-weighted pore size distribution of Figure S4 of the supplementary information. Overall, by reducing the size of the shells, we were able to significantly reduce the optical scattering of the monoliths to produce transparent, free-standing monoliths of hollow silica shells.

Effect of Gelling Procedure on the Resulting Monoliths

The shells that constitute HM-13/7-HT and HM-14/8-PA were synthesized in a similar manner. The differences in the shells and resulting monoliths, therefore offer insight to the effect of gelling procedure (HT vs. PA) on the system. The d_{tot} and d_{core} retrieved from TEM and the d_{core} measured from N_2 porosimetry from Figure 6.6 were smaller for the sample that was heat treated before gelling compared to the sample that was pH adjusted before gelling. To confirm that there was indeed a change to the hollow shell structure, the pore size distributions of other monoliths that were assembled from the same initial solution but gelled in the two different ways are presented in Figure ES3. The data shows that indeed the d_{core} increases when the pH is increased before gelling. We hypothesize that at the higher pH, some silica from the core is etched away and redeposits on the outer walls of the shells due to Ostwald ripening. When the pH of the shells increases, the surface charge of the shells is decreased, which decreases the activation barrier for the shells to aggregate to form a continuous gel network. This thermodynamically induced aggregation is more effective than simply heat treating the samples, which kinetically induces aggregation by increasing the number of collisions. As the shells gel more readily in the pH adjusted samples, the resulting inter-particle diameter (d_{i-p}) is greater, and the porosity increases, as observed in Figures 6.6(g), ES3, ES4 and Table ES1.

Conclusions

This work demonstrates the use of single micelle templating to synthesize and tailor the size of hollow silica shells. By adjusting the synthetic parameters, we were able to reduce the total diameters of the shells from approximately 30 nm to approximately 13 nm. The solutions of these shells were purified and either heat treated or pH adjusted to induce gelling of the shells. The gels then underwent a series of solvent exchanges and was then calcined to form free-standing hollow monoliths with controlled pore sizes. The porosity of the monoliths ranged from 68 to 85 % and

optical clarity ranged from 50 to 80 %. These monoliths have the potential to be used as semi-transparent low thermal conductivity coatings in skylights.

References

(1) Zhao, T.; Elzatahry, A.; Li, X.; Zhao, D. Single-Micelle-Directed Synthesis of Mesoporous Materials. *Nat. Rev. Mater.* https://doi.org/10.1038/s41578-019-0144-x.

(2) Hu, F.; Wu, S.; Sun, Y. Hollow-Structured Materials for Thermal Insulation. *Adv. Mater.* **2019**, *31* (38), 1–17. https://doi.org/10.1002/adma.201801001.

(3) Nuruzzaman, M.; Ren, J.; Liu, Y.; Rahman, M. M.; Shon, H. K.; Naidu, R. Hollow Porous Silica Nanosphere with Single Large Pore Opening for Pesticide Loading and Delivery. *ACS Appl. Nano Mater.* **2020**, *3* (1), 105–113. https://doi.org/10.1021/acsanm.9b01769.

(4) Butts, D. M.; McNeil, P. E.; Marszewski, M.; Lan, E.; Galy, T.; Li, M.; Kang, J. S.; Ashby, D.; King, S.; Tolbert, S. H.; et al. Engineering Mesoporous Silica for Superior Optical and Thermal Properties. *MRS Energy Sustain.* **2020**, *7* (1), 1–12. https://doi.org/10.1557/mre.2020.40.

(5) Marszewski, M.; King, S. C.; Yan, Y.; Galy, T.; Li, M.; Dashti, A.; Butts, D. M.; Kang, J. S.; Mcneil, P. E.; Lan, E.; et al. Thick Transparent Nanoparticle-Based Mesoporous Silica Monolithic 2 Slabs for Thermally Insulating Window Materials. *Appl. Nanomater.* **2019**, *2*, 4547–4555. https://doi.org/10.1021/acsanm.9b00903.

(6) Jensen, K. I.; Schultz, J. M.; Kristiansen, F. H. Development of Windows Based on Highly Insulating Aerogel Glazings. *J. Non. Cryst. Solids* **2004**, *350*, 351–357. https://doi.org/10.1016/j.jnoncrysol.2004.06.047.

(7) Venkateswara Rao, A.; Pajonk, G. M.; Haranath, D. Synthesis of Hydrophobic Aerogels for

Transparent Window Insulation Applications. *Mater. Sci. Technol.* **2001**, *17* (3), 343–348. https://doi.org/10.1179/026708301773002572.

(8) Yang, Y.; Wu, H.; Yang, L.; Xu, T.; Ding, Y.; Fu, P. Thermal and Day-Lighting Performance of Aerogel Glazing System in Large Atrium Building under Cooling-Dominant Climates. *Energy Procedia* **2019**, *158*, 6347–6357. https://doi.org/10.1016/j.egypro.2019.01.273.

(9) Zheng, D.; Chen, Y.; Liu, Y.; Li, Y.; Zheng, S.; Lu, B. Experimental Comparisons on Optical and Thermal Performance between Aerogel Glazed Skylight and Double Glazed Skylight under Real Climate Condition. *Energy Build.* **2020**, *222*, 110028. https://doi.org/10.1016/j.enbuild.2020.110028.

(10) Rubin, M.; Lampert, C. M. Transparent Silica Aerogels for Window Insulation. *Sol. Energy Mater.* **1983**, *7* (4), 393–400. https://doi.org/10.1016/0165-1633(83)90012-6.

(11) Xie, Y.; Kocaefe, D.; Chen, C.; Kocaefe, Y. Review of Research on Template Methods in Preparation of Nanomaterials. **2016**, *2016*.

(12) Li, C.; Yao, J.; Huang, Y.; Xu, C.; Lou, D.; Wu, Z.; Sun, W.; Zhang, S.; Li, Y.; He, L.; et al. Salt-Templated Growth of Monodisperse Hollow Nanostructures. *J. Mater. Chem. A* **2019**, *7*, 1404–1409. https://doi.org/10.1039/c8ta11318a.

(13) Du, Y.; Luna, L. E.; Tan, W. S.; Rubner, M. F.; Cohen, R. E. Hollow Silica Nanoparticles in UV - Visible Antireflection Coatings for Poly(Methyl Methacrylate) Substrates. *ACS Nano* **2010**, *4* (7), 4308–4316. https://doi.org/10.1021/nn101033y.

(14) Ernawati, L.; Ogi, T.; Balgis, R.; Okuyama, K.; Stucki, M.; Hess, S. C.; Stark, W. J. Hollow

Silica as an Optically Transparent and Thermally Insulating Polymer Additive. *Langmuir* **2016**, *32* (1), 338–345. https://doi.org/10.1021/acs.langmuir.5b04063.

(15) Qomariyah, L.; Arif, A. F.; Widiyastuti, W.; Winardi, S.; Taniguchi, S.; Ogi, T. Hexagonal Hollow Silica Plate Particles with High Transmittance under Ultraviolet-Visible Light. *RSC Adv.* **2018**, *8* (46), 26277–26282. https://doi.org/10.1039/c8ra04787a.

(16) Chen, M.; Wu, L.; Zhou, S.; You, B. A Method for the Fabrication of Monodisperse Hollow Silica Spheres. *Adv. Mater.* **2006**, *18* (6), 801–806. https://doi.org/10.1002/adma.200501528.

(17) Okada, T.; Koide, T. Uniform-Sized Silica Nanocapsules Produced by Addition of Salts to a Water-In-Oil Emulsion Template. *Langmuir* **2018**, *34* (32), 9500–9506. https://doi.org/10.1021/acs.langmuir.8b01490.

(18) Liu, J.; Hartono, S. B.; Jin, Y. G.; Li, Z.; Lu, G. Q.; Qiao, S. Z. A Facile Vesicle Template Route to Multi-Shelled Mesoporous Silica Hollow Nanospheres. *J. Mater. Chem.* **2010**, *20* (22), 4595–4601. https://doi.org/10.1039/b925201k.

(19) Dresselhaus, M. S.; Chen, G.; Tang, M. Y.; Yang, R. G.; Lee, H.; Wang, D. Z.; Ren, Z. F.; Fleurial, J.; Gogna, P. New Directions for Low-Dimensional Thermoelectric Materials. *Adv. Mater.* **2007**, *19* (8), 1043–1053. https://doi.org/10.1002/adma.200600527.

(20) Li, Y.; Kruk, M. Single-Micelle-Templated Synthesis of Hollow Silica Nanospheres with Tunable Pore Structures. *RSC Adv.* **2015**, *5* (85), 69870–69877. https://doi.org/10.1039/C5RA13492G.

(21) Tang, J.; Zhou, X.; Zhao, D.; Lu, G. Q.; Zou, J.; Yu, C. Hard-Sphere Packing and

Icosahedral Assembly in the Formation of Mesoporous Materials. *J. Am. Chem. Soc.* **2007**, *129* (29), 9044–9048. https://doi.org/10.1021/ja070999r.

(22) Mandal, M.; Kruk, M. Family of Single-Micelle-Templated Organosilica Hollow Nanospheres and Nanotubes Synthesized through Adjustment of Organosilica/Surfactant Ratio. *Chem. Mater.* **2012**, *24* (1), 123–132. https://doi.org/10.1021/cm202136r.

(23) Liu, J.; Fan, F.; Feng, Z.; Zhang, L.; Bai, S.; Yang, Q.; Li, C. From Hollow Nanosphere to Hollow Microsphere: Mild Buffer Provides Easy Access to Tunable Silica Structure. *J. Phys. Chem. C* **2008**, *112* (42), 16445–16451. https://doi.org/10.1021/jp804161f.

(24) Liu, J.; Bai, S.; Zhong, H.; Li, C.; Yang, Q. Tunable Assembly of Organosilica Hollow Nanospheres. *J. Phys. Chem. C* **2010**, *114* (2), 953–961. https://doi.org/10.1021/jp909931z.

(25) Ruckdeschel, P.; Philipp, A.; Retsch, M. Understanding Thermal Insulation in Porous, Particulate Materials. *Adv. Funct. Mater.* **2017**, *27* (38). https://doi.org/10.1002/adfm.201702256.

(26) Wittwer, V. Development of Aerogel Windows. *J. Non. Cryst. Solids* **1992**, *145* (C), 233–236. https://doi.org/10.1016/S0022-3093(05)80462-4.

(27) Kistler, S. S. Coherent Expanded Aerogels and Jellies. *Nature* **1931**, *127* (3211), 741–741. https://doi.org/10.1038/127741a0.

(28) Marszewski, M.; King, S. C.; Galy, T.; Kashanchi, G. N.; Dashti, A.; Yan, Y.; Li, M.; Butts, D. M.; McNeil, P. E.; Lan, E.; et al. Transparent Silica Aerogel Slabs Synthesized from Nanoparticle Colloidal Suspensions at near Ambient Conditions on Omniphobic Liquid Substrates. *J. Colloid Interface Sci.* **2021**. https://doi.org/10.1016/j.jcis.2021.07.159.

(29) Grudzien, R. M.; Grabicka, B. E.; Jaroniec, M. Effective Method for Removal of Polymeric Template from SBA-16 Silica Combining Extraction and Temperature-Controlled Calcination. *J. Mater. Chem.* **2006**, *16* (9), 819–823. https://doi.org/10.1039/b515975j.

(30) Fuji, M.; Takai, C. *Superior Thermal Insulation Film With Transparency Achieved by Hollow Silica Nanoparticles*; Elsevier B.V., 2018. https://doi.org/10.1016/B978-0-444-64110-6.00024-X.

(31) Skorokhod, V. V.; Get'man, O. I.; Zuev, A. E.; Rakitin, S. P. Correlation between the Particle Size, Pore Size, and Porous Structure of Sintered Tungsten. *Sov. Powder Metall. Met. Ceram.* **1988**, *27* (12), 941–947. https://doi.org/10.1007/BF00794554.

(32) Tan, H.; Liu, N. S.; He, B.; Wong, S. Y.; Chen, Z. K.; Li, X.; Wang, J. Facile Synthesis of Hybrid Silica Nanocapsules by Interfacial Templating Condensation and Their Application in Fluorescence Imaging. *Chem. Commun.* **2009**, No. 41, 6240–6242. https://doi.org/10.1039/b914366a.

(33) Hao, N.; Wang, H.; Webley, P. A.; Zhao, D. Synthesis of Uniform Periodic Mesoporous Organosilica Hollow Spheres with Large-Pore Size and Efficient Encapsulation Capacity for Toluene and the Large Biomolecule Bovine Serum Albumin. *Microporous Mesoporous Mater.* **2010**, *132* (3), 543–551. https://doi.org/10.1016/j.micromeso.2010.04.008.

(34) Manchanda, A. S.; Kruk, M. Synthesis of Xylylene-Bridged Periodic Mesoporous Organosilicas and Related Hollow Spherical Nanoparticles. *Langmuir* **2016**, *32* (3), 900–908. https://doi.org/10.1021/acs.langmuir.5b04284.

(35) Yang, B.; Guo, C.; Chen, S.; Junhe, M.; Wang, J.; Liang, X.; Zheng, L.; Liu, H. Effect of Acid on the Aggregation of Poly(Ethylene Oxide)-Poly(Propylene Oxide)-Poly(Ethylene

Oxide) Block Copolymers. *J. Phys. Chem. B* **2006**, *110* (46), 23068–23074. https://doi.org/10.1021/jp0634149.

(36) Brinker, C. . Hydrolysis and Condensation of Silicates. *J. Non-Crystalline Solid* **1988**, *100* (130), 31–50.

(37) Wu, G.; Chu, B. Light-Scattering Studies of a Block Poly(Oxyethylene-Oxypropylene-Oxyethylene) Copolymer in Water/o-Xylene Mixtures. *Macromolecules* **1994**, *27* (7), 1766–1773. https://doi.org/10.1021/ma00085a015.

(38) Manchanda, A. S.; Kruk, M. Synthesis of Large-Pore Face-Centered-Cubic Periodic Mesoporous Organosilicas with Unsaturated Bridging Groups. *Microporous Mesoporous Mater.* **2016**, *222*, 153–159. https://doi.org/10.1016/j.micromeso.2015.10.017.

(39) Dunphy, D. R.; Sheth, P. H.; Garcia, F. L.; Brinker, C. J. Enlarged Pore Size in Mesoporous Silica Films Templated by Pluronic F127: Use of Poloxamer Mixtures and Increased Template/SiO2 Ratios in Materials Synthesized by Evaporation-Induced Self-Assembly. *Chem. Mater.* **2015**, *27* (1), 75–84. https://doi.org/10.1021/cm5031624.

(40) Ivanova, R.; Lindman, B.; Alexandridis, P. Evolution in Structural Polymorphism of Pluronic F127 Poly(Ethylene Oxide)-Poly(Propylene Oxide) Block Copolymer in Ternary Systems with Water and Pharmaceutically Acceptable Organic Solvents: From `glycols' to `oils'. *Langmuir* **2000**, *16* (23), 9058–9069. https://doi.org/10.1021/la000373d.

CHAPTER 7

Using Small Angle X-ray Scattering to Examine the Gelling Mechanism in Silica Nanoparticle-based Monoliths

Introduction

In 2015, 51% of the total energy consumed by households in the United States was used to power heating, ventilation, and air conditioning systems.[1] It is therefore imperative that the insulation efficiencies of building materials be optimized for minimal energy loss to reduce energy consumption. While a number of materials exist that could adequately insulate roofs and walls, insulating windows has been challenging since any insulating coating needs to be optically transparent in addition to having low thermal conductivity. Silica aerogels are a leading candidate as a thermal insulating coating for window applications.[2] This is due to their ability to achieve porosities > 90% and thermal conductivities as low as 13 mW/mK.[3] However, most aerogel syntheses result in large pore sizes that scatter light (reducing transparency) and low material density that reduces their mechanical robustness.[4]

Silica aerogels are typically synthesized from molecular-based precursors. The silica precursors, often tetraalkoxysilanes or trialkoxylaklylsilanes, polymerize to form a gel network. This polymerization process occurs in three stages.[5] The monomers first hydrolyze and condense to form 2 - 4 nm short-chained oligomers. These oligomers then grow to form colloidal nanoparticles that aggregate into clusters that eventually span the length of the solution and form the gel network. The gel then ages and is strengthened as the crosslinking continues. Solution conditions such as pH, concentration of the reactants, and solvent type can affect the formation of the gel. Often the contributions of each condition cannot be fully separated since the overall gelling and aging process is not linear. As such, manipulating the gelation process to optimize the final aerogel structure can be difficult. Nevertheless, by using modified silica precursors, great strides have been made to produce gels with superior optical and mechanical properties.[6–9]

Marszewski *et. al*. previously used commercial silica nanoparticles as precursors to make xerogels and aerogels. In their first study, they aggregated the colloids to form a gel using an evaporation-driven approach on a liquid PFC substrate. The resulting xerogels had porosities between 46% and 56% and optical transparencies greater than 90% due to their small pores, with widths less than 10 nm. However, as a result of their low porosities, their thermal conductivities were high, at approximately 104 mW m^{-1} K^{-1}. In their second study, they reduced the pH of the colloidal solution to reduce the surface charge of the colloids. This resulted in aggregation of the colloids and facilitated quick gelation of the network. The solvent in the wet gel was then gradually exchanged to one with a lower surface tension (octane), and the gel was dried to form an aerogel monolith. The resulting nanoparticle-based aerogel had porosities from 70 % to 81 % with thermal conductivities as low as 80 mW m^{-1} K^{-1}. However, due to their large pores (between 14 and 26 nm) their optical transmittances were only as high as 83%. These materials were still not as porous as some aerogels made from molecular-based precursors and had higher thermal conductivities, and they were not as optically transparent as their predecessors that were made from the evaporation-driven approach. However, these two approaches (evaporation-driven vs solution-driven) to gelation of the particles and their resulting monoliths represent two extremes of mesoporous monolith preparation. In addition, since the colloids are formed before they aggregate to form monoliths, the aggregation process during gelling can be isolated from the hydrolysis and growth processes that occurs concurrently in aerogels made with molecular-based precursors. As such, the synthesis of these nanoparticle-based aerogels is a good model system for specifically understanding the colloidal aggregation process that leads to the gel network. This understanding can then be extended to molecular-based systems and used to optimize the optical transparency of the final aerogel.

By understanding the nanoparticle aggregation processes, the synthetic parameters can be optimized to prepare optically transparent, low thermal conductivity materials. This optimization is challenging, however, because the parameters needed to increase optical transparency work counter to those that are needed to reduce the thermal conductivity of porous materials. Specifically, thermal conductivity decreases with an increase in porosity, which is easily achieved by larger pores within the material; however, larger pores lower the transmittance of visible light as it increases volumetric and surface scattering in the visible regime.

As the heat conduction path length is determined by the silica backbone, not the size of the pores, the need to reduce pore size is driven by improving optical performance.[10] Two approaches to reduce the pore size while maintaining a high porosity are changing the aggregation mechanism of nanoparticles by fine-tuning solution conditions and using smaller nanoparticles (<12 nm) to prepare the monolithic slabs. Specifically, by changing the pH, and therefore the surface charge of the colloidal solution before casting the gel, the interactions between the repulsive double-layer and attractive dispersion forces that dictate the aggregation rate and mechanism of nanoparticles can be tuned.[11] Further, using smaller nanoparticles also decreases pore size because the pore size is directly related to nanoparticle size at a fixed porosity.[12]

Experimental

The pH of commercially available nanoparticle solutions (Nalco 2326, LiSol3 and LiSol 6) were adjusted to the desired value using HCl. Next, 8 mL of each solution was gently poured over perfluorocarbon (PFC) liquid in a cylindrical PTFE mold and placed in a 25 °C oven to gel and age. The water filled wet gel was then transferred to a jar with 50 mL of a 1:1 ethanol/water mixture for solvent exchange. After three hours, the solution was exchanged every three hours with (1) 50 mL of ethanol (three times), (2) 50 mL of 1:1 ethanol/heptane mixture, and (3) 50 mL of heptane (three times). The heptane filled gel was then placed in a container covered with plastic wrap to dry at ambient temperature and pressure.

Two-dimensional small-angle X-ray scattering (2D-SAXS) patterns were collected at the Stanford Synchrotron Radiation Lightsource using beamline 4-2 with an X-ray energy of 10 keV and detector distance of 2500 mm using Dectris Pilatus3 X 1M and Rayonix MX225HE detectors. The solutions were adjusted to the appropriate pH then quickly injected into quartz capillaries. The capillaries were placed in a multicapillary holder. The X-ray scattering data was measured using the multicapillary holder at 55 °C. The 2D-SAXS data was calibrated using silver behenate, then reduced using the SAXSPipe at the beamline. The reduced SAXS patterns were then fitted using the Unified fit macro in the Irena package[13] by applying three Guinier-Porod levels.[14–16]

Using the Unified Guinier-Porod model, the scattered intensity I(q) can be expressed as[14,17]

$$I(q) = Bc(q) + \sum_{i=1}^{N}\left[G_i exp\left(-\frac{q^2 R_{g_i}^2}{3}\right) + B_i exp\left(-\frac{q^2 R_{g_{i+1}}^2}{3}\right)\left(\frac{1}{q_i^*}\right)^{P_i}\right] S(q)_i \quad (7.1)$$

Here, Bc(q) is the background noise of the instrument, the index i refers to the scattering level, and B_i and G_i are intensity terms related to the Guinier and Porod regimes, respectively. In addition, P_i is the Porod exponent and $R_{g,i}$ is the radius of gyration of level i. The Porod exponent P_i varies

between 1 and 4 and is equal to the mass fractal dimension $D_{f,i}$ when $P_i \geq 3$. The radius of gyration $R_{g,i}$ represents the radius of the scatterers. It is defined as the mean-squared of the distances between the center of mass of the representative scatterers and the geometric center of each constitutive element (e.g., pores). The Unified Fit was used to obtain P_i, B_i, G_i, and $R_{g,i}$. Finally, since ambigels are not dilute systems, the data were corrected with a structure factor Si(q) to account for correlations in the system,[18,19] such that

$$S(q)_i = \frac{1}{1+p_i f(q\eta_i)}, \quad (7.2)$$

with

$$f(q\eta_i) = 3\frac{\sin(q\eta_i) - q\eta_i \cos(q\eta_i)}{q{\eta_i}^3}. \quad (7.3)$$

Here, p_i describes the degree of correlation ($0 \leq p_i \leq 5.92$) and is equal to 8 times the packing efficiency. A value of $p_i = 5.92$ is the maximum packing efficiency and is obtained from the packing efficiency of face-centered cubic (FCC) and hexagonal close packing (HCP) lattices. Finally, η_i represents the average center-to-surface distance between the scatterers such that $\eta_i > R_{g,i}$.

The R_g-cutoff parameter was applied to the second and third levels to treat all levels as representing one population of scatterers.[13] We were interested in four parameters from fitting the data. Namely a Porod exponent from the third level, D_3, and radius of gyration Rg_i for each Level i = 1, 2, 3. The diameters of the associated X-ray scatterers d_i was calculated assuming a dense-sphere shape according to

$$d_i = 2\sqrt{\frac{5}{3}}R_{gi} \quad (7.4)$$

Porosity and pore size distributions were obtained from N_2 porosimetry at 77 K using a Tristar 2020 equipment. Pieces of the monoliths were used. The solutions were degassed for at least 12 hours at 150 °C before each measurement.

TEM images of the solutions were obtained from a Technai G2 TF20 High-Resolution EM, CryoEM and CryoET (FEI) at an accelerating voltage 200 kV and a TIETZ F415MP 16 megapixel 4k×4k CCD detector. The TEM grids were prepared by dipping a carbon coated grid in an ethanolic resuspension of the nanoparticles.

Results

The small angle X-ray scattering pattern for the d = 6 nm sample at pH 6 after 1 hour of gelling at 55 °C is plotted on a log-log scale, is shown in Figure 7.1. There you can see the three distinct levels. Using the Unified fit, we obtain the Rg_i of each level, which allows us to hypothesize the structures that contribute to the scattering. From level 3, we retrieved an Rg_1 of 17 Å, an Rg_2 of 40 Å and an Rg_3 of 183 Å. If we assume that the networks are made up of dense, spherical particles, the diameters of the scatters (d_i) are calculated to be 4, 10 and 47 nm, for Levels 1, 2 and 3, respectively. These diameters suggest that Level 3 (pink) represents the cluster of particles in the gel network, Level 2 (blue) represents the

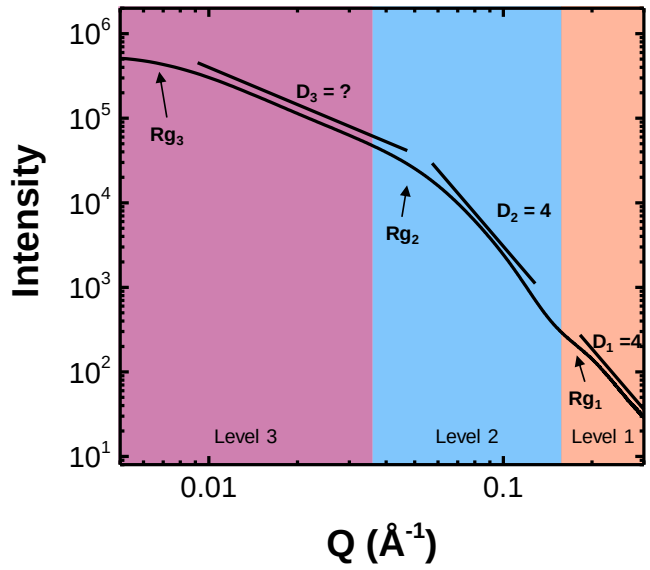

Figure 7.1. 1D-X-ray scattering data from a nanoparticle solution with diameter d = 6 nm. The pH of the solution was adjusted to 6 and the X-ray scattering data was obtained after 1 hour at 55 °C. The three clearly defined levels with the radii of gyration (Rg_i) and retrieved fractal dimensions (D_i = - slope) are clearly delineated by the orange (Level 1), blue (Level 2) and pink (Level 3) regions of the graph.

nanoparticles themselves and Level 1 (orange) is due to the hairy layer of oligomers that is often hypothesized to be anchored to the surface of the gel.[11] As the solutions gel, we expect to see changes in Level 3, as this level represents the hierarchical gel structure. As gelling occurs, the individual nanoparticles should generally aggregate to form larger clusters which would increase Rg_3. As the clusters then interact to form the gel network, the fractal dimension (D_3) should increase. A plateau in D_3 suggests that gelling in the network is complete, as no further crosslinking is occurring in the gel. The SAXS patterns of the solutions as they gel are analyzed to examine the effects of pHs, concentration, and particles sizes on the gelling mechanism.

The effect of pH:

By changing the pH, the nanoparticle surface charge can be systematically tuned. This change in surface change dictates the aggregation mechanism and thus the pore size. When the pH decreases, the charge on the colloids decreases as well. This facilitates gelation of the colloids. The time-dependent SAXS patterns of the colloidal solutions of the d = 6 nm particles with their pHs adjusted to 6, 7, 8 and 9 before the experiment are shown in Figures 7.2 (a) to 7.2 (d). Examination of this data reveals that the solutions at pH 6 and 7 show a clear increase in the Level 3 component while the solutions held at pH 8 and 9 show some Level 3 component that may be too large and therefore beyond the limit of the detector. Specifically, the sample gelled at pH 8 shows a gradual rise in the Level 3 q-range, but the rise is slow and that region is not quantifiable. The sample gelled at pH 9, however, shows no significant change in final structure for the duration of the experiment (8 hours). These observations suggest that by increasing pH, the aggregation of the gels shifts from solution driven to evaporation driven. The Unified fit was applied to the data and the results for Rg_1, Rg_2, Rg_3, and D_3 of the solution after being adjusted to pH 6, 7 and 8, and

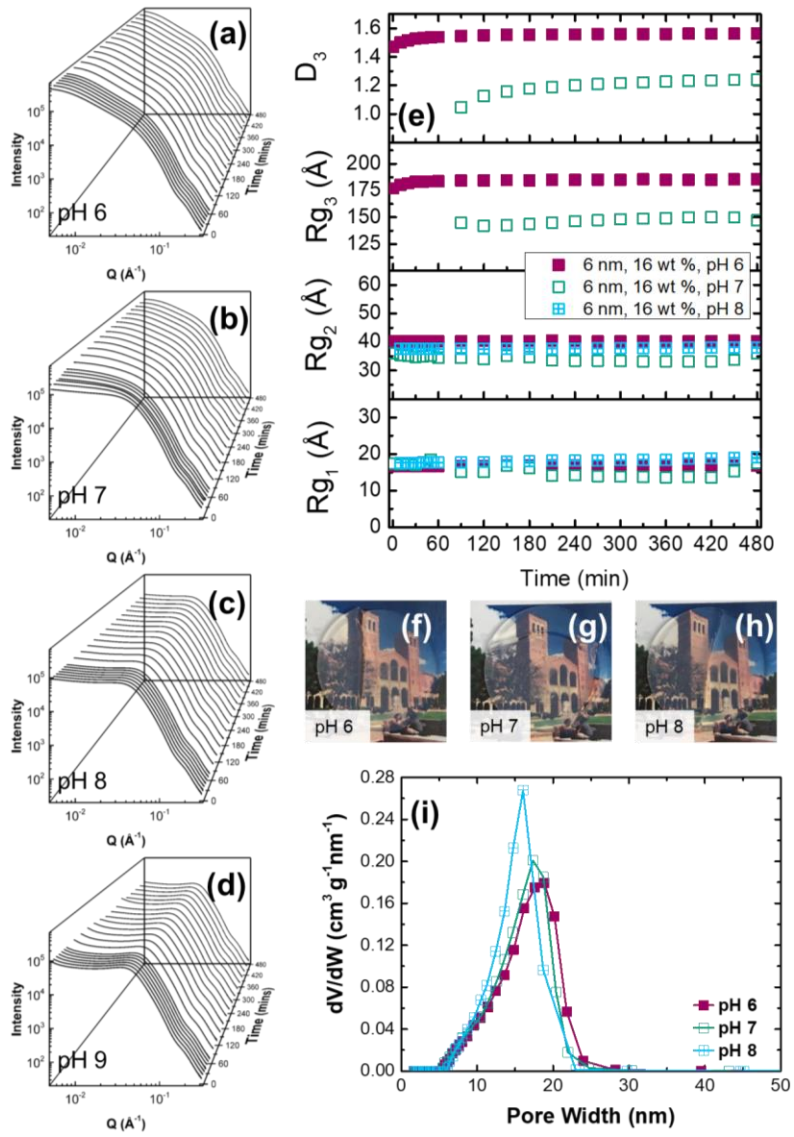

Figure 7.2. Structural characterization of solutions gelled from the 6 nm silica nanoparticle solution gelled at different pHs. (a) - (d) Time-resolved X-ray scattering patterns of samples gelled at pH 6 (a), 7 (b), 8 (c) and 9 (d). (e) Fitting parameters for Rg_1, Rg_2, Rg_3 and D_3 obtained from the Unified fit to the SAXS data from Figure 7.2(a)- (c). (f) – (h) Photographs of the mesoporous monoliths made from nanoparticle solution studied and gelled at pH 6 (f), 7 (g) and 8 (h). (i) Pore size distributions from N_2 porosimetry at 77 K of the monoliths pictured in Figure 7.2(f) – (h).

the results are plotted in Figure 7.2(e). Since Level 3 at pH 8 was not clearly defined, there is no Rg_3 or D_3 data for this sample. In addition, the Rg_3 and D_3 of the pH 7 sample could not be resolved at t < 60 minutes and was also not included. From Rg_1 and Rg_2 we see that the size of the oligomer layer and the nanoparticles are, within error, approximately the same for each sample, as was expected. Examination of R_{g3} and D_3 for the solutions at pH 6 and 7 show a gradual rise and eventual plateau in both Rg_3 and D_3.

The time to gel (marked by the plateau in D_3) increased as the pH of the solution was increased. This increase was expected, since at higher pH there is a greater surface

charge density on the particles and therefore greater repulsion and less attraction between the particles. In addition to the difference in plateau times, the values of Rg_3 and D_3 at the plateaus also increased as pH is decreased. Specifically, the sample at pH 6 had a final Rg_3 of ~ 180 Å and and D_3 of ~ 1.5, while the sample at pH 7 had a final Rg_3 of ~ 140 Å and a D_3 of ~ 1.2. The decrease in Rg_3 can lead to smaller pore sizes when the gels are eventually dried which can increase optical quality of the gels. Examination of the pore size of the gels in Figure 7.2(i) show that, like predicted from the wet gels, the peak pore widths increase as the pH decreases. When we look at photos of monoliths made at the different pH's then dried (Figures 7.2(f) – 7.2(h)), we observe an increase in optical clarity of the monoliths as the pH increases. However, increasing the pH does lead to cracking of the gels. The shift in gelling mechanism from solution driven to a more evaporation driven-approach by adjusting the pH of the solution results in gels with better optical properties without compromising porosity.

The effect of concentration:

We increased the concentration of the d = 6 nm solution from 16 wt % to 24 % and 32 wt% by rotary evaporation then examined the change in their structures as the solutions gelled at pH 6. From the data retrieved from the Unified fit in Figure 7.3(d), we see that Rg_1 are all approximately the same values, as are the Rg_2. Since all measurements were conducted on solutions made from the same batch, and at the same pH, the similarities in Rg_1 and Rg_2 were expected. However, the values diverge in Rg_3, suggesting a difference in the final gel structure. Examination of Level 3 shows that the Rg_3 of the samples from the 24 and 32 wt% concentration solutions plateau immediately, while a gradual increase in Rg_3 is seen in the most dilute sample (16 wt%). However, there is a gradual increase in D_3 for all samples. This suggests that the 24 and 32 wt% samples formed clusters immediately, which were then gradually connected to form the gel network, while

aggregation occurred more slowly in the 16 wt% solution. When the solution is more concentrated, there is an increase in the number of particles per unit volume. This increases the attractive forces exerted on each particle and would therefore facilitate aggregation more readily, as was observed. In addition, as the concentration increases, the size of Rg_3 decreases. This decrease in Rg_3 is most likely because there is less space for the nanoparticles to occupy in the more concentrated gels. When we examine D_3, we see no trend with concentration. Strangely the 24% solution has the highest D. These observations are all corroborated by the time-resolved X-ray scattering data in Figures 7.3(a) – 7.3(c). The effect of concentration on the pore structure is shown in Figures 7.3(e) and 7.3(f) obtained from porosimetry of dried monoliths (not pictured). When concentration is increased, the peak pore diameter decreases, as does the porosity and the full width at 5% of the peak pore diameter (FW5%M). The FW5%M is an indication of the tail in the pore size distribution and its decrease suggests that there are less large pores present in the more concentrated solutions. This would reduce volumetric light scattering and would result in more transparent gels as the concentration increases. However, increasing concentration also decreases the porosity of the monoliths.

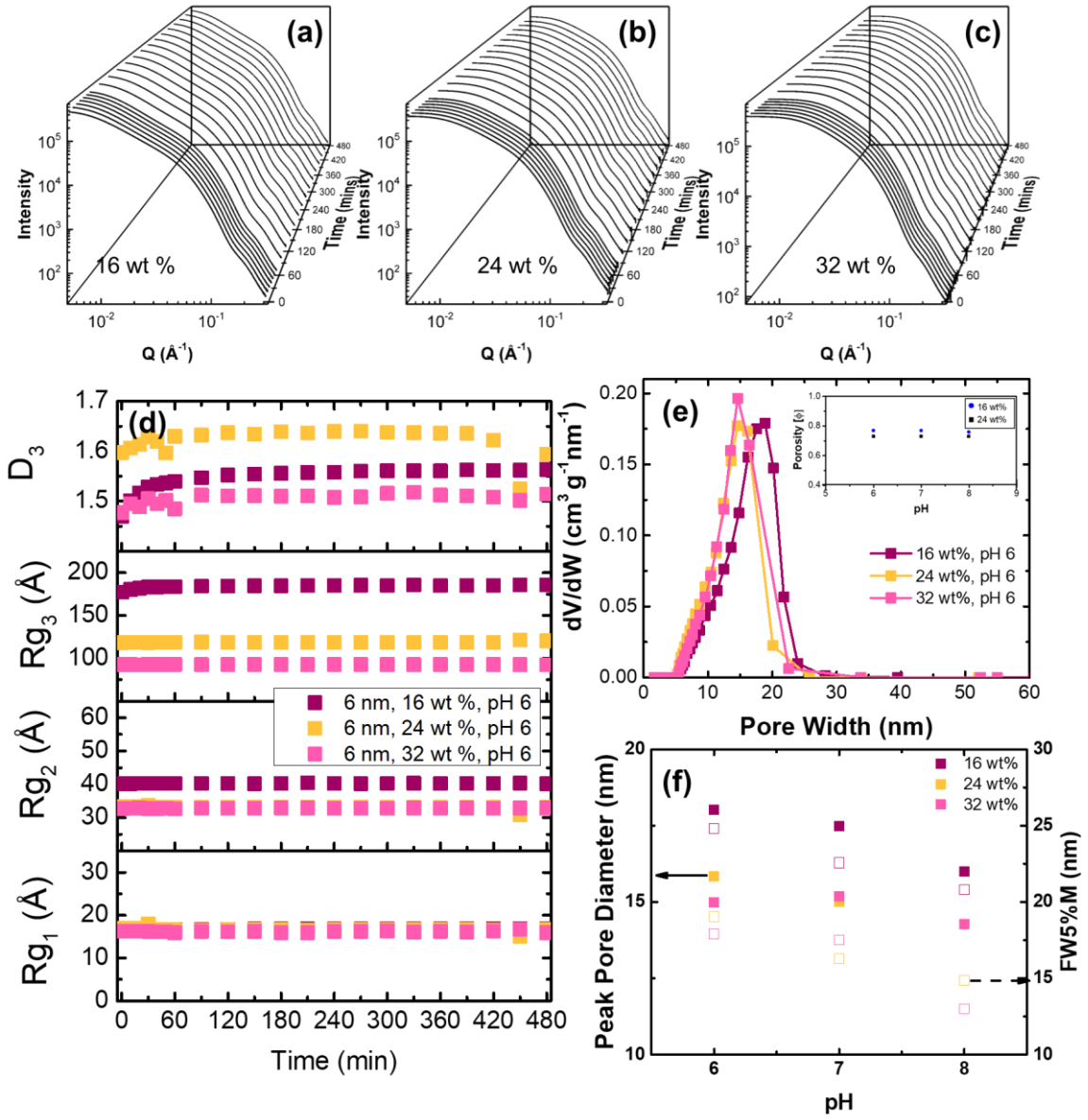

Figure 7.3. Structural characterization of different concentrations of the d = 6 nm silica nanoparticle solution. The pH of all solutions were adjusted to 6 before the measurement. (a) - (c) Time-resolved X-ray scattering patterns of solutions with nanoparticle concentrations of 16 wt% (a), 24 wt% (b), and 32 wt% (c). (d) Fitting parameters for Rg_1, Rg_2, Rg_3 and D_3 obtained from the Unified fit to the SAXS data from Figure 7.3 (a)- (c). (e) Pore size distributions, with porosities inset, from N_2 porosimetry at 77 K of monoliths made from solutions of concentrations 16, 24 and 32 wt% of 6 nm silica nanoparticles. (f) Peak pore diameter and Full width at 5% of the maximum peak pore diameter (FW5%M) of the monoliths made from solutions of concentrations 16, 24 and 32 wt% of 6 nm silica nanoparticles.

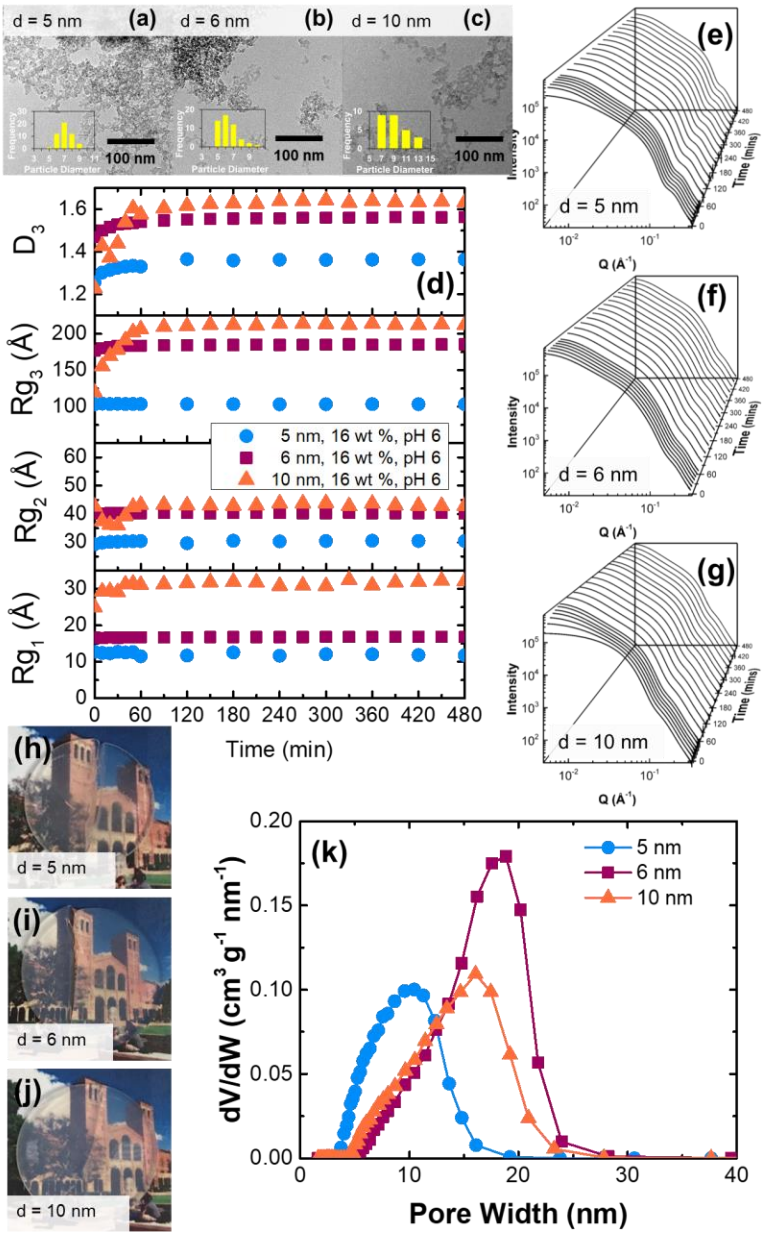

Figure 7.4. Structural characterization of 16 wt% solutions of nanoparticles with different diameters. The pH of all solutions was adjusted to 6 before the measurement. (a) - (c) Transmission electron microscopy (TEM) images with measured distribution of diameters inset for the d = 5 (a). 6 (b) and 10 nm (c) nanoparticle solutions studied. (d) Fitting parameters for Rg_1, Rg_2, Rg_3 and D_3 obtained from the Unified fit to the SAXS data from solutions (a)- (c) and time resolved SAXS patterns in (e) – (g). Time-resolved X-ray scattering patterns of solutions with nanoparticle diameters of 5 (e), 6 (f), and 10 nm (g). (h) – (j) Photographs of the mesoporous monoliths made from 16 wt% nanoparticle solutions from nanoparticles with diameters 5 (h), 6 (i) and 10 nm (j). (k) Pore size distributions from N_2 porosimetry at 77 K of monoliths photographed in (h) – (j) made from 16 wt% nanoparticle solutions from nanoparticles with diameters 5, 6 and 10 nm.

The effect of particle size:

The TEM images of the three particles used for this study are given in Figures 7.4(a) – 7.4(c). The data retrieved from the Unified fit of the time-dependent gelling experiments of nanoparticles with measured TEM sizes of 5, 6 and 9 nm are shown in Figure 7.4(d). From the radii of gyration, we see that Rg_1, Rg_2 and Rg_3 all increased with particle diameters. The increase in Rg_1 and Rg_2, which are related to the size of the coating on the nanoparticle and the size of the nanoparticles, respectively, were expected. The increase in Rg_3 with particles is twofold. Since the gels that make up Rg_3 are made up of particles with different sizes, it is no surprise that the Rg_3 increases with particle diameter. However, the differences in the Rg_3 are more than afforded to us by merely changing particle size, suggesting that size of the pores also changes with changing particle size. More specifically, the pore size increases as particle size increases, confirming that the size of particles can ultimately influence the size of the pores. The plots of the time-dependent scattering data shown in Figures 7.4(e) to 7.4(g) show the difference in the SAXS patterns of the different nanoparticles.

Table 7.1. Structural characterization of monoliths from solutions of different nanoparticle sizes, obtained from TEM and N_2 porosimetry.

Solution	TEM particle diameter (nm)	Specific surface area (m^2/g)	Porosity (%)	Peak pore width (nm)
10	10 ± 3	380	74	16.4
6	6 ± 1	460	79	18.4
5	5 ± 1	510	70	11.2

Monoliths made from the nanoparticle solutions are shown in Figures 7.4(h) to 7.4(j). Their pore size distributions are shown in Figure 7.4(k), and the structural information retrieved from TEM and porosimetry are listed in Table 1. The pore size distribution of these slabs in Figure 7.4(k) does not follow the expected trends since the peak pore diameter of the 6 nm sample is greater

than that of the 10 nm samples. This difference is most likely due to the differences in porosity, where the porosity of the 6 nm sample was a greater than the 10 nm sample. This abnormal difference in porosities and pore sizes may stem from the difference in the way these solutions undergo processing and eventual drying.

Conclusions

Overall, we were able to use SAXS as a tool to study the effects of pH, concentration, and particle size on the gelling of nanoparticle solutions. We found that increasing the pH of the solution decreases the pore size but also increases the time for the gels to form. We also found that we can reduce pore size by concentrating the gels or by using smaller nanoparticles. This work clearly outlines the complexity of retaining high optical transparencies at higher porosities.

References

(1) U.S. Energy Information Administration. Table CE3.1 Annual Household Site End-use Consumption in the U.S. — Totals and Averages, 2015. **2018**, No. May, 18–23.

(2) Berardi, U. The Benefits of Using Aerogel-Enhanced Systems in Building Retrofits. *Energy Procedia* **2017**, *134*, 626–635.

(3) Hüsing, N.; Schubert, U. Aerogels - Airy Materials: Chemistry, Structure, and Properties. *Angew. Chemie - Int. Ed.* **1998**, *37*, 22–45.

(4) Shimizu, T.; Kanamori, K.; Maeno, A.; Kaji, H.; Doherty, C. M.; Falcaro, P.; Nakanishi, K. Transparent , Highly Insulating Polyethyl- and Polyvinylsilsesquioxane Aerogels : Mechanical Improvements by Vulcanization for Ambient Pressure Drying. *Chem. Mater.* **2016**, *28*, 6860–6868.

(5) R. K. Iler. *The Chemistry of Silica*; Wiley: New York, 1979.

(6) Butts, D. M.; McNeil, P. E.; Marszewski, M.; Lan, E.; Galy, T.; Li, M.; Kang, J. S.; Ashby, D.; King, S.; Tolbert, S. H.; Hu, Y.; Pilon, L.; Dunn, B. S. Engineering Mesoporous Silica for Superior Optical and Thermal Properties. *MRS Energy Sustain.* **2020**, *7*, 1–12.

(7) Shimizu, T.; Kanamori, K.; Maeno, A.; Kaji, H.; Doherty, C. M.; Falcaro, P.; Nakanishi, K. Transparent, Highly Insulating Polyethyl- and Polyvinylsilsesquioxane Aerogels: Mechanical Improvements by Vulcanization for Ambient Pressure Drying. *Chem. Mater.* **2016**, *28*, 6860–6868.

(8) Du, Y.; Zhang, X.; Wang, J.; Liu, Z.; Zhang, K.; Ji, X.; You, Y.; Zhang, X. Reaction-Spun Transparent Silica Aerogel Fibers. *ACS Nano* **2020**, *14*, 11919–11928.

(9) Zu, G.; Kanamori, K.; Shimizu, T.; Zhu, Y.; Maeno, A.; Kaji, H.; Nakanishi, K.; Shen, J. Versatile Double-Cross-Linking Approach to Transparent, Machinable, Supercompressible, Highly Bendable Aerogel Thermal Superinsulators. *Chem. Mater.* **2018**, *30*, 2759–2770.

(10) Yan, Y.; Li, M.; King, S. C.; Galy, T.; Marszewski, M.; Kang, J. S.; Pilon, L.; Hu, Y.; Tolbert, S. H. Controlling Thermal Conductivity in Mesoporous Silica Films Using Pore Size and Nanoscale Architecture. *J. Phys. Chem. Lett. Submitt.*

(11) Kobayashi, M.; Juillerat, F.; Galletto, P.; Bowen, P.; Borkovec, M. Aggregation and Charging of Colloidal Silica Particles: Effect of Particle Size. *Langmuir* **2005**, *21*, 5761–5769.

(12) Skorokhod, V. V.; Get'man, O. I.; Zuev, A. E.; Rakitin, S. P. Correlation between the Particle Size, Pore Size, and Porous Structure of Sintered Tungsten. *Sov. Powder Metall.*

Met. Ceram. **1988**, *27*, 941–947.

(13) Ilavsky, J.; Jemian, P. R. Irena: Tool Suite for Modeling and Analysis of Small-Angle Scattering. *J. Appl. Crystallogr.* **2009**, *42*, 347–353.

(14) Beaucage, G. Small-Angle Scattering from Polymeric Mass Fractals of Arbitrary Mass-Fractal Dimension. *J. Appl. Cryst.* **1996**, *29*, 134–146.

(15) Beaucage, G.; Ulibarri, T. A.; Black, E. P.; Schaefer, D. W. Multiple Size Scale Structures in Silica—Siloxane Composites Studied by Small-Angle Scattering. 1995, pp 97–111.

(16) Beaucage, G.; Rane, S.; Sukumaran, S.; Satkowski, M. M.; Schechtman, L. A.; Doi, Y. Persistence Length of Isotactic Poly(Hydroxy Butyrate). *Macromolecules* **1997**, *30*, 4158–4162.

(17) Beaucage, G. Approximations Leading to a Unified Exponential/Power-Law Approach to Small-Angle Scattering. *J. Appl. Crystallogr.* **1995**, *28*, 717–728.

(18) Beaucage, G.; Ulibarri, T. A.; Black, E. P.; Schaefer, D. W. Multiple Size Scale Structures in Silica—Siloxane Composites Studied by Small-Angle Scattering. **1995**, 97–111.

(19) Mcglasson, A.; Rishi, K.; Beaucage, G.; Chauby, M.; Kuppa, V.; Ilavsky, J.; Rackaitis, M. Quantification of Dispersion for Weakly and Strongly Correlated Nanofillers in Polymer Nanocomposites. *Macromolecules* **2020**, *53*, 2235–2248.

CHAPTER 8

Using Small Angle X-ray Scattering to Examine the Drying Mechanism in Molecular-based Silica Aerogels

As a mesoporous gel dries, the structure shrinks to its final form as the solvent is removed and pores gradually empty. Excessive shrinkage leads to cracking of the monoliths, while the rate at which the pores empty can systematically influence the final size of the pores. In this chapter, we conducted *in situ*, SAXS studies of the gels as they dried at different air flow rates to understand the change in mesoscale structure. We found that as the gel dries, the structure changes to accommodate the loss of solvent and found that there may be a critical window of time that needs to be precisely tuned in order to influence the final optical properties of the gels.

Introduction

Silica aerogels are highly porous (> 90% porosity) materials with high specific surface areas (500 -1200 $m^2 g^{-1}$) and are used in applications such as thermal management since they have ultra-low thermal conductivities (< 0.05 W $m^{-1}K^{-1}$).[1–4]

Mesoporous monoliths like aerogels can be synthesized from molecular sol-gel precursors, that hydrolyze and condense to form the silica network,[5] or pre-formed silica colloids,[6] where the controlled aggregation of the colloidal precursors result in a gel network. The wet gels, filled with alcohol or water as the solvent, are aged to strengthen the silica network, then dried. The final porosity of the dried gels hinges greatly on the drying process. If the gels are dried ambiently, from the alcoholic or aqueous they were synthesized in, they significantly shrink and the porosity of the dried gel is low (≤50%). These dried monoliths are referred to as xerogels and this shrinkage is due to the high capillary pressure exerted on the gel as the high surface tension alcohol or water solvent evaporates. This process can also result in significant cracking in the final material unless the gels are dried very slowly. To counteract this shrinkage, a solvent exchange step is added

between aging and drying. During solvent exchange, the solvent in the gel is gradually replaced by another solvent with low surface tension that would exert less capillary stress on the gel as the solvent is removed. The shrinkage during drying is then minimized, and high porosity gels, with little to no cracking, referred to as aerogels are formed.

Classical aerogels are produced via super critical drying.[1] There, the solvent of the wet gels is exchanged to a supercritical fluid that has almost no surface tension and therefore exerts little to no capillary forces on the gel is as it leaves. In an essence, the pores are frozen in place and the resulting porosity is very high. However, supercritical drying is costly, relatively dangerous and not readily scalable. In addition, the large pores of aerogels result in significant optical scattering so they cannot be used in applications, such as window insulation, that require high transparency.[7,8] As such, there is ongoing research to produce aerogels in conditions that do not require super critical drying to reduce the cost of production as well as to tune the pore size.[2,3,9–11]

As an alternative to super critical drying, gels with porosities greater than xerogels, can be formed when the alcohol or aqueous solvent in the pores is replaced with a lower surface tension solvent such as octane and heptane before drying at ambient conditions.[12] These gels are often referred to as ambigels since they are ambiently dried. Further work has found that when the wet gels are treated with hydrophobic silane coatings during the solvent exchange process, all reactive hydroxide groups are removed and any further crosslinking of the silica gels as they dry is reduced. This increases the porosity of the material even further. This reduction in crosslinking is known as the spring back effect.[11,13] The ambient drying process can be more readily integrated in to manufacturing processes if it was faster. By studying the change in the mesoscale structure of the gels during this process, we can attempt to speed up the drying process by introducing air flow

during drying, and maximize the production of crack free gels with additional favorable properties, such as high porosity and small pore size.

Scherer documented the drying process in mesoporous materials and have broken it down to two parts.[14] In the constant rate period, solvent evaporates from the surface of the gel. The gel shrinks uniformly as the solvent is removed. When the gel can no longer shrink, the falling rate period begins. During the falling rate period, air infiltrates the solvent-filled pores and the solvent is evaporated from in the porous monolith. In mesoporous material, the onset of the falling rate period is marked by an optical transition from the transparent wet gel to a cloudy gel which then becomes transparent or translucent when the gel is fully dry.

In this work we will use small angel X-ray scattering (SAXS) to study the changes in the gel structure as it dries with or without a constant flow of air. SAXS is a powerful tool that can be used to study these mesoporous materials. From the diffuse X-ray scattering data, we can retrieve any changes to the radius of gyration (which related to the size of the scatterers – pore size) and the fractal dimension of the network (which is related to the how cross linked the network is) as the gel dries. Our goal is to compare change in nanostructure that occur during drying with different air streams, as quantified by SAXS, to the final pore sizes obtained when the gels are dried, either with or without the assistance of constant stream to decrease the drying time.

Experimental

Synthesis of silica gels: Silica ambigels were synthesized as previously described.[2] In brief, 6.3 mL MTES, 10.5 mL TEOS, 14 mL ethanol, 7.5 mL formamide and a mixture of 4.25 mL water were first combined with 180 μL of concentrated hydrochloric acid in a fume hood. The solution was stirred for an hour at room temperature, then 15.7 mL of 2 M NH_4OH was added. The stirring was continued for about 1 minute, then the mixture was quickly transferred to a polystyrene mold

before it gelled. The mold was sealed with tape and the gel was heat treated for 4 hours at 55 °C before starting the solvent exchange process. The liquid in the pores was exchanged from the ethanol-water mixture to pure heptane. The gels were treated with 2% TMCS in the penultimate heptane exchange step to increase the porosity of the gel.

SAXS measurement and modeling: The fast evaporation rate of ambigels dried from heptane and the shorter drying time made it possible to investigate the changes to the nanometer scale structure in the ambigels during drying using in-situ Small Angle X-ray Scattering (in-situ SAXS) measurements. The intensity I(q) scattered by the drying ambigels was collected at the Stanford Synchrotron Lightsource (SSRL) using beamline 1-5 with a wavelength of 0.1033 nm operated at an X-ray energy of 12.002 keV. The ambigels were placed in a custom-made environmental chamber that allowed for air flow to dry the monoliths in a shorter time frame than in stagnant air. The sample-to-detector distance was approximately 3 m and a SX-165 CCD detector was used (Rayonix, L.L.C., Evanston, IL). The in-situ SAXS data was calibrated using silver behenate and reduced using the Nika package from Igor Pro (WaveMetrics, Inc., Portland, OR).[15] The reduced data was modeled with a Unified Guinier-Porod model using the Unified Fit Macro of the Irena package from Igor Pro[16] since it is adapted to model disordered structures and it can easily combine the scattering from multiple levels.

For most materials, the typical X-ray scattering pattern of disordered structures such as the synthesized mesoporous monoliths consists of two distinct regimes, namely (i) a Guinier regime at low scattering wavevector q, which has a knee-like feature, and (ii) a Porod regime at high q. The scattering wavevector q (in $Å^{-1}$) can be defined as $q = \frac{4\pi sin(\theta)}{\lambda}$, where θ is the scattering angle. Using the Unified Guinier-Porod model, the scattered intensity I(q) can be expressed as[17,18]

$$I(q) = Bc(q) + \sum_{i=1}^{N}\left[G_i exp\left(-\frac{q^2R_{g_i}^2}{3}\right) + B_i exp\left(-\frac{q^2R_{g_{i+1}}^2}{3}\right)\left(\frac{1}{q_i^*}\right)^{P_i}\right]S(q)_i \qquad (8.1)$$

Here, Bc(q) is the background noise of the instrument, the index i refers to the scattering level, and B_i and G_i are intensity terms related to the Guinier and Porod regimes, respectively. In addition, P_i is the Porod exponent and $R_{g,i}$ is the radius of gyration of level i. The Porod exponent P_i varies between 1 and 4 and is equal to the mass fractal dimension $D_{f,i}$ when $P_i \geq 3$. The radius of gyration $R_{g,i}$ represents the radius of the scatterers. It is defined as the mean-squared of the distances between the center of mass of the representative scatterers and the geometric center of each constitutive element (e.g., pores). The Unified Fit was used to obtain P_i, B_i, G_i, and $R_{g,i}$. Finally, since ambigels are not dilute systems, the data were corrected with a structure factor Si(q) to account for correlations in the system,[19,20] such that

$$S(q)_i = \frac{1}{1+p_i f(q\eta_i)}, \qquad (8.2)$$

with

$$f(q\eta_i) = 3\frac{\sin(q\eta_i) - q\eta_i\cos(q\eta_i)}{q{\eta_i}^3}. \qquad (8.3)$$

Here, p_i describes the degree of correlation ($0 \leq p_i \leq 5.92$) and is equal to 8 times the packing efficiency. A value of p_i = 5.92 is the maximum packing efficiency and is obtained from the packing efficiency of face-centered cubic (FCC) and hexagonal close packing (HCP) lattices. Moreover, η_i represents the average center-to-surface distance between the scatterers such that $\eta_i > R_{g,i}$.

Optical measurements:

The normal-hemispherical transmittance ($T_{nh,\lambda}$) of the mesoporous silica monoliths was measured at each time interval with a double-beam UV-Vis spectrophotometer (Shimadzu 3101-PC, Kyoto, Japan) and an integrating sphere with an internal diameter of 60 mm (Shimadzu ISR 3100). The reference signal (B_λ) and the normal-hemispherical transmitted signal ($S_{nh,\lambda}$) through the sample were measured under collimated and normally incident radiation and corrected for the dark signal D_λ to yield the sample normal-hemispherical transmittance given by

$$T_{nh,\lambda} = \frac{S_{nh,\lambda} - D_\lambda}{B_\lambda - D_\lambda} \tag{8.4}$$

The dark signal D_λ was collected when no light entered the integrating sphere. The reference signal B_λ was measured in the same configuration as for $S_{nh,\lambda}$ but without sample. Note that for the measurements of drying silica ambigels, the samples were in a Petri dish to slow the drying process and to prevent cracking. Therefore, to estimate the normal-hemispherical transmittance $T_{nh,\lambda}$ and haze h_λ of silica the ambigels, the signals B_λ and M_λ were measured with an empty Petri dish in front of the integrating sphere's port to account for its transmittance and reflectance. The visible transmittance T_{vis} were calculated by weighting the spectral normal-hemispherical transmittance

$T_{nh,\lambda}$ by the photopic spectral luminous efficiency function V_λ of the human eye in daytime between wavelength of 380 and 780 nm,[21,22] i.e.,

$$T_{vis} = \frac{\int_{380}^{780} V_\lambda T_{nh,\lambda}\, d\lambda}{\int_{380}^{780} V_\lambda\, d\lambda} \tag{8.5}$$

Here, V_λ was tabulated in Ref. [21].

The pore size distribution was obtained from N_2 adsorption porosimetry at 77 K using a Micrometrics Tristar II 3020 on the dried monolith. Before each measurement, the samples were degassed under vacuum for at least 12 hours at 120 °C to remove all water from the pores.

Results and Discussion

The effect of drying on the structure of the ambigel: Small-Angle X-ray Scattering (SAXS) measurements were conducted on ambigels as they dried to examine any change to the nanostructure during drying.

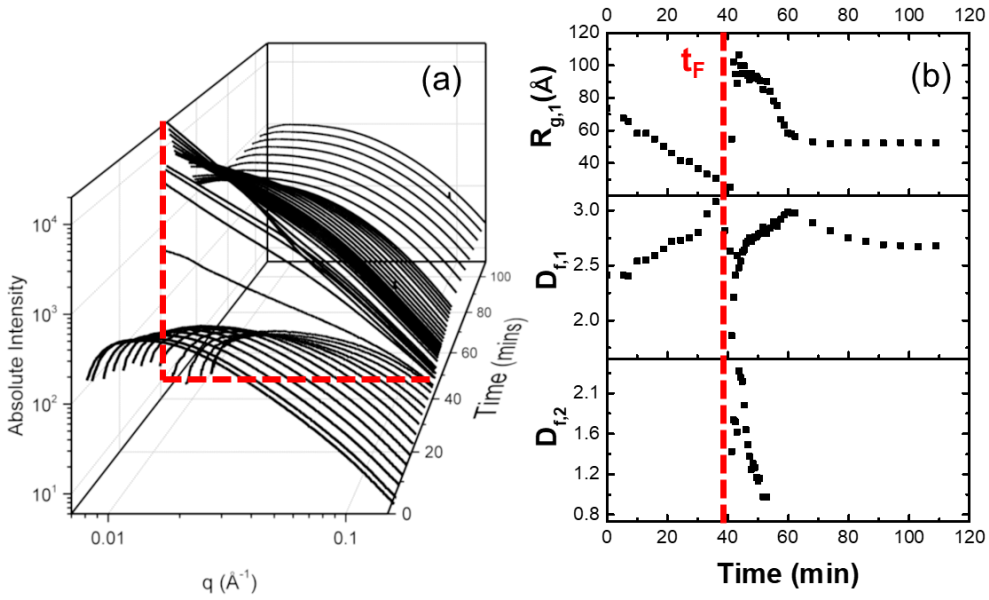

Figure 8.1. *In-situ* Small Angle X-ray Scattering (SAXS) patterns of an ambigel monolith drying in a nitrogen flow of 0.5 scfh. (b)-(d) Changes in radius of gyration $R_{g,1}$ and fractal dimensions $D_{f,1}$ and $D_{f,2}$ retrieved from SAXS patterns as a function of time.

Figure 8.1(a) presents the time dependent SAXS patterns of an ambigel drying in a nitrogen flow with a volumetric flow rate of 0.5 standard cubic feet per hour (scfh). The scattered intensity I(q) is based on the difference in X-ray scattering length densities of the solvent and silica network, and the size and volume of the scatterers[23]. Figure 8.1(a) shows that the SAXS pattern of the ambigel changed over time, indicating structural changes at the nanoscale as the ambigel dried. At t = 0, the SAXS pattern displays a Guinier region, when $q \leq 0.3$ Å^{-1} with a knee-like feature that can be modeled to give the radius of gyration that characterizes the change in size of the scatterers. The scattering pattern also features a Porod region when $q \geq 0.3$ Å^{-1}, which can be modeled to give the fractal dimension of the network characterizing the change in cross linking. The gradual changes in the scattered intensity I(q) in the first 40 min of the drying and then the abrupt change at t = 40 minutes indicate that the transition between the constant rate and falling rate periods. During the constant rate period, the intensity of the scattering pattern I(q) decreased as a result of the reduced volume of scatterers as heptane evaporated from the network and the ambigel shrank.

The changes in the nanostructure at the onset of the falling rate period (t_F = 40 min) is marked by a change in the scattering profiles of the network. For $t \geq t_F$ the scattered intensity I(q) dramatically increases and shape of the scattering pattern also changes radically. The changes in the scattering pattern results from the formation of a second scattering level that occurs dominantly at $q < 0.2$ Å^{-1}. This new level can be attributed to the formation and growth of dry domains with large sizes. Only the Porod region of this new level is observed since the domains are sufficiently large that most of the scattering is beyond the detector limit at very low angle. As a result, the radius of gyration, $R_{g,2}$, of the second level of scattering corresponding to the dry domains could not be retrieved from the SAXS patterns. In the region 40 min < t < 55 min, we are thus able to fit 3 parameters: the radius of gyration, $R_{g,1}$, and fractal dimension, $D_{f,1}$, of the first level of scattering

corresponding to the network scatterers, and the fractal dimension of the dry domains, $D_{f,2}$ (Figure 8.1(b)) When t > 55 min, the scattering from the second level disappeared, as shown by the return of the typical Guinier-Porod shape to the scattering curves. As expected, the intensity of the final curve (t = 110 min) is larger than the intensity of the initial SAXS pattern (at t = 0) due to the increase scattering contrast between air and the silica network compared to heptane and silica.[24]

The changes observed in the scattered intensity I(q) were analyzed using the Unified Fit to determine the radius of gyration $R_{g,1}$ and the fractal dimension $D_{f,1}$ of the network, and the fractal dimension $D_{f,2}$ of the second scattering level, plotted in Figures 8.1(b). Figure 8.1(b) shows that during the constant rate period, the radius of gyration $R_{g,1}$ of the network decreased, although the size of the silica particles forming the solid framework likely remained unchanged or grew slightly. This change in $R_{g,1}$ is therefore attributed to drying induced shrinkage of the pores. Interestingly, the radius of gyration $R_{g,1}$ = 24 Å at the end of this initial drying period when t = 40 min, is smaller than that at the end of the drying process, i.e., $R_{g,1}$ = 53 Å when t = 110 min. This can be attributed to the so-called “spring back effect" that occurring in organosilane gels, like the ambigels studied here.[25] The pores size decreases during drying, but because the network cannot crosslink into that compressed configuration, it expands back once the capillary forces associated with drying are removed. During the falling rate period, $R_{g,1}$ increases and then gradually decreased as a result of the incorporation of air pockets into the network. The primary X-ray scatterers consist of three phases with distinct X-ray contrast: air, heptane, and silica. $R_{g,1}$ is larger than expected from 40 to 60 minutes because small air pockets with sizes overlapping the silica pores are mixed into the level 1 fits in during this time period. After approximately 60 minutes, the value of $R_{g,1}$ again becomes constant, indicating that the structure has fully transitioned from a heptane-air-silica network to an air-silica network. Note that, to the best of our knowledge, the individual

contribution of silica in this three-phase system cannot be accurately separated from that of heptane and air unless there is some contrast variation as is done with Anomalous SAXS (ASAXS) or Small-Angle Neutron Scattering (SANS).[26,27] Finally, we note that the ending value of $R_{g,1}$ = 53 Å is smaller than its initial value of 80 Å, as expected, since the network shrank during the constant rate period.

Figure 8.1(b) further indicates that the fractal dimension of the network $D_{f,1}$ increases during the initial drying period as the network became less swollen and more clustered as the gel shrinks. During the falling rate period, the fractal dimension first plummeted to a value of 1.9 before gradually increasing to approximately 3, and then slowly decreasing until it leveled off around 2.7. We hypothesize that the initial low value $D_{f,1}$ = 1.9 at the onset of the falling rate period is due to the scatterers changing to worm-like domains of empty pores as the solvent leaves the network. The fractal dimension $D_{f,1}$ then slowly increases as more solvent is removed and the network changed from a heptane-air-silica to an air-silica network with only residual heptane in the pores. As more heptane evaporated from the structure, the fractal dimension decreased until it plateaued around 2.7 representing the final dry ambigel.

The bottom panel of Figure 8.1(b) shows the changes in the fractal dimension $D_{f,2}$ of the second scattering level that appeared after 40 min at low q that we believe corresponded to the wet and dry domains. In the first 20 min of the falling rate period (40 min < t > 60 min), this fractal dimension $D_{f,2}$ rapidly increases from 1.5 to 2.3, changes which may or may not have meaning due to the highly inhomogeneous distribution of scatterers as air pockets begin to form. Once the air pockets are established, however, the value of $D_{f,2}$ gradually decreases from 2.3 to 1 and then disappears. These observations suggest that the dry domains start as isolated nearly spherical pockets that merge as they grow until they encompass the entire monolith.

Comparing SAXS results to optical transitions during drying: Figure 8.2(a) compares the radius of gyration $R_{g,1}$ retrieved from the SAXS patterns of a drying ambigel [Figure 8.1(b)] with the visible transmittance T_{vis} of a similar ambigel. Optical images of a typical ambigel are also shown in Figure 8.2(b) Note that the final drying time of these silica amibgels are difficult to determine accurately as the final drying stages involve only removal of surface bound solvent. As such, the time was normalized by the time t_F corresponding to the transition from the constant to the falling rate period. Figure 8.2(a) indicates that the radius of gyration $R_{g,1}$ reached its maximum when the visible transmittance T_{vis} reached its minimum around $t/t_F = 1.1$.

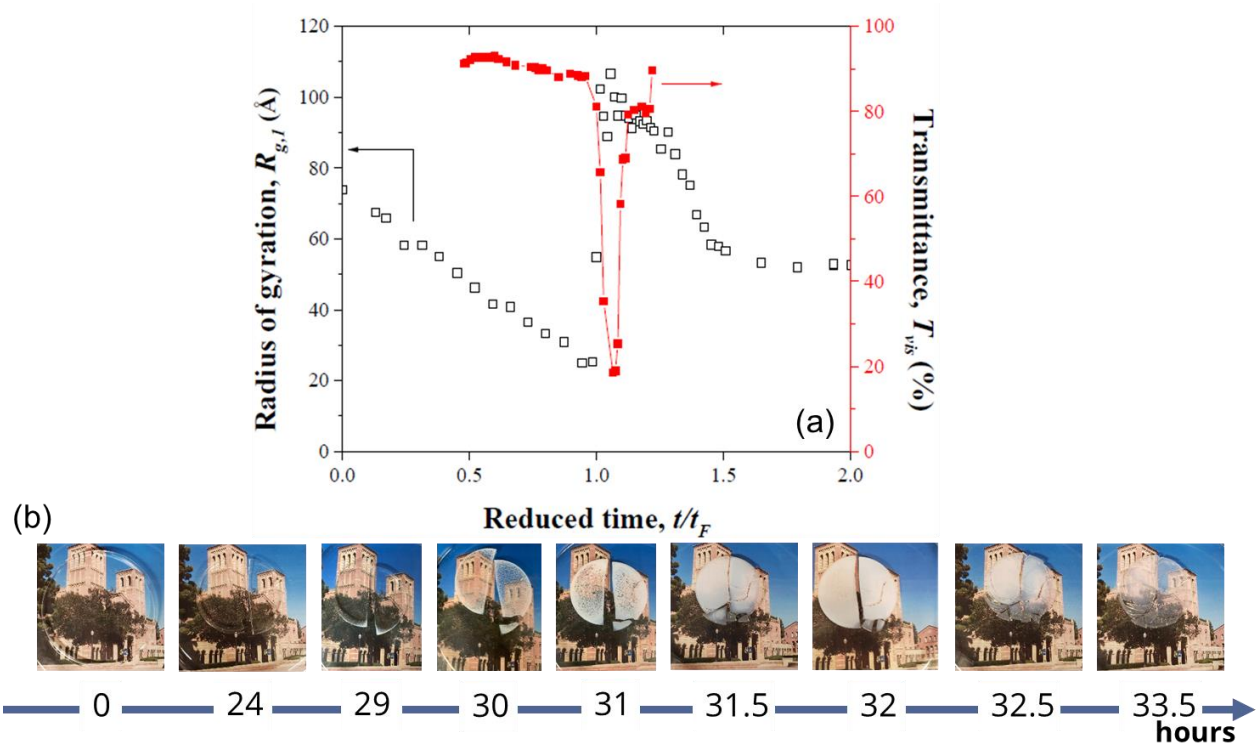

Figure 8.2. Radius of gyration $R_{g,1}$ and visible transmittance T_{vis} of drying ambigels as functions of the reduced time t/t_F.

Examining the effect of flow rate on the drying process and final pore size of the ambigels: Finally, as depicted in Figure 8.3. we compared the $R_{g,1}$ of two ambigel samples dried at different flow rates, the first at 0.25 LPM and the second dried without additional air flow at 0 LPM.

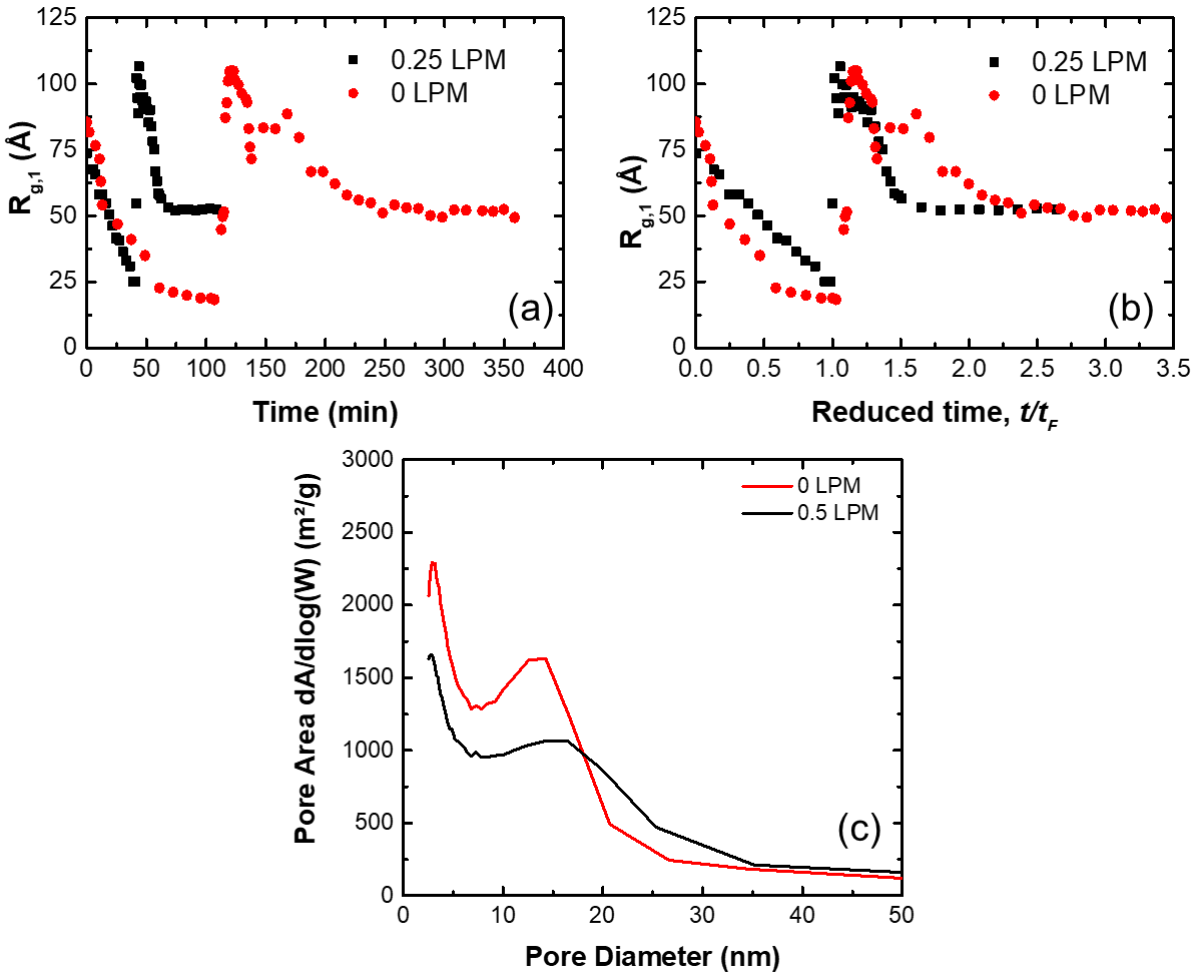

Figure 8.3. Influence of air flow rate on the structural evolution of ambigels. The change in $R_{g,1}$ of two ambigels dried at different rates on an absolute (a) and relative (b) time scales. (c) The pore size distributions of ambigels dried at two air flow rates.

When we compare values of $R_{g,1}$ on an absolute time scale, as depicted in Figure 8.3(a), we see that the samples undergo the same ubiquitous transitions in size that indicate the shifts from constant-rate period to falling-rate period and the eventual plateau as residual water evaporates from the network. However, the sample dried slowly at 0 LPM took a longer time to complete this series of transitions, as expected. To better examine the influence of flow rate on the nanostructure, we examined any changes to $R_{g,1}$ on a reduced time scale as shown in Figure 8.3(b) Examination of these samples on the normalized scale reveals that while the general trends are the same with and without airflow, the structural changes during the initial falling rate period are not identical. Most of the pore shrinkage occurs in the first 50 minutes in real time, which corresponds to a reduced time of $t/t_F = 1$ in the sample dried at 0.25 LPM and approximately $t/t_F = 0.5$ in the sample that was dried ambiently. It is presumed that the time scale for shrinkage is set by the condensation time of the ambigel combined with the heptane evaporation, and the fact that the ambiently dried sample than had significant time to sit at this most compressed size may have allowed the decreased pore size to become locked against spring-back through increase condensation.

This change may account for the subtle differences in pore size distribution depicted in Figure 8.3(c) for a pair of samples, one of which was dried ambiently and one at 0.5 LPM (the flow rate used in our current scale up efforts). The broader distribution in the 0.5 LPM sample may result from a lack of sufficient time in the constant-rate period to prevent spring-back of some of the larger pores. Understanding this mechanism can allow us to leverage different air flows at different points in the drying process to optimize the final pore size of the gel and ultimately the optical transmittance of the final ambigel. Future work in this regard would involve examining the effect of other static flow rates, as well as any influence of varying the flow rate during the drying process on the pore size of the final ambigel.

Conclusions

This work uses small angle X-ray scattering to examine the change in nanostructure as a mesoporous silica gel is dried. We observe signature changes to the X-ray scattering pattern when the gel undergoes transitions from constant rate period to falling rate period. When we compared two gels dried at different air flow rate, we found that there may be a window of time in the falling rate period that influences the final pore size of the gels.

References

(1) Kistler, S. S. Coherent Expanded Aerogels and Jellies. *Nature* **1931**, *127*, 741–741.

(2) Butts, D. M.; McNeil, P. E.; Marszewski, M.; Lan, E.; Galy, T.; Li, M.; Kang, J. S.; Ashby, D.; King, S.; Tolbert, S. H.; Hu, Y.; Pilon, L.; Dunn, B. S. Engineering Mesoporous Silica for Superior Optical and Thermal Properties. *MRS Energy Sustain.* **2020**, *7*, 1–12.

(3) Zu, G.; Shimizu, T.; Kanamori, K.; Zhu, Y.; Maeno, A.; Kaji, H.; Shen, J.; Nakanishi, K. Transparent, Superflexible Doubly Cross-Linked Polyvinylpolymethylsiloxane Aerogel Superinsulators via Ambient Pressure Drying. *ACS Nano* **2018**, *12*, 521–532.

(4) Hrubesh, L. W.; Pekala, R. W. Thermal Properties of Organic and Inorganic Aerogels. *J. Mater. Res.* **1994**, *9*, 731–738.

(5) Brinker, C. . Hydrolysis and Condensation of Silicates. *J. Non-Crystalline Solid* **1988**, *100*, 31–50.

(6) Marszewski, M.; King, S. C.; Yan, Y.; Galy, T.; Li, M.; Dashti, A.; Butts, D. M.; Kang, J. S.; Mcneil, P. E.; Lan, E.; Dunn, B.; Hu, Y.; Tolbert, S. H.; Pilon, L. Thick Transparent Nanoparticle-Based Mesoporous Silica Monolithic 2 Slabs for Thermally Insulating Window Materials. *Appl. Nanomater.* **2019**, *2*, 4547–4555.

(7) Shimizu, T.; Kanamori, K.; Maeno, A.; Kaji, H.; Doherty, C. M.; Falcaro, P.; Nakanishi, K. Transparent , Highly Insulating Polyethyl- and Polyvinylsilsesquioxane Aerogels : Mechanical Improvements by Vulcanization for Ambient Pressure Drying. *Chem. Mater.* **2016**, *28*, 6860–6868.

(8) Rubin, M.; Lampert, C. M. Transparent Silica Aerogels for Window Insulation. *Sol. Energy Mater.* **1983**, *7*, 393–400.

(9) Wei, T.; Chang, T.-F.; Lu, S.; Chang, Y. Preparation of Monolithic Silica Aerogel of Low Thermal Conductivity by Ambient Pressure Drying. *J. Am. Ceram. Soc.* **2007**, *90*, 2003–2007.

(10) Shimizu, T.; Kanamori, K.; Maeno, A.; Kaji, H.; Doherty, C. M.; Falcaro, P.; Nakanishi, K. Transparent, Highly Insulating Polyethyl- and Polyvinylsilsesquioxane Aerogels: Mechanical Improvements by Vulcanization for Ambient Pressure Drying. *Chem. Mater.* **2016**, *28*, 6860–6868.

(11) Lee, C. J.; Kim, G. S.; Hyun, S. H. Synthesis of Silica Aerogels from Waterglass via New Modified Ambient Drying. *J. Mater. Sci.* **2002**, *37*, 2237–2241.

(12) Harreld, J. H.; Dong, W.; Dunn, B. Ambient Pressure Synthesis of Aerogel-like Vanadium Oxide and Molybdenum Oxide. *Mater. Res. Bull.* **1998**, *33*, 561–567.

(13) Burger, T.; Fricke, J. Aerogels: Production, Modification and Applications. *Berichte der Bunsengesellschaft für Phys. Chemie* **1998**, *102*, 1523–1528.

(14) Scherer, G. W. Theory of Drying. *J. Am. Ceram. Soc.* **1990**, *73*, 3–14.

(15) Ilavsky, J. Nika: Software for Two-Dimensional Data Reduction. *J. Appl. Crystallogr.* **2012**, *45*, 324–328.

(16) Ilavsky, J.; Jemian, P. R. Irena: Tool Suite for Modeling and Analysis of Small-Angle

Scattering. *J. Appl. Crystallogr.* **2009**, *42*, 347–353.

(17) Beaucage, G. Approximations Leading to a Unified Exponential/Power-Law Approach to Small-Angle Scattering. *J. Appl. Crystallogr.* **1995**, *28*, 717–728.

(18) Beaucage, G. Small-Angle Scattering from Polymeric Mass Fractals of Arbitrary Mass-Fractal Dimension. *J. Appl. Cryst.* **1996**, *29*, 134–146.

(19) Beaucage, G.; Ulibarri, T. A.; Black, E. P.; Schaefer, D. W. Multiple Size Scale Structures in Silica—Siloxane Composites Studied by Small-Angle Scattering. **1995**, 97–111.

(20) Mcglasson, A.; Rishi, K.; Beaucage, G.; Chauby, M.; Kuppa, V.; Ilavsky, J.; Rackaitis, M. Quantification of Dispersion for Weakly and Strongly Correlated Nanofillers in Polymer Nanocomposites. *Macromolecules* **2020**, *53*, 2235–2248.

(21) Hunt, R. W. G. *The Reproduction of Colour*; John Wiley & Sons, Ltd: Tolworth, UK, 2004.

(22) Council, N. F. R. *Test Method for Determining the Solar Optical Properties of Glazing Materials and Systems*; 2013.

(23) Boldon, L.; Laliberte, F.; Liu, L. Review of the Fundamental Theories behind Small Angle X-Ray Scattering, Molecular Dynamics Simulations, and Relevant Integrated Application. *Nano Rev.* **2015**, *6*, 25661.

(24) Sarachan, K. L.; Curtis, J. E.; Krueger, S. Small-Angle Scattering Contrast Calculator for Protein and Nucleic Acid Complexes in Solution. *J. Appl. Crystallogr.* **2013**, *46*, 1889–1893.

(25) Hwang, S. W.; Jung, H. H.; Hyun, S. H.; Ahn, Y. S. Effective Preparation of Crack-Free Silica Aerogels via Ambient Drying. *J. Sol-Gel Sci. Technol.* **2007**, *41*, 139–146.

(26) Pedersen, J. S.; Hamley, I. W.; Ryu, C. Y.; Lodge, T. P. Contrast Variation Small-Angle

Neutron Scattering Study of the Structure of Block Copolymer Micelles in a Slightly Selective Solvent at Semidilute Concentrations. *Macromolecules* **2000**, *33*, 542–550.

(27) Goerigk, G.; Haubold, H. G.; Lyon, O.; Simon, J. P. Anomalous Small-Angle X-Ray Scattering in Materials Science. *J. Appl. Crystallogr.* **2003**, *36*, 425–429.

APPENDIX A

Supporting Information for Chapter 2:

Exploring the Effect of Porous Structure on Thermal Conductivity in Templated Mesoporous Silica Films

Table S1: Porosity, Surface Area and Specific Heat Capacity of F127 and P123 Templated Sol-Gel and Nanoparticle-Based Mesoporous Silica Powders

Sample	Surfactant	Building block	Porosity‡	Surface Area‡, S_{BET}, (m^2/g)	Specific heat capacity, c_p (J/g K)
P1*	Non-templated	Sol-gel	N/A	N/A	0.75
P2*	F127	Sol-gel	N/A	N/A	0.71
P3	F127	Sol-gel	0.33	354	0.74
P4	P123	Sol-gel	0.54	479	0.79
P5	Non-templated	NP	0.44	345	0.77
P6	F127	NP	0.49	210	0.71
P7	F127	NP	0.57	398	0.72
P7	F127	NP	0.70	402	0.71

‡Measured using a Micromeritics TriStar II 3020 porosimeter at 77 K using N_2 as the adsorbate. The surface area was then deduced from the adsorption branch of the isotherm at low relative pressures using the Brunauer-Emmett-Teller (BET) model. The porosity was calculated using the total pore volume obtained from the adsorption branch at $P/P_o = 1$.

* Samples' surface area too low to measure using N_2 porosimetry

Table S2: Porosity, Film Thickness and Thermal Conductivity of F127 and P123 Templated Sol-Gel and Nanoparticle-Based Mesoporous Silica Films

Sample No.	Surfactant	Building block	Porosity	Thermal conductivity, vac. (W/mK)
F1	F127	Sol-gel	0.69 ± 0.01	0.106 ± 0.007
F2	F127	Sol-gel	0.62 ± 0.01	0.096 ± 0.009
F3	F127	Sol-gel	0.61 ± 0.01	0.14 ± 0.01
F4	F127	Sol-gel	0.57 ± 0.01	0.133 ± 0.007
F5	F127	Sol-gel	0.49 ± 0.01	0.19 ± 0.02
F6	F127	Sol-gel	0.46 ± 0.01	0.26 ± 0.02
F7	F127	Sol-gel	0.44 ± 0.01	0.24 ± 0.01
F8	F127	Sol-gel	0.40 ± 0.01	0.24 ± 0.01
F9	F127	Sol-gel	0.35 ± 0.02	0.24 ± 0.01
F10	F127	Sol-gel	0.25 ± 0.02	0.31 ± 0.02
F11	F127	Sol-gel	0.20 ± 0.02	0.37 ± 0.02
F12	F127	Sol-gel	0.19 ± 0.02	0.41 ± 0.02
F13	F127	Sol-gel	0.10 ± 0.02	0.52 ± 0.03
F14	F127	Sol-gel	0.10 ± 0.02	0.71 ± 0.04
F15	P123	Sol-gel	0.59 ± 0.01	0.081 ± 0.007
F16	P123	Sol-gel	0.55 ± 0.01	0.123 ± 0.007
F17	P123	Sol-gel	0.50 ± 0.01	0.165 ± 0.009
F18	P123	Sol-gel	0.43 ± 0.01	0.16 ± 0.01
F19	P123	Sol-gel	0.37 ± 0.02	0.18 ± 0.02
F20	P123	Sol-gel	0.3 ± 0.02	0.22 ± 0.01
F21	P123	Sol-gel	0.18 ± 0.02	0.40 ± 0.03
F22	P123	Sol-gel	0.17 ± 0.02	0.61 ± 0.04
F23	P123	Sol-gel	0.16 ± 0.02	0.52 ± 0.03
F24	P123	Sol-gel	0.15 ± 0.02	0.61 ± 0.03
F25	F127	NP	0.69 ± 0.01	0.083 ± 0.005
F26	F127	NP	0.68 ± 0.01	0.111 ± 0.006
F27	F127	NP	0.67 ± 0.01	0.149 ± 0.009
F28	F127	NP	0.66 ± 0.01	0.097 ± 0.006
F29	F127	NP	0.63 ± 0.01	0.115 ± 0.006
F31	F127	NP	0.63 ± 0.01	0.083 ± 0.005
F32	F127	NP	0.57 ± 0.01	0.152 ± 0.008
F33	F127	NP	0.56 ± 0.01	0.19 ± 0.01
F34	F127	NP	0.53 ± 0.01	0.20 ± 0.01
F35	F127	NP	0.43 ± 0.01	0.23 ± 0.01
F36	F127	NP	0.43 ± 0.01	0.31 ± 0.02
F37	F127	NP	0.41 ± 0.01	0.21 ± 0.01
F38	F127	NP	0.41 ± 0.01	0.27 ± 0.01

F39	F127	NP	0.40 ± 0.01	0.33 ± 0.02
F40	F127	NP	0.38 ± 0.02	0.34 ± 0.02
F42	F127	NP	0.37 ± 0.02	0.25 ± 0.02
F43	F127	NP	0.35 ± 0.02	0.29 ± 0.02
F44	F127	NP	0.35 ± 0.02	0.32 ± 0.02
F45	F127	NP	0.34 ± 0.02	0.32 ± 0.02
F46	F127	NP	0.33 ± 0.02	0.31 ± 0.02
F47	P123	NP	0.63 ± 0.01	0.093 ± 0.006
F48	P123	NP	0.62 ± 0.01	0.106 ± 0.008
F49	P123	NP	0.60 ± 0.01	0.102 ± 0.007
F50	P123	NP	0.59 ± 0.01	0.126 ± 0.009
F51	P123	NP	0.56 ± 0.01	0.115 ± 0.007
F52	P123	NP	0.55 ± 0.01	0.115 ± 0.006
F53	P123	NP	0.55 ± 0.01	0.104 ± 0.006
F54	P123	NP	0.51 ± 0.01	0.22 ± 0.01
F55	P123	NP	0.45 ± 0.01	0.19 ± 0.01
F56	P123	NP	0.44 ± 0.01	0.31 ± 0.02
F57	P123	NP	0.44 ± 0.01	0.25 ± 0.01
F58	P123	NP	0.42 ± 0.01	0.28 ± 0.01
F59	P123	NP	0.41 ± 0.01	0.30 ± 0.02
F60	P123	NP	0.39 ± 0.01	0.28 ± 0.02
F61	P123	NP	0.38 ± 0.02	0.23 ± 0.01
F62	P123	NP	0.37 ± 0.02	0.29 ± 0.02
F63	P123	NP	0.36 ± 0.02	0.37 ± 0.02
F64	P123	NP	0.35 ± 0.02	0.33 ± 0.02

APPENDIX B

Supporting information for Chapter 3:

Controlling Thermal Conductivity in Mesoporous Silica Films Using Pore Size and Nanoscale Architecture

Experimental methods

1. Materials

The following materials were obtained from commercial suppliers and used without further purification: colloidal suspension of silica nanoparticles (15 wt%, Nalco 2326, ammonia-stabilized colloidal silica, d = 5 nm, Nalco Chemical Company), triblock copolymer Pluronic P123 ($EO_{20}PO_{70}EO_{20}$, M_w = 5800 Da, BASF), triblock copolymer Pluronic F127 ($EO_{100}PO_{65}EO_{100}$, M_w = 12600 Da, BASF), hexadecyltrimethylammonium bromide (CTAB, M_w=364.5 g/mol, Sigma-Aldrich), Brij®C10 ($C_{16}H_{33}(OCH_2CH_2)_nOH$, n~10, M_w=683 g/mol, Sigma-Aldrich), poly-(ethylene oxide-b-butylene oxide) (PBO-PEO, M_n=11000 g/mol, EO/BO = 6:5, PDI = 1.1, Advanced Polymer Inc), tetraethyl orthosilicate (98%, Acros Organics), hydrochloric acid (Certified ACS Plus, Fisher Scientific), ethanol (200 proof, Rossville Gold Shield), Ammonium persulfate (98%, Alfa Aesar), ammonium lauryl sulfate (~30% in H_2O, Sigma Aldrich), methyl methacrylate (contains ≤30 ppm MEHQ as inhibitor, 99%, Sigma Aldrich).

2. Synthesis

Synthesis of poly(methyl methacrylate) (PMMA) colloidal templates

The method is adapted from previous literature.[1,2] Ammonium persulfate (APS) was used as the initiator and ammonium lauryl sulfate (ALS) as the surfactant. APS, ALS and deionized water

were put into a three-neck round-bottom flask (250 mL) equipped with a magnetic stirrer, reflux condenser and thermometer. After the temperature was increased to 75 °C, the monomer methyl methacrylate was added in a differential manner (continuous addition in very small drops) using a syringe pump for about 1 h. Afterwards, the reaction temperature was kept at 80–85 °C for an additional hour before a cooling operation was applied. The concentration of reagents is varied to make different sizes of PMMA. For the 70 nm PMMA, syringe pump is not used. Table 1 gives the detailed synthesis condition.

Table S1: synthesis condition for PMMA colloids of different sizes

Average PMMA colloid size	APS	ALS	MMA	Water
10 nm	0.08 g	7 mL	14 mL	84 mL
20 nm	0.08 g	2.29 mL	14 mL	84 mL
35 nm	0.08 g	2.29 mL	14 mL	22.5 mL
70 nm	0.08 g	0.61 mL	12.56 mL	165 mL

Synthesis of nanoparticle-based mesoporous silica films

First, a stock solution of polymer was made by dissolving 0.678 g of Pluronic F127 in 3 mL deionized water. In the case of films templated with PMMA, the as-synthesized colloidal solutions were used without further purification. The stock polymer solution was mixed with the colloidal suspension of silica nanoparticles to produce a solution with polymer-to-silica mass ratio between 1 and 1.5 g/g. Then, 80 μL of the polymer-silica solution was spin-coated onto 1” × 1” Si substrates. The film’s thickness was adjusted by controlling the spin speed. The dried films were calcined in air at 350 °C for 30 min using 2 °C/min temperature ramp to remove the polymer.

Nanoparticle-based silica powder was also synthesized from the same solutions for heat capacity measurements. Instead of spin-coating, the solutions were evaporated in a Petri dish at ambient condition for a day and collected in powdered form after calcination at 350 ℃ for 3 hours in oxygen. The longer calcination time for the powders was necessary to remove all the polymer template from the micron sized grains. Since the calcination was done at such a low temperature, it is assumed that there was no significant difference in the silica structure of the films and the powders.

Synthesis of sol-gel based mesoporous silica films

The sol-gel synthesis was adapted from previous literature.[3] First, 25 mg of the desired surfactant was dissolved in 0.6 mL of ethanol and 0.16 mL of 0.05 M HCl. A certain amount of tetraethyl orthosilicate (TEOS) was added to the mixture to achieve a polymer-to-SiO_2 mass ratio between 0.3 and 2 g/g. Then, 80 μL of the polymer-silica solution was spin-coated onto 1" × 1" Si substrates. The film's thickness was adjusted by controlling the spin speed. The dried films were calcined in air at 350 °C for 30 min using 2 °C/min temperature ramp to remove the polymer.

3. Structural characterization

Scanning Electron Microscopy (SEM) images were obtained using a model JEOL JSM-6700F field emission electron microscope with 5 kV accelerating voltage and secondary electron detector configuration. Transmission Electron Microscopy (TEM) images were obtained using a Technai G^2 TF20 High-Resolution EM, CryoEM and CryoET (FEI) at an accelerating voltage 200 kV and a TIETZ F415MP 16 megapixel 4k×4k CCD detector. The TEM grids were prepared by scraping the film from its substrate and sonicating the obtained material in ethanol before deposition onto TEM grids.

Ellipsometric porosimetry was performed on a PS-1100 instrument from Semilab using toluene as the adsorbate at room temperature to quantify porosity and pore size. The instrument used a UV-visible CCD detector adapted to a grating spectrograph to analyze the signal reflected by the sample. The light source was a 75 W Hamamatsu Xenon lamp and the measurements were performed in the spectral range from 1.25–4.5 eV. Data analysis was performed using the associated Spectroscopic Ellipsometry Analyzer software with the assumption of cylindrical pores. An optical reflectance-based method was also used to verify porosity. The experimental spectral normal-hemispherical reflectance $R_{exp,\lambda}$ was measured with a Shimadzu UV3101 PC UV-VIS spectrophotometer, equipped with a Shimadzu ISR3000 integrating sphere. The reference intensity was measured using a high specular reflection standard mirror by Ocean Optics (NIST certified STAN-SSH). The reflectance was measured in the visible range between 400 nm to 800 nm every nm. The porosity (ϕ) was then evaluated using a Maxwell-Garnett model using the refractive index $(n_{c,\lambda})$ retrieved from the reflectance measurement. The uncertainty of the retrieved porosity $(\Delta\phi)$ was evaluated using the equation:

$$\Delta\phi = \sqrt{\left(\frac{\partial\phi}{\partial n_{eff,\lambda}}\Delta n_{eff,\lambda}\right)^2 + \left(\frac{\partial\phi}{\partial n_{c,\lambda}}\Delta n_{c,\lambda}\right)^2} \quad (1)$$

Where the uncertainty of the refractive index of silica $(\Delta n_{c,\lambda})$ was calculated to be twice the standard deviation of $n_{c,\lambda}$ given by the Sellmeier formula over the 400-800 nm wavelength range.[4] This was found to be $(\Delta n_{c,\lambda})$ = 0.009 for all mesoporous silica films. The uncertainty, $\Delta n_{eff,\lambda}$, associated with the retrieved $n_{eff,\lambda}$ was found to be 0.003 for mesoporous silica films. Here, $\Delta n_{eff,\lambda}$ is defined as the average absolute difference between the refractive index used to predict

the ideal spectral normal-hemispherical reflectance and the refractive index retrieved from the noisy normal-hemispherical reflectance.

Nitrogen porosimetry was carried out using a Micromeritics TriStar II 3020 porosimeter. The surface area was then deduced from the adsorption branch of the isotherm at low relative pressures using the Brunauer-Emmett-Teller (BET) model. The pore diameter and pore volume were also derived from the adsorption branch of the isotherm using the Barret-Joyner-Halenda (BJH) model.

Two-dimensional grazing incidence small-angle x-ray scattering (2D-GISAXS) data were collected at the Stanford Synchrotron Lightsource (SSRL) using beamlines 1-5 with a wavelength of 0.1033 nm operated at an X-Ray energy of 12.002 keV and detector distance of 2.870 m using a Rayonix-165 CCD detector. The data was then calibrated with silver behenate and reduced, baselined and the peaks were fit using the Nika package from Igor Pro.[5] The inter-plane spacing (d) between the repeating unit cells was calculated using the equation

$$d = \frac{2\pi}{q}, \qquad (2)$$

where q is the X-ray scattering vector.

The wall thickness (w) was then found from the inter-plane spacing (d) and radius of the pores (r) using the equation:

$$w = 2 \times \left(\frac{d}{\sqrt{3}} - r\right). \qquad (3)$$

The absolute error in w, (Δw) was found using the equation:

$$\Delta w = \sqrt{\Delta d^2 + \Delta r^2}. \qquad (4)$$

Here, Δd and Δr were quantified as the standard deviation of the peak centers, which were fitted to Voigt and Gaussian functions respectively.

4. Thermal conductivity measurements

The thermal conductivity measurements on mesoporous silica films were performed using time-domain thermoreflectance (TDTR) method. The detailed working principles and our experimental setup can be found elsewhere.[6–8] Briefly speaking, a thin aluminum film (80 nm) was deposited by e-beam evaporation on the top surface of the samples, serving as both transducer to convert laser energy to thermal energy and temperature sensor. The absorbed energy from pump beam with wavelength of 400 nm led to an instantaneous temperature rise. The probe beam with wavelength of 800 nm was used to continuously detect temperature decay by measuring the reflection portion using a photo diode. The delay time between pump pulse and probe pulse can be controlled with temporal resolution higher than sub-picosecond. Next, the full transient decay curve from -100 ps to 5000 ps was fitted with thermal diffusion model to obtain the thermal effusivity of the sample, which can be related to the thermal conductivity, κ, using the volumetric heat capacity. To avoid the difference of local thermal conductivity induced by random network of silica, big laser spot size with diameter of 20 μm was used to average the structure effects during measurement. To ensure the uniformity of the sample as well as the reliability of the thermal conductivity data, measurements were repeated at ten different locations on a 1 cm × 1 cm area of the sample. Samples were dehydrated by heating on a hot plate at 150 °C for more than 12 hours. The dehydrated samples were measured in a vacuum chamber with pressure less than 1 Pa at room temperature.

The specific heat capacity of the different mesoporous power silica samples of different porosities was measured using a Perkin Elmer® DSC 8000, a dual furnace differential scanning

calorimeter equipped with an IntraCooler. This method was reported previously.49 In brief, the samples were prepared in Al pans with vented covers to facilitate water loss at high temperatures. The specific heat capacity of each sample was measured using a step scan isothermal method from 20 °C to 30 °C with a 5 °C min-1 scan and 1.5 min hold at every 1 °C interval. The thermal conductivity of the films, κ, was retrieved from the thermal effusivity (e) obtained from TDTR and the c_p obtained from DSC using the equation

$$\kappa_{eff} = \frac{e_{eff}^2}{C_{v,eff}}. \quad (5)$$

Here, the volumetric heat capacity $(C_{v,eff})$ is estimated using the silica volume fraction $(\phi_{SiO_2} = 1 - \phi)$, the silica density (ρ_{SiO_2}), and the measured specific heat capacity (c_{p,SiO_2}) of the silica samples as shown in:

$$C_{v,eff} = \phi_{SiO_2}\rho_{SiO_2}c_{p,SiO_2}. \quad (6)$$

The relative uncertainty of the thermal conductivity was then calculated as eq (7).

$$\frac{\Delta\kappa_{eff}}{\kappa_{eff}} = \sqrt{\left(\frac{\Delta e_{eff}^2}{e_{eff}^2}\right)^2 + \left(\frac{\Delta\phi_{SiO_2}}{\phi_{SiO_2}}\right)^2 + \left(\frac{\Delta c_{p,eff}}{c_{p,eff}}\right)^2}. \quad (7)$$

Here, Δe_{eff}^2 was estimated as the standard deviation of a mean value of ten measurements, $\Delta\phi_{SiO_2} = \Delta\phi$, which was calculated using the method described in Section 2.3, and $\Delta c_{p,eff}$ was calculated based on the standard deviation of ten measured samples, five of which were nanoparticle-based and five of which were sol-gel based, as shown in Table S1.

Table S1: Porosity, Surface Area and Specific Heat Capacity of Sol-Gel and Nanoparticle-Based Mesoporous Silica Powders

Sample	Surfactant	Building block	Porosity‡	Surface Area‡, S_{BET}, (m^2/g)	Specific heat capacity, c_p (J/g K)

P1*	Non-templated	Sol-gel	N/A	N/A	0.75
P2*	PBO-PEO	Sol-gel	N/A	N/A	0.76
P3*	F127	Sol-gel	N/A	N/A	0.71
P4	F127	Sol-gel	0.33	354	0.74
P5	P123	Sol-gel	0.54	479	0.79
P6	Non-templated	NP	0.44	345	0.77
P7	20 nm PMMA	NP	0.61	412	0.74
P8	F127	NP	0.49	210	0.71
P9	F127	NP	0.57	398	0.72
P10	F127	NP	0.7	402	0.71

‡ Measured using N_2 porosimetry

* Samples' surface area too low to measure using N_2 porosimetry

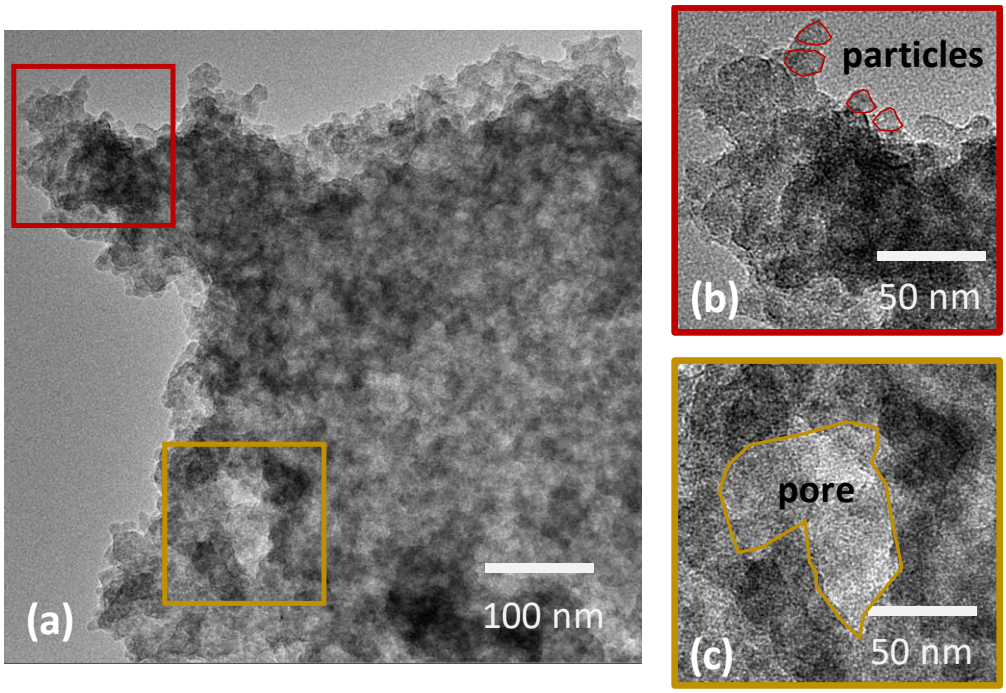

Figure S1. Transmission electron micrograph (TEM) of a nanoparticle based mesoporous silica film templated with 70 nm PMMA colloids (a) with high-magnification images outlining the nanoparticles (b) and pores (c) in the sample.

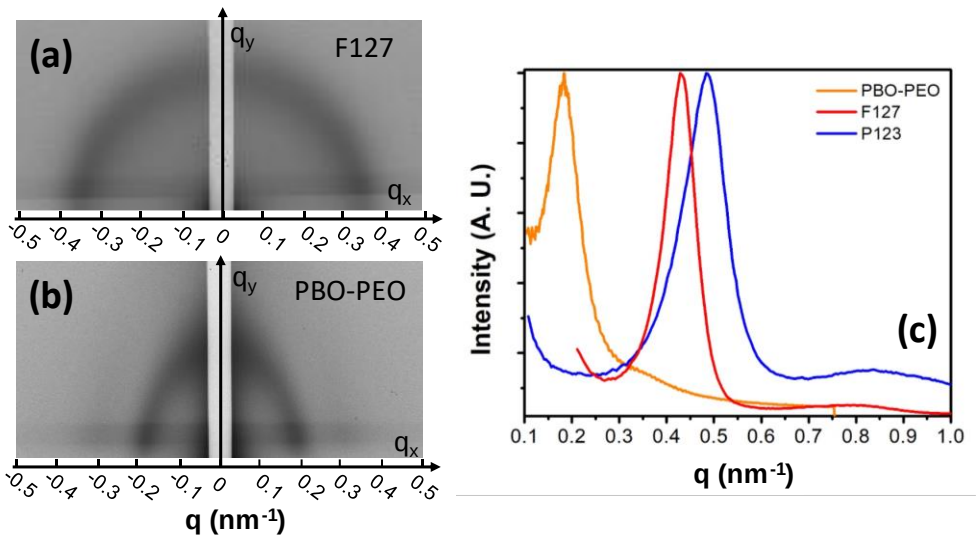

Figure S2. Small angle X-ray scattering of SG-based mp-SiO_2 films. (a) and (b) representative 2D-GISAXS patterns of SG-based mesoporous silica films template by (a) F127 and (b) PBO-PEO. (c) Integrated intensity spectra converted from a 2D-GISAXS pattern along the q_x direction corresponding to in-plane scattering for PBO-PEO, F127 and P123 templated SG-based mp-SiO_2 films. The pore-wall repeating distance increases with increasing size of the template.

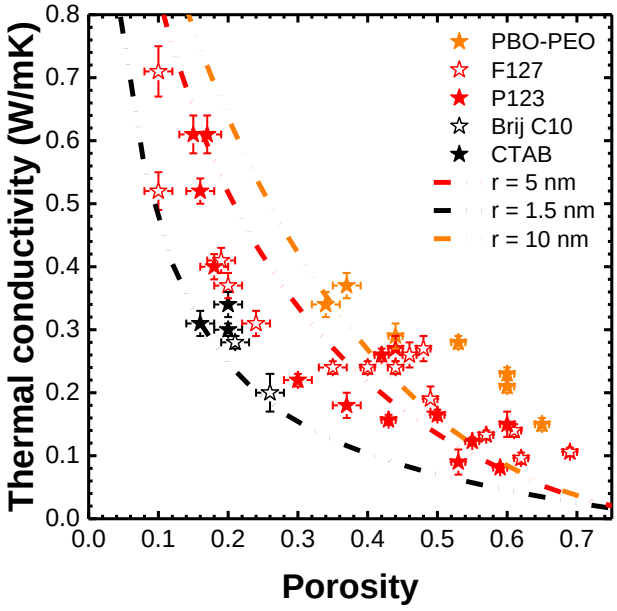

Figure S3. Thermal conductivity as a function of porosity for SG-based mesoporous silica films templated using different polymer templates to provide a range of pore diameters (Brij C10 and CTAB from 2 to 4 nm, F127 and P123 from 5 to 15 nm, PBO-PEO from 15 to 25 nm), measured under vacuum with fitting from Ref [S9].

In the model proposed by Alvarez *et. al.*,[9] the effective thermal conductivity of the samples (λ_{eff}) is described by the porosity (ϕ), bulk thermal conductivity (λ_0) and mean free path (l) of the material and radius of the pores (r) using the equation:

$$\lambda_{eff} = \lambda_0 \frac{1}{\frac{1}{f(\phi)} + \frac{9}{2}\phi \frac{(l/r)^2}{1 + A'(l/r)}\left(1 + \frac{3}{\sqrt{2}}\sqrt{\phi}\right)}$$

Where A' is a numerical function of the Knudsen number.

We used this equation to fit our experimental results with mean free path as the variable parameter at a given porosity and the average pore size of the sample sets. When the mean free path equals to 4.4 nm, the fitting works best and is shown in Figure S3. This value is in agreement with a previous experimental study of the ballistic transport in nanostructured silica.[10] When compared to the fits from the PWSM model in Fig 4 of the main text, we note that the fitting curve for samples with large pores (orange curve) in particular deviates significantly from the experimental results unless *l* approaches 0 or *r* approaches infinity. This suggests that the full range of pore sizes cannot be fit well simultaneously using this model.

Although this model attempts to more accurately isolate the effect of pore size on the thermal conductivity, it was developed for crystalline or porous crystalline materials (e.g. silicon) instead of amorphous materials (e.g. silicon oxide). The definition of phonon mean free path generally requires periodic crystal structures from solid state physics, while application of this concept to amorphous structure is still under development or debating in the literature. In addition, a single mean free path would not be sufficient to illustrate the complicated spectral vibration modes in our materials.

(1) He, G.; Pan, Q.; Rempel, G. L. Synthesis of Poly(Methyl Methacrylate) Nanosize Particles

by Differential Microemulsion Polymerization. *Macromol. Rapid Commun.* **2003**, *24* (9), 585–588. https://doi.org/10.1002/marc.200390089.

(2) Zou, D.; Ma, S.; Guan, R.; Park, M.; Sun, L.; Aklonis, J. J.; Salovey, R. Model Filled Polymers. V. Synthesis of Crosslinked Monodisperse Polymethacrylate Beads. *J. Polym. Sci. Part A Polym. Chem.* **1992**, *30* (1), 137–144. https://doi.org/10.1002/pola.1992.080300118.

(3) Dunphy, D. R.; Sheth, P. H.; Garcia, F. L.; Brinker, C. J. Enlarged Pore Size in Mesoporous Silica Films Templated by Pluronic F127: Use of Poloxamer Mixtures and Increased Template/SiO2 Ratios in Materials Synthesized by Evaporation-Induced Self-Assembly. *Chem. Mater.* **2015**, *27* (1), 75–84. https://doi.org/10.1021/cm5031624.

(4) Malitson, I. H. Interspecimen Comparison of the Refractive Index of Fused Silica. **1965**, *55* (10), 1205–1209. https://doi.org/https://doi.org/10.1364/JOSA.55.001205.

(5) Ilavsky, J. Nika: Software for Two-Dimensional Data Reduction. *J. Appl. Crystallogr.* **2012**, *45* (2), 324–328.

(6) Li, M.; Kang, J. S.; Hu, Y. Anisotropic Thermal Conductivity Measurement Using a New Asymmetric-Beam Time-Domain Thermoreflectance (AB-TDTR) Method. *Rev. Sci. Instrum.* **2018**, *89* (8), 084901. https://doi.org/10.1063/1.5026028.

(7) Kang, J. S.; Li, M.; Wu, H.; Nguyen, H.; Hu, Y. Experimental Observation of High Thermal Conductivity in Boron Arsenide. *Science.* **2018**, *361* (6402), 575–578. https://doi.org/10.1126/science.aat5522.

(8) Kang, J. S.; Wu, H.; Hu, Y. Thermal Properties and Phonon Spectral Characterization of Synthetic Boron Phosphide for High Thermal Conductivity Applications. *Nano Lett.* **2017**, *17* (12), 7507–7514. https://doi.org/10.1021/acs.nanolett.7b03437.

(9) Alvarez, F. X.; Jou, D.; Sellitto, A. Pore-Size Dependence of the Thermal Conductivity of Porous Silicon: A Phonon Hydrodynamic Approach. *Appl. Phys. Lett.* **2010**, *97* (3), 1–4. https://doi.org/10.1063/1.3462936.

(10) Yang, L.; Zhang, Q.; Cui, Z.; Gerboth, M.; Zhao, Y.; Xu, T. T.; Walker, D. G.; Li, D. Ballistic Phonon Penetration Depth in Amorphous Silicon Dioxide. *Nano Lett.* **2017**, *17* (12), 7218–7225. https://doi.org/10.1021/acs.nanolett.7b02380.

APPENDIX C

Supporting Information for Chapter 4:

Understanding the Effect of Nanoparticle Size on the Thermal Conductivity in Amorphous Materials

Experimental Methods

Materials

The following materials were obtained from commercial suppliers and used without further purification: colloidal suspensions of silica nanoparticles (15 wt%, Nalco 2326, ammonium-stabilized colloidal silica, d = 5 nm, Nalco Chemical Company; 6 – 8 wt%, Nyacol® LiSol™3, lithium-stabilized colloidal silica, d = 2 – 4 nm, Nyacol Nano Technologies; 40 wt% NexSil™ 20NH4, ammonium-stabilized colloidal silica, d = 20 nm, Nyacol Nano Technologies), triblock copolymer Pluronic F127 ($EO_{100}PO_{65}EO_{100}$, Mw = 12600 Da, BASF), ammonium persulfate (98%, Alfa Aesar), ammonium lauryl sulfate (~30% in H2O, Sigma Aldrich), methyl methacrylate (contains ≤30 ppm MEHQ as inhibitor, 99%, Sigma Aldrich).

Synthesis

Synthesis of poly(methyl methacrylate) (PMMA) colloidal templates

The synthesis is adapted from previous literature.[1,2] Ammonium persulfate (APS) was used as the initiator and ammonium lauryl sulfate (ALS) was used as the surfactant. In an oil bath, 12.56 mL of the monomer, methyl methacrylate (MMA), 0.61 mL ALS, and 165 mL deionized (DI) H_2O were combined in a three-necked round bottom flask and purged with argon gas for 30 min. In a separate container, 0.08 g of APS was dissolved in 10 mL of DI water. The solution was heated

to 73 °C at a ramp rate of 10 °C min^{-1}. When the temperature exceeded 65 °C, the aqueous solution of APS was added to the reaction flask. The temperature ramp continued to 73 °C, then held at 73 °C for 3 hours before cooling. Any excess monomer was removed from the cooled solution via liquid-liquid extraction with hexanes. The solid fraction of the polymer was then determined by drying and weighing an aliquot of the solution.

Conversion of cation exchange resin to ammonia form and exchange of nanoparticle counter-ion to ammonium

The preparation of the ammonium-based ion exchange resin was adapted from the literature.[3] Specifically, 113 g of $(NH_4)_2SO_4$ was dissolved in approximately 200 mL of 0.05 M NH_4OH. To this solution, approximately 100 mL of Amberlite IR120-H^+ resin was added. The solution was left to stir and the pH of the solution was adjusted using concentrated NH_4OH, so that it was the same as that of the nanoparticle solution to be exchanged (pH *c.a.* = 9). This solution was left to stir for about 2 hours and tested in the final 10 minutes to ensure that the pH was constant. The resin (now labeled Amberlite IR120-NH_4^+) was then vacuum filtered and washed with about 2 L of 0.05 M NH_4OH (until the filtrate tested negative for sulfates using dilute $Ba(C_2H_3O_2)_2$). The resin was left to dry on the vacuum filter for an additional 15 minutes.

The Li^+ cation of the LiSol3 nanoparticles was exchanged to NH_4^+ via a batch exchange process. To ensure complete exchange, 50 mL of LiSol3 solution was added to 2 g of the Amberlite-IR120-NH_4^+ and left to stir for about 3 hours. The 2 g of amberlite was replaced twice more. The solution was then decanted and filtered. The mass content of the solution was then obtained.

Synthesis of polymer-templated mesoporous silica films

Porous silica films were made using either Pluronic F127 or the synthesized PMMA as previously described.[4,5] For the Pluronic F127 templated films, the appropriate mass of Pluronic F127 dissolved in 5 mL of DI H_2O was added to a fixed volume of silica nanoparticles to produce solutions with polymer-to-silica ratios between 0.6 and 1.4 g/g. For the films using PMMA as the template, 5 mL of the PMMA solution was combined with varying volumes of the colloidal silica solutions to produce solutions, again with polymer-to-silica ratios between 0.6 to 1.4 g/g. For each solution, 80 μL was spin-coated on to a plasma-cleaned 1"×1" Si substrates. The film thickness was adjusted by controlling the spin speeds. The dried films were aged at 180 C for 6 hours, then calcined in air at 350 °C for 30 mins using a 2 °C min^{-1} temperature ramp to remove the polymer.

Structural characterization

Electron Microscopy: Scanning Electron Microscopy (SEM) images were obtained using a model JEOL JSM-6700F field emission electron microscope with 3 kV accelerating voltage and secondary electron detector configuration. EDS was obtained.

Transmission Electron Microscopy (TEM) images were obtained using a Technai G2 TF20 High-Resolution EM, CryoEM and CryoET (FEI) at an accelerating voltage 200 kV and a TIETZ F415MP 16 megapixel 4k×4k CCD detector. The TEM grids were prepared by dipping a carbon coated grid in an ethanolic resuspension of the nanoparticles.

Quantification of Porosity: An optical reflectance-based method was used to measure the porosity and film thickness as described previously.[6] Here, the experimental spectral normal-hemispherical reflectance $R_{exp,\lambda}$was measured with an Evolution 220 UV-Vis spectrophotometer from Thermo Scientific equipped with an ISA-220 integrating sphere accessory from Thermo Scientific. An 8° incidence angle of the light beam into the integrating sphere was used. The

reflectance was measured in the visible range between 400 and 800 nm with a 1 nm spectral resolution. The normal-hemispherical reference baseline intensity $B_{ref,\lambda}$ was measured using a high specular reflection standard mirror by Ocean Optics (NIST certified STAN-SSH). The dark signal $D_{ref,\lambda}$was measured by obstructing the detector window. Sample reflection signal $S_{exp,\lambda}$ was measured after degassing the material for two hours at 150˚C and was normalized to retrieve $R_{exp,\lambda}$ the following equation:

$$R_{exp,\lambda} = \frac{S_{exp,\lambda}\text{-}D_{ref,\lambda}}{B_{ref,\lambda}\text{-}D_{ref,\lambda}} R_{std,\lambda}$$

where $R_{std,\lambda}$ is the known normal-normal reflectance of the standard mirror provided by the supplier. The porosity (ϕ) was then evaluated using a Maxwell-Garnett model using the refractive index $(n_{c,\lambda})$ retrieved from the reflectance measurement. The uncertainty of the retrieved porosity $(\Delta\phi)$ was evaluated using the equation:

$$\Delta\phi = \sqrt{\left(\frac{\partial\phi}{\partial n_{eff,\lambda}}\Delta n_{eff,\lambda}\right)^2 + \left(\frac{\partial\phi}{\partial n_{c,\lambda}}\Delta n_{c,\lambda}\right)^2} \quad \text{(i)}$$

The uncertainty of the refractive index of silica thin film $(\Delta n_{c,\lambda})$ was calculated to be twice the standard deviation of $n_{c,\lambda}$ given by the Sellmeier formula over the 400-800 nm wavelength range. This was found to be $(\Delta n_{c,\lambda})$ = 0.005 for all mesoporous silica films. The uncertainty, $\Delta n_{eff,\lambda}$, associated with the retrieved $n_{eff,\lambda}$ was found to be 0.005 for mesoporous silica films. Here, $\Delta n_{eff,\lambda}$ is defined as the average absolute difference between the refractive index used to predict the ideal spectral normal-hemispherical reflectance and the refractive index retrieved from the noisy normal-hemispherical reflectance.

To verify the porosity, and obtain the surface area and pore size distribution, N_2 adsorption porosimetry was measured using a Micrometrics Tristar II 3020 on powdered samples of the same composition as the thin films. Brauner-Emmett-Teller (BET) and Barrett-Joyner-Halenda (BJH) methods were used to extract surfaces areas and pores size distributions, respectively. Before each measurement, the samples were degassed under vacuum for at least 12 hours at 150 °C to remove all water in the pores.

Thermal Conductivity Measurement: Thermal conductivity was measured using time domain thermoreflectance (TDTR). The detailed working principles and experimental setup can be found elsewhere.[7] A thin reflective aluminum film (80 nm) is deposited by e-beam evaporation on the top surface of the samples, which serves as an optical transducer and temperature sensor. A pump pulse at 400 nm is used to instantaneously raise the temperature at the surface of the sample. This is followed by a temperature decrease as the heat is carried away. The probe beam, at 800 nm, which is delayed by a mechanical delay stage, detects the transient temperature decay by measuring changes in reflectance. The full transient decay curve from -100 ps to 5000 ps was fitted with a thermal diffusion model to obtain the thermal effusivity of the sample, which can be related to the thermal conductivity using the volumetric heat capacity.[44] Before the measurement, all aluminum coated samples were dehydrated by heating on a hot plate at 150 °C for more than 12 hours. The dehydrated samples were measured in a vacuum chamber with pressure less than 1 Pa at room temperature. A multilayer transient heat conduction model was used to fit the data to extract thermal conductivities. A relatively large laser spot size of 20 μm diameter was used to average over any structural heterogeneity during the measurement. To ensure the uniformity of the sample as well as the reliability of the thermal conductivity data, measurements were repeated at ten different locations on the 1 cm × 1 cm area of each sample.

Volumetric heat capacities ($C_{v,eff} = \phi_{SiO_2}\rho_{solid}c_{p,SiO_2}$) of the porous silica samples were estimated using the specific heat capacity (c_{p,SiO_2}), previously measured using differential scanning calorimetry,[8] the silica volume fraction ($\phi_{SiO_2} = 1\text{-}\phi_p$), and the density of bulk silica (ρ_{solid}).

References

(1) Yan, Y.; Li, M.; King, S.; Galy, T.; Marszewski, M.; Kang, J. S.; Pilon, L.; Hu, Y.; Tolbert, S. H. Controlling Thermal Conductivity in Mesoporous Silica Films Using Pore Size and Nanoscale Architecture. *J. Phys. Chem. Lett.* **2020**, *11*, 3731–3737. https://doi.org/10.1021/acs.jpclett.0c00464.

(2) Zou, D.; Ma, S.; Guan, R.; Park, M.; Sun, L.; Aklonis, J. J.; Salovey, R. Model Filled Polymers. V. Synthesis of Crosslinked Monodisperse Polymethacrylate Beads. *J. Polym. Sci. Part A Polym. Chem.* **1992**, *30* (1), 137–144. https://doi.org/10.1002/pola.1992.080300118.

(3) Weldes, H. H. Amine and Ammonium Silicate Solutions. **1970**, *9* (2), 249–253. https://doi.org/10.1021/i360034a025.

(4) Yan, Y.; Li, M.; King, S. C.; Galy, T.; Marszewski, M.; Kang, J. S.; Pilon, L.; Hu, Y.; Tolbert, S. H. Controlling Thermal Conductivity in Mesoporous Silica Films Using Pore Size and Nanoscale Architecture. *J. Phys. Chem. Lett.* **2020**, acs.jpclett.0c00464. https://doi.org/10.1021/acs.jpclett.0c00464.

(5) Dunphy, D. R.; Sheth, P. H.; Garcia, F. L.; Brinker, C. J. Enlarged Pore Size in Mesoporous Silica Films Templated by Pluronic F127: Use of Poloxamer Mixtures and Increased Template/SiO2 Ratios in Materials Synthesized by Evaporation-Induced Self-Assembly. *Chem. Mater.* **2015**, *27* (1), 75–84. https://doi.org/10.1021/cm5031624.

(6) Galy, T.; Marszewski, M.; King, S.; Yan, Y.; Tolbert, S. H.; Pilon, L. Comparing Methods for Measuring Thickness , Refractive Index , and Porosity of Mesoporous Thin Films. *Microporous Mesoporous Mater.* **2020**, *291*, 109677. https://doi.org/10.1016/j.micromeso.2019.109677.

(7) Li, M.; Kang, J. S.; Hu, Y. Anisotropic Thermal Conductivity Measurement Using a New Asymmetric-Beam Time-Domain Thermoreflectance (AB-TDTR) Method. *Rev. Sci. Instrum.* **2018**, *89* (8), 084901. https://doi.org/10.1063/1.5026028.

(8) Yan, Y.; King, S. C.; Li, M.; Galy, T.; Marszewski, M.; Kang, J. S.; Pilon, L.; Hu, Y.; Tolbert, S. H. Exploring the Effect of Porous Structure on Thermal Conductivity in Templated Mesoporous Silica Films. *J. Phys. Chem. C* **2019**, *123* (35), 21721–21730. https://doi.org/10.1021/acs.jpcc.9b03767.

APPENDIX D

Supporting Information for Chapter 5:

Examining the Role of Atomic Scale Heterogeneity on the Thermal Conductivity of Transparent, Thermally Insulating, Mesoporous Silica-Titania Thin Films

Experimental Details

Materials:

The following materials were obtained from commercial suppliers and used without further purification: triblock copolymer Pluronic F127 ($PEO_{100}PPO_{65}PEO_{100}$, Mw = 12600, BASF), tetraethylorthosilicate (TEOS) (98%, Acros Organics), titanium isopropoxide (TIPO) (98%, Acros Organics) hydrochloric acid (Certified ACS Plus, Fisher Scientific), ethanol (200 proof, Rossville Gold Shield).

Synthesis:

The synthesis of mesoporous SiO_2:TiO_2 mixed films was adapted based on the works of Dong, W. *et. al.* and Dunphy, D. R. *et. al.*[1,2] The precursors of F127:EtOH:HCl:H_2O:TIPO:TEOS were combined in a 7.4:50:6.1:0.06:x:(1-x) molar ratio, where x was 0.1 or 0.2. In a typical synthesis of silica:titania with molar ratio 90:10 and m_{poly}/m_{inorg} = 1.5 g/g, 280 mg of Pluronic surfactant F127 ($PEO_{100}PPO_{65}PEO_{100}$) was first dissolved in 6 mL of ethanol (EtOH), 0.325 mL of doubly distilled water and 0.425 mL of 37% HCl was then rapidly added under stirred at 60 °C. Next, 0.62 mL of tetraethylorthosilicate (TEOS) was added to the reaction mixture, followed by dropwise addition of 0.1 mL of titanium isopropoxide (TIPO); the reaction was then left to stir for 5 hours at 60 °C.

To increase the homogeneity of the mixture, a modified synthesis was adapted from Chen, H-S, *et. al.*[3] In the modified synthesis of silica:titania with molar ratio 90:10 and m_{poly}/m_{inorg} = 1.5 g/g, 0.1 mL of TIPO was combined with 0.03 mL of acetylacetonate in 1 mL of ethanol and left to stir for one hour at 60 °C. Concurrently, in a separate flask, 0.62 mL of TEOS was combined with 0.053 mL of H_2O in 1 mL of ethanol and also left to stir for one hour at 60 °C. Both solutions were then added to a solution of 280 mg of F127 in 4 mL of ethanol, 0.27 mL of water and 0.425 mL of 37% HCl and left to stir for 4 hours.

To obtain films of thicknesses > 500 nm, the solutions were concentrated by rotary evaporation at 80 mTorr in a 60 °C temperature bath for 10 minutes. Films were made by spin coating the solution on to silicon or microscope slide substrates. The films were then calcined under flowing O_2 and held at 350 °C for 6 hours, then 400 °C for 2 hours with a ramp rate of 2 °C min^{-1} to remove all polymer template and ensure that the titania was in its fully oxidized form.

Substrate free powdered samples for NMR, FTIR and DSC analyses were made by evaporating the solution in a Petri dish for 3-7 days at humidity > 50%. The resulting powder was then calcined in flowing O_2 at 400 °C for approximately 12 hours (until all traces of the polymer was removed).

Characterization:

Transmittance and haze: The normal-hemispherical transmittance $T_{nh,\lambda}$ and the diffuse transmittance $T_{d,\lambda}$ were measured with a double-beam UV-Vis spectrometer (3101-PC Shimadzu, Kyoto, Japan) and an integrating sphere with an internal diameter of 60 mm (ISR 3100 Shimadzu, Kyoto, Japan) as described elsewhere.[4] The normal-hemispherical transmitted signal $S_{nh,\lambda}$ was measured and corrected for the reference signal B_λ and the dark signal D_λ according to

$$T_{nh,\lambda} = \frac{S_{nh,\lambda} - D_\lambda}{B_\lambda - D_\lambda}$$

The dark signal D_λ was collected when no light entered the integrating sphere while the reference signal B_λ was measured in the same configuration as for $S_{nh,\lambda}$, but without a sample present.

The diffuse transmitted signal $S_{d,\lambda}$ represents the fraction of light that is scattered and transmitted by the sample. It was measured by removing the highly reflecting plate facing the sample in the integrating sphere so that the unscattered light left the integrating sphere.

The haze h_λ was computed according to ASTM D1003-11 as

$$h_\lambda = \frac{S_{d,\lambda}}{S_{nh,\lambda}} - \frac{M_\lambda}{B_\lambda}$$

where M_λ is the signal measured in the same configuration as for $S_{d,\lambda}$ but without a sample present.

Electron Microscopy: Scanning Electron Microscopy (SEM) images were obtained using a model JEOL JSM-6700F field emission electron microscope with 3 kV accelerating voltage and secondary electron detector configuration. Scanning transmission electron microscopy (S/TEM) images were obtained using a Titan S/TEM (FEI) at 300 kV using a double-tilt holder and an Ultrascan, 2k×2k digital camera. EDS of the S/TEM images was acquired using the Oxford software.

X-Ray Diffraction: Two-dimensional grazing incidence small-angle x-ray scattering (2D-GISAXS) data were collected at beamline 1-5 at the Stanford Synchrotron Lightsource (SSRL) at an incident angle of 0.02° with a wavelength of 0.1033 nm, corresponding to an X-ray energy of 12.002 keV. The sample-to-detector distance was about 3000 mm and the detector was a Rayonix-165 CCD. The data was then calibrated using silver behenate and reduced using the Nika package for Igor Pro.[5] Two-dimensional grazing incidence wide angle scattering (2D-GIWAXS) data was

also collected at SSRL using beamline 11-3 with a wavelength of 0.097357 nm, corresponding to an X-ray energy of 12.735 keV. The sample-to-detector distance was 150 mm and a Rayonix-165 CCD detector was used. The data was then calibrated using LaB_6 and reduced using the WAXSTools package from Igor Pro.

Quantification of Porosity: Ellipsometric porosimetry was performed on a PS-1100 instrument from Semilab using toluene as the adsorbate at ambient conditions to quantify porosity and pore size. The instrument used a UV-visible CCD detector adapted to a grating spectrograph to analyze the signal reflected by the sample. The light source was a 75 W Hamamatsu Xenon lamp and the measurements were performed in the spectral range from 1.25–4.5 eV. Data analysis was performed using the associated Spectroscopic Ellipsometry Analyzer software assuming that the pores were cylindrical.

An optical reflectance based method was also used to verify the porosity and measure the film thickness.[6] The experimental spectral normal-hemispherical reflectance $R_{exp,\lambda}$ was measured with a Shimadzu UV3101 PC UV-Vis spectrophotometer equipped with a Shimadzu ISR3000 integrating sphere. The reference intensity was measured using a high specular reflection standard mirror by Ocean Optics (NIST certified STAN-SSH). The reflectance was measured in the visible range between 400 and 800 nm with a 1 nm spectral resolution. The porosity (ϕ) was then evaluated using a Maxwell-Garnett model using the refractive index $(n_{c,\lambda})$ retrieved from the reflectance measurement. The uncertainty of the retrieved porosity ($\Delta\phi$) was evaluated using the equation:

$$\Delta\phi = \sqrt{\left(\frac{\partial\phi}{\partial n_{eff,\lambda}}\Delta n_{eff,\lambda}\right)^2 + \left(\frac{\partial\phi}{\partial n_{c,\lambda}}\Delta n_{c,\lambda}\right)^2} \quad \text{(i)}$$

Here, the uncertainty of the refractive index of silica-titania composite $(\Delta n_{c,\lambda})$ was calculated to be twice the standard deviation of $n_{c,\lambda}$ given by the Sellmeier formula over the 400-800 nm wavelength range. This was found to be $(\Delta n_{c,\lambda})$ = 0.005 for all mesoporous silica-titania films. The uncertainty, $\Delta n_{eff,\lambda}$, associated with the retrieved $n_{eff,\lambda}$ was found to be 0.005 for mesoporous silica-titania films. Here, $\Delta n_{eff,\lambda}$ is defined as the average absolute difference between the refractive index used to predict the ideal spectral normal-hemispherical reflectance and the refractive index retrieved from the noisy normal-hemispherical reflectance. Film thickness extracted from these measurements was confirmed using profilometry. A scratch was made on the films and a Veeco Dektak 150 Surface Profiler was used to characterize the film thickness.

For powdered samples, N_2 adsorption porosimetry with Micrometrics Tristar II 3020 was used along with Brauner-Emmett-Teller (BET) and Barrett-Joyner-Halenda (BJH) theories to measure the surface area, porosity and pore size.

Spectroscopy: The relative homogeneity of the SiO_2:TiO_2 films was examined using FTIR and solid-state NMR. For the latter, ^{29}Si solid-state NMR experiments were performed on a Bruker AV600 instrument operating at 119 MHz while spinning at 10 kHz using a 3.2 mm zirconia rotor. The area of the Q^2, Q^3 and Q^4 peaks between -80 to -140 ppm were quantified using PeakFit. Peaks widths were shared during fitting to reduce the number of independent variables; this assumption is generally valid since the Q peaks all arise from siloxane-type bonds. The areas of the peaks are given in Table 1. FTIR measurements were conducted on a Perkin Elmer Spectrum One FTIR Spectrometer. The FTIR transmittance was normalized to Si-O-Si peaks at ~1050 cm^{-1}.

A Kratos Axis Ultra DLD spectrometer was used for X-ray photoelectron spectroscopy (XPS) with a monochromatic Al K(α) radiation source. A charge neutralizer filament was used to reduce

sample charging. A pass energy of 20 eV, with a step size of 0.1 eV and 300 ms dwell time was used. All spectra were calibrated to the advantageous carbon 1s peak at 284.8 eV.

Thermal Conductivity Measurement: Thermal conductivity was measured using time domain thermoreflectance (TDTR). The detailed working principles and experimental setup can be found elsewhere.[7] Briefly, a femtosecond laser pulse is generated by a Ti:Sapphire oscillator (Tsunami, Spectra-physics) and split into pump and probe beams by a beam splitter. The pump pulse is used to instantaneously raise the temperature at the sample surface. This is followed by a temperature decrease as the heat is carried away. The probe beam, which is delayed by a mechanical delay stage, detects the transient temperature decay by measuring changes in reflectance. A thin reflective aluminum film (80 nm) is deposited by e-beam evaporation on the top surface of the samples, which serves as an optical transducer. Before the measurement, all aluminum coated samples were dehydrated by heating on a hot plate at 150 °C for more than 12 hours. The dehydrated samples were measured in a vacuum chamber with pressure less than 1 Pa at room temperature. A multilayer transient heat conduction model was used to fit the data to extract thermal conductivities. A relatively large laser spot size of 20 μm diameter was used to average over any structural heterogeneity during the measurement. To ensure the uniformity of the sample as well as the reliability of the thermal conductivity data, measurements were repeated at ten different locations on the 1 cm × 1 cm area of each sample.

Volumetric heat capacities ($C_{v,\,eff}$) of the porous silica-titania samples were estimated using the specific heat capacity (c_{p,SiO_2,TiO_2}), the silica-titania volume fraction ($\phi_{SiO_2,TiO_1} = 1\text{-}\phi_p$), and the density of solid silica-titania (ρ_{solid}) as shown below:

$$C_{v,eff} = \phi_{SiO_2TiO_2}\rho_{solid}c_{p,SiO_2TiO_2}$$

For the mixed SiO_2:TiO_2 films, the density of the mixed solid framework (ρ_{solid}) is given by:

$$\rho_{solid} = SiO_2\%_{wt}\rho_{SiO_2} + TiO_2\%_{wt}\rho_{TiO_2}$$

The specific heat capacities of porous powered samples were obtained from differential scanning calorimetry (DSC) using a Perkin Elmer® DSC 8000, a dual furnace differential scanning calorimeter equipped with an IntraCooler, as described elsewhere.[8] The specific heat capacity (c_p) of each sample was measured using a step scan isothermal method from 20 °C to 30 °C with a 5 °C/min scan and 1.5 min hold at every 1 °C interval. The samples were prepared in vented Al pans to facilitate water loss at high temperatures.

Table S1: Reagent amounts used for the synthesis of polymer template silica-titania films. The porosity and silica-titania ratios are readily tunable. The homogeneity of the scattering centers is also easily controlled by adjusting the hydrolysis rates of the silica and titania precursors.

Sample	Polymer solution				Silica precursor solution			Titania precursor solution		
	F127 (mg)	EtOH (mL)	H_2O (mL)	HCl (mL)	EtOH (mL)	TEOS (mL)	H_2O (mL)	EtOH (mL)	TIPO (mL)	acac (mL)
ST10-reg	186-466	6.0	0.325	0.425	-	0.62	-	-	0.1	-
ST10-mod	186-411	4.0	0.272	0.425	1.0	0.62	0.053	1.0	0.1	0.033
ST20-reg	197-437	6.0	0.325	0.425	-	0.57	-	-	0.2	-
ST20-mod	197-437	4.0	0.270	0.425	1.0	0.57	0.05	1.0	0.2	0.066

Table S2: Peak positions and areas obtained from solid-state ^{29}Si NMR for the four mesoporous silica-titania composites explored in this work.

Sample		ST10reg	ST10mod	ST20reg	ST20mod
FWHM		10.6	10.2	9.2	10.4
Q^2	Position (ppm)	-90.3	-89.1	-89.9	-89.6
	Relative Area	6.1	7	9.3	6.1
Q^3	Position (ppm)	-100.5	-100.3	-100.2	-100.3
	Relative Area	35	38.6	39.8	41.5
Q^4	Position (ppm)	-109.2	-109.1	-109.6	-109.7
	Relative Area	58.8	54.4	50.9	52.4
Relative Area (Q^3/Q^4)		0.6	0.71	0.78	0.79

Table S3: Surface Area and Specific Heat Capacity of Mesoporous Silica-Titania Powders. The average of these values were used to calculate the thermal conductivity from the thermal effusivity obtained from the time domain thermoreflectance measurements.

Sample	Regular or modified	Ratio silica-titania at%-at%	Ratio polymer/inorganic (g/g)	Surface Area, S_{BET} (m^2/g)	Specific heat capacity, c_p ($J\ kg^{-1}\ K^{-1}$)
1	Reg	90-10	1.5	476	700
2	Mod	90-10	1.4	523	770
3	Reg	90-10	1.4	528	770
4	Mod	90-10	1.5	845	770
5*	Reg	90-10	0.0	N/A	840
6	Reg	80-20	1.5	382	830
7	Reg	80-20	1.6	427	800
8	Reg	80-20	1.4	475	830
9	Mod	80-20	1.7	552	800
10	Reg	80-20	1.7	595	850

* Non-templated sample with surface areas that were too low to measure using N_2 porosimetry

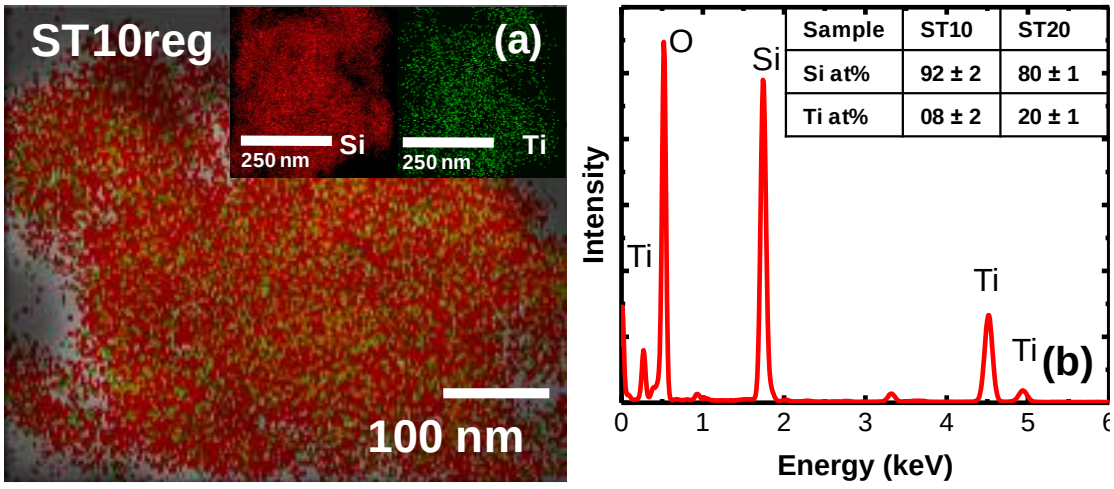

Figure S1. (a) EDS map of an ST10reg sample showing well mixed domains of Si and Ti. (b) Typical EDS analysis of the samples studied with quantification of the Si and Ti content shown in the inset.

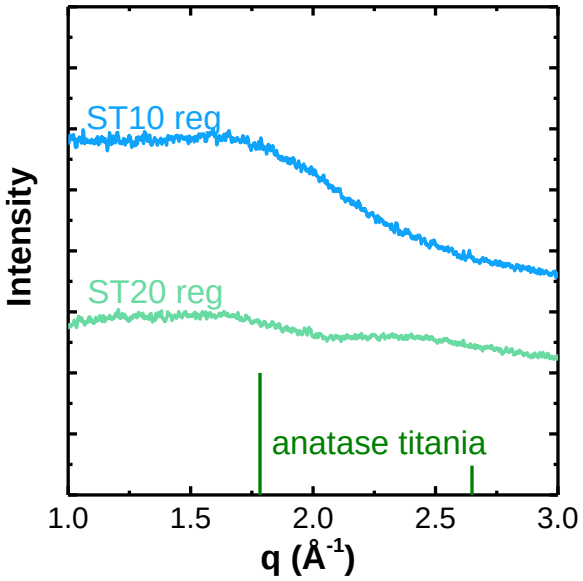

Figure S2. Reduced 1-D grazing incidence wide angle X-ray scattering (GIWAXS) pattern for ST10reg and ST20reg samples. No scattering from crystalline titania (included as a reference pattern) or any other crystalline phases is observed, confirming the amorphous nature of these nanoporous films.

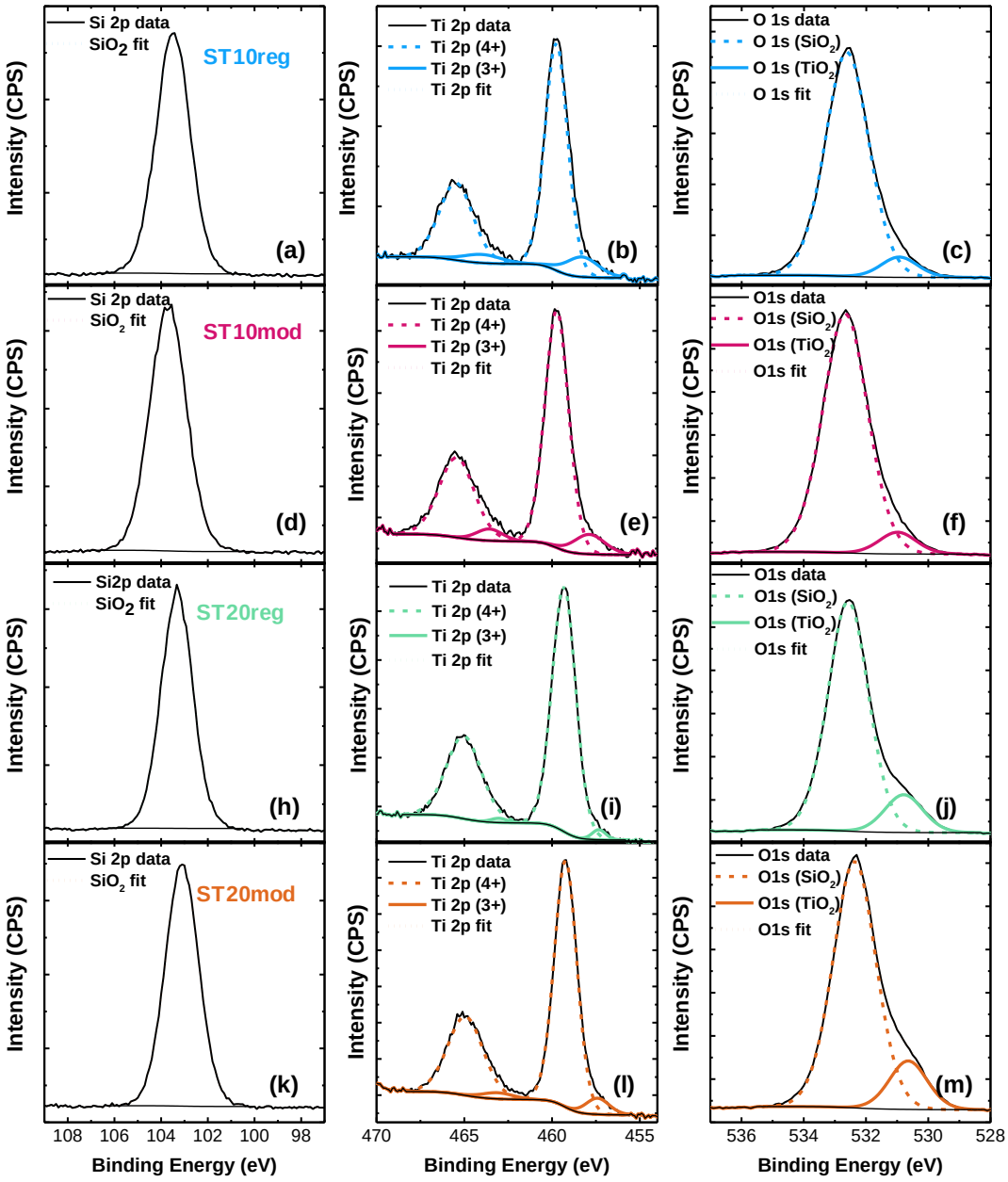

Figure S3. Examining the composition of silica, titania and defects in mixed silica-titania films using X-ray photoelectron spectroscopy. Si 2p, Ti 2p and O 1s core lines for ST10reg (a) - (c), ST10mod (d) - (f), ST20reg (h) - (j) and ST20mod (k) - (m). All films were synthesized with an F127/inorganic ratio of 2 g/g.

References:

1 W. Dong, Y. Sun, W. L. Chul, W. Hua, X. Lu, Y. Shi, S. Zhang, J. Chen and D. Zhao, *J. Am. Chem. Soc.*, 2007, **129**, 13894–13904.

2 D. R. Dunphy, P. H. Sheth, F. L. Garcia and C. J. Brinker, *Chem. Mater.*, 2015, **27**, 75–84.

3 H. Chen, S. Huang and T. Perng, *Appl. Mater. Interfaces*, 2012, **4**, 5188–5195.

4 M. Marszewski, S. C. King, Y. Yan, T. Galy, M. Li, A. Dashti, D. M. Butts, J. S. Kang, P. E. McNeil, E. Lan, B. Dunn, Y. Hu, S. H. Tolbert and L. Pilon, *ACS Appl. Nano Mater.*, 2019, **2**, 4547–4555.

5 J. Ilavsky, *J. Appl. Crystallogr.*, 2012, **45**, 324–328.

6 T. Galy, M. Marszewski, S. King, Y. Yan, S. H. Tolbert and L. Pilon, *Microporous Mesoporous Mater.*, 2019, **291**, 109677.

7 M. Li, J. S. Kang and Y. Hu, *Rev. Sci. Instrum.*, 2018, **89**, 084901.

8 M. Marszewski, D. Butts, E. Lan, Y. Yan, S. C. King, P. E. McNeil, T. Galy, B. Dunn, S. H. Tolbert, Y. Hu and L. Pilon, *Appl. Phys. Lett.*, 2018, 201903.

APPENDIX E

Supporting Information for Chapter 6:

Hierarchical monoliths from sub-50 nm hollow silica shells

Material Characterization

Electron Microscopy: Transmission Electron Microscopy (TEM) images were obtained using a Technai G2 TF20 High-Resolution EM, CryoEM and CryoET (FEI) at an accelerating voltage 200 kV and a TIETZ F415MP 16 megapixel 4k×4k CCD detector. The TEM grids were prepared by dipping a carbon coated grid in an ethanolic resuspension of the nanoparticles.

Quantification of Porosity: Nitrogen adsorption–desorption isotherms were measured at 77 K using a TriStar II 3020 (Micromeritics Instrument Corp., Norcross, GA, USA). The samples were all degassed in vacuum at 150 °C for at least 12 hours prior to the measurements. The specific surface area S_{BET} (in $m^2\ g^{-1}$) was calculated from the Brunauer–Emmett–Teller (BET) model, the total pore volume V_t (in $cm^3\ g^{-1}$) was estimated based on the number of moles of nitrogen adsorbed at relative pressure $p/p_0 = 0.98$ and assuming that the nitrogen in the pores was in the liquid state with molar density of 34.38 $cm^3\ mol^{-1}$. Then, the porosity ϕ of the monoliths was calculated as

$$\phi = \frac{V_t}{\frac{1}{\rho_{SiO_2}} + V_t}. \quad (1)$$

where $\rho_s = 2.2\ g\ cm^{-3}$ is the density of bulk silica.

The pore size distribution dV_p/dw was calculated using the Kruk–Jaroniec–Sayari method based on the Barrett–Joyner–Halenda (BJH) method and using the adsorption branch of nitrogen isotherm.

Transmittance and haze: The normal-hemispherical transmittance $T_{nh,\lambda}$ and the diffuse transmittance $T_{d,\lambda}$ were measured with a double-beam UV-Vis spectrometer (3101-PC Shimadzu, Kyoto, Japan) and an integrating sphere with an internal diameter of 60 mm (ISR 3100 Shimadzu, Kyoto, Japan) as described elsewhere.[4] The normal-hemispherical transmitted signal $S_{nh,\lambda}$ was measured and corrected for the reference signal B_λ and the dark signal D_λ according to

$$T_{nh,\lambda} = \frac{S_{nh,\lambda} - D_\lambda}{B_\lambda - D_\lambda}$$

The dark signal D_λ was collected when no light entered the integrating sphere while the reference signal B_λ was measured in the same configuration as for $S_{nh,\lambda}$, but without a sample present.

The diffuse transmitted signal $S_{d,\lambda}$ represents the fraction of light that is scattered and transmitted by the sample. It was measured by removing the highly reflecting plate facing the sample in the integrating sphere so that the unscattered light left the integrating sphere.

The haze h_λ was computed according to ASTM D1003-11 as

$$h_\lambda = \frac{S_{d,\lambda}}{S_{nh,\lambda}} - \frac{M_\lambda}{B_\lambda}$$

where M_λ is the signal measured in the same configuration as for $S_{d,\lambda}$ but without a sample present.

Table ES1. Synthetic parameters and structural characterization of monoliths of hollow silica shells

Sample	Alternative Title	Molar Ratio HCl:F108:xylenes:TEOS	Gelling Procedure	TEM			N_2 porosimetry				
				d_{tot} (nm)	d_{core} (nm)	t_{shell}	d_{core} (nm)	d_{i-p} (nm)	V_{tot} (cm^3 g^{-1})	φ_p (%)	S_{BET} (m^2 g^{-1})
1	HM-18/10-HT	6.3:0.02:3.6:2	Heat treated	18 ± 2	10 ± 1	4 ± 1	10 ± 1	38	1.6	78	715
2	HM-13/7-HT	6.3:0.03:5.4:3	Heat treated	13 ± 3	7 ± 2	3 ± 1	7 ± 2	22	1.3	74	757
3	HM-14/8-PA	6.3:0.03:5.4:3	pH adjusted	14 ± 2	8 ± 1	3 ± 1	10 ± 2	32	2.6	85	901
4		6.3:0.03:5.4:3	Heat treated				8 ± 1	36	1.8	80	792
5		6.3:0.03:5.4:3	pH adjusted				10 ± 4	36	2.3	84	707
6		6.3:0.03:5.4:3	Heat treated				6 ± 2	18	1.0	68	815
7		6.3:0.03:5.4:3	pH adjusted				10 ± 2	35	2.7	86	879
8		6.3:0.03:5.4:3	Heat treated				6 ± 2	25	1.2	72	738
9		6.3:0.01:1.8:1	Heat treated				8 ± 1	34	1.6	78	742

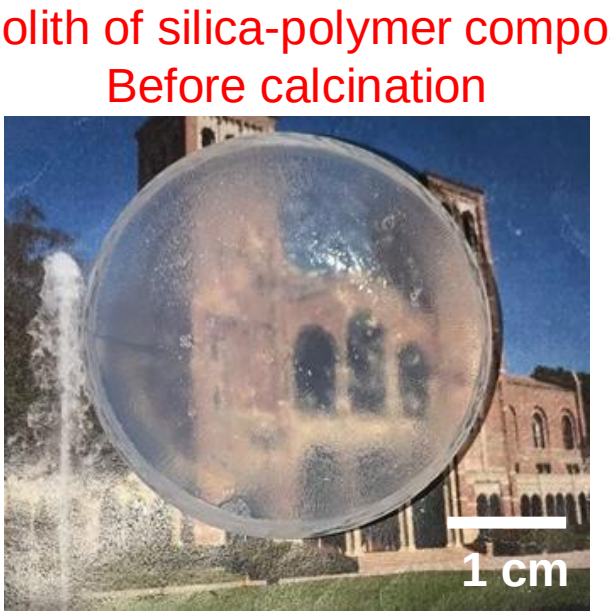

Figure ES1. Photograph of dried polymer-filled monolith

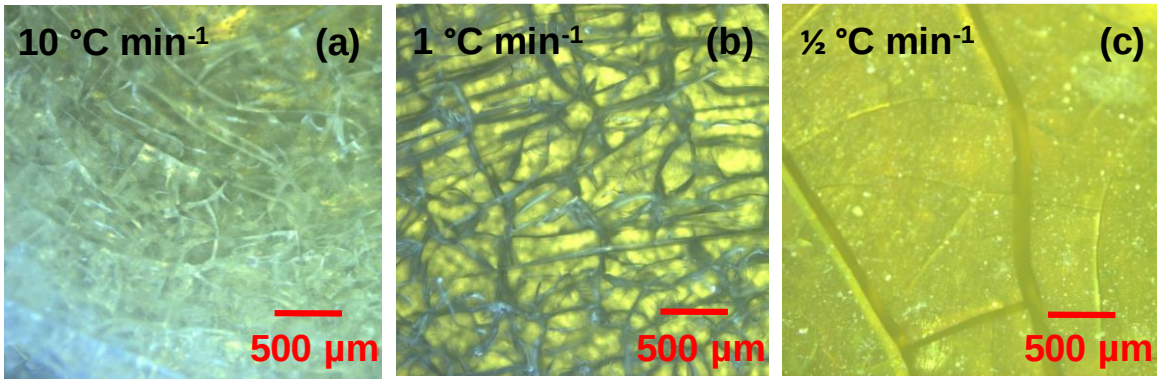

Figure ES2. Optical microscopy images of polymer-filled monoliths calcined at different heating rates

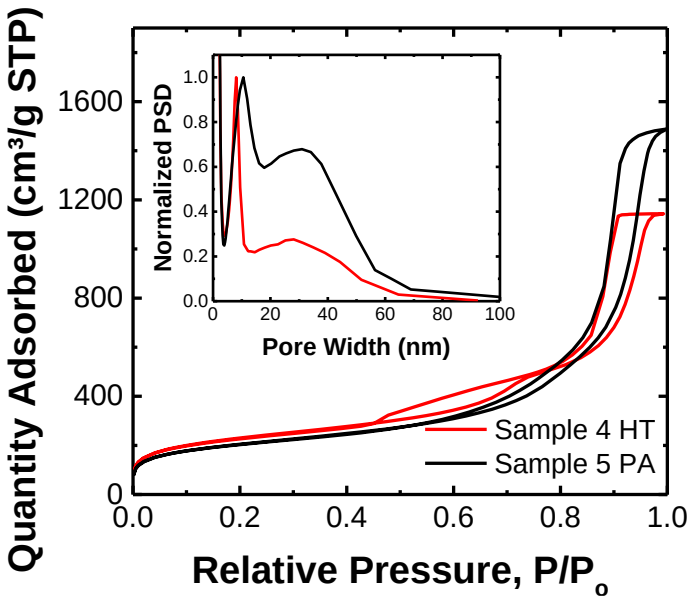

Figure ES3. N_2 porosimetry isotherm with pore size distribution inset of Samples 4 and 5 that were heat treated and pH adjusted, respectively. Samples 4 and 5 were assembled from the same hollow shell solution

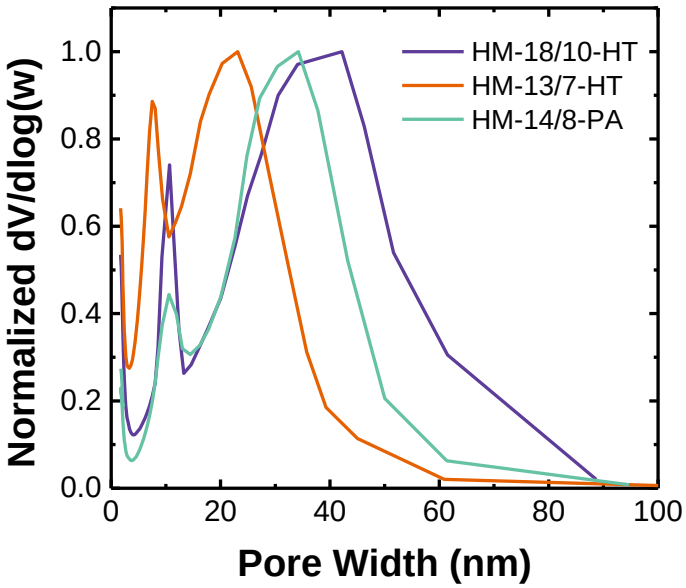

Figure ES4. Normalized pore volume distribution of Samples 1, 2 and 3 highlighting the differences in interparticle pore width ($d_{i\text{-}p}$)

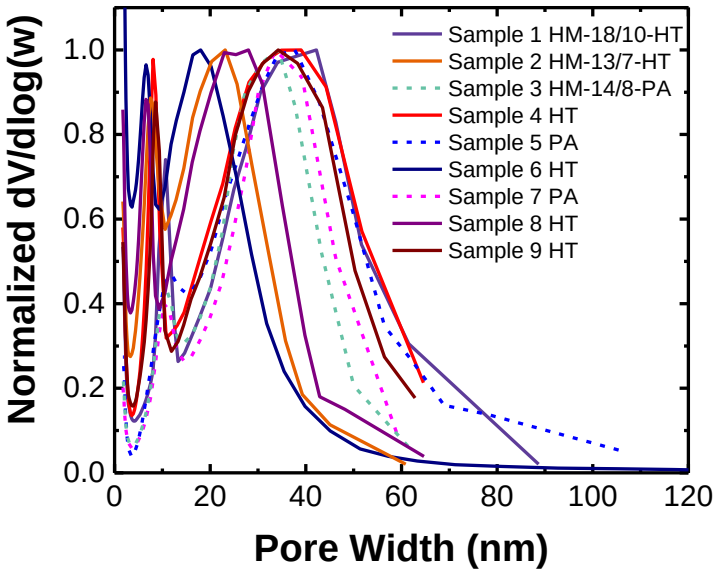

Figure ES5. Normalized pore volume distribution of Samples 1-9